

# New TCO for Use as Transparent Front Contact in Chalcopyrite Thin Film Solar Cells

vorgelegt von

M. Sc.

Darja Erfurt

geb. in Nowosibirsk, Russland

von der Fakultät IV - Elektrotechnik und Informatik  
der Technischen Universität Berlin  
zur Erlangung des akademischen Grades

Doktorin der Ingenieurwissenschaften

- Dr.-Ing. -

genehmigte Dissertation

Promotionsausschuss

Vorsitzender: Prof. Dr. Jürgen Bruns

Gutachter: Prof. Dr. Bernd Szyszka

Prof. Dr. Rutger Schlatmann

Prof. Dr. Günter Bräuer

Tag der wissenschaftlichen Aussprache: 10.01.2019

Berlin 2019



---

## Table of Contents

---

<b>Abstract</b>	<b>iv</b>
<b>Zusammenfassung</b>	<b>v</b>
<b>1 Introduction</b>	<b>1</b>
<b>2 Fundamentals</b>	<b>5</b>
2.1 Transparent Conductive Oxide . . . . .	5
2.1.1 Electrical Conductivity . . . . .	5
2.1.2 Scattering mechanisms . . . . .	7
2.1.3 Optical properties . . . . .	9
2.1.4 Indium oxide based high mobility TCOs . . . . .	11
2.2 CIGS solar cells . . . . .	15
2.2.1 Basic Principles of a CIGS Solar Cell . . . . .	15
2.2.2 Solar Cell parameters . . . . .	16
2.2.3 Module structure . . . . .	19
<b>3 Experimental Details</b>	<b>21</b>
3.1 Sample Preparation . . . . .	21
3.1.1 Indium Oxide Based Layer Preparation . . . . .	21

3.1.2	CIGS Solar Cell Fabrication . . . . .	25
3.2	Characterization Techniques . . . . .	28
3.2.1	Material Characterization . . . . .	29
3.2.2	Device Characterization . . . . .	34
<b>4</b>	<b>Sputtered Hydrogen doped Indium Oxide</b>	<b>36</b>
4.1	Structural Properties . . . . .	37
4.2	Electrical Properties . . . . .	41
4.3	Optical Properties . . . . .	45
4.4	Stability . . . . .	47
4.5	Strategies to improve the electro-optical properties after annealing in air . . . . .	50
4.6	Conclusion . . . . .	52
<b>5</b>	<b>Substrate Influences on Growth Mechanism and Properties</b>	<b>54</b>
5.1	Sputtered Zn(O,S) and ZnO films on glass . . . . .	54
5.2	Sol-Gel Indium - and Gallium Oxide Layers on glass . . . . .	67
5.3	Polycrystalline CIGS and textured glass . . . . .	71
5.3.1	Detrimental effects on the electron mobility . . . . .	75
5.4	Strategies to improve the electron mobility of hydrogen doped indium oxide based TCOs on CIGS . . . . .	88
5.4.1	Spin Coated Sol-Gel Layers . . . . .	88
5.4.2	Etching of the CIGS Surface . . . . .	90
5.4.3	Influence of TCO thickness . . . . .	93
5.5	Stability of IOH thin films . . . . .	95
5.6	Conclusion . . . . .	98

---

<b>6</b>	<b>Application of Indium Oxide based TCOs in CIGS solar cells</b>	<b>101</b>
6.1	Basic Requirements for the Application as Front Contact . . . . .	102
6.1.1	Band alignment IOH/ZnO . . . . .	102
6.1.2	Effect of Post Deposition Thermal Treatment on CIGS Solar Cells . . . . .	106
6.2	Challenges in the Application as Front Contact in CIGS Modules . . . . .	115
6.3	Application of strategies for improved TCO electron mobility in CIGS solar cells	121
6.3.1	Spin Coated Sol-Gel Layer . . . . .	121
6.3.2	Etched CIGS . . . . .	125
6.3.3	Increase of TCO thickness . . . . .	128
6.4	Conclusion . . . . .	130
<b>7</b>	<b>Conclusions and Outlook</b>	<b>133</b>
<b>A</b>	<b>Supplementary Information</b>	<b>138</b>
A.1	General description of standard characterization methods . . . . .	138
A.2	Additional information concerning investigations of IOH layers on ZnO . . . . .	142
A.3	Additional information concerning investigations of the low TCO electron mobility on CIGS samples . . . . .	145
	<b>Symbols and Acronyms</b>	<b>151</b>
	<b>Bibliography</b>	<b>153</b>
	<b>List of Publications</b>	<b>171</b>
	<b>Acknowledgement</b>	<b>174</b>

## Abstract

In this thesis the applicability of high-mobility indium oxide based transparent conductive oxides (TCOs) as front contact in  $\text{Cu}(\text{In,Ga})(\text{S,Se})_2$  (CIGS) solar cells and modules was investigated. The unique trade-off between optical and electrical properties promises improved short circuit current densities compared to conventional CIGS device configurations, in particular in CIGS modules. By doping indium oxide films with hydrogen an amorphous growth can be achieved. A subsequent thermal treatment results in solid phase crystallization and high electron mobilities.

In order to process CIGS modules the deposition process of hydrogen doped indium oxide was first scaled up using an in-line pulsed DC magnetron sputtering tool. The structural, electrical and optical properties were studied in dependence on the deposition conditions water vapor and oxygen partial pressure as well as on the annealing atmosphere.

Furthermore, influences of sputtered  $\text{Zn}(\text{O,S})$  and  $\text{ZnO}$  as well as spin coated sol-gel  $\text{In}_x\text{O}_y$  and  $\text{Ga}_x\text{O}_y$  sub-layers on the structural and electrical properties of  $\text{In}_2\text{O}_3\text{:H}$  were investigated. It was found, that the poly-crystalline structure of  $\text{ZnO}$  promotes crystalline growth of  $\text{In}_2\text{O}_3\text{:H}$  films during deposition and thus results in poor electrical properties. In contrast an amorphous sub-layer, such as, here,  $\text{Zn}(\text{O,S})$  or  $\text{Ga}_x\text{O}_y$  had no adverse effect on the properties of  $\text{In}_2\text{O}_3\text{:H}$  films. The rough structure of CIGS layers, in particular spiky grain edges and sharp recessions induced void formation in indium oxide TCOs deposited by sputtering or reactive plasma deposition, regardless of their crystallinity fraction after deposition or the deposition conditions in general. Due to the presence of voids the films exhibit low electron mobilities, which did not improve sufficiently after annealing. The consequently increased sheet resistance resulted in a limited fill factor when applied in CIGS modules. We therefore developed strategies to improve the electron mobility of the indium oxide based TCOs when grown on rough CIGS samples and tested the applicability in CIGS devices. Furthermore, the influence of the thermal treatment, as required in order to crystallize the amorphous grown indium oxide films, on the solar cell performance was studied.

The investigations point out challenges and provide appropriate strategies and possible solutions for the successful implementation of TCOs with high mobility in CIGS devices in order to demonstrate the potential for improving CIGS solar cell and module efficiencies.

## Zusammenfassung

In dieser Arbeit wurde die Anwendbarkeit von Indiumoxid-basierten transparenten leitfähigen Oxiden (TCOs) mit hoher Elektronenbeweglichkeit als Frontkontakt in  $\text{Cu(In,Ga)(S,Se)}_2$  (CIGS) Solarzellen und -Modulen untersucht. Der spezifisch gute Kompromiss zwischen optischen und elektrischen Eigenschaften verspricht im Vergleich zu herkömmlichen Konfigurationen, insbesondere bei CIGS-Modulen, verbesserte Kurzschlussstromdichten. Durch Dotierung von Indiumoxidschichten mit Wasserstoff kann ein amorphes Wachstum erreicht werden. Eine anschließende thermische Behandlung führt zu Festphasenkristallisation und hohen Elektronenbeweglichkeiten.

Zur Herstellung von CIGS-Modulen wurde der Abscheidungsprozess von wasserstoffdotiertem Indiumoxid zunächst unter Verwendung einer in-line gepulsten DC-Magnetron-Sputteranlage skaliert. Die strukturellen, elektrischen und optischen Eigenschaften wurden in Abhängigkeit von den Abscheideparametern Wasserdampf- und Sauerstoffpartialdruck, sowie der Atmosphäre der Wärmebehandlung untersucht.

Weiterhin wurden Einflüsse von gesputterten  $\text{Zn(O,S)}$  und  $\text{ZnO}$  sowie von spin - beschichteten Sol-Gel  $\text{In}_x\text{O}_y$  und  $\text{Ga}_x\text{O}_y$  Unterschichten auf die strukturellen und elektrischen Eigenschaften von  $\text{In}_2\text{O}_3\text{:H}$  untersucht. Es wurde festgestellt, dass die polykristalline Struktur von  $\text{ZnO}$  das kristalline Wachstum von  $\text{In}_2\text{O}_3\text{:H}$ -Filmen schon während der Abscheidung fördert und somit zu schlechten elektrischen Eigenschaften führt. Im Gegensatz dazu hatte eine amorphe Unterschicht, wie hier  $\text{Zn(O,S)}$  oder  $\text{Ga}_x\text{O}_y$  keine negativen Auswirkungen auf die diesbezüglichen Eigenschaften von  $\text{In}_2\text{O}_3\text{:H}$ -Filmen. Die raue Struktur der CIGS-Schichten, insbesondere scharfe Kornränder und spitze Täler, induzieren die Bildung von Hohlräumen in den durch Sputtern oder reaktiver Plasmaabscheidung abgeschiedenen Indiumoxid-TCOs, unabhängig von deren Kristallinität nach der Abscheidung oder den Abscheidebedingungen im Allgemeinen. Durch das Auftreten der Hohlräume wiesen die Schichten eine geringe Elektronenbeweglichkeit auf, die sich nach dem Tempern nicht ausreichend verbesserte. Der damit verbundene erhöhte Schichtwiderstand führte beim Einsatz in CIGS-Modulen zu einem begrenzten Füllfaktor. Wir entwickelten daher Strategien zur Verbesserung der Elektronenbeweglichkeit der auf Indiumoxid basierenden TCOs für den Einsatz in rauen CIGS-Proben und testeten deren Anwendbarkeit in Bauteilen. Weiterhin wurde der Einfluss der thermischen Behandlung auf die Eigenschaften der Solarzelle untersucht. Das Tempern ist erforderlich, um die amorph gewachsenen Indiumoxidschichten zu kristallisieren.

Die Untersuchungen weisen auf Probleme hin und liefern entsprechende Strategien und Lösungsmöglichkeiten für die erfolgreiche Implementierung von TCOs mit hohen Beweglichkeiten in CIGS-Bauteilen, um das Potenzial zur Verbesserung der CIGS-Solarzellen- und Modulwirkungsgrade aufzuzeigen.



# CHAPTER 1

---

## Introduction

---

In the last decades the demand for energy has increased drastically, impacting the environment by e.g. CO<sub>2</sub> emission and the corresponding increase in global temperature. In order to protect the environment, a change in energy production and consumption is needed. In 2015 the historic climate accord aspired a limit of the rise of the average global temperature to 2 °C until 2050. A key aspect for the fulfilment of this target is the development of renewable energies. In 2015 only 25 % of the electricity were generated by renewables. According to the Roadmap of the International Renewable Energy Agency (IRENA) [1] an increase of up to 85 % has to be realized to limit the temperature rise to 2 °C. As the main sources for electricity generation wind (36 %) and solar photovoltaic (22 %) are suggested. To satisfy this need, photovoltaic devices have to be further developed to achieve higher efficiencies and to reduce the costs. Additionally new application ranges, such as building integrated photovoltaic, need to evolve. One approach is the application of thin film photovoltaic.

Cu(In,Ga)(S,Se)<sub>2</sub> (CIGS) is one of the most promising materials in this field due to high efficiencies, which are comparable to Si-based solar cells, low energy consumption, short energy payback time and minimized material consumption [2]. In 2017 SolarFrontier presented a record cell efficiency of 22.9 % [3]. However, the commercial module efficiency is far behind this value, in the range of 14 % to 15 %. Bermudez et al. [4] reviewed the challenges of the cell-to-module efficiency gap in Cu(In,Ga)(S,Se)<sub>2</sub>. According to this study the main power losses in CIGS modules with respect to CIGS solar cells are optical and caused by the front contact (transparent conductive oxide (TCO), typically ZnO:Al). Thus the relative power losses due to the increased optical absorption of the TCO in a module is stated to be  $\approx 40\%$  with regard to the application in solar cells.

To counteract these losses new alternative TCOs are required, which have to satisfy several demands. The films must have a wide bandgap of  $> 3$  eV and high transmittance to ensure a high

amount of photons absorbed by the CIGS layer. Furthermore the films must be highly conductive with resistivity in the range of  $< 10^{-3} \Omega\text{cm}$  and typical sheet resistances of around  $10 \Omega/\text{Sq}$  or less due to the absence of a contact grid. To achieve such low sheet resistances, the TCO film thickness consequently must be higher in modules compared to cells, where the lateral current collection paths are shorter, resulting in additional optical losses. One approach to minimize these losses is the implementation of new high-mobility TCOs. Due to their excellent trade-off between optical and electrical properties they show high conductivity with low optical absorption in the relevant range. Therefore the same sheet resistances can be reached as with ZnO, but the optical losses can be minimized, resulting in higher photo current. Amorphous grown indium oxide based films with various dopants, such as hydrogen, W, Zr, Mo or Ti showed electron mobilities  $> 80 \text{ cm}^2/\text{Vs}$  [5–10] after solid phase crystallization, initiated by a post deposition thermal treatment. These properties make these materials promising candidates as front contact in CIGS modules. Therefore in this thesis we investigate the applicability of high mobility indium oxide based TCOs, namely  $\text{In}_2\text{O}_3:\text{H}$  and  $\text{In}_2\text{O}_3:\text{H,W}$  and the feasibility of a large-scale deposition process.

This thesis is structured as follows:

*Chapter 2* provides basic fundamental knowledge concerning the materials and devices studied in this thesis. This includes a review of the principles of transparent conductive oxides, the material indium oxide in general, and CIGS solar cells and modules.

*Chapter 3* provides detailed information about the experimental methods used in this thesis. First the sample preparation is explained. Then, the characterization techniques used to determine the material and device properties are described.

*Chapter 4* presents the properties of hydrogen doped indium oxide, which was deposited by a large scale in-line pulsed direct current magnetron sputtering tool. Here the influence of the deposition conditions water vapor pressure and oxygen supply are identified. Furthermore the influence of the annealing in different atmospheres is investigated.

*Chapter 5* identifies influences of the substrate and sub-layers on the growth of indium oxide based TCOs. This includes investigations of the growth on sputtered ZnO and Zn(O,S), as well as on spin coated  $\text{In}_x\text{O}_y$  and  $\text{Ga}_x\text{O}_y$  layers on planar glass substrates. Furthermore the impact of textured substrates, such as textured glass, and sub-layers, such as poly-crystalline CIGS, is studied. Here the roughness and the local slope of the sub-layers was correlated with the structure and the resulting electrical properties of the indium oxide films. Strategies to mitigate these influences and possible adverse effects are presented. Lastly the stability of hydrogen doped indium oxide on rough substrates is discussed.

---

*Chapter 6* addresses the application of indium oxide based TCOs as front contact in CIGS solar cells and modules. First general requirements for the implementation are discussed. This includes investigations of the band alignment at the interface of the highly resistive layer and the TCO and the impact of the post deposition thermal treatment on the solar cell performance. Annealing is required in order to initiate solid phase crystallization of the amorphous phase in the indium oxide based films. Based on these results, hydrogen doped indium oxide is implemented as a front contact in CIGS modules. The impact of the growth and properties of the indium oxide based films on the module performance is discussed in more detail. The approaches presented in chapter 5 to overcome the adverse effect of the CIGS roughness are applied and the performance of the corresponding CIGS solar cells is investigated.

*Chapter 7* summarizes the findings of this thesis and presents suggestions for future research.

At the end of each section the main findings are summarized. The main approaches that will be studied in this thesis can be summarized as followed:

- **Development of a large-scale deposition process with a subsequent post deposition thermal treatment feasible for industry-like production** The application of high mobility TCOs require a large scale deposition and annealing process which is feasible for industry-like production. We therefore investigated hydrogen doped indium oxide films which were deposited by in-line pulsed direct current magnetron sputtering and the influences of the deposition parameters water vapor, oxygen supply as well as the annealing conditions.
- **Growth on typical sub-layers** In CIGS solar cells the front contact is deposited on different sub-layers, typically ZnO or in an alternative configuration Zn(O,S). These layers can influence the growth of indium oxide based TCOs, such as  $\text{In}_2\text{O}_3\text{:H}$ . This influence is investigated using model structures of sub-layers deposited directly on planar glass.
- **Growth on textured sub-layers/substrates** As CIGS absorber have a specific roughness, the influence on the growth is investigated in detail for  $\text{In}_2\text{O}_3\text{:H}$  and  $\text{In}_2\text{O}_3\text{:H,W}$  thin films for different deposition techniques.
- **Band-line up** The successful implementation of high mobility TCOs such as  $\text{In}_2\text{O}_3\text{:H}$  requires a suitable band-alignment to the sub-layer in the CIGS cell, typically intrinsic ZnO. Therefore the valence and conduction band offsets of  $\text{In}_2\text{O}_3\text{:H}$  and ZnO are studied.
- **Impact of thermal treatment on CIGS solar cells** In order to initiate solid phase crystallization of the amorphous phase of indium oxide based TCOs a post deposition thermal treatment is required, which will also influence the CIGS solar cell.

- **Front contact in CIGS modules** The implementation of hydrogen doped indium oxide as front contact in CIGS modules is investigated in order to improve the short circuit current density and thus the overall efficiency of CIGS modules.

# CHAPTER 2

---

## Fundamentals

---

### 2.1 Transparent Conductive Oxide

Conductive materials (e.g. metals) typically have a low optical transparency while oxide insulators (e.g. glass) are very transparent. Transparent conductive oxides, which are wide band gap semiconductors ( $E_g > 3$  eV), combine both benefits by possessing high conductivity and high transmittance in the visible (and near infrared) optical range at the same time. Due to this unique trade-off of the opto-electrical properties transparent conductive oxides are of high interest for a broad field of applications, such as flat panel displays, optical coatings or photovoltaic devices [11, 12]. The most common materials used are n-type aluminum doped zinc oxide (ZnO:Al or AZO) and tin doped indium oxide ( $\text{In}_2\text{O}_3\text{:Sn}$  or ITO). Over the last years high-mobility TCOs have attracted much attention and have been investigated by several research groups, as their opto-electrical properties are even more promising. An alternative to TCOs is graphene, which is a single layer of carbon and shows very high electron mobility, but has no band gap [13].

#### 2.1.1 Electrical Conductivity

The high conductivity of n-type TCOs results from degenerate doping, as the fermi level is shifted into the conduction band, due to the very high charge carrier density ( $n_e$ ), which can be treated as a free electron gas. Therefore, no additional activation energy is required to excite electrons in the conduction band. According to the Mott criteria [14, 15]

$$n_{deg}^{1/3} a_0^* \approx 0.25 \tag{2.1}$$

the required charge carrier density to induce degeneration ( $n_{deg}$ ) can be estimated. Here  $a_0$  is the effective Bohr radius

$$a_0^* = \frac{\hbar^2 \epsilon^M \epsilon_0}{\pi m_e^* e^2} \quad (2.2)$$

where  $\epsilon^M$  is the static dielectric constant of the host lattice,  $\epsilon_0$  the vacuum permittivity,  $m_e^*$  the effective electron mass and  $e$  the elementary charge [16]. Hamberg et al. estimated for  $\text{In}_2\text{O}_3$ <sup>1</sup>  $a_0^* \approx 1.3$  nm and degeneration when  $n_e > n_c \approx 6 \times 10^{18} \text{ cm}^{-3}$ . As typical charge carrier densities in indium oxide based TCOs lie in range of  $10^{20} \text{ cm}^{-3}$  to  $10^{21} \text{ cm}^{-3}$ , the films are considered to be degenerated. The free electrons can hence be described by the Drude model [17]. Within the free electron gas the electrons diffuse and are accelerated by an external field with

$$\vec{E} = \vec{e}_x E_0. \quad (2.3)$$

The equation of motion describes the interactions of a single electron in the electric field:

$$-e \vec{E} = m_e^* \frac{d^2 x}{dt^2} + \frac{m_e^*}{\tau} \frac{dx}{dt}. \quad (2.4)$$

Due to collisions, e.g. with impurities in the lattice, the electrons are scattered. For the stationary case in a constant electric field the drift velocity  $\vec{v}_d$  can be calculated to

$$\vec{v}_d = \frac{dx}{dt} = \frac{e\tau}{m_e^*} \vec{E} = \mu_e \vec{E} \quad (2.5)$$

where  $\tau$  is the average time between collisions and  $\mu_e$  the electron mobility with

$$\mu_e = \frac{e\tau}{m_e^*}. \quad (2.6)$$

Hence the ensemble of free electrons results in the current density  $\vec{j}$  with

$$\vec{j} = -n_e e \vec{v}_d = n_e e \mu_e \vec{E} = \sigma \vec{E} \quad (2.7)$$

where  $\sigma$  is defined as the conductivity with

$$\sigma = \frac{1}{\rho} = \frac{n e^2 \tau}{m_e^*} = n_e e \mu_e. \quad (2.8)$$

The inverse of the conductivity is defined as the resistivity  $\rho$ . In technical studies commonly the sheet resistance  $R_{Sq}$  with

$$R_{Sq} = \frac{\rho}{d} \quad (2.9)$$

is used to describe the films properties with  $d$  as the thickness of the film. Hence, an improved film conductivity can be realized by an increased charge carrier density or electron mobility. Additionally the sheet resistance of the films can be reduced by an increase of the film thickness [18, 19]. The electron mobility depends on the relaxation time  $\tau$ . With increased scattering, the electron mobility drops. Therefore scattering mechanism are described in the following.

---

<sup>1</sup> $m_e^* = 0.35 m_e$  for  $\text{In}_2\text{O}_3$  [16];  $\epsilon^M = \epsilon(0) = 8.9$

### 2.1.2 Scattering mechanisms

As mentioned above, low resistivities can be achieved with high carrier concentrations and high mobilities. Heavy doping can result in several adverse effects, such as the formation of scattering centers, e.g. ionized dopant atoms, which can reduce the electron mobility. Furthermore phase separation can occur if the impurity concentration exceeds the solubility limit. Also a high charge carrier concentration results in the absorption of light at longer wavelengths. This effect is called free carrier absorption and will be described in detail later. To overcome these effects and nevertheless reduce the resistivity the electron mobility can be increased. However, the electron mobility can be limited by several effects. The most important scattering mechanisms reported in literature are ionized impurity scattering ( $\mu_i$ ), neutral impurity scattering ( $\mu_n$ ), scattering at grain boundaries ( $\mu_g$ ) and lattice vibration scattering ( $\mu_l$ ). These effects are described in the following, based on the explanations stated in Luque et al. [20]. However, scattering due to further effects (addressed here as  $\mu_x$ ) is also possible. These aspects are for example surface roughness scattering, as shown e.g. for films applied in n-type metal-oxide semiconductor (NMOS) transistors [21] or scattering at the interface of amorphous and crystalline phases, as described for indium oxide by Buchholtz et al. [22].

The scattering effects on the electron mobility can therefore be described by the following equation:

$$\frac{1}{\mu_e} = \frac{1}{\mu_i} + \frac{1}{\mu_l} + \frac{1}{\mu_g} + \frac{1}{\mu_n} + \frac{1}{\mu_x} \quad (2.10)$$

#### **Ionized impurity scattering**

In heavily doped TCOs a large number of ionized impurities can occur, such as oxygen vacancies, dopants or excess metal atoms. Such impurities act as strong scattering centers for electrons in degenerated semiconductors, where typically the scattering increases with increased charge carrier density. According to the Brooks-Herring-Dingle model [23, 24] the contribution to the electron mobility  $\mu_i$  can be described with [20]

$$\mu_i = \frac{3(\epsilon_0\epsilon_r)^2 h^3 n_e}{Z^2 (m_e^*)^2 e^3 n_i F_i(\xi)} \quad (2.11)$$

where  $\epsilon_0$  and  $\epsilon_r$  are the vacuum and relative static permittivity, respectively,  $h$  is Planck's constant,  $Z$  and  $n_i$  are the charge and concentration of the impurities, respectively and

$$F_i(\xi) = \ln(1 + \xi) - \frac{\xi}{1 + \xi} \quad (2.12)$$

and

$$\xi = (3\pi^2)^{1/3} \frac{\epsilon_0 \epsilon_r \hbar^2 n_e^{1/3}}{m_e^* e^2}. \quad (2.13)$$

In an uncompensated semiconductor with fully ionized charge carriers the charge carrier density is equal to the impurity density ( $n_e = n_i$ ).

### Neutral impurity scattering

Neutral impurities, such as atoms, induce scattering. The corresponding contribution to the mobility  $\mu_n$  can be written as

$$\mu_n = \frac{m_e^* e^3}{20 \epsilon_0 \epsilon_r \hbar^3 n_N} \quad (2.14)$$

where  $\hbar = \frac{h}{2\pi}$  and  $n_N$  is the density of neutral centers [25, 26]. In heavily doped TCOs neutral impurity scattering is assumed to have a minor impact.

### Grain boundary scattering

Grain boundaries are present in poly-crystalline materials and can be described as a quasi-two dimensional disruption of the atomic structure which contain interface states. These states can trap charges and result in a potential barrier that hinders electrons to pass between neighboring grains. This becomes typically crucial, when the grain size is comparable to the mean free path of the electrons  $\lambda_{mfp}$ , which is given by [19]:

$$\lambda_{mfp} = \frac{\hbar \mu_e}{e} (3\pi^2 n_e)^{(1/3)} \quad (2.15)$$

and is valid for values  $n_e > 1 \cdot 2 \times 10^{19} \text{ cm}^{-3}$ . In TCOs these values typically are in the range of a few nm and thus much smaller than typical grain sizes. However, for electron traps, a depletion region forms on the sides of the grain boundary. The current transport over the barrier can be described by thermionic emission [27]. Petritz [28] developed a model to describe the mobility which results from grain boundary scattering. The model was extended by Seto [29] and Baccarani et al. [30] and can be written as

$$\mu_g = \frac{eL}{\sqrt{2\pi m_e^* kT}} \exp\left(-\frac{\phi_b}{kT}\right) \quad (2.16)$$

where  $L$  is the grain size,  $k$  the Boltzmann constant,  $T$  the temperature and  $\phi_b$  is the grain boundary potential (barrier height)

$$\phi_b = \frac{e^2 N_T^2}{8 \epsilon_0 \epsilon_r N}, \text{ for } L * N > N_T \quad (2.17)$$

$$\phi_b = \frac{e^2 L^2 N}{8\epsilon_0 \epsilon_r}, \text{ for } L * N < N_T \quad (2.18)$$

where  $N_T$  is the surface trap density. In general intergrain properties can be identified by hall mobilities, as here the influence of the grain boundaries is included. According to the Drude theory the electro-optical properties are connected [17]. But, however, optical mobilities do only provide information on the intragrain properties. The amplitude of oscillating electrons under the influence of an electromagnetic field is about  $10^{-7}$  nm for each volt per meter at visible and near infrared frequencies, thus much smaller than typical grain sizes of TCO films. Therefore grain boundaries are typically not encountered by the oscillating electrons. Grain boundary scattering has typically only a minor influence in TCOs, but must still be considered.

### Lattice vibration scattering

Lattice vibration scattering generally increases at higher temperatures, as the lattice vibration increases and the lattice may deform. Thus the electron mobility can be limited by acoustic phonon scattering. The mobility can be described by the following equation

$$\mu_l = \frac{2\sqrt{2\pi}e\hbar^4 C_l}{2(m_e^*)^{5/2} E_d^2 (kT)^{3/2}} \quad (2.19)$$

with  $C_l$  as the longitudinal elastic constant and  $E_d$  is the deformation potential constant in eV. Furthermore also optical phonons can lead to scattering [19].

### 2.1.3 Optical properties

The interaction of an electro-magnetic field (i.e., light) and matter can lead to three fundamental wavelength ( $\lambda$ ) dependent phenomena, typically taking place simultaneously: transmittance (T), reflection (R) and absorption (R). The relation can be expressed as

$$1 = A(\lambda) + T(\lambda) + R(\lambda). \quad (2.20)$$

Figure 2.1 (a) shows as an example the transmittance, reflectance and absorption spectra of a typical TCO, deposited on glass. The spectra can be categorized in 3 significant areas: I) fundamental absorption due to excitation of electrons from the valence into the conduction band, dependent on the optical band gap; II) optical window, typical area for use in several applications, as the absorption is very low (typically < 10 %); III) free carrier absorption due to collective oscillations of the free carriers.

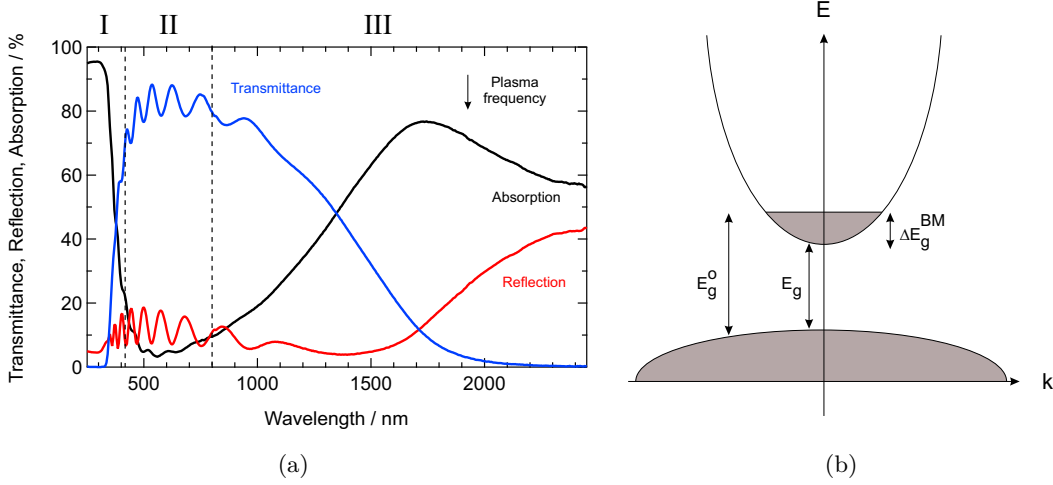


Figure 2.1: (a) Transmittance, reflectance and absorption as example of a hydrogen doped indium oxide film after deposition on glass in dependence of the wavelength; three specific areas are marked: I) fundamental absorption, II) optical window, III) free carrier absorption; (b) Schematic explanation of the Burstein Moss shift

The absorption of light in a material is described by Lambert-Beer's Law

$$A_{int}(d, \lambda) = 1 - e^{-\alpha(\lambda)d} \quad (2.21)$$

where  $d$  is the distance passed by the light within the medium and  $\alpha$  is the specific absorption coefficient. In degenerate semiconductors the states at the bottom of the conduction band are filled with electrons. Thus the lowest empty states of the conduction band shift towards higher energies. The difference of the conduction band minimum and the energy of the lowest empty states, that can be filled with electrons from the valence band is called Burstein-Moss shift  $\Delta E_g^{BM}$  [31]:

$$\Delta E_g^{BM} = E_g^o - E_g = \frac{\hbar^2}{2m_e^*} (3\pi^2 n_e)^{2/3} \quad (2.22)$$

with  $E_g^o$  as the enlarged band gap.

The interaction of matter with light can further be described by the the complex dielectric constant  $\epsilon$

$$\epsilon(\omega) = \epsilon_1(\omega) + i\epsilon_2(\omega) = (n + ik)^2. \quad (2.23)$$

where  $\omega$  is the frequency,  $n$  as the refractive index and  $k$  as the extinction coefficient, which is related to the absorption coefficient  $\alpha$  with

$$\alpha = \frac{2k\omega}{c}. \quad (2.24)$$

with  $c$  as the speed of light. According to Pflug et al. [32] the dielectric constant in TCOs can be expressed as

$$\epsilon_{TCO}(\omega) = \epsilon_{\infty} + \chi_{BG} + \chi_{FC} \quad (2.25)$$

where  $\epsilon_{\infty}$  is a constant, the high-frequency permittivity limit.  $\chi_{BG}$  is the contribution of the band gap and  $\chi_{FC}$  the contribution from the free carriers, which can be expressed as

$$\chi_{FC} \approx \frac{\omega_p^2}{\omega^2 + i\omega\omega_{\tau}}. \quad (2.26)$$

Here  $\omega_p$  is the plasma frequency

$$\omega_p = \sqrt{\frac{e^2 n_e}{\epsilon_0 m^*}} \quad (2.27)$$

and  $\omega_{\tau}$  the damping frequency, which in first approximation can be expressed as

$$\omega_{\tau} = \frac{1}{\tau} = \frac{e}{m^* \mu_e}. \quad (2.28)$$

To illustrate the correlation of the electrical and optical properties of TCOs, we estimated the absorption of two TCO films with electron mobilities of 20 cm<sup>2</sup>/Vs and 100 cm<sup>2</sup>/Vs with varied charge carrier densities according to the calculation procedure described by Luque et al. [20]. The absorption was correlated with  $E_{AM1.5G}(\lambda)$  the AM1.5 global solar spectrum (ASTM standard G173-03 [33]) by the following equation [34]:

$$A_{int.AM1.5G} = \frac{\int_{400nm}^{1100nm} A(\lambda) E_{AM1.5G}(\lambda) d\lambda}{\int_{400nm}^{1100nm} E_{AM1.5G}(\lambda) d\lambda}. \quad (2.29)$$

The evaluation of the estimated integral Absorption  $A_{int.AM1.5G}$  over the corresponding sheet resistance of the two TCO films is shown in Figure 2.2.

Due to the low electron mobilities (here 20 cm<sup>2</sup>/Vs) higher charge carrier densities are required to achieve similar sheet resistances compared to films with higher electron mobilities (here 100 cm<sup>2</sup>/Vs), according to equations (2.8) and (2.9). The increased charge carrier density results in an increased free carrier absorption in the NIR region and thus to higher integral absorption values. The graph demonstrates the importance of high electron mobilities in transparent conductive oxides to minimize parasitic absorption.

#### 2.1.4 Indium oxide based high mobility TCOs

As shown in Figure 2.2 high electron mobilities are required to achieve low sheet resistances and low optical absorption at the same time. According to equation (2.6) the electron mobility can be improved by increasing  $\tau$ , the time between collisions of electrons, or by reducing the effective

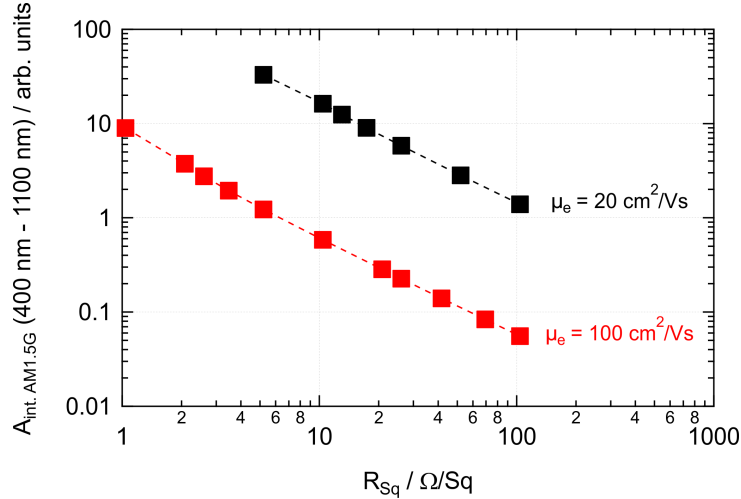


Figure 2.2: Development of the integral absorption  $A_{int.AM1.5G}$  in the range 400 nm to 1100 nm over the calculated sheet resistance for TCO films with 300 nm thickness and electron mobilities of  $\mu_e = 20 \text{ cm}^2/Vs$  and  $\mu_e = 100 \text{ cm}^2/Vs$ , respectively; the carrier density was varied to achieve different sheet resistances

mass  $m_e^*$ . An increased  $\tau$  can be achieved when the material exhibit a low defect density, e.g. low carrier density (ionized impurities), few grain boundaries or few neutral defects. Reduction of the effective mass requires semiconductors with a widely dispersed conduction band [35].

One of the most common transparent conductive oxides is ZnO:Al (AZO) due to its availability and adequate trade-off between optical and electrical properties. However, typical electron mobilities of sputtered ZnO:Al films with substrate temperatures below 300 °C are in the range of 10  $\text{cm}^2/Vs$  to 40  $\text{cm}^2/Vs$  [36–41]. Another common TCO is  $\text{In}_2\text{O}_3:\text{Sn}$  (ITO). Typical electron mobilities are in the range of 20  $\text{cm}^2/Vs$  to 50  $\text{cm}^2/Vs$  [42–45] for sputtered ITO films with substrate temperatures below 300 °C. Higher electron mobilities were also reported for both materials, but for special conditions, such as high deposition temperatures or specific substrates.

In recent years researchers reported about high mobility TCOs with electron mobilities above 80  $\text{cm}^2/Vs$  by doping indium oxide with H [46–48] and/or metals, such as Zr [49], W [5, 7], Mo [6], Ce [5, 50] or Ti [6]. The deposition and post deposition thermal treatment, if required, were conducted at temperatures below 300 °C. Thus, low resistivities with low absorption can be achieved. These materials show therefore a high potential for the application in photovoltaic devices, such as CIGS solar cells.

In this thesis indium oxide based transparent conductive oxides are studied, in particular hydrogen doped indium oxide ( $\text{In}_2\text{O}_3:\text{H}$ , or IOH) and indium oxide co-doped with hydrogen and tungsten ( $\text{In}_2\text{O}_3:\text{H,W}$  or IWO:H). Thus, in the following first fundamental characteristics of undoped  $\text{In}_2\text{O}_3$  are presented before the properties of  $\text{In}_2\text{O}_3:\text{H}$  and  $\text{In}_2\text{O}_3:\text{H,W}$  films are discussed.

## In<sub>2</sub>O<sub>3</sub>

In general In<sub>2</sub>O<sub>3</sub> crystallizes in three main polymorphic structures: (i) a high-temperature rhombohedral corundum structure (space group R $\bar{3}c$ ), (ii) a cubic bixbyite structure (space group I2<sub>1</sub>3) and (iii) the body centered cubic (bcc) bixbyite structure (space group Ia $\bar{3}$ ) [51]. The latter structure is the most common and stable under standard condition. The lattice parameter is  $a = 10.117 \text{ \AA}$  [52, 53]). Crystalline indium oxide films within this thesis also exhibit the bcc bixbyite structure, which is therefore explained in more detail. Each cubic unit cell consists of 80 atoms, which form 16 formula units. The unit cell can be derived from a  $2 \times 2 \times 2$  supercell structure of calcium fluoride. To retain an ordered structure 25 % of the oxygen atoms are removed from the fluorite structure, thus 48 equivalent oxygen atoms fill the edge positions Wycoff 48e. The indium atoms are located at two different lattice positions, 8 indium atoms occupy In-b (Wycoff 8a) while 24 indium atoms occupy In-d (Wycoff 24d) sites. The atomic positions in bcc structure are shown in Table 2.1. The In-b position is located at the body diagonal of two oxygen vacancies, the bonding length In-O is 2.160  $\text{\AA}$ . The In-d position is located at the face diagonal of the cube and is surrounded by two oxygen vacancies  $V_O$ . This results in 3 different In-O bond lengths: 2.133  $\text{\AA}$ , 2.187  $\text{\AA}$ , and 2.248  $\text{\AA}$  [53].

Table 2.1: Atomic positions in body centered cubic bixbyite structure of indium oxide [53]

Atom	Site	X	Y	Z
In-b	8a	0.2500	0.2500	0.2500
In-d	24d	0.4668	0.0000	0.2500
O	48e	0.3905	0.1529	0.3832

The fundamental (direct) band gap of In<sub>2</sub>O<sub>3</sub> is in the range of 2.6 eV to 2.9 eV and was topic of several studies [54–58], as optical measurements revealed significantly higher band gaps. Walsh et al. [59] revealed that electrical dipole transitions between the valence and conduction bands at the  $\Gamma$  point are prohibited up to 0.8 eV below the valence band maximum. Optical measurements therefore overestimate the band gap. The upper limit of the fundamental band gap was determined as 2.9 eV. The optical band is in the range of 3.75 eV. The effective electron mass  $m_e^*$  of indium oxide is  $0.35m_e$  [16].

### In<sub>2</sub>O<sub>3</sub>:H and In<sub>2</sub>O<sub>3</sub>:H,W

In 2007 Koida et al. [46] reported first that electron mobilities of up to 130 cm<sup>2</sup>/Vs can be reached with hydrogen doped indium oxide deposited by RF sputtering. During the deposition water vapor is introduced into the sputter chamber where water molecules H<sub>2</sub>O can be easily decomposed by plasma into H and OH [60]. H and OH can form In-OH bonds at the growing

surface with an oxygen dangling bond and an In dangling bond, respectively, thus preventing the construction of In-O-In bond networks [61]. Films deposited at lower  $p_{H_2O}$  show an increased density of crystalline nuclei compared to films deposited at increased  $p_{H_2O}$ .

A post deposition thermal treatment leads to solid phase crystallization of the film in the structure of bcc bixbyite  $In_2O_3$  [46]. The presence of abundant crystalline nuclei within the as-deposited film can lead to full crystallization at lower temperatures. Consequently the films exhibit smaller grains [5].

During annealing structural rearrangement eliminates oxygen vacancies  $V_O^{++}$  and releases  $H^+$ . The charge carrier density of the crystallized films is in the range of  $n_e = 1-2 \times 10^{20} \text{ cm}^{-3}$ . Limpijumng et al. [62] reported that both interstitial hydrogen ( $H_i^+$ ) and substitutional hydrogen ( $H_O^+$ ) act as shallow donors in  $In_2O_3$  and are energetically more favorable than doubly charged oxygen vacancies  $V_O^{++}$ , which are deep donors in  $In_2O_3$ . Similar findings were obtained for metal dopants, such as W. The metal dopant substitutes the indium atom, resulting in charged donors (e.g.  $W_{In}^{+++}$ ) [5, 10, 46]. These findings were supported by results of several studies [63–65]. In fact it was found that only a minor amount of hydrogen serves as donors. According to Koida et al. [65] free carrier generation is estimated to occur from 8 %, 17 % and 24 % of hydrogen in the post-annealed films grown at 200 °C at  $p_{H_2O}$  of  $5 \times 10^{-5} \text{ Pa}$ ,  $1 \times 10^{-4} \text{ Pa}$  and  $1 \times 10^{-3} \text{ Pa}$ , respectively. This is similar to the findings of Macco et al. [64], who observed that only  $\approx 4$  % of the hydrogen atoms in crystallized  $In_2O_3:H$  were active dopants. It was found, that the dopant W did not act as an electron donor in the amorphous phase, but got activated as donor by the crystallization process, even in the presence of hydrogen [5].

The high electron mobility of up to  $130 \text{ cm}^2/Vs$  of crystallized films results from the suppressed scattering of doubly charged ionized impurities and the reduced carrier scattering by H-doping. It was found that H atoms that do not contribute to doping are not ionized or neutral impurity scattering centers [46, 64, 65]. Wardenga et al. [66] further proposed hydrogen passivation at grain boundaries as a further origin for the high electron mobility. After crystallization phonon scattering becomes dominant and limits the electron mobility of hydrogen doped indium oxide films [61]. Additionally tungsten doping in  $In_2O_3:H$  was found to produce additional carrier scattering centers. The point defects were associated with W and H or OH species within the  $In_2O_3:H,W$  films.

Following the work of Koida et al. [46] several studies reported about high mobility  $In_2O_3:H$  films deposited by Atomic Layer Deposition [67, 68], Reactive Plasma Deposition [5], radio frequency [48, 68–71] or direct current [72] magnetron sputtering. High mobility  $In_2O_3:H,W$  films could be deposited by Reactive Plasma Deposition [5, 7, 73].

## 2.2 CIGS solar cells

### 2.2.1 Basic Principles of a CIGS Solar Cell

The aim of a solar cell is to convert light into electrical energy. Its configuration can be categorized generally into three parts: a back contact (metal layer), the main absorber layer (semiconductor) and the window layer (several semiconductors). In this thesis CIGS solar cells were used, the layer configuration is sketched in Figure 2.3 (a). Typically on top of the TCO a metal contact grid is evaporated mostly on cells for improved current collection, but, however, also causing shading. In a CIGS solar cell these layers are typically molybdenum as the back contact and  $\text{Cu}(\text{In,Ga})(\text{S,Se})_2$  (or CIGS) as the absorber layer. The window layer comprises the buffer layer, typically CdS, a highly resistive layer, typically intrinsic ZnO, and the front contact, which is the transparent conductive oxide, typically ZnO:Al, or other materials, as discussed in this thesis. The semiconductors are charged oppositely in each sides. The absorber layer is a p-type semiconductor, thus holes are majority charge carriers and electrons are minority charge carriers. The semiconducting components of the window layer are n-type, thus electrons are the majority charge carriers and holes the minority charge carriers. An electrical voltage is generated when the electrons and holes are separated and migrate to the contacts (back and front contact). When connected to an electrical circuit, electrons flow from one contact through the circuit to the other contact. This electron flow is the electrical current generated by a solar cell.

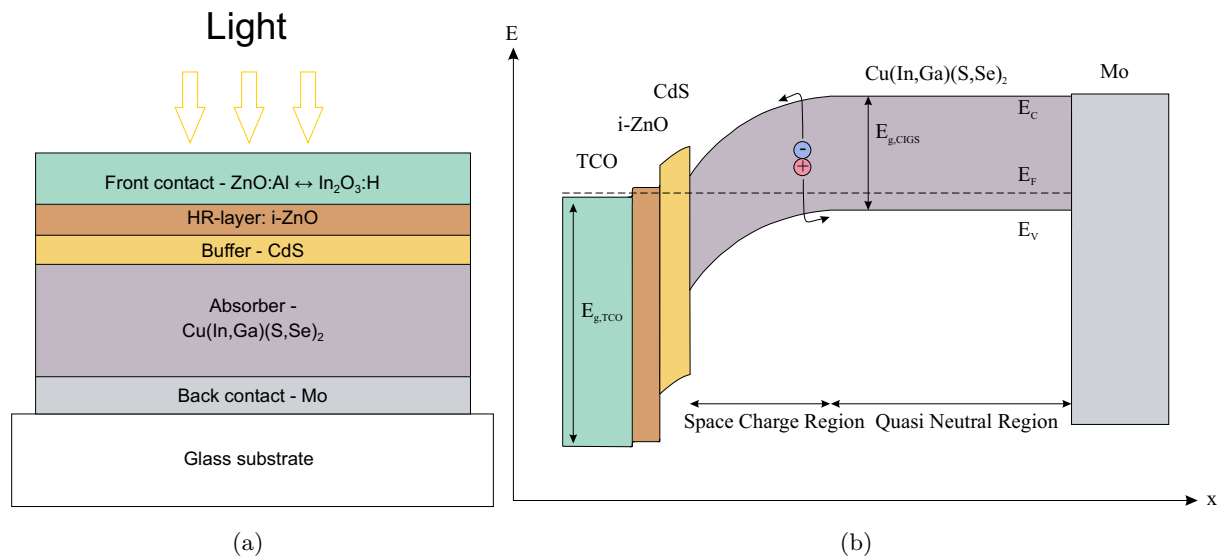


Figure 2.3: (a) Structure of a typical CIGS solar cell; (b) Simplified energy band diagram of a CIGS solar cell in equilibrium

To characterize a solar cell generally a voltage is applied. Operation of the solar cell in the forward direction corresponds to a polarity of the voltage with a negative potential at the front contact (n-range) and a positive potential at the back contact (p-range).

When the solar cell is exposed to light, photons with energy  $h\nu$  penetrate the window layer. Photons with energies lower than the band gap of the window ( $E_g(\text{ZnO}) = 3.3 \text{ eV}$ ;  $E_g(\text{CdS}) = 2.4 \text{ eV}$ ) are transmitted to the CIGS absorber layer. Depending on the composition of the layer, the band gap can vary between about 1.0 eV and 1.7 eV. When the energy of a photon is absorbed, an electron is excited from the valence band ( $E_V$ ) into the conduction band ( $E_C$ ), creating a hole in the valence band (electron hole pair). If the energy of the photon is higher than the band gap, the excited electron will fall back from a higher energy level to the conduction band minimum while the excess energy ( $\Delta E = h\nu - E_g$ ) is converted to heat (thermalization). Typically a CIGS absorber is therefore graded in its composition for optimized photon absorption. The electrons and holes are separated within the space charge region, which leads to the generation of current, otherwise the electron-hole pairs recombine. The space charge region is typically located within the absorber layer, close to the interface window/Cu(In,Ga)(S,Se)<sub>2</sub> and can reach several nm. Photons that are absorbed in the front contact layer typically do not contribute to photo-current collection, but are recombination losses. However, it was shown, that a part of the photons with  $3.2 > h\nu > 2.4 \text{ eV}$  can contribute to photo-current collection, as the thin CdS layer does not absorb all the photons. Furthermore a part of the electron hole pairs created in the buffer layer can still contribute to the photo-current [74]. However, the main part originates from electron hole pairs, which were photogenerated in the absorber layer [75]. The application of wide band gap materials as window layers is therefore of great importance. Figure 2.3 (b) shows a simplified band diagram of a CIGS solar cell as an example. The Fermi level  $E_F$  indicates the occupation of energy states of the bands with charge carriers in the equilibrium. However, when the semiconductors are depicted under non-equilibrium conditions (e.g. under illumination), electrons and holes have their own quasi Fermi level,  $E_{Fn}$  and  $E_{Fp}$ , respectively [76].

### 2.2.2 Solar Cell parameters

A solar cell can be in general described by a one-diode model. The equivalent circuit model is shown in Figure 2.4. The current source indicates the photo-generated current density  $j_{Ph}$ , the diode represents the dark characteristics of the junction with the corresponding current density  $j_{Dark}$ . The series resistance  $R_S$  indicates internal and external ohmic losses while the parallel or shunt resistance  $R_{Sh}$  indicate ohmic shunts. Ideally the series resistance is as low as possible while the shunt resistance is as high as possible to reduce ohmic losses.

The corresponding  $j$ - $V$  characteristic can hence be written as

$$j = j_{Ph} - \underbrace{j_0 \left[ \exp\left(\frac{q(V - jR_S)}{AkT}\right) - 1 \right]}_{j_{Dark}} - \frac{V - jR_S}{R_{Sh}}. \quad (2.30)$$

where  $j_0$  is the reverse saturation current density and  $A$  the diode quality factor, which is in the easiest case  $A = 1$  for back surface and neutral zone recombination, as well as for recombination at the buffer/absorber interface and  $A = 2$  for space charge recombination [75]. However, for real solar cells the one-diode model might be too simple, as different recombination processes can occur. Therefore a second diode is typically introduced parallel to the first diode (two diode model). The two diode model was used in this thesis to simulate the obtained  $j$ - $V$  curves and to calculate the corresponding solar cell parameters. Another approach to describe non-ideal solar cells is given by Scheer et al. [76]. Here in series to the diode, shunt resistance and current source a back-contact diode (reverse direction of the main diode), a series resistance and a so called space charge current limiter are connected. Furthermore inhomogeneities within a solar cell can be described by a multi-diode model [77]. A solar cell can be considered as a network of sub-cells with different electronic qualities, which are represented by the subcells' electronic characteristics with local inhomogeneous material qualities [78].

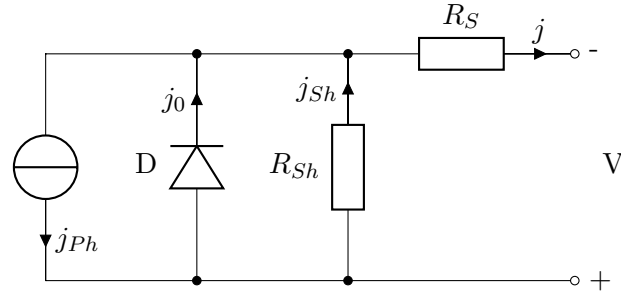


Figure 2.4: Equivalent circuit of the one-diode model of a solar cell

Figure 2.5 presents typical  $j$ - $V$  curves. The characteristics of a solar cells are the open circuit voltage ( $V_{oc}$ ), short circuit current density ( $j_{sc}$ ), fill factor ( $FF$ ) and efficiency ( $\eta$ ). The maximum power point mmp is the largest product of the voltage and current and represents the point, where the most power is produced by the solar cell.

The **short circuit current density**  $j_{sc}$  is the photo-current when no voltage is applied:

$$j_{sc} = j_{Ph, V=0} \quad (2.31)$$

The **open circuit voltage**  $V_{oc}$  results when the current is equal to zero. The  $V_{oc}$  can be calculated with

$$V_{oc} = \frac{AkT}{q} \ln\left(\frac{j_{Ph}}{j_0} + 1\right) \quad (2.32)$$

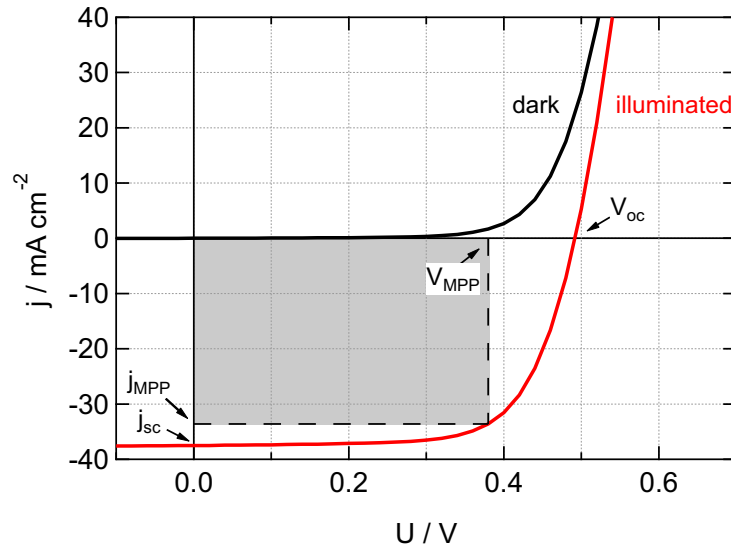


Figure 2.5:  $j$ - $V$  curves of a typical CIGS solar cell (dark and illuminated); characteristic values are marked

The **fill factor**  $FF$  describes the quality of the hetero-junction and can be calculated with

$$FF = \frac{P_{mpp}}{V_{oc}j_{sc}} \quad (2.33)$$

It is limited by the diode quality factor, the series and shunt resistance and voltage-dependent collection. The dependence on the series resistance ( $R_s$ ) can be described with [79]

$$FF = FF_0(1 - r_s) \quad (2.34)$$

where  $FF_0$  is the ideal fill factor without parasitic resistance and

$$r_s = \frac{R_s}{V_{oc}/I_{sc}} \quad (2.35)$$

The **efficiency** is the ratio of the generated power ( $P_{el}$ ) to the irradiation power ( $P_{in}$ ) and can be determined with

$$\eta = \frac{P_{el}}{P_{in}} = \frac{j_{sc}V_{oc}FF}{P_{in}} \quad (2.36)$$

In standard test conditions the measurements are conducted at a temperature of 25 °C and irradiation power density of 1000 Wm<sup>-2</sup> with the global spectrum AM1.5g [33].

The external quantum efficiency represents the ratio of the number of generated carriers per incident photon. With respect to the spectral response SR the QE is defined as

$$QE(\lambda) = \frac{SR(\lambda)hc}{\lambda e} \quad (2.37)$$

where  $h$  is the Planck constant,  $c$  the speed of light and  $e$  is the elementary charge of an electron. The external quantum efficiency (EQE) is referred when the total photon flux, which is impinging the solar cell is taken into account. The internal quantum efficiency (IQE) is referred when only the photon flux that is absorbed in the cell is taken into account and can be calculated as

$$IQE(\lambda) = \frac{EQE(\lambda)}{1 - R(\lambda)} \quad (2.38)$$

### 2.2.3 Module structure

In CIGS modules several solar cells are interconnected in series, realized by three scribes in the solar cell structure (P1, P2, P3). First the molybdenum back contact layer, which is typically sputtered on a glass substrate, is patterned by a laser, creating the P1. After the subsequent deposition of the CIGS absorber, buffer and highly resistive layer the second scribe (P2) is processed mechanically next to the P1. After deposition of the TCO front contact the isolation scribe (P3) is done mechanically close to the P2. A sketch of the interconnect region of a CIGS module with a simplified equivalent circuit is presented in Figure 2.6.

For improved visualization, the buffer and the highly resistive layer have been omitted. The solar cells, which are connected in series (cell  $n$  and cell  $n+1$ ), were assumed to be each composed of several sub-cells, denoted with  $(m)$ , to represent inhomogeneity. The P1 disconnects the molybdenum stripes, thus a high resistance is assumed in between, represented by  $R_{GP1}$ . The connection of the front and back contact is realized by the P2, the contact resistance is noted as  $R_{w,BC}$ . The area of the three scribes does not contribute to current generation and is therefore called "dead area". In parallel, the remaining area of the cell is addressed as "active area". Typically a cell of the module has a width of about 5 mm. To transport the current within the TCO without significant losses, the resistance of this layer must be very low, generally  $R_{TCO} < 10 \Omega/Sq$ . In a conventional solar cell a metal grid is evaporated on the front contact, minimizing the distance the generated current has to flow through the TCO to the contact grid. Therefore the sheet resistance of the TCO layer in a single solar cell can be significantly higher (up to about 70  $\Omega/Sq$ ) than in a module. Large TCO sheet resistances in a module result in high series resistances and can thus limit the fill factor, as discussed in section 6.2. The results of modules obtained in this thesis are presented as cell equivalent, for improved comparison to results of solar cells.

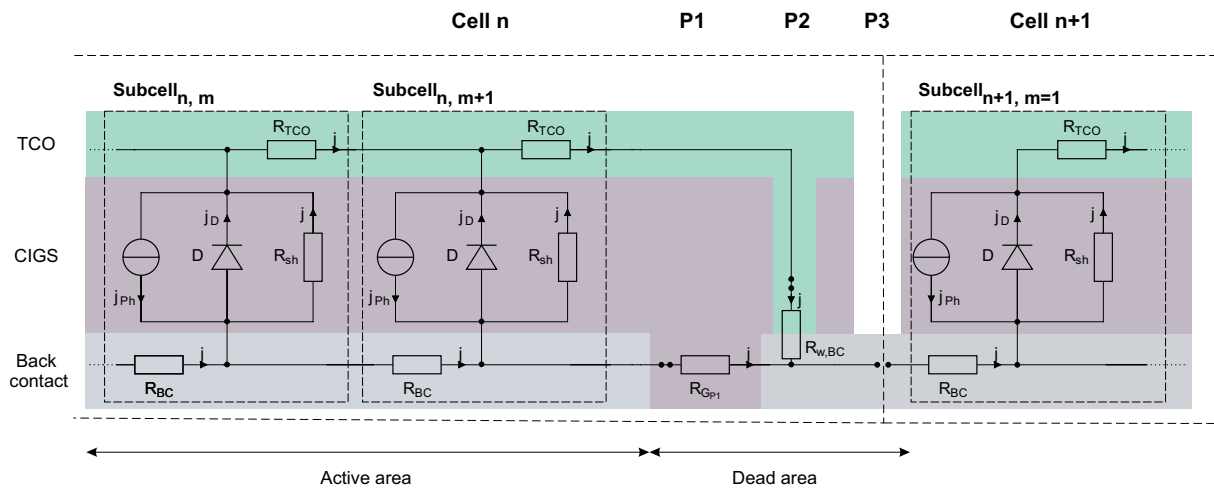


Figure 2.6: Sketch of the interconnection of 2 cells of a CIGS module with the corresponding simplified equivalent circuit

# CHAPTER 3

---

## Experimental Details

---

### 3.1 Sample Preparation

#### 3.1.1 Indium Oxide Based Layer Preparation

##### Deposition by Magnetron Sputtering

Sputtering is a physical vapor deposition process in vacuum conditions. A sputter gas, typically Ar due to its inertness and availability, is admitted into the sputter chamber between two electrodes, resulting in total pressures of 0.1 Pa - 1 Pa. Reactive gases (e.g. O<sub>2</sub>) can be added for a reactive process. The application of a voltage between the anode (typically chamber walls and substrate carrier) and cathode (target) leads to ignition of a plasma. The required voltage is in the range of a few hundred volts. The target consists of the the material that is going to be deposited or a corresponding composition for reactive sputter processes. Due to the applied electric field positive Ar-ions are accelerated towards the cathode, which can result in ionization of additional Ar-atoms. When the highly energetic particles hit the surface of the sputter target, they can eject particles from the sputter material. These particles condensate at the chamber walls and on the substrate, which is located opposite the target. The particles can react with ions from the reactive gas, when admitted. Apart from this, the ions from the reactive gas can also react at the target surface, changing the surface conditions. In case of magnetron sputtering permanent magnets are located behind the target, causing an overlay of the electric field. Consequently electrons are forced on cycloid trajectories, increasing the ionization rate and thereby also the sputter rate. Non-conductive or semi-conductive target materials will charge during a direct current sputtering process, resulting in an opposing electric field regarding the applied electric field. Thus, the sputtering process is disturbed.

*Pulsed Direct Current (DC) Magnetron Sputtering*

During pulsed direct current magnetron sputtering the voltage is periodically set to zero or to a few positive volts for a few  $\mu\text{s}$ , also called pulse off time ( $\tau_{off}$ ) within one complete cycle. The pulse duration when a negative voltage is applied is called pulse on time ( $\tau_{on}$ ). The duration of one complete cycle is set by the pulse frequency, typically in the range of a few 10 kHz to 100 kHz. The duty cycle represents the ratio of the pulse on time and the duration of one complete cycle. During the pulse off time electrostatic charges are neutralized. In this thesis a typically applied pulse frequency was 65 kHz and the pulse off time  $\tau_{off} = 3.2 \mu\text{s}$ , resulting in a duty cycle of 79 %. The pulse parameters have a high impact on the deposition condition and the process stability and must be given special attention when determining the working point. During deposition heating of the deposited layer can be initiated controlled by a heating unit or by process related effects, such as radiative heating from the target or bombardment of highly energetic secondary electrons. The last mentioned effects are hard to control and can adversely affect the growth of the corresponding films.

In this work hydrogen doped indium oxide was deposited without intentional heating by a pulsed DC magnetron sputtering process in a large inline sputtering tool (Model A600V7) from Leybold Optics. Indium oxide planar ceramic targets with dimensions of 12.5 cm x 60 cm, produced from several target manufacturers were used. The power was adjusted for changing the deposition rates, power densities of 0.8 W/cm<sup>2</sup> to 5.3 W/cm<sup>2</sup> could be applied. The total pressure was varied in the range of 0.26 Pa to 0.51 Pa. Argon was used as the main sputtering gas. An argon/oxygen gas mixture and water vapor, introduced by a needle valve to the sputter chamber served as reactive gases. The corresponding partial pressures were monitored by a residual gas analyzer (RGA) before and during deposition. However, cleaning of the chamber walls and change of the RGA filament resulted in different water vapor pressures though the needle valve positions remained unchanged. The substrate carrier oscillated through the plasma in front of the target. Due to process instabilities, caused by low sputter power densities, low sputter pressures and unfavorable pulse parameters, readjusting of the deposition parameters was required. Therefore deposition parameters are mentioned in the corresponding sections separately. Nevertheless a homogeneous process over a substrate size of 30 cm x 60 cm was demonstrated. On one 30 cm x 30 cm glass substrate the deviation in film thickness was  $\pm 2.1 \%$ , fitted from optical spectra, deviations of the charge carrier density and electron mobility of the as grown films were  $\pm 4.2 \%$  and  $\pm 2.1 \%$ , respectively. After annealing the deviations decreased to  $\pm 2.4 \%$  and  $\pm 1.2 \%$ , respectively. Over a 30 cm x 30 cm glass substrates average electron mobilities of  $\approx 124 \text{ cm}^2/\text{Vs}$  could be achieved. In this thesis the major sputter technique was pulsed DC magnetron sputtering. Only hydrogen doped indium oxide films, which are discussed in section 6.1.1 were deposited by radio frequency (RF) magnetron sputtering.

### *Radio Frequency (RF) Magnetron Sputtering*

During radio frequency (RF) magnetron sputtering the ions and electrons are accelerated by a radio-frequency electric field. The electrons oscillate in the plasma and thus sustain the discharge of the target. As the impedance is reduced with increasing frequency, any kind of material can be sputtered by applying appropriate alternating voltages. The most common frequency is 13.56 MHz and was also used for the experiment carried out in this thesis.

In this thesis the 150 nm thick hydrogen doped indium oxide layer in section 6.1.1 was deposited by RF magnetron sputtering on Mo-coated glass substrates using a 3 inch ceramic  $\text{In}_2\text{O}_3$  target. The deposition process was based on the study of Steigert et al. [71].

### **Deposition by Reactive Plasma Deposition (RPD)**

Reactive plasma deposition is considered to be a physical vapor deposition process using a pressure-slope type plasma ion gun. Advantages are low-ion damage, low deposition temperatures, large area deposition and high growth rates [80]. Following the work of Koida et al. [5], we deposited hydrogen doped or hydrogen and tungsten co-doped indium oxide thin films by in-line reactive plasma deposition (Sumitomo Heavy Industries, URT-IP2). Ar gas was injected through the plasma ion gun into the process chamber. A beam controller focused the plasma towards the indium oxide and 1 wt.% tungsten doped indium oxide tablets. Target material is ejected and condensates on the moving substrate and on the chamber walls.  $\text{O}_2$  and  $\text{H}_2\text{O}$  were used as reactive gases. Depending on  $p_{\text{H}_2\text{O}}$  the base pressure was in the range of  $0.5 \times 10^{-4}$  Pa to  $2 \times 10^{-4}$  Pa and the sputter pressure around 0.3 Pa, measured by quadrupole mass spectrometry (Inficon, Transpector XPR3). The depositions were conducted at low  $p_{\text{H}_2\text{O}} \approx 1 \times 10^{-5}$  Pa or high  $p_{\text{H}_2\text{O}} \approx 1 \times 10^{-4}$  Pa without intentional heating. The temperature of the substrates did not exceed 60 °C during depositions, as determined with temperature stickers on glass and Si-substrates.

### **Post-Deposition Thermal Treatment**

The post-deposition thermal treatment was carried out in order to initiate solid phase crystallization of the amorphous phase in the indium oxide based TCOs. Annealing was performed in three different atmospheres with different conditions:

- The annealing was conducted in ambient air in a preheated oven from Binder. For annealing the samples were placed on glass substrates which served as carriers. The annealing temperature was set to 220 °C, the annealing duration was varied between 15 min

and 120 min. After annealing the samples were taken out and cooled down in air on a metallic plate.

- The annealing was conducted in vacuum in different conditions.
  - The annealing was carried out at a base pressure of  $1 \times 10^{-3}$  Pa using infrared radiant heaters. The temperature was set by adjustment of the relative power of the heaters. The relative power of Heaters in the middle (m) was set lower than for heaters located at the edges (e) to yield a homogeneous temperature distribution over the whole sample (30 cm x 30 cm area). The relative power ratio is addressed as "m/e", respectively. The temperature profile was measured on glass substrates with the temperature logging system SuperM.O.L.E. ® on different positions. Two different annealing conditions were used. (i) The relative powers were set to 60 % / 50 % for 7 min, resulting in an average temperature of  $(196 \pm 9)$  °C before they were reduced to 40 % / 10 % for 30 min for a approximately constant temperature. The measured temperature profile revealed  $(221 \pm 0.6)$  °C after 23 min in the relevant range. (ii) The relative powers were set to 60 % / 50 % for 4 min, resulting in a temperature of approx.  $(114 \pm 6)$  °C. Reduction to 30 % / 8 % for 56 min resulted in a steady increase of the temperature up to  $(211 \pm 1)$  °C. After annealing the chamber was floated with nitrogen and ambient air to initiate cooling of the samples.
  - Annealing was carried out at a pressure of about  $5 \times 10^{-5}$  Pa by placing the samples on a hot plate. Before annealing the samples were placed on a Si-wafer, which served as carrier. The wafer was installed in the load lock of a sputter tool from Roth&Rau and the chamber was evacuated. The heaters in the sputter chamber were preheated and the wafer placed on the heaters. This resulted in a constant temperature of approx. 180 °C over the annealing duration of 1h, as indicated by temperature stickers. After annealing the carrier transferred the Si-wafer back to the load lock, which was vented with nitrogen to cool the samples.
  - The annealing was carried out in ultra high vacuum at 250 °C for 40 min. The samples cooled down in vacuum. This method was applied for the RF sputtered  $\text{In}_2\text{O}_3\text{:H}$  film presented in section 6.1.1.
- Film deposited by Reactive Plasma Deposition (RPD) were annealed in nitrogen atmosphere. Before annealing the chamber was evacuated and vented with nitrogen up to a pressure of  $p = 7 \times 10^4$  Pa. The samples were placed on a carbon plate, which was heated during annealings, the temperatures were monitored by thermocouples. The temperature profile was programmed, the heating rate was set to 20 K/min. The annealing temperature was varied between 150 °C and 250 °C. The annealing duration at the target temperature was between 30 min and 60 min. After annealing the heaters were switched off and the samples were cooled down to room temperature inside the chamber.

### 3.1.2 CIGS Solar Cell Fabrication

#### CIGS Absorber

$\text{Cu(In,Ga)(S,Se)}_2$  (CIGS) films were used as sub-layers and as the absorber layer of photovoltaic devices analyzed within this study. Typically the layers were grown by co-evaporation or by a sequential process on Mo-coated soda lime glass substrates and had a thicknesses between  $1.1 \mu\text{m}$  and  $3.1 \mu\text{m}$ . For evaluation of the growth of amorphous indium oxide layers on rough substrates, CIGS film were deposited directly on glass substrates without the Mo coating. The two main fabrication processes are described in more detail.

- CIGS layers were deposited by multi-source evaporation, also referred to as the 3-stage-process. In different compositions all elements are evaporated separately from crucibles. Therefore the composition and growth of the CIGS layer is controlled directly during the evaporation process. Co-evaporated films used in this study were fabricated at Helmholtz-Zentrum Berlin für Materialien und Energie (HZB), Berlin, Germany and National Institute of Advanced Industrial Science and Technology (AIST), Tsukuba, Japan. A detailed description of the 3-stage process, as well as a description of the deposition chamber at HZB were reported by Heinemann [81]. Key aspects are the following. The  $\text{Cu(In,Ga)Se}_2$  layer grows Cu-poor until shortly before the end of the process, where a Cu-rich growth is required. When the composition passes the stoichiometric point re-crystallization is induced, resulting in reduced stress and crystallographic disorder. During the Cu-rich growth  $\text{CuSe}_x$  forms at the surface, which is transformed into CIGS with supply of Ga-In-Se in the 3<sup>rd</sup> stage. After consumption of  $\text{CuSe}_x$ , new nucleation rather than continued growth of existing grains can occur, resulting in a surface layer with poorer film quality compared to the re-crystallized grains in the bulk. Beneficial aspects of the deposition technique are the ability to control the film composition e.g. the Ga-gradient. A post deposition treatment (PDT) can be applied [82–84]. Typically alkali fluorides, such as NaF and KF are thermally evaporated on the CIGS surface, which is aimed to improve the doping concentration of the absorber layer. The typical thickness of the CIGS layer is about  $2 \mu\text{m}$ . For thickness variations of the CIGS layer the durations of the corresponding stages were reduced.
- CIGS layers were fabricated by a sequential process. First the metallic precursors are deposited on the Mo-coated glass substrates, typically by sputtering. This step defines the overall composition of Cu/In/Ga of the later grown CIGS layer. Selenization and sulfurization of the metallic precursors are conducted in a specific oven with several reaction chambers.  $\text{H}_2\text{S}$  or evaporated Se can be in operation as reactive gases. For  $\text{Cu(In,Ga)Se}_2$  films the selenium supply, referred to as Se partial pressure, was found to be crucial for the resulting elemental depth profile of the CIGS layer and the corresponding solar cell

performance [85]. Advantages of this process are short cycle times and the possibility to process at atmospheric pressure. At HZB such Cu(In,Ga)Se<sub>2</sub> absorber were fabricated in an oven from Smit Thermal Solution (previously Smit Ovens) at soaking temperatures of 580 °C. The precursor layers were sputtered. A detailed description of the process can be found elsewhere [86]. Cu(In,Ga)(S,Se)<sub>2</sub> samples were also provided by Avancis GmbH & Co KG (Avancis), a detailed description of the process can be found elsewhere [87].

## Window layer

In this section the deposition of the window layers (buffer, highly resistive layer and ZnO:Al front contact) are presented. Buffer layers are aimed minimizing recombination at the absorber/window interface by improving the band alignment at the absorber/buffer layer and interface properties. In this thesis different buffer layers were applied.

- CdS buffer layers were deposited by chemical bath deposition (CBD). A general description of the process was summarized by Kaufmann [88]. During the CBD-process at HZB CIGS absorbers were placed in a solution of NH<sub>3</sub>, Cd-acetat and Thiourea, which was heated up to temperatures of 45 °C for multi-source-evaporated CIGS absorbers, and 65 °C for sequentially processed CIGS absorbers, both processed at HZB. The resulting CdS thickness was  $\approx 60$  nm. CIGS samples provided by AIST and CIGS absorbers, which are referred as "etched", as in sections 5.4.2 and 6.3.2, were processed with a CBD-CdS buffer layer, following, however, a similar recipe.
- Zn(O,S) buffer layer were deposited by Atomic Layer Deposition (ALD) or RF magnetron sputtering.
  - The ALD deposition was conducted in a Beneq TFS500 reactor at 130 °C. As precursors diethylzinc (DEZ), H<sub>2</sub>S and H<sub>2</sub>O were used for zinc, sulfur and oxygen, respectively. N<sub>2</sub> served as purging gas. After 9 cycles of ZnO layer depositions 1 ZnS cycle was processed. This procedure resulted in a S/(S+O) ratio of about 25 % [89]. The target Zn(O,S) film thickness was 50 nm.
  - The RF-sputtering process of Zn(O,S) was conducted in the in-inline sputtering tool Von Ardenne Anlagentechnik VISS300 from a ceramic target with a ZnO:ZnS composition of 75:25 at%. The films were deposited without intentional heating at a total pressure of 0.5 Pa and target power density of 2 W/cm<sup>2</sup> for a film thickness of 60 nm. The described sputtering process was used for CIGS absorber fabricated at HZB. Zn(O,S) buffer layer used in combination with provided CIGS samples from Avancis were fabricated by sputtering in the Munich R&D pilot line from Avancis [87].

The following materials were applied as highly resistive (HR) layer, typically between the buffer and front contact layer. However, some CIGS devices were produced without a HR layer.

- Intrinsic zinc oxide (i-ZnO) films were used as HR layer and deposited by sputtering or ALD from ceramic targets. Sputtering was operated in RF-mode. Three different deposition tools were used. Typically the films were deposited without intentional heating at a pressure of 0.8 Pa at the Von Ardenne Anlagentechnik VISS300. In section 5.1 ZnO films were additionally deposited with substrate heating and at a reduced total pressure of 0.2 Pa. The target power density was set to 2 W/cm<sup>2</sup>, Ar was used as the purging gas. The thickness was varied between 40 nm and 200 nm. For indium oxide thin films that were deposited by RPD, another in-line sputtering tool, located at AIST was used. In this the films were deposited at approx. 140 °C and a O<sub>2</sub>/(Ar + O<sub>2</sub>) flow ratio of 1 % [90]. The ZnO layer discussed in section 6.1.1 was deposited using a stationary sputtering tool with a target diameter of 3 inch. The substrate was not intentionally heated. Further ZnO films were deposited in the ALD reactor Beneq TFS500. As for the Zn(O,S) deposition, the precursors diethylzinc and H<sub>2</sub>O were used for zinc and oxygen, respectively. Also here nitrogen was used as the purging gas. For CIGS cell a film thickness of 75 nm, for CIGS modules a thickness of 220 nm was targeted.
- Amorphous In-Ga-Zn-O layer were deposited without intentional heating by RF magnetron sputtering from a ceramic target (In:Zn:Ga = 1:1:1). Ar and O<sub>2</sub> were used as sputtering gases, the total pressure was 0.5 Pa, the power density 3.3 W/cm<sup>2</sup> [91].
- Sol-gel Ga<sub>x</sub>O<sub>y</sub> and In<sub>x</sub>O<sub>y</sub> films were deposited by spin coating. In and Ga precursors were prepared following the work of Zhou et al. [92]. One deposition cycle is processed as following: substrates were coated with a few hundred μl of the precursors solutions and spin coated with a specific amount of resolutions per minute (rpm) for 1 min. Then the substrates were transferred to a preheated hot plate and heated for 2 min at a specific temperature. For a sample that is referred as e.g. "6xGaO<sub>x</sub>" this deposition procedure was repeated 6 times with Ga precursor. For depositions on glass substrates with sizes of 5 cm x 5 cm, 200 μl of the precursors were used. Ga precursors were spin coated with 300 rpm, In precursors with 1500 rpm. Afterwards the sol-gel layers were annealed at 150 °C to 300 °C. For the deposition on CdS/buffered CIGS samples 400 μl of the Ga precursors were spin coated with 500 rpm and annealed at 200 °C.

Aluminum doped zinc oxide (AZO) was used as the reference front contact. The layers were deposited by DC sputtering at different deposition conditions and sputtering tools.

- The films were deposited at  $T_S \approx 160$  °C at the Von Ardenne Anlagentechnik VISS300. Ceramic ZnO:Al<sub>2</sub>O<sub>3</sub> targets with 1.5 wt.% Al<sub>2</sub>O<sub>3</sub> were used. Typical thicknesses were 240 nm (for cells) and 865 nm (for modules).
- The films were deposited without intentional heating in a large inline sputtering tool (Model A600V7) from Leybold Optics from a rotatable target with 1.0 wt.% Al<sub>2</sub>O<sub>3</sub>. The films had a thickness of approx. 240 nm.
- The ZnO:Al front contact prepared by Avancis was deposited by sputtering and serves as a reference [87].

### Metallization, structuring and light soak

For the fabrication of solar cells a Ni-Al-Ni layered contact grid with thicknesses of 25 nm / 3000 nm / 25 nm was deposited on top of the TCO by electron beam evaporation in the system Creamet® 400 by Creavac. Solar cells processed at HZB had typically an area of about 1 cm<sup>2</sup> and were structured manually, mechanically. Solar cells processed at AIST had a Ni/Al contact grid and were scribed mechanically in an automated setup for solar cell areas of 0.52 cm<sup>2</sup> [90]. The cells discussed in section 6.3.2 had an area of 0.35 cm<sup>2</sup>.

Modules were structured with a P1, P2 and P3, as described in section 2.2. The P1 was done by laser scribing, P2 and P3 scribes were done mechanically. The same applies for samples produced for transmission line measurements.

Transmission line structures were fabricated following the work of Marinkovic et al. [93]. The samples were processed with increasing cell widths in steps of 0.2 cm from 0.5 cm to 1.5 cm. The cell length was 1.0 cm.

Light soak of CIGS devices is common practice to evaluate the stability of samples under continued irradiation (typically under standard test conditions). In this thesis light soak was carried out for modules described in section 6.3.1 and 6.3.3.

## 3.2 Characterization Techniques

This section provides information of the used characterization methods. A short general description of the used methods can be found in the appendix A.1.

### 3.2.1 Material Characterization

#### Film thickness

The film thickness is an important parameter to evaluate the film properties (e.g. charge carrier density, optical absorption) and the deposition conditions (e.g. deposition rate). In this thesis the thickness was determined by two methods. Thicknesses of sputtered hydrogen based indium oxide films were evaluated by profilometry (DektakXT, Bruker). In this thesis the glass substrate was marked with edding prior to the TCO deposition and removed afterwards with acetone to create a step in the film profile. The thickness of films, which were prepared with reactive plasma deposition, was evaluated by spectral ellipsometry. Details concerning this method can be found in the following subsection.

#### Optical Characterization

##### *Ultraviolet-Visible-Near Infrared (UV-Vis-NIR) spectroscopy*

Optical properties are a key characteristic of transparent conductive oxides. In this study the reflection (R) and transmittance (T) of thin films on glass substrates were evaluated by UV-Vis-NIR spectroscopy, typically in the range of 250 nm to 2450 nm. The measurements were performed using a Perkin Elmer spectrophotometer (Lambda 1050) equipped with deuterium and halogen lamps, a monochromator and an integrating sphere. Optical absorption (A) was calculated with

$$A = 1 - R - T \quad (3.1)$$

The optical band gap of hydrogen doped indium oxide films was estimated from the relation [94]:

$$(\alpha h\nu)^2 = A'^2(h\nu - E_g) \quad (3.2)$$

where  $\alpha$  is the absorption coefficient,  $h$  is Planck's constant,  $\nu$  is the photon's frequency,  $E_g$  is the optical band gap and  $A'$  is a constant.

##### *Spectral Ellipsometry (SE)*

In this thesis the method was used to assess the thickness of films deposited by reactive plasma deposition on glass substrates. The measurements were done using the spectral ellipsometer J.A.Woolam, M-2000. Prior to fitting the data, the measurements were corrected due to reflection of the back site of the glass substrate As model SLG/TCO/EMA/Air was set. EMA represents

the effective medium approximation, a composition of TCO 50 % : 50 % Air was assumed. The thickness of the film was set as the sum of the TCO thickness and half of the EMA thickness.

## Electrical Characterization

### *4 point probe*

In this thesis 4 point probe measurements were done using the Model RM3-AR by Jandel. The sheet resistance can be obtained by measurements in the von der Pauw geometry.

### *Hall effect measurements*

In this thesis Hall measurements were conducted in van der Pauw geometry with the system HMS-3000, Ecopia (at HZB) and ResiTest8300, Toyo (at AIST). Multi-layered stacks of the transparent conductive oxide (n-type) and sub-layers (n and p type) with a much higher resistance were measured. The simplifying assumption has been made that due to the big difference in conductivity, current is only transported through the transparent conductive oxide and that the influence of the sub-layers is negligible.

### *Transmission line measurements*

Transmission line structures were processed to evaluate the sheet resistance of TCOs grown on CIGS samples, as discussed in section 6.2. The procedure is described elsewhere [93].

## Structural Characterization

### *Glow Discharge Optical Emission Spectroscopy (GDOES)*

The elemental profile was measured by GDOES. Measurements were conducted with a GDA650 analyzer from Spectruma Analytik GmbH.

### *Transmission Electron Microscopy (TEM)*

In this thesis two procedures were used. Hydrogen doped indium oxide films deposited on ZnO/glass, as discussed in section 5.1 were prepared conventionally and analyzed with a Zeiss LIBRA 200FE. CIGS samples, as discussed in section 5.3 were coated with 10 nm thick carbon for improved conductivity during SEM-focused ion beam (FIB) and with 1  $\mu\text{m}$  thick Pt for protection during mechanical dimpling. A  $\approx 30 \mu\text{m} \times 20 \mu\text{m} \times 10 \mu\text{m}$  "trench" was cut for an observation window. The cross-section of the CIGS sample was ion polished with decreased ion current of 1 nA, 0.5 nA, 0.1 nA and 50  $\mu\text{A}$ . Scanning Transmission Electron Microscopy (STEM) measurements were performed with a JEOL JEM-ARM 200CF electron microscope. In order to

see grain boundaries clearly, an annular dark field (ADF) detector was used to collect medium angle annular dark field (MAADF) and annular bright field (ABF) signal for an improved defect signal.

### *Scanning Electron Microscopy (SEM)*

Scanning electron Microscopy measurements were conducted at acceleration voltages of 5 kV to 10 kV at a LEO Gemini 1530 or Hitachi S-4300.

### *Electron Backscatter Diffraction (EBSD)*

Electron backscatter diffraction measurements were carried out with EDAX-TSL equipment [95, 96]

### *X-Ray Diffraction (XRD)*

X-ray diffraction is a wide used technique for phase identification and evaluation of the structure of (poly-)crystalline materials. Within this thesis XRD measurements were an important characterization method to evaluate the chrystalline structure of the films. Thus the method is described in more detail. Monochromatic X-rays are directed towards the sample, where they interact with the sample and are scattered from a series of lattice planes. Constructive interference occurs when Braggs Law is satisfied [95]:

$$n\lambda = 2d_{hkl}\sin\theta \quad (3.3)$$

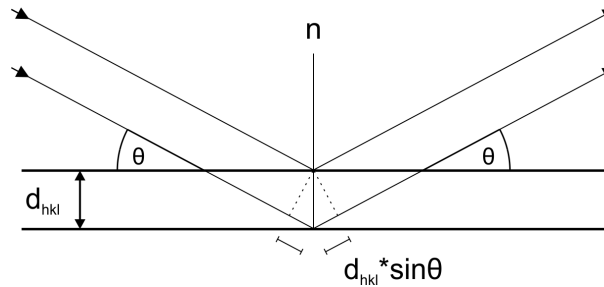


Figure 3.1: Schematic representation of the Bragg equation; waves are reflected from lattice planes

where  $n$  is an integer,  $\lambda$  is the characteristic wavelength of the X-rays, which impinge the crystallite,  $d_{hkl}$  is the interplanar spacing between lattice planes and  $\theta$  is the angle of the X-ray beam with respect to the planes. A simplified scheme can be seen in Figure 3.1. To collect all scattered X-ray intensities, the angle  $\theta$  is changed continuously in a specific range (a scan is performed). The intensities are measured with a detector, which is typically moving around the sample. The maximum intensity of the reflected rays results when the reflected X-rays are in phase for an specific angle  $\theta$  (Bragg angle). The  $\theta/2\theta$  diffractometer is an often-used instrument

to measure Bragg reflections. In this configuration the angles of the incoming and exiting beam are continuously varied, but remain equal throughout the whole scan ( $\theta_{in} = \theta_{out}$ ). The exit angle is  $2\theta$  with respect to the extended incoming beam. The crystallographic lattice planes contributing to the scattering of X-rays are all parallel to the substrate. In this thesis this measurement set-up is referred as Bragg Brentano X-ray diffraction (BB-XRD). An other set-up used in this study is grazing incidence X-ray diffraction (GI-XRD). In this configuration the angle of the incoming beam is fixed, typically at very small angles and is referred as  $\alpha$ , while the detector is moving along the  $2\theta$  circle. Due to this configuration the path of the x-rays within the thin film can be maximized, leading to larger intensities than during  $\theta/2\theta$  scans. Further the lattice planes that cause scattering of X-rays are not necessarily parallel to the substrate. Therefore a random orientation of the crystallites, can be measured. However, due to the changed configuration the Bragg reflections are slightly shifted compared to a symmetrically measured pattern. In amorphous phases atoms are arranged in a random way and thus do not cause sharp Bragg peaks but result in a broad feature [97]. Thus by fitting the crystalline part and/or the amorphous part of XRD pattern the crystalline fraction  $X_C$  of, here,  $\text{In}_2\text{O}_3:\text{H}$  films can be determined by [98]:

$$X_C(\text{In}_2\text{O}_3 : \text{H}) = \frac{A_C(\text{In}_2\text{O}_3 : \text{H})}{A_C(\text{In}_2\text{O}_3 : \text{H}) + A_A} \quad (3.4)$$

where  $A_C(\text{In}_2\text{O}_3:\text{H})$  is the sum of all integrated peaks of  $\text{In}_2\text{O}_3$  that were observed in the XRD pattern (here GI-XRD) and  $A_A$  is the total area under the amorphous components in the XRD pattern measurements, namely the broad feature.

Other evaluation procedures of X-ray diffraction patterns are summarized in the following. Cu  $K\alpha$  ( $\lambda = 0.154$  nm) radiation was used as the source of the X-rays. Evaluation of the crystalline fraction and the texture coefficient was done based on measurements in GI-XRD configuration. Calculation of structural parameters, i.e., the lattice constants of ZnO and  $\text{In}_2\text{O}_3:\text{H}$  thin films, crystallites size and strain were conducted based on measurement in BB-XRD configuration. Crystalline ZnO films exhibit a hexagonal wurtzite structure. The ZnO lattice parameter  $c$  of the (002) reflex was calculated:

$$c = d \cdot l = 2d \quad (3.5)$$

with the corresponding Miller indices  $l = 2$ . Crystalline indium oxide has a body centered cubic byxbite structure with lattice parameter  $a = 10.117$  Å [52, 53], thus the following relationship applies:

$$d_{hkl} = \frac{a}{\sqrt{h^2 + k^2 + l^2}} \quad (3.6)$$

The plot of  $d_{hkl}$  against the reciprocal of  $\sqrt{h^2 + k^2 + l^2}$  is used to calculate the lattice constant  $a$  of the crystallites. The slope of the linear fit represents the average value of  $a$ .

The instrumental broadening was estimated by a LaB<sub>6</sub> standard and the integral breadth  $\beta$  was corrected using the relation [99]:

$$\beta_{Lf} = \beta_{Lh} - \beta_{Lg} \quad (3.7)$$

for the Lorentian (L) component and

$$\beta_{Gf}^2 = \beta_{Gh}^2 - \beta_{Gg}^2 \quad (3.8)$$

for the Gaussian (G) component of the Voigt profile. The denotations  $f, h$  and  $g$  represent the components of the integral breadth of intrinsic profile, experimental profile and instrumental profile. Assuming a Lorentzian size-broadened profile ( $\beta_{Lf} = \beta_S$ ), the volume-weighted crystallite size  $\langle D \rangle_V$  can be calculated as:

$$\langle D \rangle_V = \frac{\lambda}{\beta_S \cos \theta} \quad (3.9)$$

The weighted average strain  $\varepsilon$  can be calculated as:

$$\tilde{\varepsilon} = \frac{1}{4} \beta_D \cot \theta \quad (3.10)$$

if a Gaussian strain-broadened profile ( $\beta_{Gf} = \beta_D$ ) is assumed [99]<sup>1</sup>.

### *Photoelectron Spectroscopy*

In this study X-ray photoelectron spectroscopy (XPS) and ultraviolet photoelectron spectroscopy (UPS) measurements were conducted to obtain the band alignment of hydrogen doped indium oxide and intrinsic zinc oxide. UPS/XPS measurements of gold were conducted for each sample configuration and serve as reference for calibration. XPS spectra were corrected for background and corrected corresponding to the Au core level 4f<sub>7/2</sub> at 84 eV. XPS spectra were fitted using a linear background and voigt functions. Valence band maximum VBM measured by UPS (He I; 21.2 eV) were corrected corresponding to the Au fermi level  $E_F$ , which was set to 0 eV, for each sample configuration. The valence band maximum (VBM)  $E_{VBM}$  was determined by linear extrapolation of the leading edge towards the extended base line of the VB spectra [101], measured at two positions of the sample.

### *Atomic Force Microscopy*

The surface topography of sub-layers was found to be a key aspect for successful growth of high mobility amorphous indium oxide based TCOs. The topography was evaluated by atomic force microscopy (AFM) measurements. The sample is scanned with a nano-scaled tip, attached to the end of a cantilever. The measurement signal is controlled by a laser beam, which is reflected at the cantilever. Measurements conducted within this thesis were done using tapping mode

---

<sup>1</sup>Part of the calculations were adapted from mathematical derivations published in the manuscript and support information of Erfurt et al. [100]

AFM. Two systems were used: 1) Park Systems XE70 with the cantilever type PPP-NCHR; 2) SII NanoNavi E-Sweep with the cantilever type SI-DF40. Measurements were done with a resolution of 512 pixel x 512 pixel, the image size varied, in dependence of the sample and required information, from 2  $\mu\text{m}$  x 2  $\mu\text{m}$  to 40  $\mu\text{m}$  x 40  $\mu\text{m}$ . Data was evaluated with the software Gwyddion [102]. The grain size was estimated by the watershed method. The median local slope was assessed by applying the integral transformation "local slope".

### *Fourier Transform Infrared Spectroscopy (FTIR)*

Fourier-transform infrared spectroscopy (FTIR) was used to evaluate the amount of residual water in spin coated  $\text{Ga}_x\text{O}_y$  sol-gel layers. The layers were deposited on Si-wafers. Transmission spectra were measured under nitrogen atmosphere at room temperature from 370  $\text{cm}^{-1}$  to 7500  $\text{cm}^{-1}$  using a Bruker Tensor 27. The measured spectra were evaluated using the software OPUS 7 [103]. The following procedures were applied: correction for atmospheric absorption, baseline correction and transformation of the transmission spectra to absorption spectra.

### **Accelerated Aging**

The stability of the electrical properties of the TCOs was investigated by damp heat tests, where the relative humidity was set to 85 % and the temperature to 85 °C. The electrical properties were studied by hall effect measurements before and after 24 h, 48 h, 120 h, 288 h, 500 h and 1000 h of damp heat. This settings fulfill the requirements of the standard IEC 61646 (10.13). The damp heat tests were carried out in the climate chamber WK 11 - 600/40 from Weiss Umwelttechnik GmbH.

### **3.2.2 Device Characterization**

#### **Current-Voltage Characterization**

The main characteristics of the solar cells ( $j_{sc}$ ,  $V_{oc}$ ,  $FF$ ,  $\eta$ ) are determined by current density - voltage measurement ( $j$ - $V$ ) under standard test conditions (AM1.5g spectrum [33], 1000  $\text{W}/\text{m}^2$ , 25 °C). To determine the diode quality factor, saturation current density, shunt and sheet resistance the  $j$ - $V$  curve of a cell was fitted with a two-diode model with the software IGOR Pro [104] and the evaluation procedure PV-Evaluate, developed by Roland Mainz, HZB.

### **Quantum Efficiency**

The quantum efficiency (QE) of the solar cells was measured in the range of 300 nm to 1400 nm using a homemade set-up with a monochromator. A LED-based white light (spectrum and intensity close to AM1.5) generates normal operation conditions, the current is measured for every wavelength. The EQE measurements were performed without applied bias voltage.

### **Capacitance Voltage Characterization**

Capacitance-Voltage measurements were performed to evaluate the ionized acceptor concentration profile of the cells. Two different setups were used: (i) a LCR meter (Agilent E4980) at a frequency of 100 kHz with bias voltage from 0.6 to (-3.0) V; (ii) a homemade setup using an Agilent 4284A LCR meter at a frequency of 100 kHz with voltages between 0.5 V and (-0.5) V.

## CHAPTER 4

---

### Sputtered Hydrogen doped Indium Oxide

---

Hydrogen doped indium oxide and other related compounds are promising materials due to their high electron mobility and low absorption. However, the fabrication of e.g. hydrogen doped indium oxide (IOH) is limited to a laboratory scale, yet. To transfer the fabrication to the industry, a feasible process has to be demonstrated, thus e.g. by large scale inline DC magnetron sputtering. In this chapter<sup>1</sup> we therefore investigate IOH films which were deposited by such a process, namely by in-line pulsed DC magnetron sputtering with a possible deposition area of 30 cm x 60 cm, as described in section 3.1.1 on page 22. We present the film properties after annealing in vacuum or ambient air for 30 min at a temperature of 220 ° C, respectively, and compare both annealing procedures, as a post deposition thermal treatment is required to initiate solid phase crystallization of the amorphous phase of the films and results in high electron mobilities. If not mentioned otherwise, the films had a thickness of  $\approx 200$  nm. In particular we investigate the structural properties in section 4.1, the electrical properties in section 4.2 and the optical properties in section 4.3. Additionally we studied the stability of the annealed film, as this is another critical key aspect for the successful transfer to the industry production. We observed, that the air annealed films showed lower charge carrier densities than the films annealed in vacuum while the optical absorption of the films were comparable. However, an annealing in air might be more feasible for a large scale production line. We therefore developed a strategy to improve the charge carrier density and therefore the conductivity of air annealed films without adversely affect the electron mobility or optical absorption. The strategy is presented in section 4.5. Finally we summarize the findings in section 4.6.

---

<sup>1</sup>This chapter is based on the paper *Darja Erfurt, Marc D. Heinemann, Stefan Körner, Bernd Szyszka, Reiner Klenk, Rutger Schlatmann; Improved electrical properties of pulsed DC magnetron sputtered hydrogen doped indium oxide after annealing in air; Materials Science in Semiconductor Processing 89 (2019) 170–175; doi: 10.1016/j.mssp.2018.09.012 [105]*, licensed under a [Creative Commons Attribution 4.0 International License](https://creativecommons.org/licenses/by/4.0/) (CC-BY)

The investigations presented in the following are based on preliminary studies for the evaluation of an suitable working point. In the preliminary studies a wide range of combinations of the deposition parameter water vapor and oxygen partial pressure were processed. Values for the total pressure and the pulse parameter were adapted from an already established  $\text{In}_2\text{O}_3\text{:Sn}$  deposition process. The deposition condition of the  $\text{In}_2\text{O}_3\text{:H}$  film, which showed the highest electron mobilities after annealing, were defined as the suitable working point. In this point the water vapor pressure was  $p_{\text{H}_2\text{O}} = 0.33 \times 10^{-3}$  Pa and the oxygen partial pressure  $p_{\text{O}_2} = 0.88 \times 10^{-3}$  Pa. In the following the structural, electrical and optical properties of films deposited around this point are evaluated. In particular, two sets of samples were deposited: (i) the water vapor pressure was varied while the oxygen partial pressure was held constant, (ii) the oxygen partial pressure was varied while the water vapor pressure was held constant. Furthermore the influence of the annealing atmosphere was studied. The detailed parameter are summarized in Table 4.1. Furthermore an additional experiment was carried out, which will be shortly discussed later<sup>2</sup>.

Table 4.1: Deposition and annealing parameter of hydrogen doped indium oxide films, grown by a pulsed DC magnetron sputtering process on bare glass substrates

Parameter	Variation
Temperature	deposited without intentional heating
Power density	0.8 W/cm <sup>2</sup>
Total pressure	0.31 Pa
$p_{\text{H}_2\text{O}}$	varied from $0.2 \times 10^{-3}$ Pa to $0.68 \times 10^{-3}$ Pa, constant $p_{\text{O}_2} = 0.88 \times 10^{-3}$ Pa
$p_{\text{O}_2}$	varied from $0.64 \times 10^{-3}$ Pa to $1.11 \times 10^{-3}$ Pa, constant $p_{\text{H}_2\text{O}} = 0.33 \times 10^{-3}$ Pa
q(Ar & O <sub>2</sub> )	28 sccm to 48 sccm
annealing	in vacuum or ambient air for 30 min at $\approx 220$ ° C
pulse	$f = 40$ kHz; $\tau_{\text{off}} = 1$ $\mu\text{s}$

## 4.1 Structural Properties

First the structure of as grown films, deposited at a constant  $p_{\text{H}_2\text{O}} = 0.33 \times 10^{-3}$  Pa but varied  $p_{\text{O}_2}$  is presented in Figure 4.1 (a). The films all exhibit a mainly amorphous structure, indicated by the broad feature in the range of  $28^\circ \leq 2\theta \leq 35^\circ$ . Only a small (222) peak at  $2\theta \approx 30.5^\circ$  can be assumed, indicating the presence of a few small crystallites inside the amorphous matrix. No change of the structure can be observed due to the change of oxygen partial pressure during

<sup>2</sup>Two films were deposited with varied water and oxygen supply: (i) very high  $p_{\text{H}_2\text{O}}$  of  $20 \times 10^{-3}$  Pa without additional oxygen supply  $q(\text{Ar} \ \& \ \text{O}_2) = 0$  sccm; (ii)  $p_{\text{H}_2\text{O}}$  of  $3.7 \times 10^{-3}$  at  $q(\text{Ar} \ \& \ \text{O}_2) = 25$  sccm; note that the films were deposited at a reduced total pressure of  $p = 0.26$  Pa and changed configurations of the residual gas analyzer for the quantification of  $p_{\text{H}_2\text{O}}$ , which probably resulted in an overestimation of the values

deposition. However, the water vapor pressure is known to be the most crucial parameter during sputtering for the deposition of an amorphous indium oxide film. During the deposition we varied the water vapor pressure in the range of  $0.2 \times 10^{-3} \text{ Pa} \leq p_{H_2O} \leq 0.68 \times 10^{-3} \text{ Pa}$ , the oxygen partial pressure was constant at  $p_{O_2} = 0.88 \times 10^{-3} \text{ Pa}$ . At  $p_{H_2O} = 0.2 \times 10^{-3} \text{ Pa}$  partial film crystallinity was observed already after deposition by GI-XRD measurements, as shown in Figure 4.1 (b). In contrast, high water vapor pressures in this range led already to fully amorphous films when deposited by RF sputtering [65]. By increasing the water vapor pressure during pulsed DC sputtering to  $p_{H_2O} \geq 0.33 \times 10^{-3} \text{ Pa}$  the crystalline fraction can be decreased, leading to a mainly amorphous structure of the film. The overall amorphous growth indicates the incorporation of hydrogen during the deposition [46].

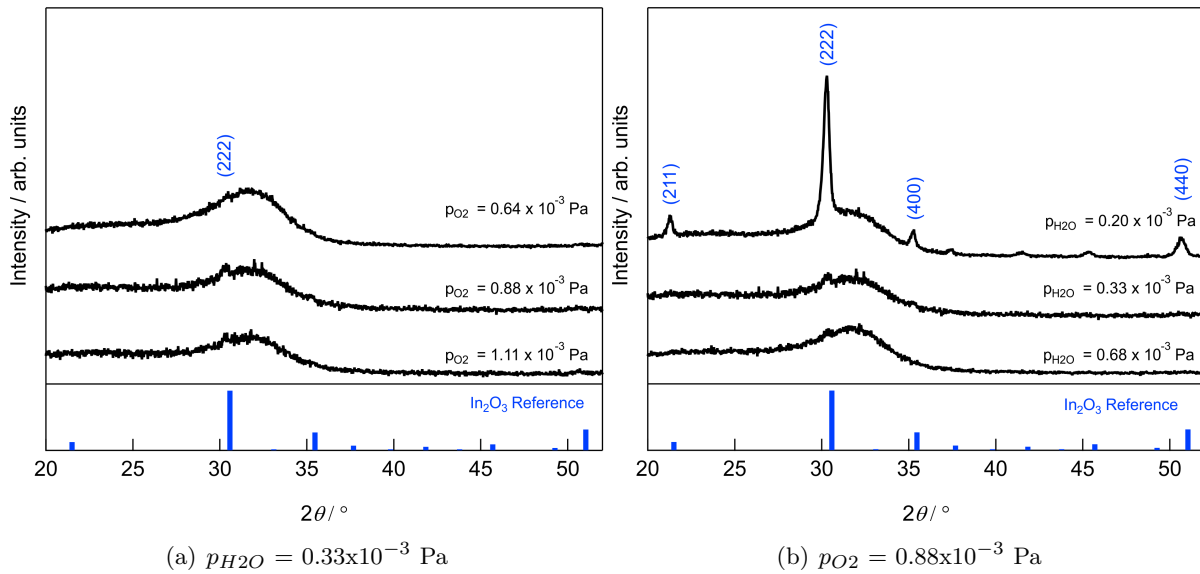


Figure 4.1: X-ray diffraction patterns of hydrogen doped indium oxide films in the as grown state deposited by pulsed DC magnetron sputtering with (a) constant  $p_{H_2O}$  and varied  $p_{O_2}$  and (b) constant  $p_{O_2}$  and varied  $p_{H_2O}$ ; the  $In_2O_3$  reference pattern was taken from PDF 00-006-0416, patterns were shifted vertically for improved clarity

A post deposition thermal treatment leads to solid phase crystallization of the amorphous films. The crystallization process can be influenced by its temperature, duration and atmosphere but is also dependent on the initial film structure. Annealing in both vacuum and air at  $220 \text{ }^\circ\text{C}$  for a duration of 30 min result in solid phase crystallization of the amorphous film. In Figure 4.2 X-ray diffraction patterns of the air and vacuum annealed films, which were deposited at  $p_{H_2O} = 0.33 \times 10^{-3} \text{ Pa}$  and  $p_{O_2} = 0.88 \times 10^{-3} \text{ Pa}$ , are shown as examples. The observed peaks can be assigned to cubic bixbyite  $In_2O_3$  structure. The peak intensity ratios of (222)/(400) and (222)/(440) are 3.4 and 3.7 for the air annealed film and 3.4 and 3.4 for the vacuum annealed film, respectively. The peak intensity ratio of (222)/(400) is close to the reference value of 3.3 for

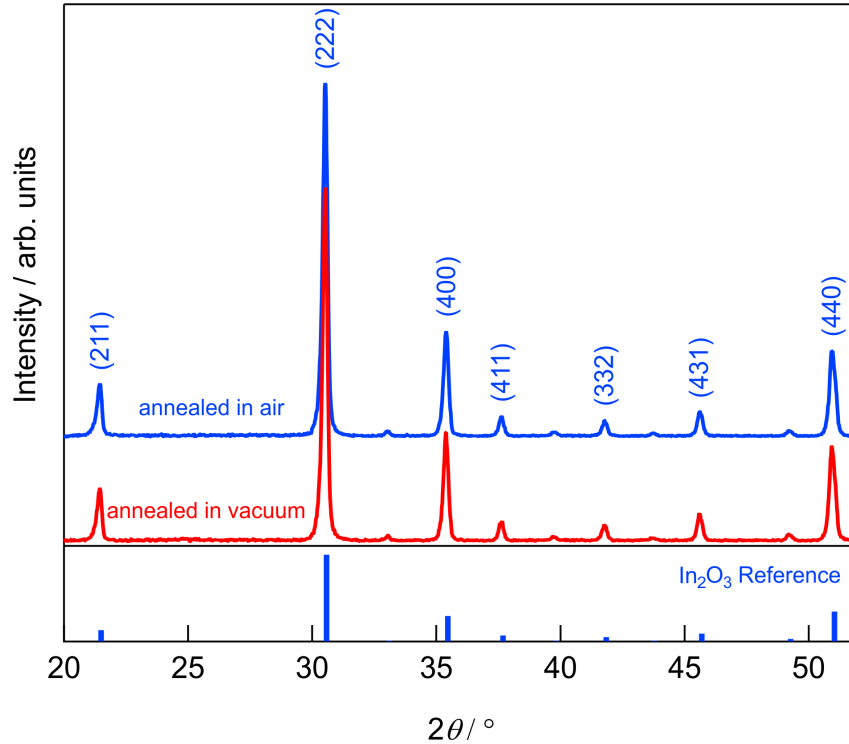


Figure 4.2: X-ray diffraction patterns of hydrogen doped indium oxide films annealed in vacuum or air for 30 min at 220 °C; the  $\text{In}_2\text{O}_3$  reference pattern was taken from PDF 00-006-0416, patterns were shifted vertically for improved clarity

both films while the peak intensity ratio of (222)/(440) is higher than the reference value of 2.9, indicating slightly less crystal growth in (440) orientation.

Figure 4.3 shows EBSD images of air annealed samples sputtered at  $p_{\text{H}_2\text{O}} = 0.33 \times 10^{-3}$  Pa and (a)  $p_{\text{O}_2} = 0.64 \times 10^{-3}$  Pa and (b)  $p_{\text{O}_2} = 1.11 \times 10^{-3}$  Pa, respectively. A randomly oriented grain structure can be observed for both films by EBSD. The domains of the film sputtered at lower oxygen content reach sizes up to 600 nm and only a few small domains are located in between. In contrast the air annealed film sputtered at higher  $p_{\text{O}_2}$  shows a significantly higher amount of small domains. Further pixelated areas can be observed, which have a share of almost half of the total area.

The finding provides evidence that the film morphology of the pulsed DC magnetron films depends strongly on the deposition parameters. As an amorphous growth could be observed for films sputtered at  $p_{\text{H}_2\text{O}} \geq 0.33 \times 10^{-3}$  Pa, we assume that during deposition hydrogen is incorporated in the film structure. A high oxygen flow during the deposition can lead to an increased nano-crystallinity in sputtered IOH films [106]. The nuclei do not coalesce during solid phase crystallization and thus prevent the formation of large grains. The pixelated areas observed in the EBSD images can be caused by either amorphous regions or domains smaller

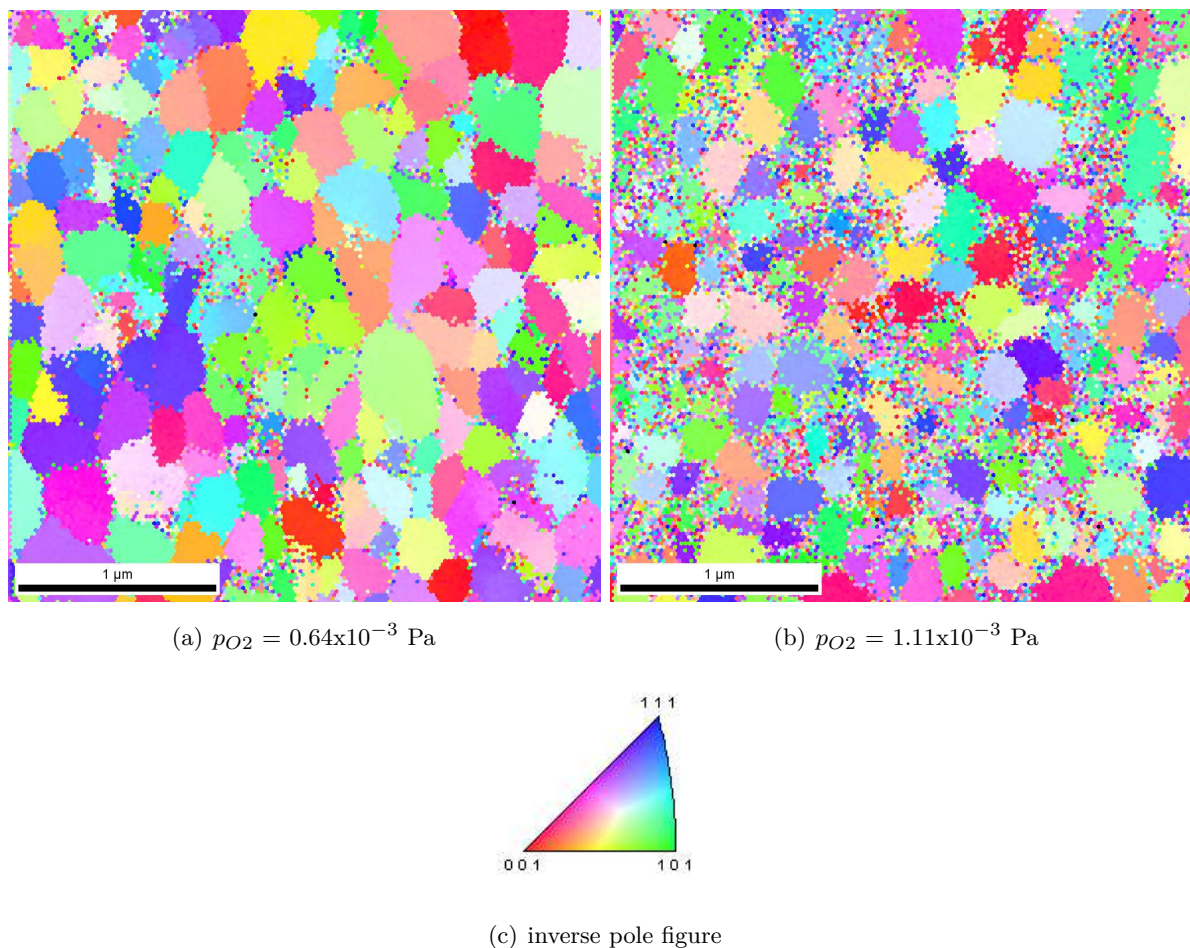


Figure 4.3: EBSD measurements of air annealed IOH layers sputtered at constant  $p_{H_2O} = 0.33 \times 10^{-3}$  Pa and varied oxygen partial pressure (a)  $p_{O_2} = 0.64 \times 10^{-3}$  Pa and (b)  $p_{O_2} = 1.11 \times 10^{-3}$  Pa; (c) inverse pole figure; adapted from Erfurt et al. [105]

than the resolution minimum of the measurement setup. If this were caused by an amorphous structure, however, a clear difference between the films would have to be observed by GIXRD. In fact the measurements showed an even higher amount of crystallinity for the film sputtered at higher oxygen supply, as shown in Figure 4.4. No amorphous hump can be observed. Thus it can be assumed that these areas are caused by nanocrystals and presumably defect rich areas, which form during the solid phase crystallization.

*The main findings can be summarized as follows:*

- The process window for the deposition of amorphous  $In_2O_3:H$  seems to be more narrow for pulsed DC magnetron sputtering than RF. magnetron sputtering, regarding the parameter "water vapor pressure"

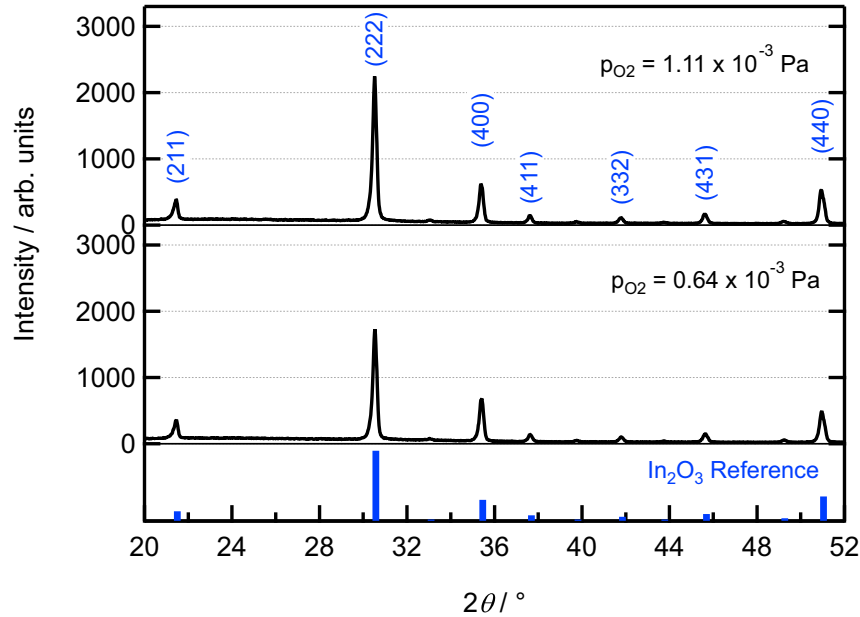


Figure 4.4: GIXRD diffraction pattern for air annealed films deposited at  $p_{O_2} = 0.64 \times 10^{-3}$  Pa and  $p_{O_2} = 1.11 \times 10^{-3}$  Pa, respectively; Reference diffraction pattern of  $\text{In}_2\text{O}_3$  (Ref. 00-006-0416); adapted from Erfurt et al. [105]

- Films sputtered at increased oxygen supply showed a more porous surface morphology after the annealing in air than films deposited at low oxygen content.

## 4.2 Electrical Properties

In the following first the electrical properties of the sputtered films before annealing are discussed. Based on this results the properties after annealing in vacuum or air are compared.

In Figure 4.5 the charge carrier density, the electron mobility and the resistivity of the as grown films are shown in dependence of the oxygen partial pressure (a) and water vapor pressure (b). With increasing oxygen supply the charge carrier density was found to decrease, presumably as a higher amount of oxygen atoms is incorporated into the films. This consequently decreases the amount of oxygen vacancies  $V_O^{++}$ , which are known to act as doubly charged donors [62]. At the same time the electron mobility increases from  $41 \text{ cm}^2/\text{Vs}$  up to  $54 \text{ cm}^2/\text{Vs}$  due to the reduced impurity scattering by doubly charged oxygen vacancies. These results are consistent with results found in literature [106]. In combination, the dominating decrease of the charge carrier density results in an increased resistivity with higher  $p_{O_2}$ .

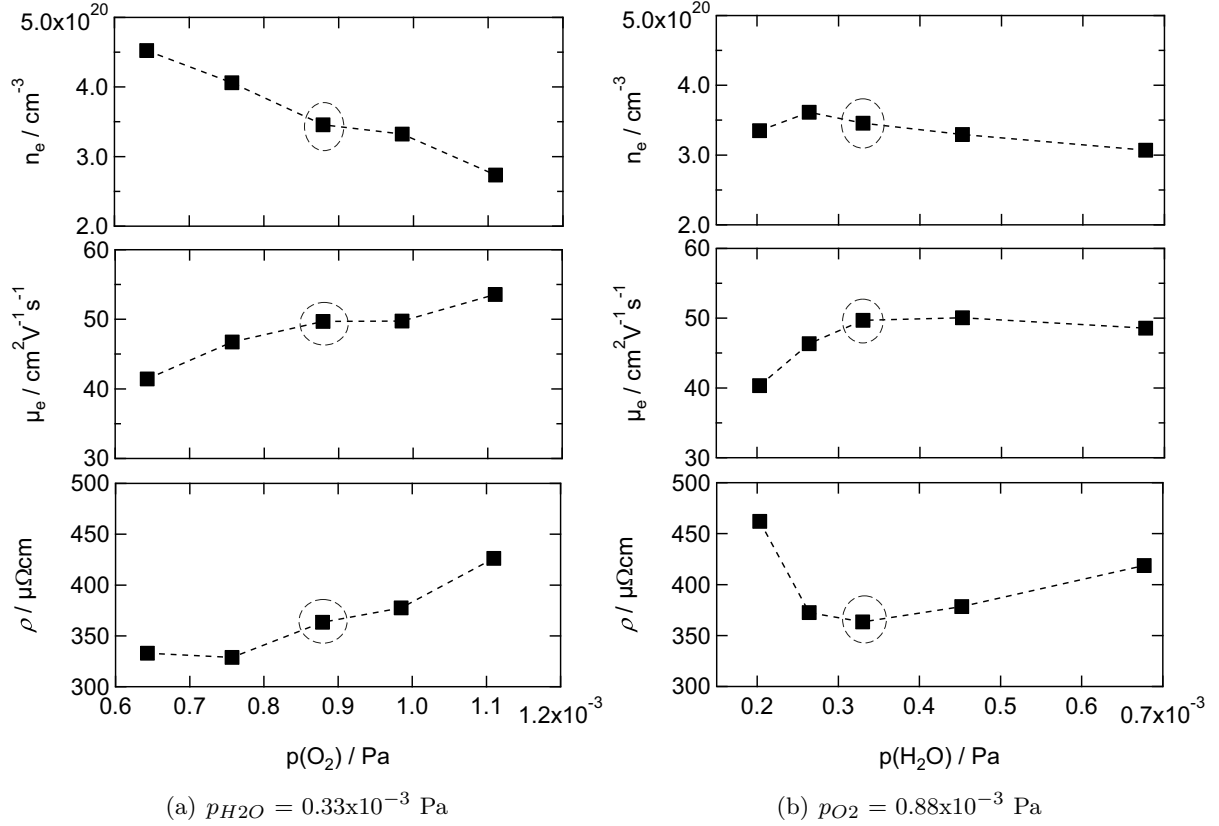


Figure 4.5: Development of the electrical properties of as grown  $\text{In}_2\text{O}_3:\text{H}$  films deposited at (a) constant  $p_{H_2O} = 0.33 \times 10^{-3} \text{ Pa}$  and varied  $p_{O_2}$  and (b) constant  $p_{O_2} = 0.88 \times 10^{-3} \text{ Pa}$  and varied  $p_{H_2O}$ ; samples that were deposited at the same conditions are circled

With increasing  $p_{H_2O}$  from  $0.26 \times 10^{-3} \text{ Pa}$  to  $0.68 \times 10^{-3} \text{ Pa}$  a slight decrease of the charge carrier density from  $3.62 \times 10^{20} \text{ cm}^{-3}$  to  $3.07 \times 10^{20} \text{ cm}^{-3}$  can be observed. In this range the films grow amorphous. In contrast, the electron mobility was found to increase from  $40 \text{ cm}^2/\text{Vs}$  to  $50 \text{ cm}^2/\text{Vs}$  with increase of the water vapor pressure. Consequently the resistivity reaches a minimum of  $360 \mu\Omega \text{cm}$  at  $p_{H_2O} = 0.33 \times 10^{-3} \text{ Pa}$ .

The electrical properties of the crystallized films are strongly correlated with the film structure, which can be influenced by the deposition parameters oxygen partial pressure and water vapor pressure and the subsequent annealing. For all films the charge carrier density, electron mobility and resistivity were investigated, the results are shown in Figure 4.6 (a) and (b), respectively. With increasing Oxygen partial pressure ( $p_{O_2}$ ) the carrier density decreases for both annealing atmospheres, as already observed for the as deposited films, shown in Figure 4.5 (a). However the charge carrier density of layers annealed in air is consistently lower than that of vacuum annealed films and the spread increases from  $\Delta n_e = 0.12 \times 10^{20} \text{ cm}^{-3}$  to  $\Delta n_e = 0.58 \times 10^{20} \text{ cm}^{-3}$  when increasing  $p_{O_2}$  from  $0.64 \times 10^{-3} \text{ Pa}$  to  $1.11 \times 10^{-3} \text{ Pa}$ , respectively. In parallel to the decreasing

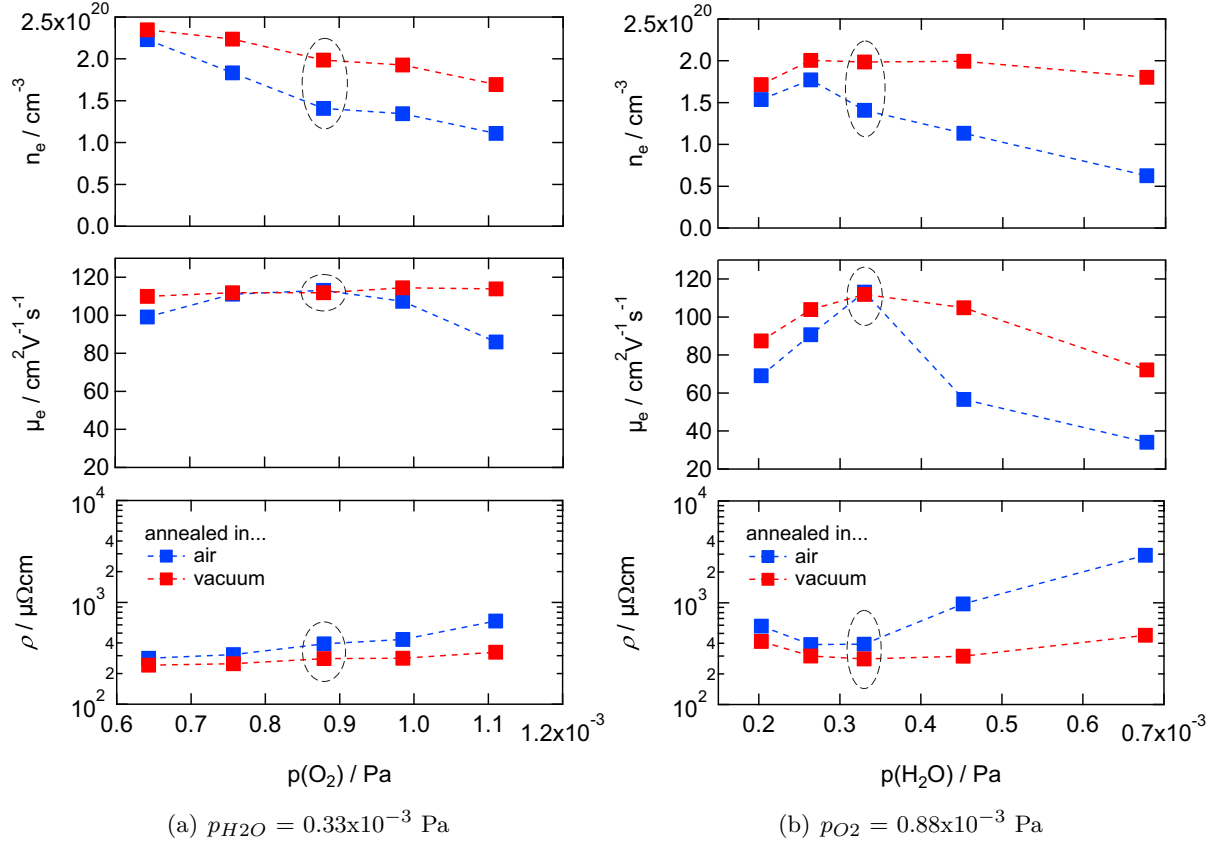


Figure 4.6: Development of the electrical properties of  $\text{In}_2\text{O}_3:\text{H}$  films deposited at (a) constant  $p_{H_2O} = 0.33 \times 10^{-3}$  Pa and varied  $p_{O_2}$  and (b) constant  $p_{O_2} = 0.88 \times 10^{-3}$  Pa and varied  $p_{H_2O}$  after annealing in vacuum or air, respectively, at 220 °C for 30 min; samples that were deposited at the same conditions are circled; adapted from Erfurt et al. [105]

carrier density the mobility of vacuum annealed films increases slightly up to  $113 \text{ cm}^2/\text{Vs}$ . An increase of the electron mobility with increasing  $p_{H_2O}$  was already observed for the as grown films. For films annealed in air this could not be observed. Electron mobilities of  $113 \text{ cm}^2/\text{Vs}$  were determined only at  $p_{O_2} = 0.88 \times 10^{-3}$  Pa for an annealing duration of 30 min. Here, the electron mobility of films sputtered at lower  $p_{O_2}$  increased by a prolonged thermal treatment while no improvement is observed for films sputtered at higher  $p_{O_2}$  for shorter or longer annealing durations, respectively. Additionally the electron mobility of all air annealed films dropped when prolonging the annealing time further (not shown here).

As seen in Figure 4.6 (b), the film properties are also sensitive to the water partial pressure within the pulsed DC sputtering process. Electron mobilities of more than  $100 \text{ cm}^2/\text{Vs}$  could only be achieved in the range of  $0.25 \times 10^{-3} \text{ Pa} < p_{H_2O} < 0.45 \times 10^{-3} \text{ Pa}$  after annealing in vacuum and only for  $p_{H_2O} = 0.33 \times 10^{-3}$  Pa after annealing in air. For  $p_{H_2O} > 0.33 \times 10^{-3}$  Pa the electron

mobility starts to decrease, regardless of the annealing atmospheres but with a stronger decline for the layers annealed in air. In analogy to the as deposited films the charge carrier density of vacuum annealed films decreased slightly with increasing  $p_{H_2O}$ , but dropped drastically for air annealed films.

The findings of the present study show that the electrical properties can be influenced by the deposition parameter water vapor and oxygen partial pressure as well as the annealing atmosphere. By increasing the water vapor pressure during deposition it is likely that a higher amount of In-OH and In(OH)<sub>3</sub> is incorporated in the film eliminating more doubly charged oxygen vacancies. This can lead to the decreased charge carrier density, as observed in Figure 4.5 (b).

In fact an additional experiment showed that films sputtered with a very high  $p_{H_2O} \approx 20 \times 10^{-3}$  Pa and without any additional oxygen supply ( $q(\text{Ar}/\text{O}_2) = 0$  sccm) had a reduced charge carrier density of  $n_e = 3.1 \times 10^{20} \text{ cm}^{-3}$  in the as grown state. In contrast films deposited at  $p_{H_2O} \approx 3.7 \times 10^{-3}$  Pa with additional oxygen supply ( $q(\text{Ar}/\text{O}_2) = 25$  sccm) showed an increased charge carrier density of  $n_e = 4.2 \times 10^{20} \text{ cm}^{-3}$ . The electron mobility of both as grown films was  $\mu_e \approx 43 \text{ cm}^2/\text{Vs}$ . Note that both films were sputtered at otherwise equal conditions, but still different compared to the films further discussed in this chapter. This result indicates that during deposition oxygen vacancies are eliminated and that the increased amount of hydrogen does not necessarily act as donor. We assume that the increase of electron mobility in Figure 4.5 (b) can be explained by the increasingly amorphous structure of the layers, as shown in Figure 4.1 (b), as scattering at grain boundaries or at the interface of the crystalline and amorphous phase [22] is reduced. Thus the low  $\mu_e$  of films sputtered at  $p_{H_2O} = 0.2 \times 10^{-3}$  Pa could be explained by the films not being completely amorphous after the deposition and before annealing.

The results suggests that during the post deposition thermal treatment in air atmospheric species like O<sub>2</sub>, H<sub>2</sub>O or CO<sub>2</sub> can diffuse into the layer and act as charge carrier traps or bond the dopant hydrogen [107] and thus lower the charge carrier density of air annealed films compared to films annealed in vacuum. The stronger decrease of  $n_e$  with increased oxygen partial pressure during desposition is attributed to the differences in film morphology. The nanocrystalline structure of layers sputtered at higher  $p_{O_2}$  is assumed to provide a higher amount of percolation paths at the grain boundaries. Consequently more atmospheric species may diffuse into the layer and thus promote the decrease of the charge carrier density. The diffused atmospheric species may also act as impurity scattering centers or lead to an increase of the electron barrier at the grain boundaries due to chemical modifications [107]. Both effects may explain the decreased electron mobility of air annealed films which were sputtered at higher  $p_{O_2}$ .

Furthermore a dependence of the electrical properties on the water vapor pressure during deposition was observed. We assume that this can be correlated with the resulting film structure. A higher amount of H or OH can be incorporated in the films when increasing  $p_{H_2O}$  [46]. During

crystallization these species can diffuse to the grain boundaries, especially interstitial hydrogen is highly mobile [108], forming a void rich structure, as shown by Koida et al [109], or an overall reduced film crystallinity. This leads to increased impurity scattering and decreased electron mobility. When annealing these films in air these structures provide diffusion paths for different atmospheric species, as described before, leading to the lower mobility and carrier density. Also Scherg-Kurmes et al [110] predicted that a porous film structure, which forms at sputter pressures as high as 0.6 Pa, is harmful for the electrical properties of IOH after annealing in air.

*The main findings can be summarized as follows:*

- IOH films obtained lower charge carrier densities after annealing in air compared to films, which were annealed in vacuum, presumably due to diffusion of atmospheric species during annealing, acting as charge carrier traps.
- The films showed similar high electron mobilities after annealing in vacuum and air only for a specific set of deposition parameters, otherwise electron mobilities of film annealed in vacuum were typically higher than the ones of air annealed films.

### 4.3 Optical Properties

In this section we compare the optical properties of a film, which showed reasonable high electron mobilities after annealing. First the transmittance, reflectance and absorption of the film before and after annealing in vacuum or air are compared. Second the optical band gaps of the films are estimated and the results discussed.

Figure 4.7 presents the reflectance, transmittance and absorption spectra of the as deposited, air or vacuum annealed IOH films, which were deposited at an oxygen partial pressure of  $p_{O_2} = 0.88 \times 10^{-3}$  Pa and a water vapor pressure of  $p_{H_2O} = 0.33 \times 10^{-3}$  Pa, respectively. From this data we can see, that the transmittance increases after annealing while the absorption decreases over the whole wavelength range. The absorption of the vacuum annealed film is higher in the NIR than that of the air annealed film. In the visible region no difference can be observed between the samples. Additionally the graph shows the absorption spectra of an AZO thin film with  $d = 550$  nm,  $n_e = 2.8 \times 10^{20}$  cm<sup>-3</sup>,  $\mu_e = 25$  cm<sup>2</sup>/Vs and  $R_{Sq} = 16$  Ω/Sq. The vacuum annealed film showed a comparable sheet resistance of  $R_{Sq} = 14$  Ω/Sq but had a much lower film thickness of only  $d = 200$  nm. Due to its high electron mobility of  $\mu_e = 112$  cm<sup>2</sup>/Vs a lower charge carrier density of only  $n_e = 2.0 \times 10^{20}$  cm<sup>-3</sup> is sufficient to achieve a similar sheet resistance at the decreased film thickness. This combination leads to the lower absorption of the vacuum annealed IOH film compared to the AZO film over the whole spectra.

Figure 4.8 illustrates the dependence between  $(\alpha h\nu)^2$  and the photon energy  $h\nu$  of the air and vacuum annealed films. The extrapolation of the linear part of the curves onto the energy axis indicates the optical band gap of the vacuum annealed film to be 3.79 eV and 3.73 eV for the air annealed sample. In contrast the as grown film had a optical band gap of only 3.47 eV.

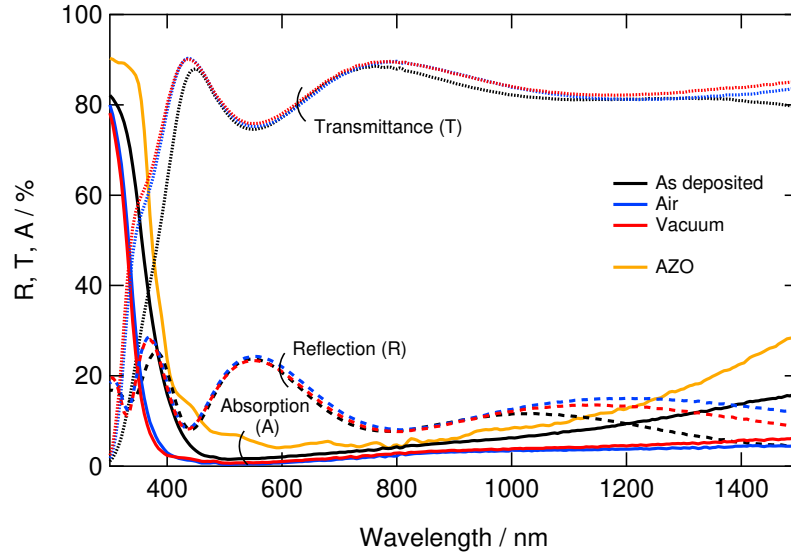


Figure 4.7: Reflection (R), transmittance (T) and absorption (A) spectra of IOH, deposited at  $p_{O_2} = 0.88 \times 10^{-3}$  Pa and  $p_{H_2O} = 0.33 \times 10^{-3}$  Pa, after annealing in vacuum or air; for comparison the absorption spectra of an AZO film is shown

These findings highlight the beneficial aspect of the annealing on the optical properties. The shift of the absorption edge towards lower wavelengths indicates the crystallization process. The slightly higher absorption of the vacuum annealed films in the NIR can be related to the free carrier absorption, as the charge carrier density of the vacuum annealed film is higher compared to the air annealed film. The relationship of the optical band gap and the photon energy indicates that the electronic transitions are direct transitions across the band gap of the films [111]. The slightly higher optical band gap of the vacuum annealed ( $\Delta E_g = 0.06$  eV) film can be explained by the higher charge carrier concentration and filling of electronic states in the conduction band (Burstein-Moss shift) [112, 113]. According to the Burstein Moss equation the difference was estimated to be 0.07 eV, which is in good agreement with the measured value.

*The main findings can be summarized as follows:*

- Due to the lower charge carrier density of air annealed IOH films the parasitic absorption in the NIR is lower than that of vacuum annealed films.
- Due to the lower charge carrier density of air annealed IOH films the optical band gap is lower than that of vacuum annealed films, according to the Burstein-Moss-shift.

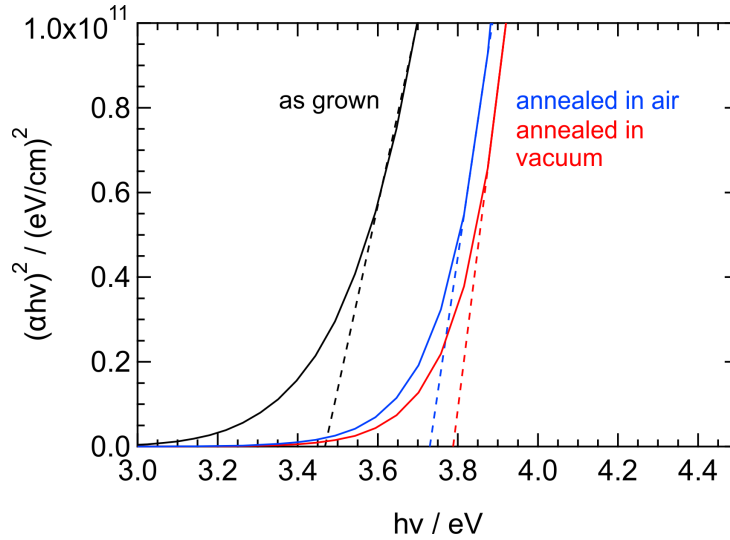


Figure 4.8: Tauc plot of IOH film, deposited at  $p_{O_2} = 0.88 \times 10^{-3}$  Pa and  $p_{H_2O} = 0.33 \times 10^{-3}$  Pa, after annealing in vacuum or air

## 4.4 Stability

The implementation of high mobility TCOs in e.g. solar cells require a certain stability of their properties over several years and can be estimated by accelerated aging during damp heat tests. We investigated the stability of the electrical properties of vacuum and air annealed films, which were sputtered at high and low water vapor pressures and high/low oxygen partial pressures, respectively. The results are presented in the following.

The changes of the electrical properties over time can be found in Figure 4.9 (a) and (b), respectively. After 1000 h of damp heat the resistivity of the vacuum and air annealed films sputtered at  $p_{O_2} = 0.64 \times 10^{-3}$  Pa increased from  $243 \mu\Omega\text{cm}$  to  $280 \mu\Omega\text{cm}$  (+ 15 %) and from  $283 \mu\Omega\text{cm}$  to  $358 \mu\Omega\text{cm}$  (+ 27 %), respectively. In contrast, the resistivity of the annealed films sputtered at high oxygen partial pressure increased significantly by 223 % from  $325 \mu\Omega\text{cm}$  to  $1048 \mu\Omega\text{cm}$  and by 345 % from  $654 \mu\Omega\text{cm}$  to  $2913 \mu\Omega\text{cm}$ , respectively. The main cause is the strong decrease of the electron mobility. For films sputtered at  $p_{O_2} = 1.11 \times 10^{-3}$  Pa the decrease was observed already after 24 h. In contrast, annealed films sputtered at  $p_{O_2} = 0.64 \times 10^{-3}$  Pa were stable up to 500 h of damp heat, regardless of the annealing atmosphere. The charge carrier density was overall stable and decreased only slightly for the air annealed film which was sputtered at  $p_{O_2} = 0.64 \times 10^{-3}$  Pa.

This study indicates that the differences in the film morphology of air annealed films observed in the EBSD images can explain the corresponding poor damp heat stability of films sputtered at higher  $p_{O_2}$ . A higher amount of percolation paths would promote diffusion of atmospheric

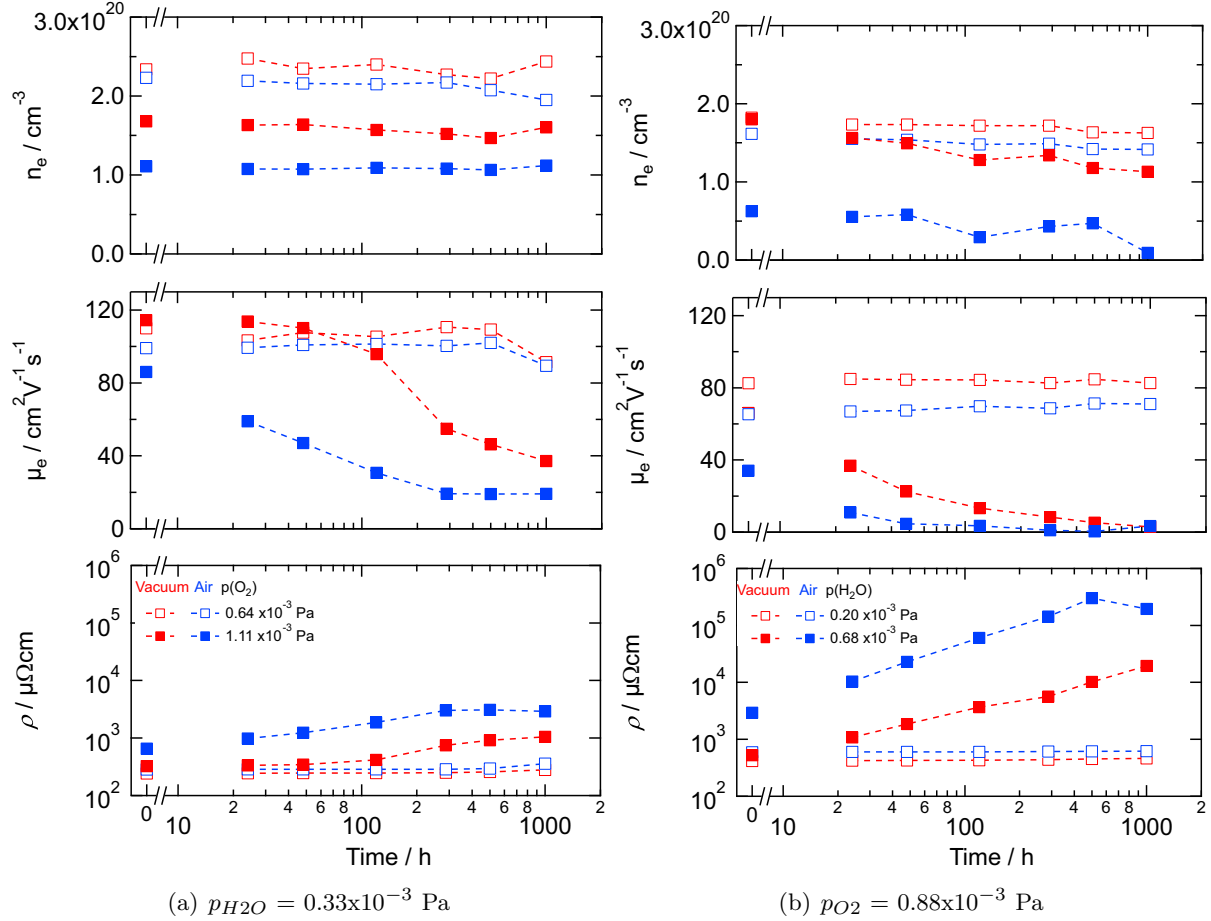


Figure 4.9: Change of the electrical properties during damp heat tests of films annealed in vacuum or air, deposited at (a) constant  $p_{H_2O} = 0.33 \times 10^{-3}$  Pa (adapted from Erfurt et al. [105]) and (b) constant  $p_{O_2} = 0.88 \times 10^{-3}$  Pa

species during the damp heat into the bulk. In contrast to the processes taking place during air annealing, no further drop of the carrier density is observed. Nevertheless, these species can bond hydrogen. Tohsophon et al [114] proposed the removal of H atoms at grain boundaries by adsorbed OH-radicals which form  $H_2O$  molecules. The formation and desorption of  $H_2O$  would lead to a loss of passivation at grain boundaries and to a drop of electron mobility [66, 114]. Atmospheric species which already diffused into the films during the annealing in air can accelerate this process and therefore lead to a more pronounced loss of electron mobility, as observed here for films annealed in air compared to the films annealed in vacuum.

Similarly, a more distinct  $\mu_e$  decrease was also found for the annealed films which were deposited at higher  $p_{H_2O}$ , as can be seen in Figure 4.9 (b). This is consistent with the finding of Jost et al. [107] and Koida et al. [109]. It was shown that a porous grain boundary structure, which forms when the films contain a high amount of H, accelerate the degradation of  $\mu_e$ , as they would

have indium hydroxide or weakly bonded structures incorporating large amounts of OH species around the grain boundary [109]. However, this might not be the main cause for the different degradation of films sputtered at low and high oxygen partial pressure, as here the water vapor pressure was held constant during deposition. Thus the incorporated amount of hydrogen is assumed to be equal.

To evaluate the stability of IOH films the results are compared to the stability of an AZO film of  $\approx 290$  nm thickness. The initial electrical properties before the damp heat tests were  $n_e = 2.9 \times 10^{20} \text{ cm}^{-3}$  and  $\mu_e = 18.5 \text{ cm}^2/\text{Vs}$  resulting in  $\rho = 1177 \mu\Omega\text{cm}$ . After 1000 h of damp heat the charge carrier density and electron mobility decreased by 23 % and 21 % respectively, resulting in an increase of resistivity of 65 % to  $1944 \mu\Omega\text{cm}$ . The finding is consistent with findings of past studies by Greiner et al [115], who also reported an increase in resistivity of 70 % for 420 nm thin films, which is similar to the film thickness of the AZO film in this study. The study of the IOH stability revealed that IOH thin films are more stable ( $\rho$ : + 15 %) if prepared at low water vapor pressure and oxygen partial pressure, respectively and annealed in vacuum (here:  $p_{\text{H}_2\text{O}} = 0.33 \times 10^{-3} \text{ Pa}$  and  $p_{\text{O}_2} = 0.64 \times 10^{-3} \text{ Pa}$ ) and still have a lower resistivity of  $\rho = 310 \mu\Omega\text{cm}$  after 1000 h of damp heat than the investigated AZO film. All films were deposited on a smooth glass substrate. However, it is known that the substrate roughness can influence the stability of TCOs. As highlighted by Greiner et al [115,116] an accelerated degradation of the conductivity of AZO thin films was found when deposited on rough substrates. Similar to these findings, also for IOH thin films such an influence could be observed. The results are discussed in section 5.3.

*The main findings can be summarized as follows:*

- Air annealed films were slightly less stable during damp heat tests than films annealed in vacuum, presumably due to the presence of incorporated atmospheric already after annealing.
- Annealed films deposited at respectively high water or oxygen partial pressured showed pronounced degradation during damp heat tests, most likely due to a porous structure.

## 4.5 Strategies to improve the electro-optical properties after annealing in air

For successful transfer to an industrial production annealing in air may be advantageous compared to annealing in vacuum. However, the sheet resistance of the air annealed films is higher compared to vacuum annealed films at similar weighted optical absorption values (400 nm to 1100 nm), as can be seen in Figure 4.10 (a). This is caused by the lower carrier density of air annealed films, as discussed before. To increase the carrier density after annealing in air we developed a bi-layered IOH film structure. The approx. 160 nm thick bulk-layer was sputtered at  $p_{H_2O} = 0.33 \times 10^{-3}$  Pa and  $p_{O_2} = 0.88 \times 10^{-3}$  Pa, as here the highest mobilities were achieved after 30 min of annealing in air. At these conditions an amorphous growth can be realized, as seen in 4.1 (b). The approx. 30 nm thick cap-layer was deposited at a reduced water vapor pressure of  $p_{H_2O} = 0.2 \times 10^{-3}$  Pa, which led to a partly crystalline growth. The combined bi-layer film showed an amorphous structure in XRD, as the influence of the partly crystalline thin cap-layer is very low compared to the amorphous structure of the 160 nm thick bulk-layer underneath. In Figure 4.11 GI-XRD measurements of the bi-layer film and 200 nm thick reference layers are shown. The X-ray diffraction patterns of the reference layers were equal to the ones of the corresponding layers from Figure 4.1.

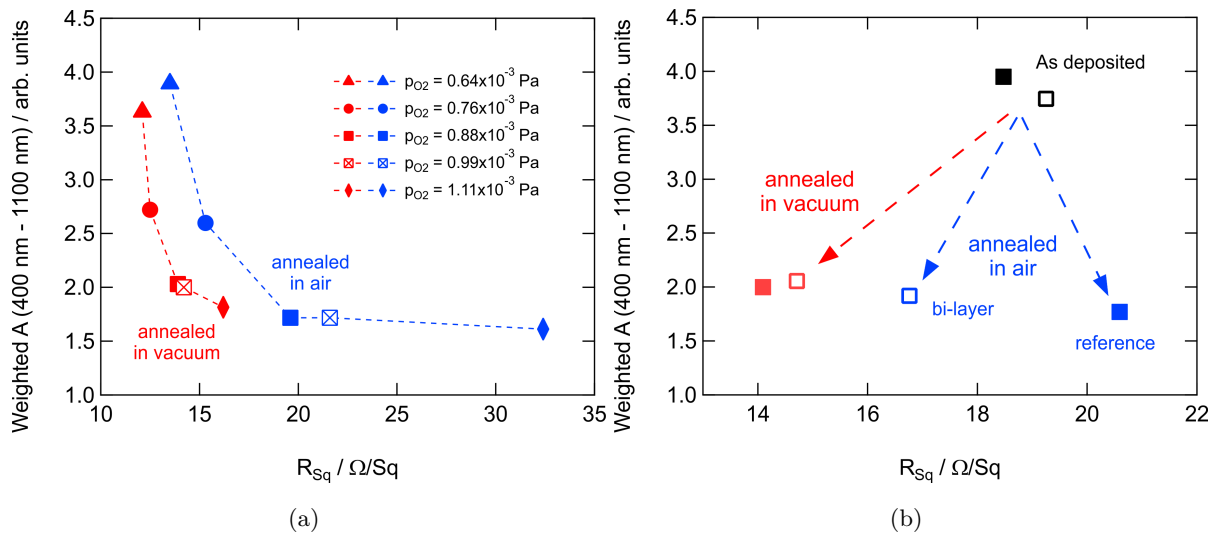


Figure 4.10: Weighted optical absorption in dependence of the sheet resistance of (a) IOH films annealed in vacuum or air with varied oxygen supply during sputtering; (b) uncapped (solid symbols) and capped (empty symbols) IOH films before and after annealing; the weighted optical absorption of the glass substrate was calculated to 1.01; adapted from Erfurt et al. [105]

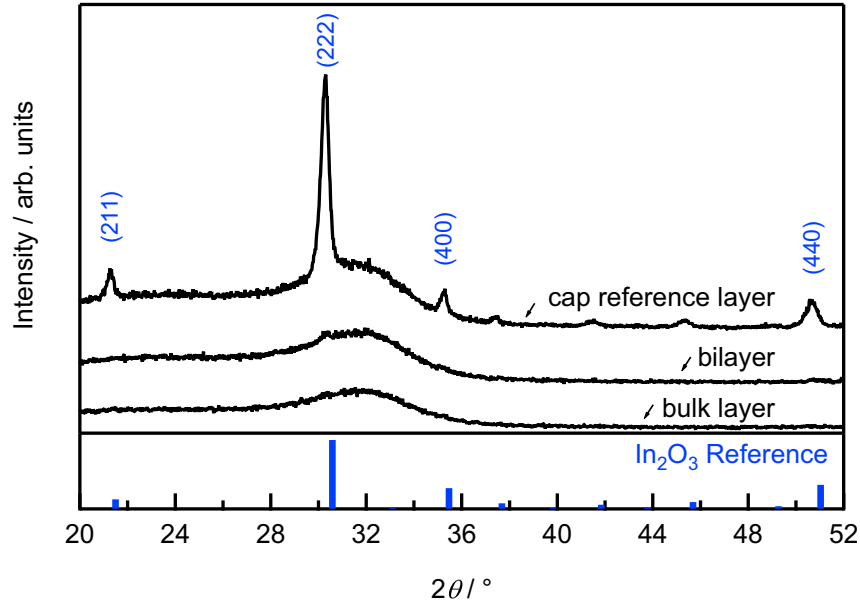


Figure 4.11: X-ray diffraction patterns of hydrogen doped indium oxide films in the as grown state as a single bulk layer, bi-layer and capped layer, respectively; the  $\text{In}_2\text{O}_3$  reference pattern was taken from PDF 00-006-0416, patterns are shifted for improved differentiation; adapted from Erfurt et al. [105]

Table 4.2: Electrical film properties and integral absorption ( $A_{int,400nm-1100nm}$ ) of capped and uncapped IOH before and after annealing in vacuum or air; partly adapted from Erfurt et al. [105]

Annealing	Sample	$n_e$ ( $\text{cm}^{-3}$ )	$\mu_e$ ( $\text{cm}^2/\text{Vs}$ )	$\rho$ ( $\mu\Omega\text{cm}$ )	$R_{Sq}$ ( $\Omega/\text{Sq}$ )	$A_{int,400nm-1100nm}$ (a.u.)
as deposited	reference	$3.7 \times 10^{20}$	47	362	18.5	3.95
as deposited	bi-layer	$3.6 \times 10^{20}$	48	368	19.3	3.74
vacuum	reference	$2.0 \times 10^{20}$	115	276	14.1	2.00
vacuum	bi-layer	$2.0 \times 10^{20}$	113	281	14.7	2.06
air	reference	$1.4 \times 10^{20}$	109	404	20.6	1.77
air	bi-layer	$1.8 \times 10^{20}$	108	320	16.8	1.92

In Figure 4.10 (b) the integral optical absorption (400 nm to 1100 nm) and sheet resistance of the approx. 190 nm bulk reference and the bi-layer sample before and after annealing are shown, the electrical properties and weighted absorption values are summarized in Table 4.2. Before annealing and after annealing in vacuum, the properties of capped and uncapped films, respectively, are very similar. However, in case of air annealing, the bi-layer film shows an increased charge carrier density of  $n_e = 1.8 \times 10^{20} \text{ cm}^{-3}$  compared to the charge carrier density of the bulk reference film with  $n_e = 1.4 \times 10^{20} \text{ cm}^{-3}$ . The electron mobilities were similar for the bi-layer and the bulk reference film, around  $\mu_e \approx 108 \text{ cm}^2/\text{Vs}$  to  $109 \text{ cm}^2/\text{Vs}$ . This leads to a significant improvement of the sheet resistance of  $\Delta R_{Sq} = 3.8 \text{ } \Omega/\text{Sq}$  for the capped film.

The results suggest that interactions of the film with atmospheric species during the annealing in air can be counteracted by a bi-layered film structure with a partly crystalline cap layer. An amorphous structure (uncapped bulk reference) is rich in lattice defects, distortions and vacancies, which can also act as percolation paths [107]. By growing a partly crystalline layer on the sample surface we can reduce the amount of percolation paths and thus the diffusion of atmospheric species into the bulk material already prior to and during annealing. Due to the higher amount of crystalline nuclei in the cap layer the film surface can be fully crystallized more easily during the annealing, while the bulk can still contain an increased amount of amorphous phase. This may lead to the observed higher charge carrier density for the bi-layer sample. As the partly crystalline cap layer does not harm the film quality significantly, electron mobilities over  $100 \text{ cm}^2/\text{Vs}$  can still be reached easily. The slightly increased weighted absorption is caused by the increased free carrier absorption in the NIR. Due to the still low defect density in the film, the absorption in the visible range does not increase significantly. As interactions with atmospheric species are negligible before annealing and after annealing in vacuum, the properties of capped and uncapped films, respectively, are very similar. Consequently, films crystallized in air with an increased conductivity and similar absorption values were realized.

*The main findings can be summarized as follows:*

- The decreased charge carrier density of air annealed films results in higher sheet resistances but comparable optical absorption with regard to vacuum annealed films.
- Due to implementation of a thin cap-layer with a higher crystalline fraction after deposition the charge carrier density of air annealed films was improved without significant losses in optical absorption or electron mobility.

## 4.6 Conclusion

In this chapter we showed how the deposition conditions water and oxygen partial pressure as well as the annealing atmosphere influence the properties of hydrogen doped indium oxide films, which were deposited by a pulsed DC magnetron sputtering process. We observed that the process window for the deposition of amorphous IOH is more narrow than for a RF sputtering process. For a water vapor pressure of  $p_{H_2O} = 0.2 \times 10^{-3} \text{ Pa}$  during deposition, already a pronounced crystalline growth was observed within this study, while such water vapor pressures were shown to result in mainly amorphous grown films, when deposited by RF sputtering [46]. When the films were deposited at respectively high oxygen partial pressures, a more porous structure was observed after annealing. We assume that this is similar for films deposited at high water vapor pressures. The annealing in vacuum or air initiates solid phase crystallization. During annealing

in air atmospheric species might diffuse into the films and act as charge carrier traps, thus reducing the charge carrier density of air annealed films. These films showed reduced parasitic absorption in the near infrared region and a reduced optical band gap due to the Burstein-Moss effect. However, a porous structure after annealing and further the presence of incorporated atmospheric species led both to accelerated degradation during damp heat, presumably due to enhanced diffusion of -OH at grain boundaries. The charge carrier density of air annealed films was improved by the implementation of a thin partly crystalline cap layer on a standard bulk film. Such a cap layer presumably counteracts the diffusion of atmospheric species during annealing in air, as a dense crystalline layer forms accelerated at the surface.

## CHAPTER 5

---

### Substrate Influences on Growth Mechanism and Properties

---

As front contact in CIGS solar cells indium oxide based TCOs can be deposited on different sublayers, dependent on the CIGS configuration. These layers as well as the topography of the CIGS samples can influence the growth of indium oxide based TCOs. In this chapter these influences are discussed separately. First the influence of layers such as sputtered Zn(O,S) and intrinsic zinc oxide (i-ZnO) on planar glass substrates on the properties of IOH is identified in section 5.1, as such layers are widely used in CIGS solar cells [117–119]. Alternatives to these layers may be indium gallium oxide thin films [120]. In section 5.2 their influence on the properties of IOH thin films is discussed when deposited on flat glass. Additionally the substrate morphology and topography of the CIGS absorber influence the growth of the indium oxide based TCOs. Therefore in section 5.3 influences of rough CIGS samples and textured glass substrates are evaluated. A limitation of the electron mobility of indium oxide based TCOs was found for several sub-layer conditions, mainly due to rough surfaces. Thus in section 5.4 strategies to improve the electron mobility on CIGS samples are presented. Furthermore the stability of IOH films on rough substrates is discussed in section 5.5. Lastly we summarize the findings in a chart, see section 5.6.

#### 5.1 Sputtered Zn(O,S) and ZnO films on glass

ZnO is a common material for the highly resistive layer in CIGS solar cells. In the last years also alternative materials, such as Zn(O,S) or (Zn,Mg)O are getting more attention. These materials can be applied as highly resistive or as the buffer layer. The zinc oxide based layers would be the template for the deposition of hydrogen doped indium oxide based TCOs, when applied in CIGS solar cells. Therefore it is important to study the combined layer stack and to identify possible influences of the sub-layer on the TCO. As example we investigated how sputtered ZnO

and Zn(O,S) layers affect the growth of sputtered  $\text{In}_2\text{O}_3\text{:H}$ . To exclude any further effects, the films were deposited on planar glass substrates. The roughness of CIGS is a further influence factor, the combination of both effects will be considered, in section 5.3.1. First the crystalline structure of the Zn(O,S) and several ZnO films is studied. Based on this we investigate the crystalline structure of  $\text{In}_2\text{O}_3\text{:H}$  and correlate the findings with the electrical properties of the films. Finally we discuss the obtained results<sup>1</sup>.

For the investigations 6 different films were deposited, one Zn(O,S) film and 5 ZnO films, deposited at varied conditions, as shown in Table 5.1. The sample ID consists of the material and the film thickness in nm for the ZnO films (40 nm, 130 nm or 200 nm). Additionally to the ZnO thickness variation, 130 nm films were deposited with intentional substrate heating (marked with "T"), or with a reduced total pressure (marked with "p"). The structure of the Zn(O,S) and ZnO films was investigated by X-ray diffraction measurements in the  $\theta - 2\theta$  and grazing incidence configuration. In Figure 5.1 GI-XRD measurements of  $\text{In}_2\text{O}_3\text{:H}$  on glass, Zn(O,S) and i-ZnO are shown. For the Zn(O,S) film no assignable peak was observed, thus the film was assumed to be amorphous. In contrast, the ZnO films were crystalline in the wurtzite type structure. In particular, the ZnO (002) diffraction peak is much stronger than other ZnO corresponding diffraction peaks, indicating oriented growth with the crystallographic c axis perpendicular to the substrate surface. To evaluate the film structure of the ZnO films, the lattice parameters  $c$  and the average domain sizes  $L$  were calculated, the results are shown in Table 5.1. The calculation is explained in section 3.2.1 on page 31. Furthermore the lateral grain size was estimated by AFM measurements ( $\langle D \rangle_{AFM}$ ). The calculated values are listed in Table 5.1.

Table 5.1: Deposition parameter and structural properties of sputtered Zn(O,S) and ZnO films; adapted from Erfurt et al. [100]

Sample	film thickness (nm)	$p_{tot}$ (Pa)	Heating (a.u.)	$c$ (Å)	$\langle D \rangle_V$ (nm)	$\langle D \rangle_{AFM}$ (nm)	$\tilde{\epsilon}$ (a.u.)
Zn(O,S)	60	0.5	no	-	-	-	-
ZnO40	40	0.8	no	5.2235	22.0	30.5	$3.47 \times 10^{-3}$
ZnO130	130	0.8	no	5.2146	29.0	43	$2.34 \times 10^{-3}$
ZnO200	200	0.8	no	5.2132	33.4	47	$2.20 \times 10^{-3}$
ZnO130T	130	0.8	yes	5.2109	28.1	49	$2.74 \times 10^{-3}$
ZnO130p	130	0.2	no	5.2307	21.7	33.4	$3.66 \times 10^{-3}$

<sup>1</sup>Reproduced in part with permission from *Darja Erfurt, Marc D. Heinemann, Sebastian S. Schmidt, Stefan Körner, Bernd Szyszka, Reiner Klenk, Rutger Schlatmann; Substrate influence on the growth of hydrogen doped indium oxide; ACS Appl. Energy Mater. 2018, 1, 5490-5499; doi: 10.1021/acsaem.8b01039*, Copyright 2018 American Chemical Society.; <https://pubs.acs.org/articlesonrequest/AOR-vSC6y2YnvNhDtSbYrpi3> [100], licensed under a [Creative Commons Attribution 4.0 International License](https://creativecommons.org/licenses/by/4.0/) (CC-BY)

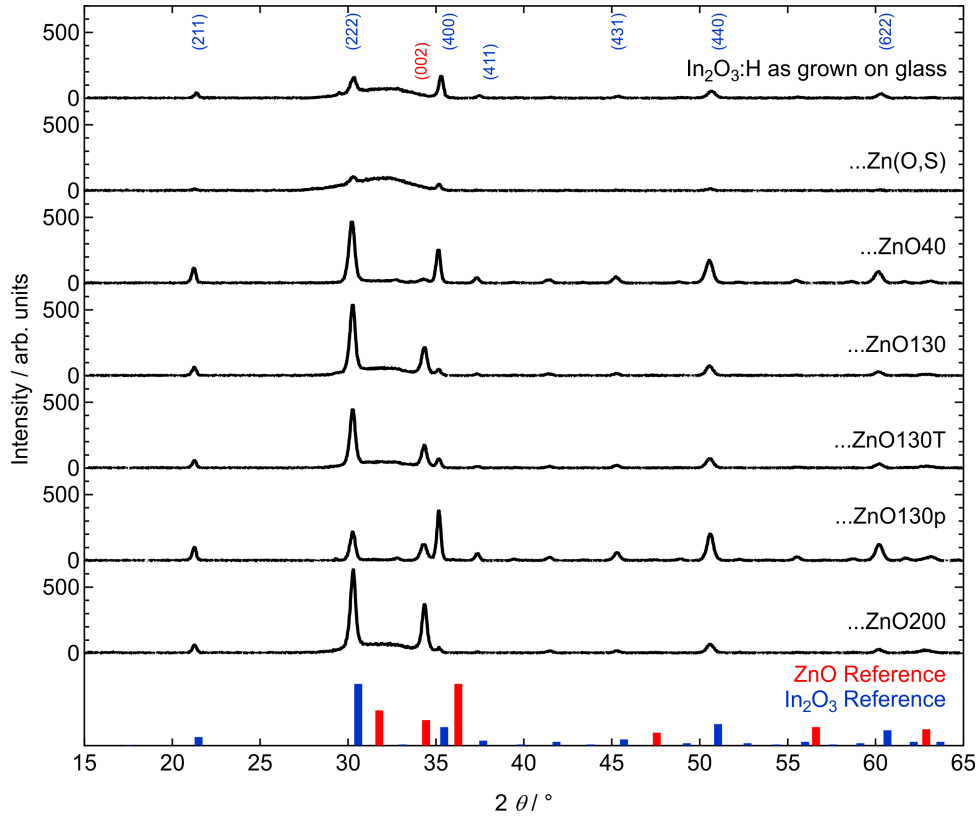


Figure 5.1: X-ray diffraction patterns of as grown  $\text{In}_2\text{O}_3\text{:H}$  films grown on bare,  $\text{Zn}(\text{O,S})$ -coated and  $\text{ZnO}$ -coated planar glass substrates; Sample names and descriptions can be found in Table 5.1; Reference pattern of  $\text{In}_2\text{O}_3$  and  $\text{ZnO}$  were taken from PDF 00-006-0416 and PDF 01-070-8070, respectively; patterns were shifted vertically for improved clarity; adapted from Erfurt et al. [100]

The increase in film thickness for samples  $\text{ZnO40}$ ,  $\text{ZnO130}$  and  $\text{ZnO200}$  results in an increase of the (002) volume-weighted crystallite size  $\langle D \rangle_V$  and AFM grain size  $\langle D \rangle_{AFM}$  and slight decrease of the lattice parameter  $c$  and weighted average strain  $\tilde{\epsilon}$  respectively. When the substrate was heated, the film ( $\text{ZnO130T}$ ) exhibit smaller  $\langle D \rangle_V$  and lattice constant, but a larger lateral grain size  $\langle D \rangle_{AFM}$  and strain  $\tilde{\epsilon}$ . A decrease of the total pressure from 0.8 Pa to 0.2 Pa results in decreased lateral and vertical grain size, but increased lattice constant and strain. These values were furthermore the smallest/largest within this series. For all  $\text{ZnO}$  films the calculated lattice parameter  $c$  is larger than the  $\text{ZnO}$  reference value  $c = 5.2066 \text{ \AA}$  [121]. The results suggest the unit cell is elongated along the  $c$  axis and the films are presumably under uniform stress with compressive components parallel to the substrate. This is in good agreement with other reported values for sputtered  $\text{ZnO}$  films [122–125]. The lattice constant  $a$  could not be calculated from the diffraction patterns, as the peak intensities of the corresponding peaks were too small to be evaluated. An increase of the  $\text{ZnO}$  crystallite size perpendicular to the substrate ( $\langle D \rangle_V$ , obtained by BB-XRD) typically correlates with an increase of the lateral grain size at the surface

( $\langle D \rangle_{AFM}$ , obtained by AFM). However, the lateral grain size is overall larger than the calculated volume-weighted (vertical) crystallite size. For further investigations  $\langle D \rangle_V$  is used, since  $\langle D \rangle_{AFM}$  does not contain information on the crystalline orientation of the films, which might be an important parameter. The weighted average strain  $\bar{\epsilon}$  was found to increase with decreased  $\langle D \rangle_V$ .

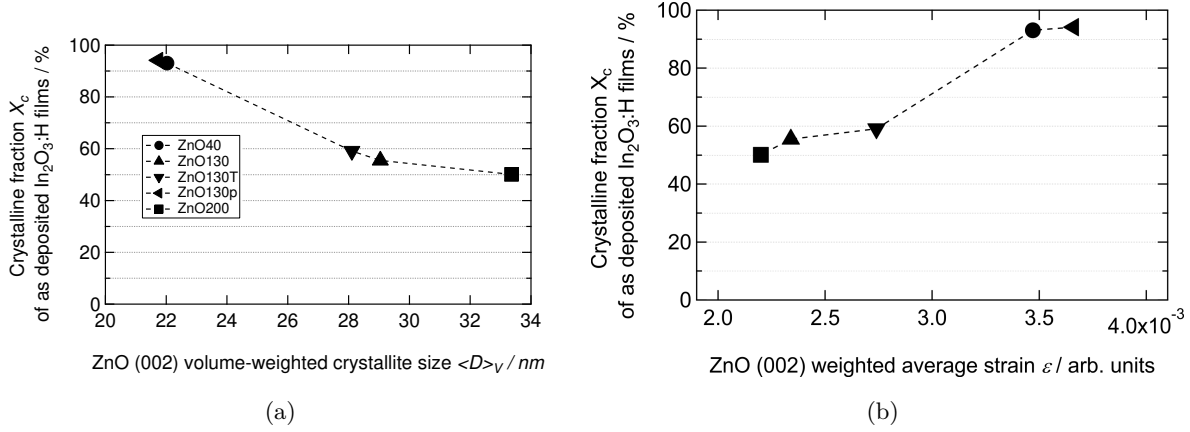


Figure 5.2: Dependence of crystallinity of as grown  $In_2O_3:H$  films on (a) ZnO (002) volume-weighted crystallite size and (b) ZnO (002) weighted average strain; dashed line serves as a guide to the eye; adapted from Erfurt et al. [100]

The GI-XRD measurements in Figure 5.1 revealed a mainly amorphous structure of  $In_2O_3:H$  films grown on amorphous Zn(O,S) and glass substrates, indicated by the low  $In_2O_3$  peak intensities and the broad feature in the range  $28^\circ < 2\theta < 36^\circ$ . In contrast, films grown on poly-crystalline ZnO showed significantly higher  $In_2O_3$  peak intensities, indicating a higher crystallinity. Furthermore changes in the preferred orientation were observed, which will be discussed later. Note that the deposition conditions of the  $In_2O_3:H$  layers were identical and that the sample were not annealed, yet. These results indicate that the crystalline structure of ZnO promotes crystalline growth of  $In_2O_3:H$ . Generally, the formation of crystalline bonds during the deposition of  $In_2O_3:H$  is suppressed by the incorporation of hydrogen, as suggested by Koida et al. [46]. The crystalline fraction of as grown hydrogen doped indium oxide  $X_C(In_2O_3 : H)$  was estimated using equation (3.4), as described in section 3.2.1. As the amorphous components in the GI-XRD measurements the broad feature in the range  $28^\circ < 2\theta < 36^\circ$  was considered. Here, it is assumed that the ZnO films are fully crystalline and have no amorphous components. The crystallinity of  $In_2O_3:H$  films was found to decrease with increasing ZnO (002) volume-weighted crystallite size and weighted average strain, as can be seen in Figure 5.2 a) and b), respectively.  $In_2O_3:H$  films grown on ZnO films with the smallest  $\langle D \rangle_V \approx 22$  nm and  $\bar{\epsilon} \approx 3.6 \times 10^{-3}$  respectively, are almost fully crystalline as they show a crystalline fraction of approximately 90 %. The crystalline fraction of  $In_2O_3:H$  was found to decrease to 50 % with increasing crystallite size of the ZnO sub-layers. A similar trend was observed for the dependence of the crystalline fraction

on the lateral grain size, as shown in Figure A.1 in the appendix. In contrast, the crystallinity of  $\text{In}_2\text{O}_3:\text{H}$  films grown on amorphous  $\text{Zn}(\text{O,S})$  was calculated to be only 10 %. A post deposition thermal treatment led to solid phase crystallization, as shown in Figure A.2.

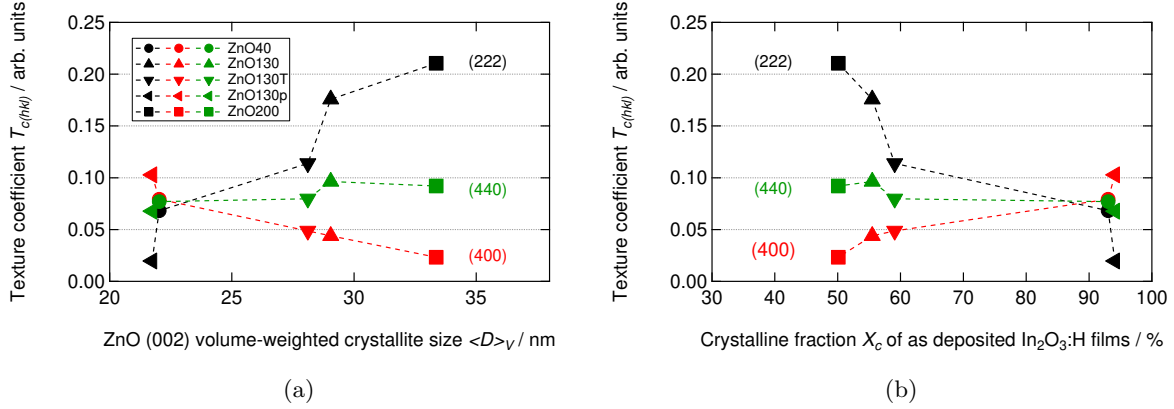


Figure 5.3: Texture coefficient of  $\text{In}_2\text{O}_3:\text{H}$  (222), (400) and (440) planes in dependence of (a) ZnO (002) volume-weighted crystallite size and (b) crystalline fraction of  $\text{In}_2\text{O}_3:\text{H}$  after deposition; dashed line serves as a guide to the eye; adapted from Erfurt et al. [100]

The degree of the preferred orientation of  $\text{In}_2\text{O}_3:\text{H}$  films grown on different ZnO sub-layers was estimated by calculating the texture coefficient for  $\text{In}_2\text{O}_3$  planes (222), (400) and (440) by the following equation [126]:

$$T_{C(hkl)} = \frac{I_{(hkl)}/I_{0(hkl)}}{1/N[\sum_N I_{(hkl)}/I_{0(hkl)}]} \quad (5.1)$$

where  $T_{C(hkl)}$  is the texture coefficient of the plane specified by Miller Indices  $(hkl)$ ,  $I_{(hkl)}$  is the integrated measured peak intensity,  $I_{0(hkl)}$  is the corresponding reference intensity of PDF 00-006-0416 (i.e., the measured peak intensities were normalized to the corresponding reference peak intensity) and  $N$  is the number of diffraction peaks. For the calculations all observed peaks, correlated to  $\text{In}_2\text{O}_3:\text{H}$  were taken into account. The texture coefficient was found to depend on the ZnO (002) volume-weighted crystallite size, as shown in Figure 5.3 (a). A decreasing ZnO (002)  $\langle D \rangle_V$  results in a decreased texture coefficient of the (222) plane, but an increased texture coefficient of the (400) plane. In fact, a change of the preferred orientation from (222) to (400) was determined for the  $\text{In}_2\text{O}_3:\text{H}$  film grown on the ZnO film with the smallest  $\langle D \rangle_V$  ( $\approx 22$  nm). No significant change of  $T_{C(440)}$  was observed. A similar correlation was found in dependence on the lateral grain size estimated by AFM, as shown in Figure A.3. Assuming that the ZnO (002) volume-weighted crystallite size and grain size of the ZnO films increase equally, these results suggest that the growth mechanism of  $\text{In}_2\text{O}_3:\text{H}$  differs on ZnO grain boundaries and grains, as the amount of grain boundaries decreases with increased grain sizes. Furthermore the change of the texture coefficient was correlated with the crystalline fraction of the as deposited  $\text{In}_2\text{O}_3:\text{H}$  films, as shown in Figure 5.3 (b). The increase in crystallinity can be attributed to

pronounced (400) orientation of the  $\text{In}_2\text{O}_3\text{:H}$  crystallites, while films with lower crystallinity show a pronounced (222) orientation. These results are consistent with the findings presented in Figure 5.2 (a), where an increased crystalline fraction was correlated with the ZnO crystallite size.

To evaluate the growth mechanism of indium oxide crystallites on ZnO films TEM measurements of a cross section of sample ZnO200 (coated with  $\text{In}_2\text{O}_3\text{:H}$ , as deposited) were carried out. Figure 5.4 (a) presents an overview of the  $\text{In}_2\text{O}_3\text{:H}/\text{ZnO}$  interface. Additional images can be found in Figure A.4 in the Supplementary. From this data we can see that ZnO grains have a columnar structure while the  $\text{In}_2\text{O}_3\text{:H}$  film shows a structure with stacked grains, starting directly from the ZnO surface. Figure 5.4 (b) shows two grains which are located in the  $\text{In}_2\text{O}_3\text{:H}$  film growing on top of the ZnO surface at the interface of two ZnO grains, respectively. The marked area is illustrated in Figure 5.4 (c).

The area on the lower left hand side of the image corresponds to the ZnO film and is marked in red, the area on the upper right hand side corresponds to the  $\text{In}_2\text{O}_3\text{:H}$  film and is marked in yellow, respectively. The colored boxes represent the area used for FFT analysis to determine the inter-planar distances, which are labeled in white, respectively. The corresponding determined lattice plane is written next to the box.

In the ZnO film inter-planar distances with  $d = (2.674 \pm 0.107) \text{ \AA}$  and  $d = (2.608 \pm 0.104) \text{ \AA}$  were measured. These values are close to the reference value of the ZnO (002) lattice plane with  $d = 2.6024 \text{ \AA}$ . The (002) planes are approximately parallel to the substrate and the film surface. Thus, the observed grains exhibit (002) orientation. Additionally a lower inter-planar distance  $d = (2.372 \pm 0.095) \text{ \AA}$  was measured in an area located in the ZnO film. As the measured area is close to the surface, additional measurement spots located deeper in the ZnO film were evaluated. The images of the evaluated region can be found in Figure A.5 in the Supplementary. The determined inter-planar distances were  $d = (2.378 \pm 0.095) \text{ \AA}$  and  $d = (2.395 \pm 0.096) \text{ \AA}$  are in good correlation with the value determined close to the surface. Note that the inter-planar distance increased with larger distance to the interface. This suggests that the determined value close to the interface corresponds to the ZnO (101) lattice plane with  $d = 2.4751 \text{ \AA}$  as this is the most reasonable ZnO reference value.

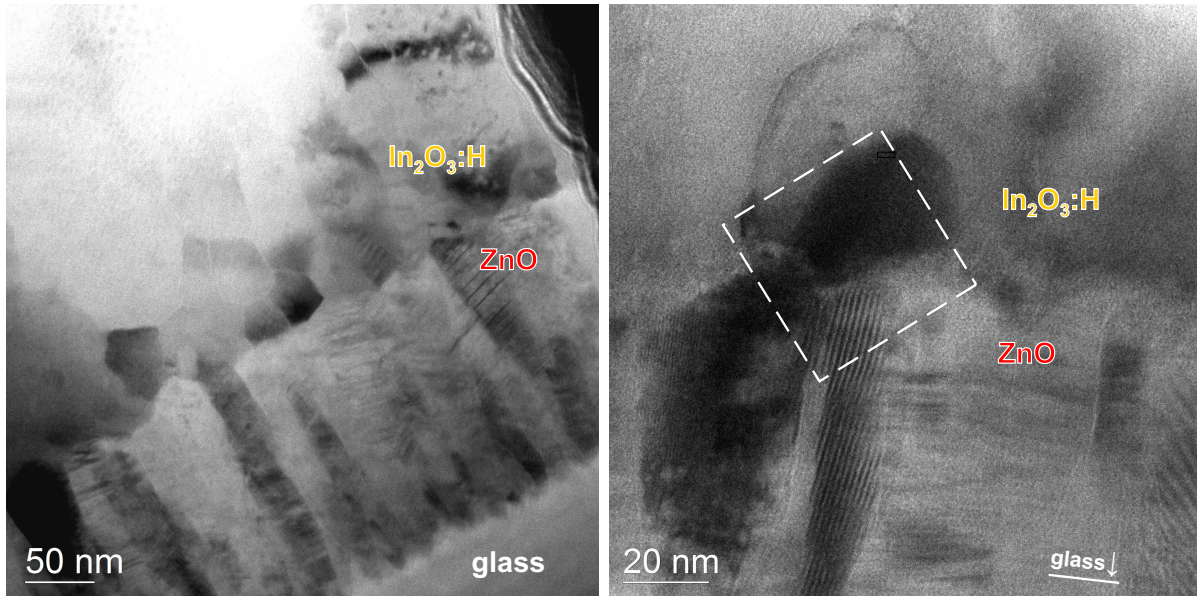
The large deviation of the measured and reference value, which increases towards the interface, indicates that the lattice is highly strained. In the  $\text{In}_2\text{O}_3\text{:H}$  film two different inter-planar distances were determined. In the lower region of the image an inter-planar distance of  $d = (2.950 \pm 0.118) \text{ \AA}$  was measured, which is close to the reference value of the  $\text{In}_2\text{O}_3\text{:H}$  (222) lattice plane with  $d = 2.921 \text{ \AA}$ . Furthermore the (222) lattice planes are approximately parallel to the ZnO (002) lattice planes and the glass substrate below. Accordingly, this grain exhibits (222) orientation. The second determined inter-planar spacing in the  $\text{In}_2\text{O}_3\text{:H}$  film was  $d = (2.463 \pm 0.099) \text{ \AA}$ . The

most reasonable  $\text{In}_2\text{O}_3$  reference value is  $d = 2.529 \text{ \AA}$  of the  $\text{In}_2\text{O}_3$  (400) lattice plane. The large deviation indicates that the lattice is strained. From Figure 5.4 (b) it becomes apparent, that the corresponding crystallite is rather small and forms at the interface of the two ZnO (002) grains. Additionally the grain seems to be overgrown by the indium oxide crystal with (222) orientation.

Crystalline indium oxide has a body centered cubic structure with lattice parameter  $a = 10.117 \text{ \AA}$  [52, 53]. The calculation of the lattice parameter for the presented samples is explained in section 3.2.1. For the as grown films, the lattice parameter is representative for the crystallites included in the amorphous phase. Here only films deposited on ZnO were evaluated as the peak intensities of films deposited on Zn(O,S) and glass were too low to be evaluated due to the mainly amorphous structure. As the thermal treatment of the films led to solid phase crystallization of the amorphous phase in  $\text{In}_2\text{O}_3\text{:H}$ , the lattice parameter of the annealed films was determined for  $\text{In}_2\text{O}_3\text{:H}$  films deposited on ZnO, Zn(O,S) and bare glass due to the increased peak intensities observed for all films. Figure 5.5 shows the dependence of the lattice constant  $a$  on the crystalline fraction of as grown  $\text{In}_2\text{O}_3\text{:H}$  films. The determined lattice parameters of the as grown films are overall larger than the reference value and larger for films with an increased crystalline fraction after deposition. This indicates, that the lattice is more strained when the films exhibit a crystalline growth. The post deposition thermal treatment led to relaxation of the lattice and to an overall reduction of the lattice parameter. However, films with a higher crystalline fraction after deposition retained an increased lattice parameter also after annealing. Here, the calculated lattice parameter is lower than the reference value, indicating compressive stress.

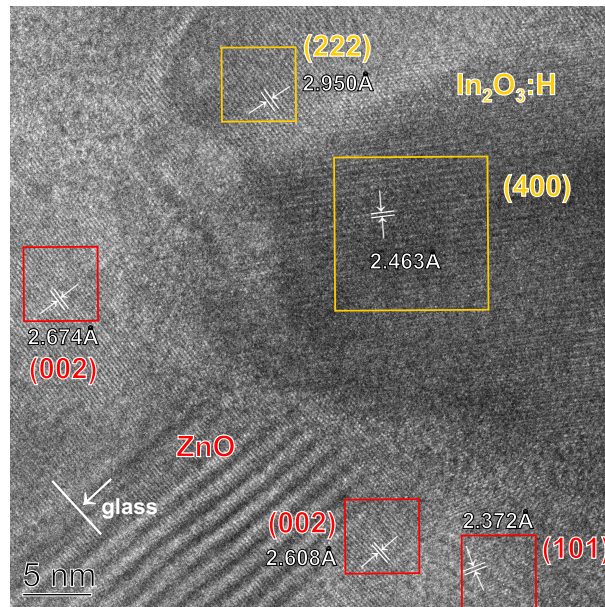
The crystallinity of as grown  $\text{In}_2\text{O}_3\text{:H}$  films has a major influence on the electrical properties, as can be seen in Figure 5.6. Here the charge carrier density ( $n_e$ ), electron mobility ( $\mu_e$ ) and resistivity ( $\rho$ ) of as grown as well as annealed  $\text{In}_2\text{O}_3\text{:H}$  films on bare glass, Zn(O,S) and ZnO layers are shown in dependence on the corresponding  $\text{In}_2\text{O}_3\text{:H}$  crystallinity after deposition. The increase of the crystalline fraction of as grown  $\text{In}_2\text{O}_3\text{:H}$  from 10 % to 90 % can be correlated with a loss in charge carrier density from  $4.7 \times 10^{20} \text{ cm}^{-3}$  to  $1.7 \times 10^{20} \text{ cm}^{-3}$  and a loss in electron mobility from  $36 \text{ cm}^2/\text{Vs}$  to  $24 \text{ cm}^2/\text{Vs}$ . Thus the specific resistivity increases fourfold. After the annealing and solid phase crystallization the charge carrier density decreased while the electron mobility increased. For the mainly amorphous films after deposition, the charge carrier density was found to decrease to half of the initial value. In contrast, crystalline grown films showed a less pronounced drop in charge carrier density after annealing. The electron mobilities of the annealed films were in the range of  $80 \text{ cm}^2/\text{Vs}$  to  $90 \text{ cm}^2/\text{Vs}$ . Here, a dependence on the lattice parameter of the annealed films was found. The results are shown in Figure 5.7. A higher (lower) electron mobility results for films with lower (higher) lattice parameter.

First, the structure of the ZnO films is discussed. It was shown in literature that ZnO film growth starts with a bottom layer of small grains. The grains coalesce at increased thicknesses, when



(a)

(b)



(c)

Figure 5.4: TEM images of the In<sub>2</sub>O<sub>3</sub>:H / ZnO interface of sample ZnO200 in the as grown state; (a) overview of the sample structure; (b) grains located in the In<sub>2</sub>O<sub>3</sub>:H film are observed on the surface of ZnO grains; (c) zoom in of the white marked area in (b) with measured inter-planar distances and the corresponding crystalline assignment, colored boxes represent the area taken for FFT analysis; the glass substrate is indicated in white; adapted from Erfurt et al. [100]

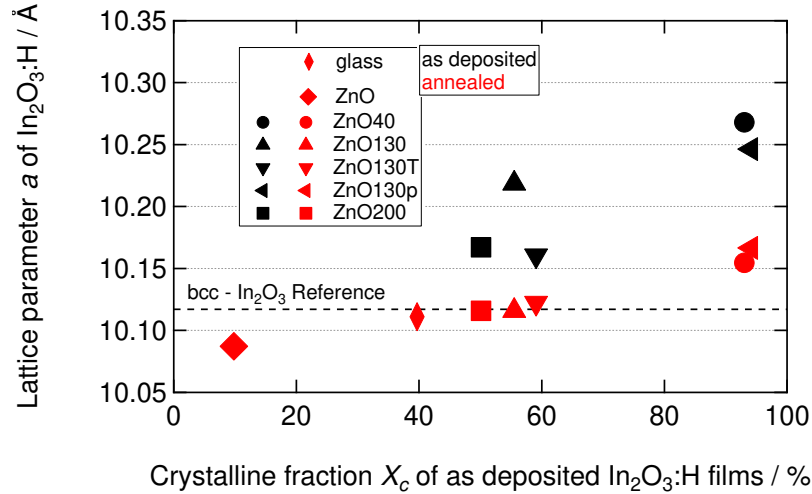


Figure 5.5: Dependence of the lattice constant of as grown and annealed  $\text{In}_2\text{O}_3:\text{H}$  crystallites, respectively on the crystallinity of the films in the as grown state; as the crystalline fraction of  $\text{In}_2\text{O}_3:\text{H}$  films grown on Zn(O,S) and bare glass was too low in the as grown state, the lattice parameter of these films could not be calculated; adapted from Erfurt et al. [100]

the surface temperature is high enough, leading to increased grain sizes (taperwise growth) [127]. Also for the films described in this study we observed an increase of the vertical and lateral grain size with increased film thickness, indicating taperwise growth. The coalescence of grains seems to result in a reduction of strain. An increase of the substrate temperature during deposition improves the adatom diffusion at the surface. This might lead to enhanced coalescence at lower thicknesses and thus larger lateral and smaller vertical grain sizes at the bottom of the film towards the glass substrates, as  $\langle D \rangle_V$  is an average value. In literature a lower sputter pressure is predicted to result in denser films, since the arriving particles on the substrate have a higher energy and thus a higher surface mobility with the possibility to form larger grains [128, 129]. However, Bachari et al. [123] showed, that pressures as low as 0.25 Pa result in a decreased grain size compared to films deposited at 1 Pa. The authors suggest, that at low total pressures, combined with low oxygen pressure and high RF sputter power, the high energy particles produce recoil implantation when arriving at the substrate surface, resulting in higher compressive stress. These findings might explain the results observed for ZnO films sputtered at a reduced total pressure of 0.2 Pa. Here a reduced lateral and vertical grain size was determined. At the same time the films exhibit the highest compressive strain parallel to the substrate. The strain was estimated from the lattice parameter  $c$  of the films, which was higher than the reference value. It is unlikely that this difference is caused by a high error during the BB-XRD measurements, but cannot be excluded completely.

Next, we will discuss the results of  $\text{In}_2\text{O}_3:\text{H}$  films grown on bare, Zn(O,S) and ZnO - coated planar glass substrates, respectively. It is known that the amorphous growth of  $\text{In}_2\text{O}_3:\text{H}$  is based

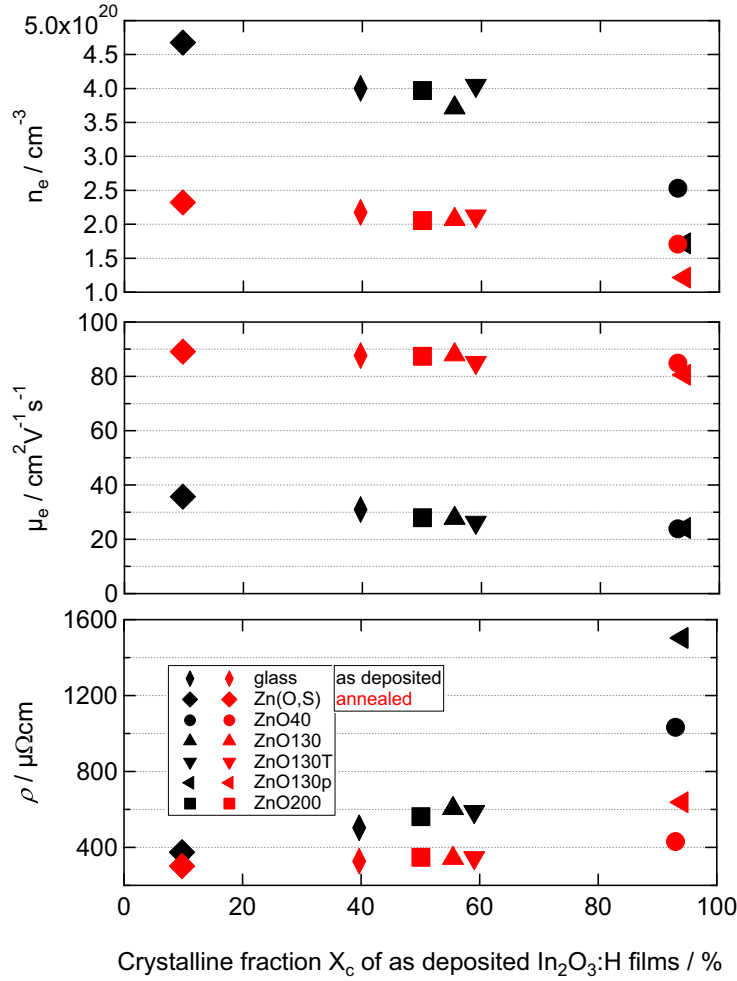


Figure 5.6: Electrical properties of as grown and annealed  $\text{In}_2\text{O}_3:\text{H}$  films in dependence on the crystalline fraction after deposition; adapted from Erfurt et al. [100]

on the incorporation of hydrogen during the film deposition [46]. Koida et al. suggested that oxygen-hydrogen bonds (O-H) disturb the formation of (O-In-O) bonds and thus the formation of the crystalline network [61]. As a mainly amorphous growth was observed on substrates with an amorphous structure like glass and Zn(O,S), the amount of hydrogen offered during the deposition process was in principle sufficient to suppress crystalline growth on these substrates. Furthermore the water vapor pressure is in good agreement with values found in literature which resulted in a mainly amorphous growth of  $\text{In}_2\text{O}_3:\text{H}$  [5, 46]. Nevertheless, an increased film crystallinity occurred for as grown  $\text{In}_2\text{O}_3:\text{H}$  films deposited on poly-crystalline ZnO. Thus the growth of  $\text{In}_2\text{O}_3:\text{H}$  films was influenced by the sub-layer. The findings highly indicate that the ZnO structure determines the structure of  $\text{In}_2\text{O}_3:\text{H}$ . We assume, that no or only negligible amounts of hydrogen diffused through grain boundaries into the ZnO during  $\text{In}_2\text{O}_3:\text{H}$  deposition. It was found that during  $\text{In}_2\text{O}_3:\text{H}$  deposition ZnO with (002) preferred orientation promotes the

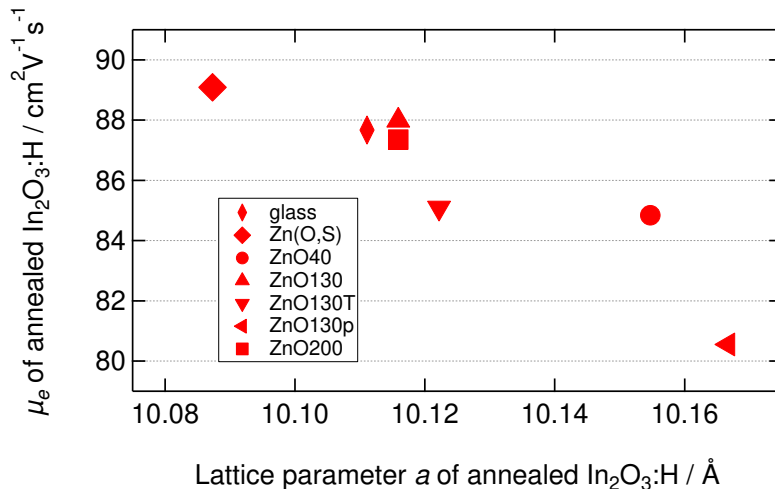


Figure 5.7: Influence of the lattice parameter  $a$  of annealed  $\text{In}_2\text{O}_3:\text{H}$  films on the resulting electron mobility; adapted from Erfurt et al. [100]

growth of  $\text{In}_2\text{O}_3:\text{H}$  crystallites with a (222) preferred orientation, especially when the ZnO grain size increases. Thus we suggest that the two structures intergrow along the hexagonal c-axis direction, as proposed by Cannard and Tilley [130]. They showed that two  $\{111\}$  planes of the cubic  $\text{In}_2\text{O}_3$  structure form on  $\{001\}$  ZnO planes in ZnO- $\text{In}_2\text{O}_3$  systems. Each of the two  $\{111\}$  planes would thus have a composition of  $\text{InO}_{1.5}$ . The planes most densely packed with oxygen atoms are parallel to  $(111)_{\text{In}_2\text{O}_3}$  and  $(001)_{\text{ZnO}}$  and the average oxygen-oxygen distance weighted by number/unit for  $(111)_{\text{In}_2\text{O}_3}$  was calculated to be 0.33534 nm while it was 0.32498 nm for  $(001)_{\text{ZnO}}$ , resulting in a misfit of 3 % [131].

Thus (002)-textured ZnO films can provide a suitable template for the growth of (222) oriented  $\text{In}_2\text{O}_3$  films. This finding was further confirmed by other research groups [132–134]. However, we observed a change of the preferred orientation of as grown  $\text{In}_2\text{O}_3:\text{H}$  from (222) to (400) when grown on ZnO with smaller crystallites and (002) preferred orientation. We assume that the decreased crystallite size results from an increased density of ZnO grain boundaries. Grain boundaries are regions which can be distorted, contain different coordination of atoms and a higher density of lattice defects. This may lead to change in the average oxygen-oxygen distance of  $(001)_{\text{ZnO}}$  which may promote  $\text{In}_2\text{O}_3:\text{H}$  crystal growth in other orientations like (400), as observed by GI-XRD. In literature a more pronounced (400) layer growth could be shown for low oxygen conditions during deposition [134–137]. In contrast, Keller et al. [47] did not observe a correlation of the oxygen content and texture of films deposited by ALD. Nevertheless an increased (400) orientation was demonstrated for increased deposition temperatures. The authors suggest that the films nucleate in (222) orientation, but that the orientation changes to (400) with increased film thickness. This might occur, when the grains get in touch. In regard of the observed findings in this work, such an effect could enhance the formation of (400) crystallites

during  $\text{In}_2\text{O}_3\text{:H}$  deposition at increased thicknesses, if we assume that a higher amount of (222) nuclei form at the interface to ZnO films with smaller grains, resulting in a higher density of grains which get in touch and change the orientation. To overcome the crystalline growth of  $\text{In}_2\text{O}_3\text{:H}$  on poly crystalline ZnO layers, the amount of hydrogen during the deposition must be increased to facilitate the incorporation during the growth of the interlayer at the ZnO surface, as observed in additional experiments (not shown here). Also an increased deposition rate may be generally beneficial to prevent crystalline growth.

Hydrogen was proposed to act as a shallow donor in  $\text{In}_2\text{O}_3\text{:H}$  [62, 63, 138] and thus to increase the carrier density compared with undoped films. Further, previous studies have suggested that the source of doping is attributed to interstitial hydrogen ( $\text{H}_i^+$ ) or substitutional hydrogen ( $\text{H}_\text{O}^+$ ) rather than to doubly charged oxygen vacancies ( $\text{V}_\text{O}^{++}$ ) [63–65], as discussed in section 2.1.4. Wu et al. [139] reported that in  $\text{In}_2\text{O}_3\text{:H}$  films that contained both, amorphous and crystalline parts, a higher amount of hydrogen was incorporated in the amorphous region compared to the crystalline region. We therefore assume that after deposition a lower amount of hydrogen is incorporated in the crystalline grown  $\text{In}_2\text{O}_3\text{:H}$  films. The charge carrier density of these films must consequently be lower compared to the amorphous grown film, if only H contributes to doping and the doping efficiency remains unchanged. This is supported by the measurement results of the charge carrier density, as shown in Figure 5.6. Furthermore, the electron mobility of as grown and annealed  $\text{In}_2\text{O}_3\text{:H}$  films was found to decrease with increased crystalline fraction of the  $\text{In}_2\text{O}_3\text{:H}$  films before annealing. In transparent conductive oxides, the electron mobility is limited by scattering processes which can be induced by phonons, ionized or neutral impurities and in polycrystalline material also by grain boundaries. In  $\text{In}_2\text{O}_3\text{:H}$  compounds that contain both, amorphous and crystalline phases, the incoherent boundaries in-between can additionally act as scattering centers [22]. When first crystallites form in a mainly amorphous phase, they can act as scattering centers and thus lower the electron mobility. An increased amount of crystallites will lead to further decrease of the electron mobility until the crystalline phase becomes the dominating phase. The results presented within this thesis show that the electron mobility of as grown  $\text{In}_2\text{O}_3\text{:H}$  decreases with increased crystallinity, similar to the model proposed by Buchholz et al. [22]. However, a reduced electron mobility was still observed in films with crystallinity as high as 90 %. The estimated lattice constant of these films was significantly higher than for films with lower crystallinity after deposition and higher than the  $\text{In}_2\text{O}_3$  reference value. This suggests, that especially the crystalline grown films are strained and the crystals may contain defects and impurities which serve as scattering centers resulting in a decreased electron mobility [46, 65]. Additional scattering may occur at the grain boundaries. In crystalline  $\text{In}_2\text{O}_3\text{:H}$  films, hydrogen that does not contribute to doping is proposed to passivate grain boundaries thus lowering the transport barrier for electrons [66] or passivating microscopic and macroscopic defects, respectively [65]. Both effects result in general in an increased electron mobility. We

assume that less hydrogen is incorporated in the crystalline grown  $\text{In}_2\text{O}_3:\text{H}$  films. In this case the scattering at grain boundaries is most likely even more pronounced.

A thermal treatment led to solid phase crystallization of the amorphous phase in  $\text{In}_2\text{O}_3:\text{H}$ . The determined lattice constant after annealing was found to be lower than that of the crystallites present after deposition. Thus we assume that strain in the crystalline grown films could be reduced during annealing, but is still higher than in amorphous grown films, as they exhibit a larger lattice parameter  $a$ . This determines the electron mobility, which decreases with increased lattice parameter. Therefore we assume that the remaining strain of the initially crystalline grown films limits the electron mobility of annealed films. However, electron mobilities of over  $80 \text{ cm}^2/\text{Vs}$  could still be achieved for films grown on ZnO. Nevertheless the reduced charge carrier density of these films leads to a twofold increased resistivity.

These findings enhance our understanding of the growth of hydrogen doped indium oxide on crystalline ZnO and amorphous Zn(O,S) layers. The results of this investigation indicate the need of an amorphous layer underneath hydrogen doped indium oxide for improved electrical properties.

*The main findings can be summarized as follows:*

- Poly-crystalline ZnO promotes crystalline growth of hydrogen doped indium oxide; in contrast films grown on amorphous Zn(O,S) were mainly amorphous.
- The  $\text{In}_2\text{O}_3:\text{H}$  films had an higher crystalline fraction (up to 90 %) when grown on small and strained ZnO grains.
- The preferred orientation of  $\text{In}_2\text{O}_3:\text{H}$  changed from (222) to (400) in films that were deposited on small ZnO grains.
- Crystalline grown  $\text{In}_2\text{O}_3:\text{H}$  films were strained and showed poor electrical properties before and after annealing compared to the mainly amorphous grown films.
- The crystalline growth can be suppressed by an increased hydrogen supply during the deposition of the first  $\text{In}_2\text{O}_3:\text{H}$  layers at the ZnO interface.

## 5.2 Sol-Gel Indium - and Gallium Oxide Layers on glass

As alternative to the high resistant intrinsic ZnO layer, sol-gel indium and gallium oxide layers were studied. Researchers showed that such layers can be used as buffer layers in CIGS solar cells. Koida et al. [120] analyzed CIGS solar cells in substrate coordination with sputtered amorphous indium gallium oxide ( $a\text{-In}_{2-2x}\text{Ga}_{2x}\text{O}_3$ ) as buffer layer. The solar cells with  $x = 0.9$  and  $x = 1$  exhibited  $V_{oc}$  values comparable with that of a reference cell with standard i-ZnO/CdS layer stack. In addition, Heinemann et al. [140] showed that low temperature deposited amorphous  $\text{Ga}_x\text{O}_y$  and alloys with amorphous  $\text{In}_x\text{O}_y$  were suitable buffer layer materials for CIGS solar cells in superstrate coordination. Related to this thesis, these amorphous materials could give a suitable template to achieve amorphous grown IOH thin films with high mobilities after post-annealing. Additionally the materials exhibit a higher band gap than the conventional i-ZnO or CdS layer, thus showing a high potential for reduced parasitic absorption when applied in the window layer of solar cells. It was shown, that a raise of the short circuit current density could be achieved when substituting a low band gap material (e.g. CdS) with a higher band gap material (e.g. Zn(O,S)) [141]. Therefore in this section we investigate the properties of pulsed DC magnetron sputtered IOH films grown on indium oxide and gallium oxide layers which were deposited by a sol-gel spin coating process, as described in section 3.1.2 on page 27. As discussed in section 5.4 such a deposition process can be beneficial for the electron mobility of IOH on CIGS samples. For an improved understanding the sol-gel layers were first investigated in dependence of the spin coat deposition conditions on planar glass substrates. In this case 15 repetitions of the spin coat process were done. Based on this studies IOH thin films were deposited on several sol-gel layers and their structure and electrical properties were investigated before and after annealing.

The structure of the spin coated sol-gel films could be highly influenced by the annealing temperature during the deposition routine. In Figure 5.8 X-ray diffraction patterns are shown for sol-gel indium oxide (left) and gallium oxide (right) layers which were annealed at different temperatures, respectively. From this data we can see that the crystallinity of the indium oxide films increases with higher annealing temperatures. At 300 °C the films were found to be crystalline in the bcc  $\text{In}_x\text{O}_y$  bixbyte structure. The films which were annealed at 200 °C and 250 °C, respectively, showed a hump in the range of  $27^\circ \leq 2\theta \leq 37^\circ$ , indicating increased nano-crystallinity. In contrast no peak was observed for sol-gel gallium oxide films. Thus these films were amorphous regardless of the annealing temperature. The broad peak in the range around  $15^\circ \leq 2\theta \leq 30^\circ$  is assumed to be caused by the quartz glass substrate.

Due to the sol-gel deposition procedure water is incorporated into the indium and gallium oxide layers. During annealing  $\text{H}_2\text{O}$  desorbs, leading to a reduced film thickness. This process can be accelerated by higher temperature. To investigate the residual amount of water in the sol-gel layers FTIR measurements were done on sol-gel  $\text{Ga}_x\text{O}_y$  layers, which were deposited on a Si-wafer

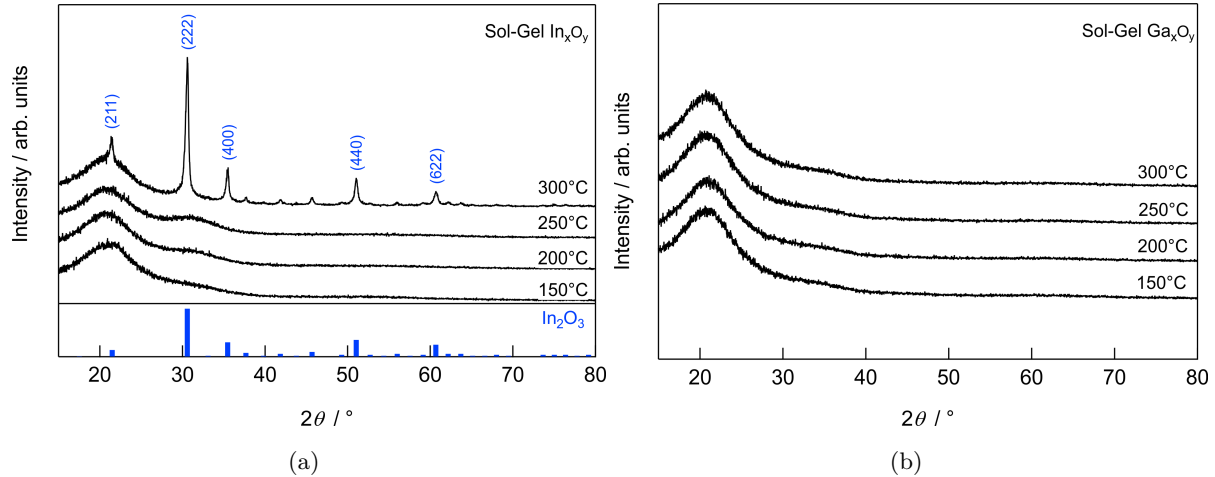


Figure 5.8: X-ray diffraction patterns of indium oxide (a) and gallium oxide (b) layers deposited by a sol-gel procedure and annealed at different temperatures; the  $\text{In}_x\text{O}_y$  reference pattern was taken from PDF 00-006-0416; patterns were shifted for improved differentiation

(5 repetitions of the spin coat process) and annealed at 150 °C and 250 °C, respectively. A bare Si-wafer served as reference. The results are shown in Figure 5.9. The insert represents a close up of the marked area. In the range  $3200\text{ cm}^{-1}$  to  $3650\text{ cm}^{-1}$  a broad peak can be observed for the  $\text{Ga}_x\text{O}_y$  layers. The peak intensity is significantly higher for the film which was annealed at 150 °C than for the film annealed at 250 °C. This peak can be correlated to stretching modes of hydrogen bonded OH groups [142]. In contrast in the mentioned region no peak was observed for the bare silicon wafer. Consequently the sol-gel layers contain residual water and the amount decreases with increase in annealing temperature.

The purpose of this study was to evaluate a suitable sol-gel layer as a template for an amorphous grown IOH film with reasonable electrical properties. Therefore the growth of  $\approx 370\text{ nm}$  thick sputtered IOH films was investigated by X-ray diffraction, as shown in Figure 5.10. The films were deposited on sol-gel gallium oxide and indium oxide layers (5 repetitions of the spin coat process), which were annealed at 150 °C and 200 °C, respectively. For these sol-gel deposition conditions a mainly amorphous film structure was found. Additionally an IOH reference layer was deposited on quartz glass. While the IOH films grown on gallium oxide and quartz glass were overall amorphous in XRD, an increased crystallinity was observed for IOH films grown on sol-gel indium oxide layers. The crystalline fraction of IOH increased with annealing temperature of the indium oxide sol-gel layers.

Figure 5.11 presents the change of the charge carrier density and electron mobility of IOH films before and after 1 h and 2 h of annealing at 160 °C in vacuum, respectively. The IOH layers were deposited on glass substrates, sol-gel  $\text{Ga}_x\text{O}_y$  and  $\text{In}_x\text{O}_y$  layers, which were annealed at 150 °C

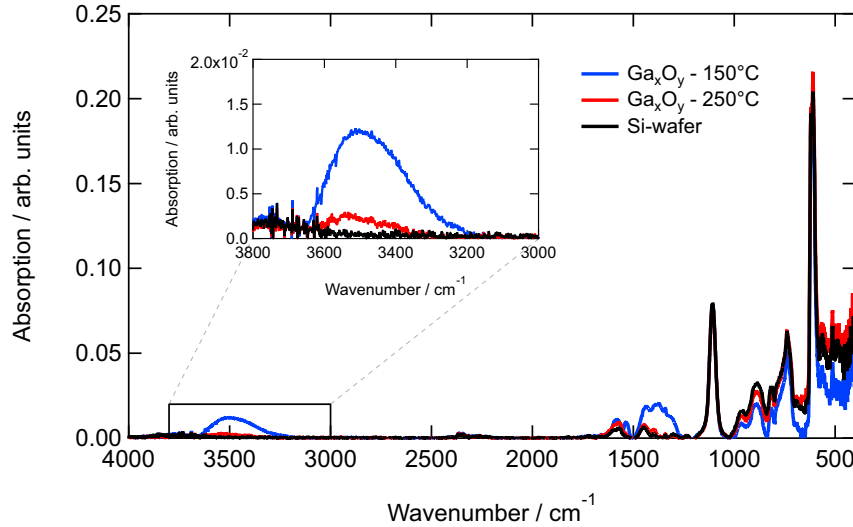


Figure 5.9: FTIR spectra of sol-gel  $\text{Ga}_x\text{O}_y$  layers which were annealed at 150 °C and 200 °C, respectively and a reference Si-wafer; the insert represents a close up of the marked area

and 200 °C, respectively. Before annealing ( $t = 0$  h) the charge carrier density was in the range of  $3.0 \times 10^{20} \text{ cm}^{-3}$  to  $3.3 \times 10^{20} \text{ cm}^{-3}$ , except for the sample deposited on  $\text{In}_x\text{O}_y - 200$  °C. Here a lower charge carrier density of  $n_e = 2.2 \times 10^{20} \text{ cm}^{-3}$  was observed. A similar trend was found for the electron mobility. It was  $32.9 \text{ cm}^2/\text{Vs}$  for the IOH layer deposited on  $\text{In}_x\text{O}_y - 200$  °C, significantly lower than for the other IOH layers with  $40 \text{ cm}^2/\text{Vs} \leq \mu_e \leq 44.5 \text{ cm}^2/\text{Vs}$ . During annealing the charge carrier density decreases for all samples. After 2 h of annealing the charge carrier density of IOH films deposited on both sol-gel  $\text{In}_x\text{O}_y$  layers and on  $\text{Ga}_x\text{O}_y - 150$  °C was in the order of magnitude of  $10^{19} \text{ cm}^{-3}$ . In contrast the IOH films deposited on  $\text{Ga}_x\text{O}_y - 200$  °C and bare glass substrate had higher charge carrier densities of  $n_e = 1.5 \times 10^{20} \text{ cm}^{-3}$  and  $n_e = 2.4 \times 10^{20} \text{ cm}^{-3}$ , respectively. Here, a similar trend can be observed for the electron mobility. A significant drop to values of  $3 \text{ cm}^2/\text{Vs}$  to  $9 \text{ cm}^2/\text{Vs}$  was found after 2 h of annealing for IOH films deposited on both sol-gel  $\text{In}_x\text{O}_y$  layers and on  $\text{Ga}_x\text{O}_y - 150$  °C. In contrast, the electron mobility of IOH films deposited on  $\text{Ga}_x\text{O}_y - 200$  °C and bare glass substrate was found to increase to  $78 \text{ cm}^2/\text{Vs}$  and  $85 \text{ cm}^2/\text{Vs}$ , respectively.

The discussion of the results starts with the structure of the sol-gel layers. According to the XRD measurements shown in Figure 5.8, we assume that crystalline nuclei form in the indium oxide sol-gel layers already at temperatures as low as 150 °C and 200 °C and that their growth is accelerated by an increased annealing temperature. When depositing IOH onto these films, the nuclei seem to induce crystalline growth, leading to increased IOH crystallinity as shown in Figure 5.10. The increased crystallinity after deposition results in a lower charge carrier density and electron mobility, as observed in Figure 5.11 and as already discussed in general in sections 4.2 and 5.1. The drop in charge carrier density and electron mobility of IOH films deposited on

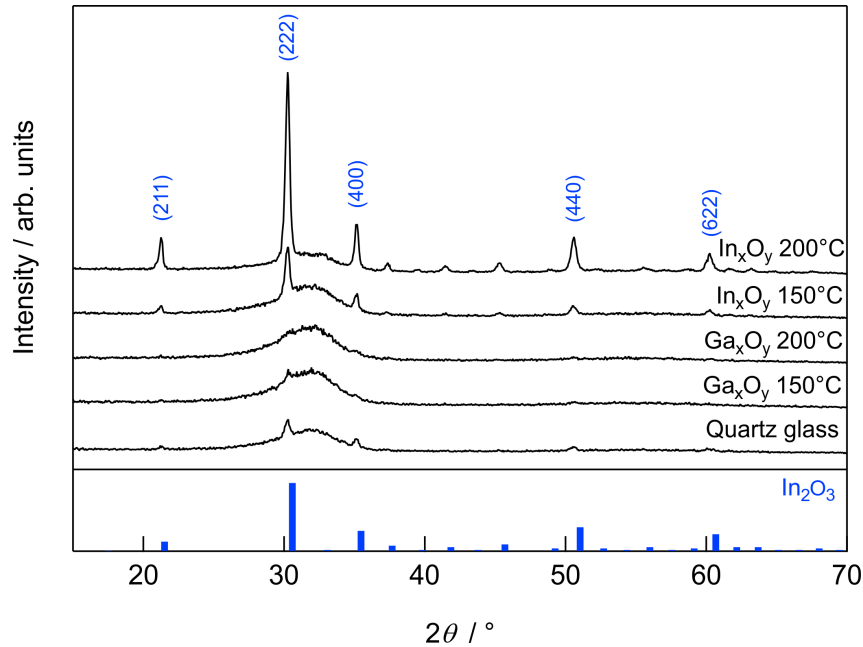


Figure 5.10: X-ray diffraction patterns of as grown IOH films deposited on quartz glass, indium oxide and gallium oxide sol-gel layers which were annealed at 150 °C and 200 °C, respectively; the In<sub>2</sub>O<sub>3</sub> reference pattern was taken from PDF 00-006-0416; patterns were shifted for improved differentiation

the sol-gel layers which were annealed at 150 °C may be explained by the structure of these films. As observed by FTIR measurements, Ga<sub>x</sub>O<sub>y</sub> - 150 °C sol-gel layers still contain a high amount of water which decreases with higher annealing temperatures during the sol-gel deposition process. This can also be assumed for sol-gel In<sub>x</sub>O<sub>y</sub> layers. It is possible that H<sub>2</sub>O or -OH molecules from the sol-gel layers diffuse into the IOH layers during deposition or even through the IOH film to the surface during annealing. Both effects might lead to deteriorated film structures and electrical properties. Similarly, such a significant decrease of charge carrier density and electron mobility after annealing could be observed for IOH films which were deposited at high water vapor pressures, as discussed in section 4.2.

This study has found that generally sol-gel layers can be suitable templates for the growth of IOH thin films, but certain conditions must be fulfilled. The sol-gel layers must be amorphous and free of crystalline nuclei after the deposition process, as they otherwise might support a crystalline growth of IOH films. Furthermore a high amount of residual water in the sol-gel layers is a disadvantage as it limits the electrical properties of IOH films after annealing. These findings will serve as a base for future studies within this thesis.

*The main findings can be summarized as follows:*

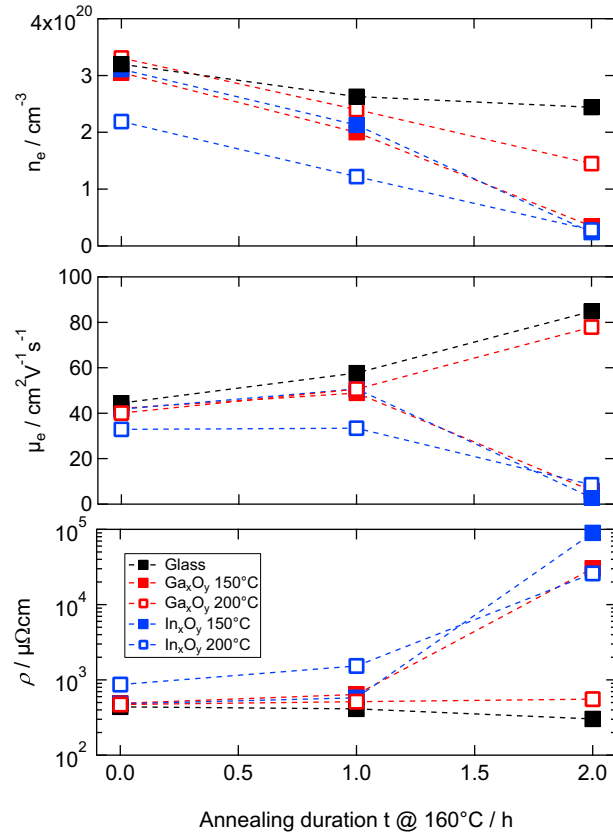


Figure 5.11: Change of the charge carrier density and electron mobility of IOH films during annealing at 160 °C in vacuum; IOH films were deposited on glass substrates, sol-gel  $\text{Ga}_x\text{O}_y$  and  $\text{In}_x\text{O}_y$  layers, which were annealed at 150 °C and 200 °C, respectively

- Amorphous spin coated  $\text{Ga}_x\text{O}_y$  layers are suitable templates for the deposition of  $\text{In}_2\text{O}_3\text{:H}$  layers, when the amount of residual water is reasonable low.
- Spin coated sol-gel  $\text{In}_x\text{O}_y$  layers induce crystalline growth of  $\text{In}_2\text{O}_3\text{:H}$  during deposition, resulting in poor electrical properties.
- Similar electrical properties of as grown and annealed  $\text{In}_2\text{O}_3\text{:H}$  are reached on glass and  $\text{Ga}_x\text{O}_y$  layers, which were annealed at 200 °C.

### 5.3 Polycrystalline CIGS and textured glass

The aim to implement IOH as front contact in CIGS modules requires a sheet resistance  $R_{Sq} < 10 \Omega/\text{Sq}$  for a CIGS module cell width of approx. 5 mm cell width to avoid increase of the module series resistance and a low fill factor. Thus, the electrical properties of the TCO grown on CIGS samples are decisive. In this section we show how a CIGS sub-layer affect the

growth and the resulting properties. For this, the electrical properties of films deposited at varied conditions, before and after annealing, and the film structure were investigated.

In this study a significant detrimental effect of the CIGS topography on the electrical properties, eminently the electron mobility of amorphous indium oxide based TCOs was observed. As example serve hydrogen and tungsten co-doped indium oxide ( $\text{In}_2\text{O}_3\text{:H,W}$ ) (or IWO:H) thin films deposited by RPD (see section 3.1.1 on page 23) on planar soda lime glass substrates and CIGS samples (IGZO/CdS/CIGS/Mo/glass), respectively. The CIGS samples are expected to have a RMS roughness value of 80 nm to 90 nm due to the deposition method. For the deposition of  $\text{In}_2\text{O}_3\text{:H,W}$  the oxygen supply was varied between 30 ml/min and 60 ml/min at "high" ( $\approx 1 \times 10^{-3}$  Pa) and "low" ( $\approx 1 \times 10^{-4}$  Pa) water vapor pressures. Figure 5.12 shows the corresponding charge carrier density, electron mobility and resistivity of the deposited IWO:H thin films. While the charge carrier density is similar for films on SLG and CIGS, the electron mobility of the IWO:H films is overall lower for the films deposited on CIGS. Furthermore the electron mobility of IWO:H/CIGS does not exceed the value of  $30 \text{ cm}^2/\text{Vs}$  while the electron mobility of IWO:H/SLG increases from  $29.8 \text{ cm}^2/\text{Vs}$  to  $42.4 \text{ cm}^2/\text{Vs}$  and from  $37.0 \text{ cm}^2/\text{Vs}$  to  $49.5 \text{ cm}^2/\text{Vs}$  with increased oxygen flow for films deposited at "low" and "high" water vapor pressures, respectively. The decreased electron mobility results in a higher resistivity of the IOH/CIGS samples with an increased spread for oxygen rich deposition conditions. An additional experiment (not shown) revealed, that no beneficial effect on the electron mobility resulted from an increased deposition rate, realized by an increased DC current during deposition.

Figure 5.13 shows as example an SEM cross section image of an IWO:H layer in the as deposited state grown on IGZO/CdS/CIGS. In the middle of the SEM image disconnected parts of the IWO:H layer film were observed. On the right side the cross section shows a smooth IWO:H film structure. In contrast on the left side specific structures occur. These structures are found to be present over the whole cross section towards the interface of the sub-layers.

A post deposition thermal treatment in nitrogen atmosphere at  $p = 7 \times 10^4$  Pa of samples deposited at  $q(\text{O}_2) = 60$  ml/min led to solid phase crystallization resulting in a decrease of the charge carrier density and an increase of the electron mobility. In Figure 5.14 the charge carrier density and electron mobility of IWO:H thin films grown on SLG or CIGS samples and deposited at (a) "high" ( $p_{\text{H}_2\text{O}} \approx 1 \times 10^{-3}$  Pa) and (a) "low" ( $p_{\text{H}_2\text{O}} \approx 0.7 \cdot 4 \times 10^{-4}$  Pa) water vapor pressure are shown as a function of the annealing temperature. The corresponding hall measurements were done after 30 min of annealing of each of the temperatures. In general an increased  $p_{\text{H}_2\text{O}}$  leads to a highly amorphous film structure and only few crystalline nuclei. Films that were deposited at reduced  $p_{\text{H}_2\text{O}}$  are known to have a higher density of crystalline nuclei, which results in a decreased crystallization temperature, as shown by Koida et al [5]. This also applies for films presented in this study. Thus the change of the electrical properties due to crystallization can be

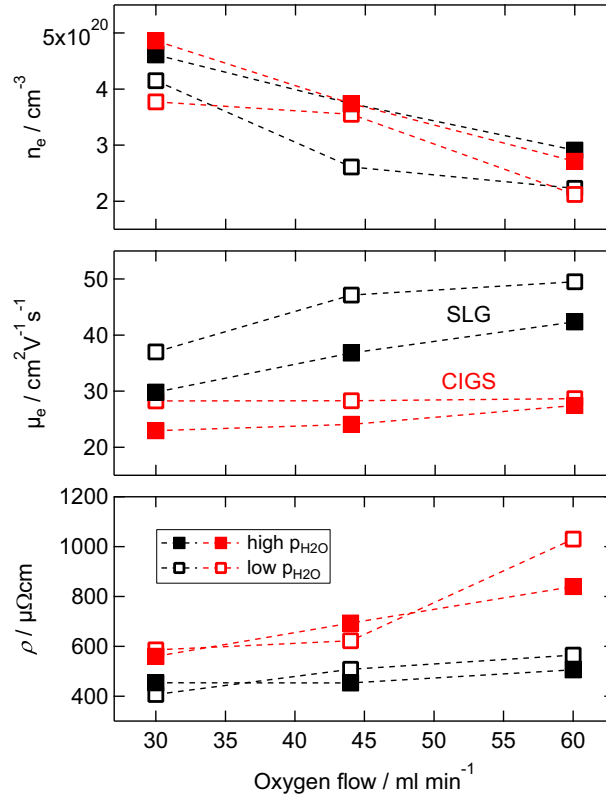


Figure 5.12: Comparison of the electrical properties of IWO:H thin films on flat soda lime glass and rough CIGS samples in dependence of their deposition conditions

observed at 220 °C to 230 °C and 150 °C to 160 °C for films deposited at "high" and "low"  $p_{H_2O}$ , respectively. In fact, IWO:H-CIGS samples deposited at "high"  $p_{H_2O}$  showed a decrease in  $n_e$  and increase in  $\mu_e$  at lower temperatures in comparison to the corresponding film on SLG. Thus additional crystalline IWO:H nuclei may form at the interface to the CIGS sample, promoting the solid phase crystallization of the film. Although also the electron mobility of IWO:H films deposited on CIGS samples increased due to the solid phase crystallization, the values remain significantly lower than that of the film on SLG. In fact, the spread  $\Delta\mu_e = \mu_e(IWO : H - SLG) - \mu_e(IWO : H - CIGS)$  increases from  $\Delta\mu_e = 14.9 \text{ cm}^2/\text{Vs}$  to  $\Delta\mu_e = 28.3 \text{ cm}^2/\text{Vs}$  and from  $\Delta\mu_e = 20.8 \text{ cm}^2/\text{Vs}$  to  $\Delta\mu_e = 29.4 \text{ cm}^2/\text{Vs}$  after annealing up to 250 °C for samples deposited at "high" and "low"  $p_{H_2O}$ , respectively.

The results show that the electrical properties of indium oxide based TCOs, here IWO:H, change dramatically when grown on CIGS samples instead of planar glass. The conductivity is limited by the electron mobility, independent of the deposition condition when the films are deposited by RPD. The SEM image in Figure 5.13 shows disconnected parts in the films, as observed in the middle of the image. On the left side the cross section film appearance is cauliflowers-like. Such a structure is usually observed at the surface of films deposited by sputtering or other deposition

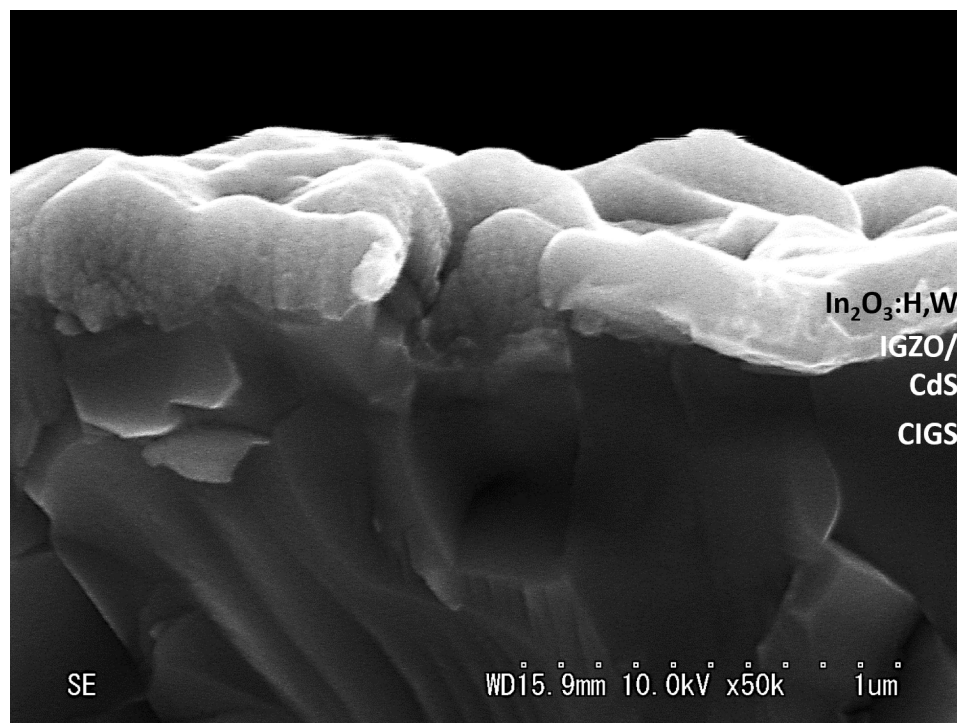


Figure 5.13: SEM image of an IWO:H layer on IGZO/CdS/CIGS

techniques [143–145]. This indicates, that prior to the measurement the sample broke along such a disconnected part, which becomes visible in the cross section view. The appearance of the IWO:H structure on the right side of the SEM is smooth and indicates breakage through the bulk of the amorphous film. We assume that the disconnected parts, such as cracks or voids, are the origin of the limited electron mobility. Research by Keller et al. [68] also points towards the formation of cracks and voids as the origin of the increased sheet resistance in, here, sputtered IOH films on CIGS samples. As the electron mobility of the films is still low after crystallization, we assume that the cracks do not coalesce during the thermal treatment. Thus, to achieve high electron mobilities in indium oxide based TCOs on CIGS samples it is required to further investigate the limiting effects. The electron mobility of the films grown on rough CIGS samples has to be improved already in the as deposited state, since solid phase crystallization did not lead to sufficient improvement, compared to films deposited on planar glass substrates.

*The main findings can be summarized as follows:*

- Regardless of the deposition conditions significantly low electron mobilities evolved, as demonstrated with  $\text{In}_2\text{O}_3\text{:H,W}$  films, which were grown on rough CIGS samples compared to films grown on planar glass substrates.
- No sufficient improvement of the electron mobility occurred after annealing.

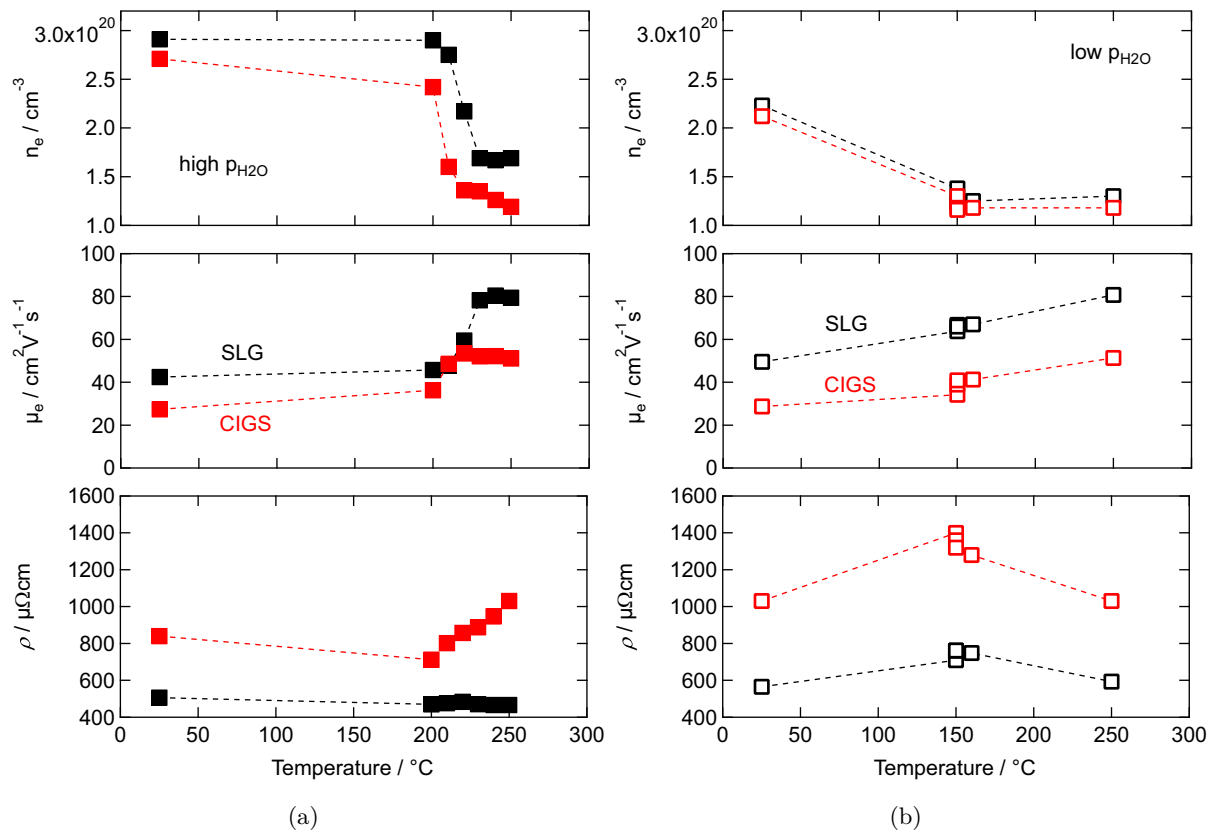


Figure 5.14: Dependence of the electronic properties of IWO:H films grown on planar SLG and rough CIGS samples on the annealing conditions; the IWO:H films were deposited with  $q(O_2) = 60$  ml/min at high (a) and low (b) water vapor pressures; Hall measurements were done after 30 min of annealing, each

- Indium oxide based TCOs deposited on CIGS samples have much higher resistances.

### 5.3.1 Detrimental effects on the electron mobility

CIGS samples are known to show a specific roughness which is usually described by the root mean square (RMS) roughness value [146–149] and can be influenced by growth conditions and treatments after deposition. In this section<sup>2</sup> we therefore investigate the influence of the surface morphology on the electrical properties, i.e., the electron mobility, of  $In_2O_3:H$  and  $In_2O_3:H,W$  films. The investigations were conducted twofold. First (i) we study the morphology

<sup>2</sup>Reproduced in part with permission from *Darja Erfurt, Marc D. Heinemann, Sebastian S. Schmidt, Stefan Körner, Bernd Szyszka, Reiner Klenk, Rutger Schlatmann; Substrate influence on the growth of hydrogen doped indium oxide; ACS Appl. Energy Mater. 2018, 1, 5490-5499; doi: 10.1021/acsaem.8b01039*, Copyright 2018 American Chemical Society.; <https://pubs.acs.org/articlesonrequest/AOR-vSC6y2YnvNhDtSbYrpi3> [100], licensed under a [Creative Commons Attribution 4.0 International License](https://creativecommons.org/licenses/by/4.0/) (CC-BY)

of CIGS samples, grown by multi-source evaporation with different deposition durations by AFM measurements. The films showed different roughness, but the main structure type remained the same. After this we correlate the structure and electrical properties of  $\text{In}_2\text{O}_3\text{:H}$  in dependence on different topographic values. Second (ii) we compare the morphology of multi-source CIGS samples, grown using different recipes and study the impact on the structure and electron mobilities of  $\text{In}_2\text{O}_3\text{:H}$  and  $\text{In}_2\text{O}_3\text{:H,W}$  films, deposited by either sputtering or RPD. Finally we discuss the obtained results.

The roughness of CIGS absorber, deposited by multi-source-evaporation at HZB, was adjusted by varying the process duration, resulting in changes of the absorber thickness on bare and Mo-coated glass substrates. Additionally smooth and textured glass substrates were used for investigations of the influence of the substrate roughness on the electrical properties of indium oxide based TCOs. The samples were coated with 60 nm Zn(O,S) or 60 nm Zn(O,S) and 130 nm i-ZnO, respectively, prior to the IOH deposition by pulsed dc magnetron sputtering. The IOH films had a thickness of  $\approx 300$  nm. Figure 5.15 illustrates the rise of the RMS roughness of CIGS/Zn(O,S)/i-ZnO samples in dependence of the CIGS process time. The figure showed that the RMS roughness increases more significantly when the films were deposited on Mo-coated glass substrates. The main cause for the increased RMS values is an increase of the CIGS grain size, which was determined by AFM measurements and the Watershed method of the program Gwyddion [102] (see Figure A.6 on page 146 in the appendix). For comparison AZO thin films were deposited on bare and i-ZnO coated flat glass and on i-ZnO/Zn(O,S) coated CIGS samples. The total sample assignment can be found in Table A.1 in the appendix.

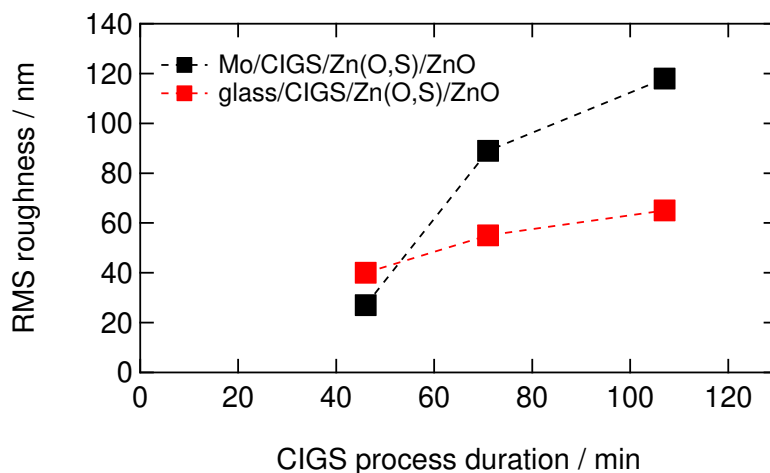


Figure 5.15: Change of the RMS roughness of CIGS/Zn(O,S)/i-ZnO samples deposited on bare and Mo-coated glass substrates in dependence of the CIGS process duration

In Figure 5.16 the profile height, local slope and AFM topography images with the corresponding measurement line as example of 3 different sample types. Figure 5.16 (left) shows a rather

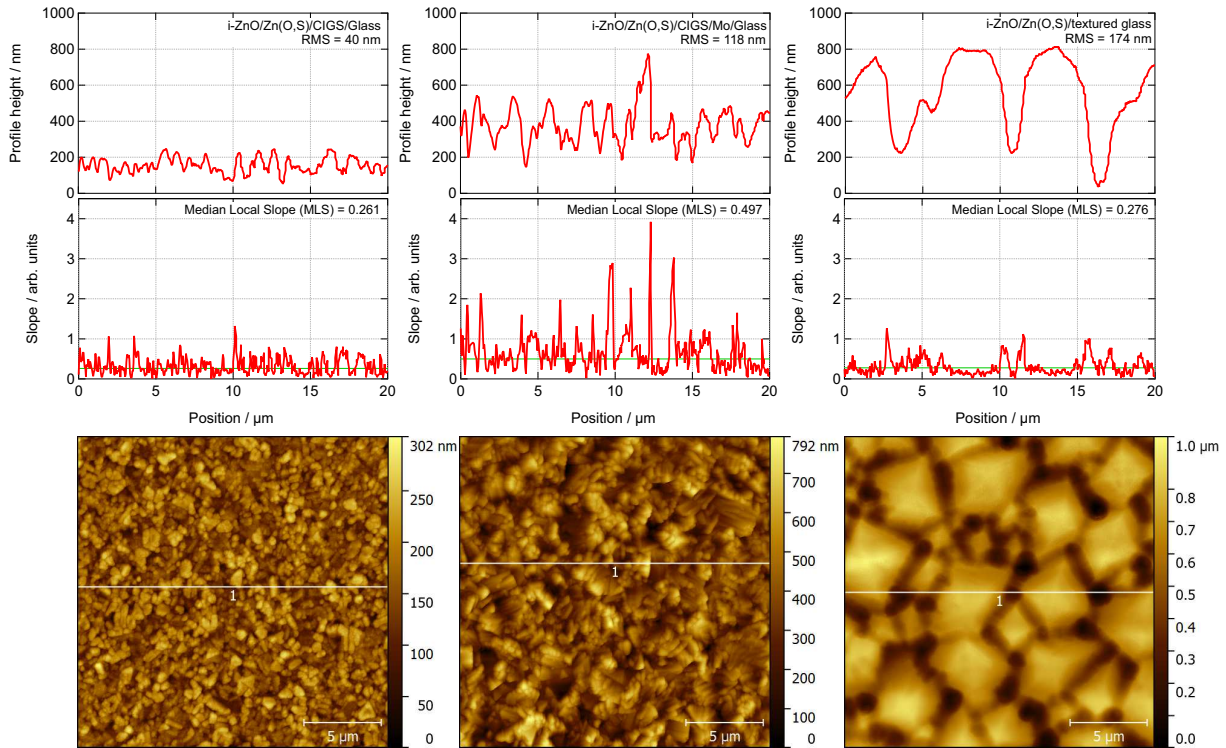


Figure 5.16: Profile height, local slope and corresponding AFM topography images with profile line of (left) a rather smooth CIGS sample (ID 4-3998-4-2), (middle) a rather rough CIGS sample (ID 4-3995-1-2) and (right) a textured glass sample (ID 5-15-2-83) before IOH deposition; the sample configuration can be found in Table A.1 in the appendix

smooth CIGS sample (glass/CIGS-46 min/Zn(O,S)/ZnO) with  $RMS = 40$  nm; (middle) a rather rough CIGS sample (Mo/CIGS/Zn(O,S)/ZnO) with  $RMS = 118$  nm; (right) a textured glass sample (textured glass/Zn(O,S)/ZnO) with  $RMS = 174$  nm. The samples will be addressed as *smooth CIGS sample*, *rough CIGS sample* and *textured glass sample*, respectively, from now on. Values of the RMS roughness and median local slope (MLS) were added to the Figures. The *rough CIGS sample* shows significantly larger grains, higher profile heights and local slopes than the *smooth CIGS sample*. In contrast the *textured glass sample* shows even larger structures and an increased RMS roughness, but a median local slope ( $MLS = 0.276$ ) comparable to the one of the *smooth CIGS sample* ( $MLS = 0.261$ ). Both the profile height and local slope of the *textured glass sample* show less fluctuation over the measured range than both *CIGS samples*. Within one sample the relatively highest slopes were found at the edges of grains on the *CIGS samples* or structures on the *textured glass sample*. Thus not only the median local slope, but also its frequency has to be taken into account. Therefore we calculated the median local slope per grain/structure size (MLS/GS), determining the grain size by AFM measurements using the Watershed method. It was found, that the *textured glass sample* had a lower MLS/GS value ( $MLS/GS = 0.29 \times 10^{-3} \text{ nm}^{-1}$ ) than the *smooth CIGS sample* ( $MLS/GS = 0.75 \times 10^{-3} \text{ nm}^{-1}$ )

or the *rough CIGS sample* ( $MLS/GS = 1.24 \times 10^{-3} \text{ nm}^{-1}$ ), due to the low median local slope but large structures of the *textured glass sample*

The samples mentioned in Table A.1 were coated with IOH within the same deposition run as the samples discussed in section 5.1, where a pronounced crystalline growth of IOH was observed when deposited on ZnO layers. Similar to these results also on rough samples a more pronounced crystalline growth occurred when the films were deposited on ZnO-coated samples. IOH films which were deposited on Zn(O,S)-coated samples were mainly amorphous, similar to the results in section 5.1. In Figure 5.17 (a) GI-XRD measurements of glass/CIGS/Zn(O,S)/IOH and glass/CIGS/Zn(O,S)/ZnO/IOH in the as deposited state are shown, the RMS value of the samples before IOH deposition was approx. 65 nm. Intensities of the  $\text{In}_2\text{O}_3$  peaks were clearly higher for the films which were deposited directly on ZnO than on Zn(O,S). In Figure 5.17 (b) patterns of GI-XRD measurements of IOH/ZnO/Zn(O,S)-coated samples with different roughness are shown. For all samples an increased  $\text{In}_2\text{O}_3$  peak intensity can be observed, independent from the RMS roughness value. Thus, no influence of the CIGS roughness on the crystalline structure of IOH can be observed, when the growth conditions are determined by the IOH sub-layers, as here ZnO and Zn(O,S).

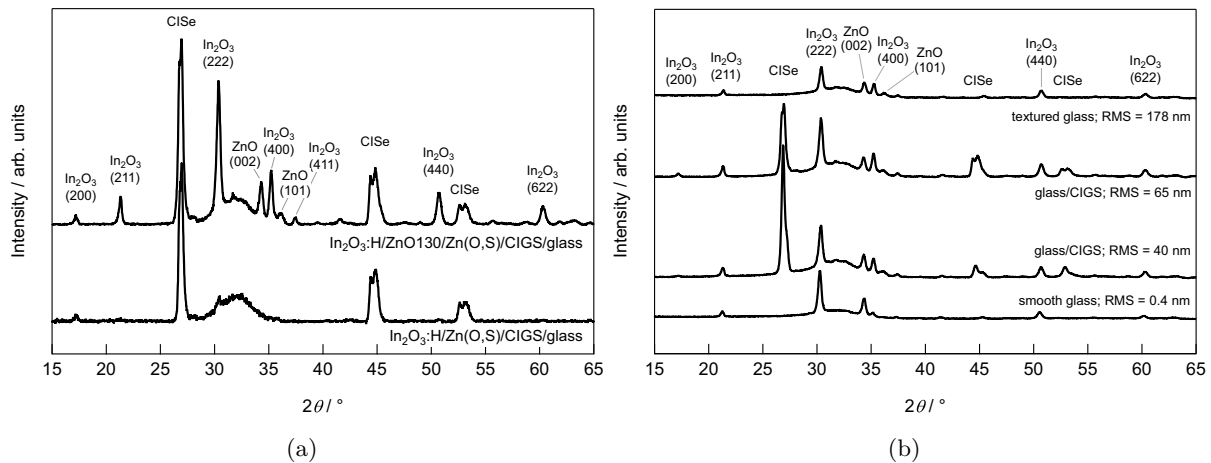


Figure 5.17: X-ray diffraction patterns of (a) IOH grown on ZnO/Zn(O,S)- and Zn(O,S)-coated CIGS samples with RMS = 65 nm (adapted from Erfurt et al. [100]) and (b) IOH grown on ZnO/Zn(O,S)-coated CIGS and glass samples with different RMS roughness values

Figure 5.18 shows the change of the IOH and AZO sheet resistance over the RMS roughness of the samples described in Table A.1 in the as deposited state. For the AZO coated samples no influence of the roughness on the sheet resistance can be observed, it remains unchanged at  $\approx 8.2 \Omega/\text{Sq}$  on smooth glass and rough CIGS samples. In contrast the IOH sheet resistance increases linearly when deposited on rough CIGS samples. In fact, the slope is more than 3 times larger for the crystalline grown IOH films, which were deposited on ZnO/Zn(O,S)-coated CIGS

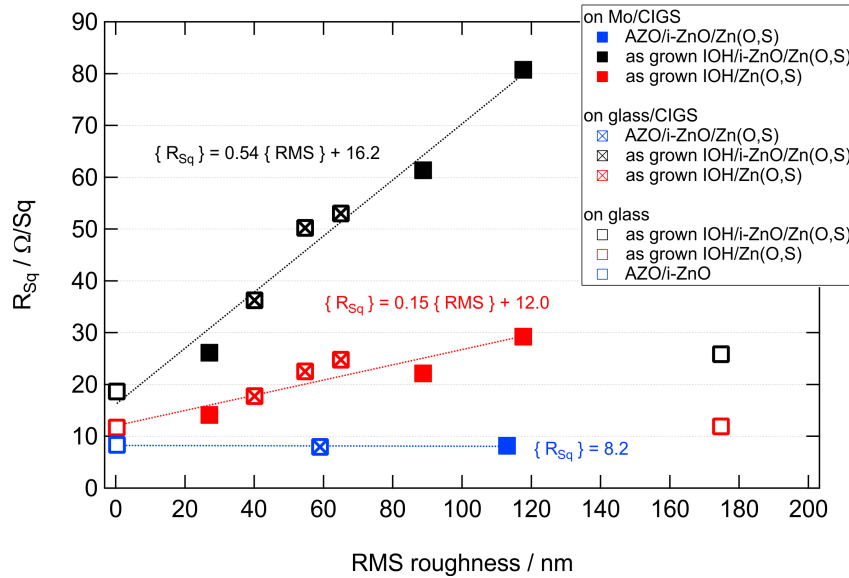


Figure 5.18: Comparison of the change of the sheet resistance of IOH and AZO when grown on different substrates and layers

samples compared to IOH films which were grown on Zn(O,S)-coated CIGS samples, as they showed a mainly amorphous structure. However, no or only a slight  $R_{sq}$  increase was observed when the films were grown on Zn(O,S)- and ZnO/Zn(O,S)-coated textured glass substrates, although a significantly higher RMS value was measured. From this we conclude that the RMS roughness value is not a sufficiently meaningful value to describe the substrate surface topography and the cause of the increase in sheet resistance of IOH if the morphology of the samples changes significantly. Within one structure type, as here CIGS, the RMS value gives an adequately good characterization value. For quantitative comparison a linear expression is used to empirically describe the sheet resistance increase in this and similar graphs.

The increased sheet resistance can be caused by a decreased charge carrier density and/or a decreased electron mobility of the IOH films. In Figure 5.19 the dependence of these values on the RMS roughness (left), the median local slope (middle) and median local slope per grain/structure size (right) is shown. The charge carrier density and electron mobility were determined by Hall effect measurements for IOH films grown on ZnO/Zn(O,S)- and Zn(O,S)-coated smooth and textured glass substrates and glass/CIGS samples, respectively. No dependence of the charge carrier density can be observed for IOH films grown on Zn(O,S) on the surface morphology in general and for IOH films grown on ZnO/Zn(O,S)/textured glass. In contrast for IOH films grown on ZnO/Zn(O,S)/CIGS the charge carrier density decreases with increased RMS, median local slope and median local slope per grain size. In total IOH films grown on ZnO have a lower charge carrier density than IOH films grown on Zn(O,S). This offset can be explained by the crystalline growth of IOH on ZnO, as discussed in section 5.1. This also applies to the electron

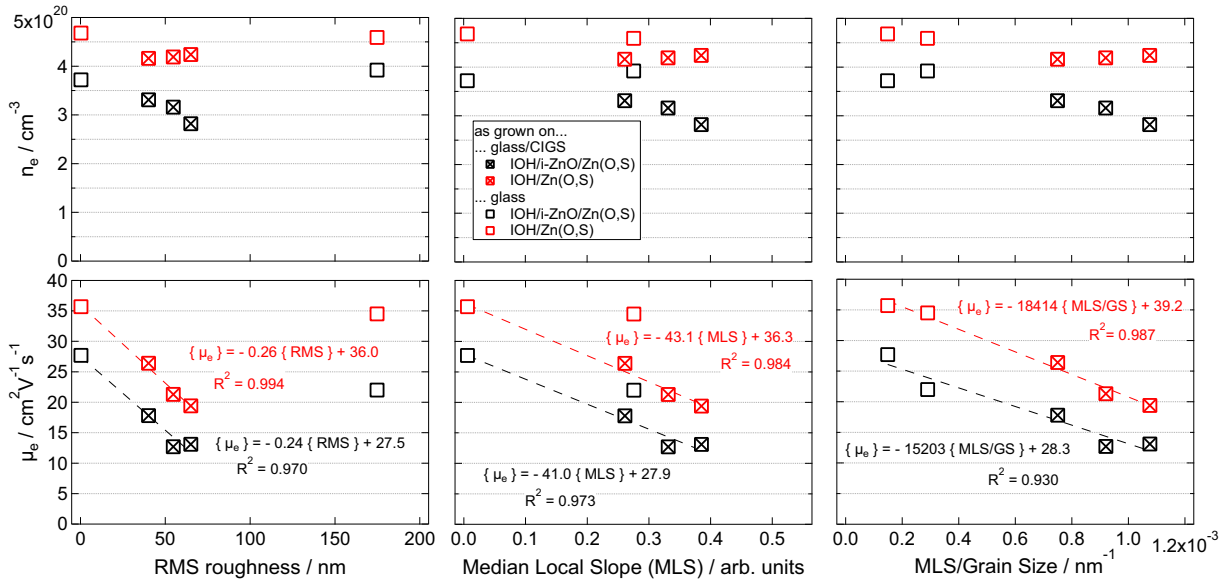


Figure 5.19: Comparison of the impact of the RMS roughness, median local slope and median local slope per grain/structure size of the substrate/sub-layers on the charge carrier density and electron mobility of sputtered IOH films deposited on ZnO/Zn(O,S)- and Zn(O,S)-coated samples; for the linear fits the films on the textured glass sample were only taken into account for the fit on the dependence on the median local slope per grain size

mobility of IOH films grown on Zn(O,S) and ZnO layers. The electron mobility of IOH films decreased linearly with increased RMS value when the films were grown on CIGS samples. The slope of the decrease is similar for amorphous grown IOH films on Zn(O,S) and partly crystalline grown IOH films on ZnO. In spite of the high RMS value of the textured glass sample, the IOH electron mobility is significantly higher than that of films grown on CIGS samples with lower RMS value. In comparison the strongest dependence of the IOH electron mobility was observed on the median local slope per grain size. Here a linear decrease of  $\mu_e(\text{IOH})$  can be observed for IOH films grown on textured glass as well as CIGS samples. A similar dependence was observed after annealing, as shown in Figure A.7 in the appendix. However, the slope of the linear regression was higher compared to the fit before annealing. In fact, the slope increased 1.3 times for the mainly amorphous grown films on Zn(O,S)/CIGS, while it increased 2.3 times for the pronounced crystalline grown films on i-ZnO/Zn(O,S)/CIGS. These rises apply for the dependence on the RMS, the median local slope as well as the median local slope / grain size.

In general we can say, that the increase of the IOH sheet resistance grown on rough CIGS samples is mainly caused by a decreased electron mobility. The more pronounced increase of  $R_{sq}$  for films grown on ZnO can be explained by additional decrease of the charge carrier density due to a more pronounced crystalline structure after deposition.

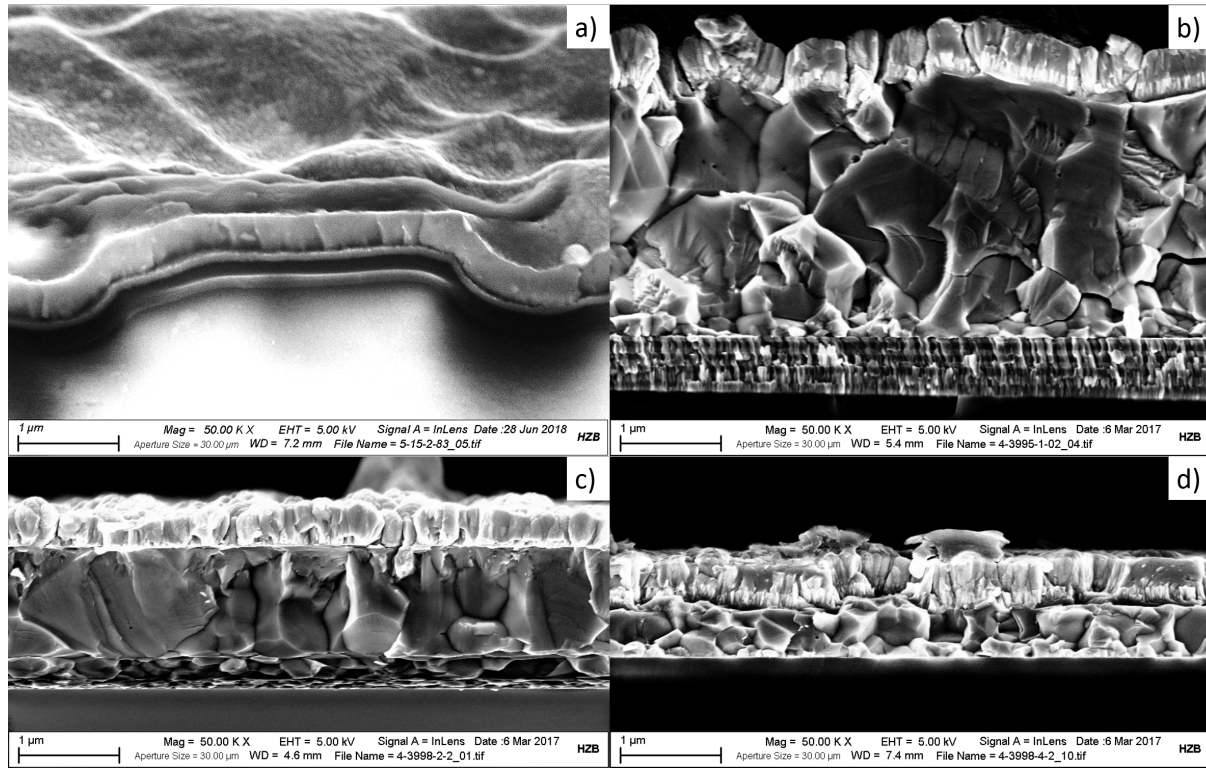


Figure 5.20: SEM images of samples a) 5-15-2-83 (IOH/ZnO/Zn(O,S)/textured glass), b) 4-3995-1-2 (IOH/ZnO/Zn(O,S)/CIGS/Mo/glass), c) 4-3998-2-2 (IOH/ZnO/Zn(O,S)/CIGS/glass) and d) 4-3998-4-2 (IOH/ZnO/Zn(O,S)/CIGS/glass)

Figure 5.20 shows SEM cross section images of the coated textured glass sample (a), and coated CIGS samples with different thicknesses (b) - (d). All samples were coated with an IOH/ZnO/Zn(O,S) window layer. As already observed by AFM measurements the textured glass substrate shows large but smooth structures. In contrast the CIGS layer consists of smaller grains and has an increased surface height fluctuation. This value increases for thicker CIGS absorber (Figure 5.20b). The CIGS surface becomes smoother with decreased CIGS thickness (Figure 5.20(c) and (d)). The IOH layer which was deposited on the textured glass sample seems to be closed and to cover the whole sample without void formation. In contrast darker areas are observed inside the IOH layers which were deposited on CIGS samples. The dark areas are assumed to be voids which separate the material. Similar findings were shown by Jäger et al. [150]. The amount and size of the voids inside the IOH layer increase with increased CIGS thickness, surface roughness and height fluctuation. From the images it seems that the voids mainly appear above CIGS grain boundaries.

These findings are consistent with the following study of  $\text{In}_2\text{O}_3:\text{H}$  and  $\text{In}_2\text{O}_3:\text{H,W}$  films, deposited by Reactive Plasma Deposition and  $\text{In}_2\text{O}_3:\text{H}$  films, deposited by pulsed DC magnetron sputtering.

Koida et al. [5] studied the material properties of the RPD - indium oxide based TCOs on flat glass, the results served as basis for this study. The CIGS layers were fabricated by co-evaporation by two different recipes and institutes, HZB in Berlin, Germany and AIST, Tsukuba, Japan, resulting in different CIGS morphologies. In Figure 5.21 SEM top view images of both CIGS types after CdS deposition are shown. The presented samples were produced without a post deposition treatment (PDT). The HZB sample has sharper edges, rather triangle shaped grains and seems rougher than the sample fabricated at AIST. Here the surface shows flatter, rounder shaped grains. AFM measurements confirmed the rougher structure of the HZB sample (RMS = 85 nm) in comparison to the AIST sample (RMS = 39 nm). The corresponding topography images can be found in Figure 5.22.

Note that a CIGS PDT can influence the surface topography of the absorber and lead to diffusion of alkali metals into the TCO layer. In fact, GDOES measurements confirmed that sodium, supplied by a NaF PDT, diffused into the used IOH layer. However, no correlation between the sodium amount in the TCO layer and the electron mobility was observed. Additional information can be found in the Appendix A.3. To evaluate the electronic properties of the indium oxide based TCOs the films were deposited on four types of CIGS samples, 2 fabricated by each institute with and without a PDT. An overview of the the topographic values of the CdS coated CIGS samples can be found in Table 5.2. The values were calculated from  $10 \mu\text{m} \times 10 \mu\text{m}$  AFM topography images.

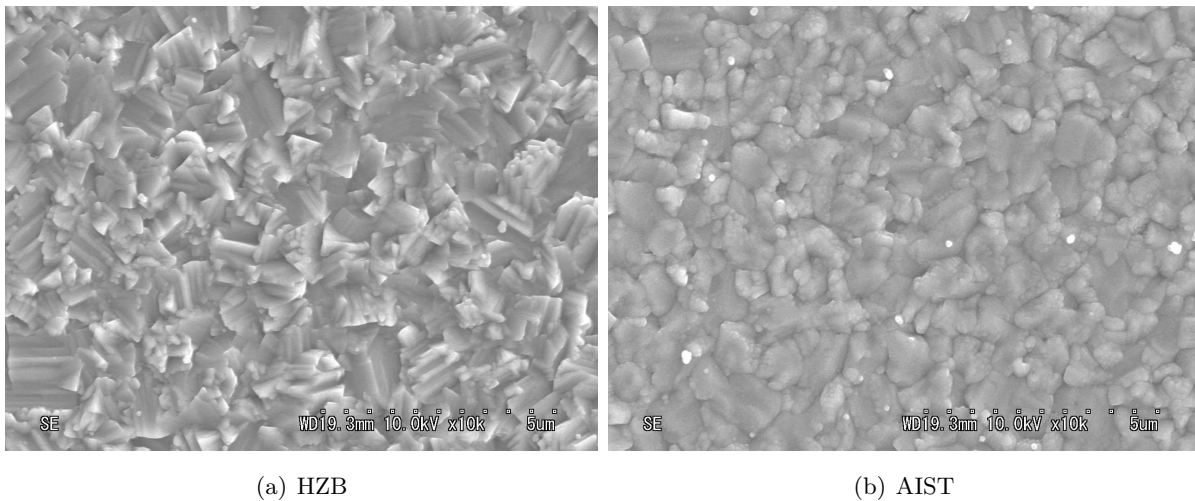


Figure 5.21: SEM top view images of CdS coated CIGS samples fabricated at (a) HZB and (b) AIST

Table 5.3 summarizes the electronic properties of the three TCO films on flat soda lime glass and the four rough CIGS samples. The data shows that the charge carrier density of the TCO layers does not change systematically when deposited on samples with different topographies, similar to the results presented in Figure 5.19 on page 80. Another similarity is the decrease of

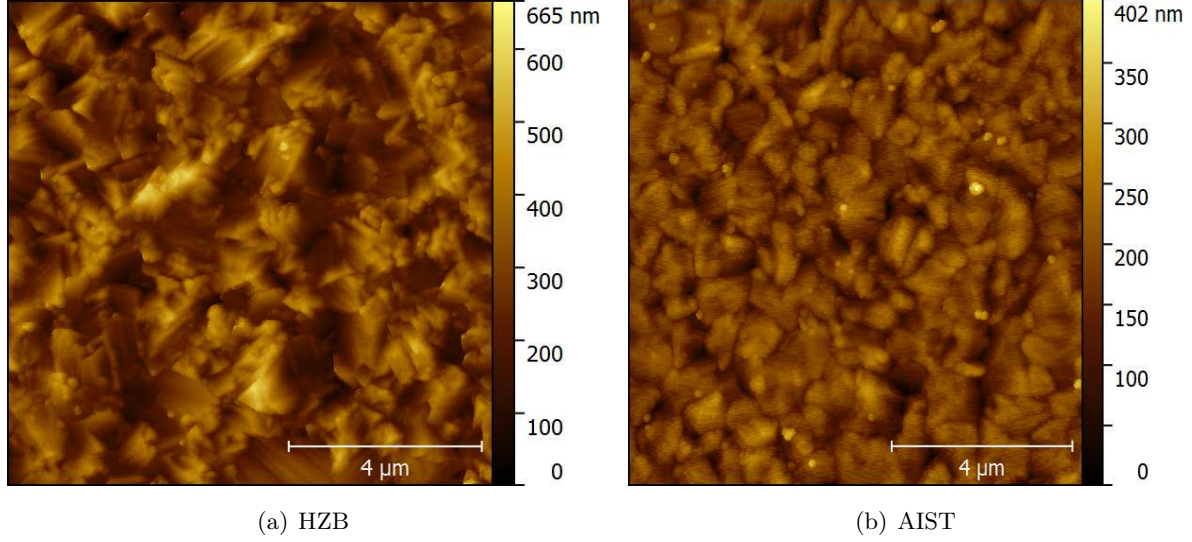


Figure 5.22: AFM topographic images of CdS coated CIGS samples fabricated at (a) HZB and (b) AIST

Table 5.2: Overview of the topographic values root mean square (RMS) roughness, median local slope (MLS) and median local slope per grain size (MLS/GS) of four types of CIGS samples

Sample	PDT	RMS (nm)	MLS (arb. units)	MLS/GS (nm <sup>-1</sup> )
flat SLG		0.3	-	-
HZB-1	none	84.9	0.62	3.41x10 <sup>-3</sup>
HZB-2	NaF	81.2	0.66	4.52x10 <sup>-3</sup>
AIST-1	NaF, KF	55.7	0.47	2.83x10 <sup>-3</sup>
AIST-2	none	39	0.39	2.35x10 <sup>-3</sup>

Table 5.3: Overview of the electrical properties charge carrier density ( $n_e$ ) and electron mobility ( $\mu_e$ ) of IWO:H, IOH thin films grown by RPD and sputtered IOH which were deposited on four types of CIGS samples

Film Property	IWO:H - RPD		IOH - RPD		IOH - sputtered	
	$n_e$ (cm <sup>-3</sup> )	$\mu_e$ (cm <sup>2</sup> /Vs)	$n_e$ (cm <sup>-3</sup> )	$\mu_e$ (cm <sup>2</sup> /Vs)	$n_e$ (cm <sup>-3</sup> )	$\mu_e$ (cm <sup>2</sup> /Vs)
flat SLG	3.70x10 <sup>20</sup>	37.0	3.80x10 <sup>20</sup>	43.5	3.56x10 <sup>20</sup>	39.6
HZB-1	3.10x10 <sup>20</sup>	27.1	3.64x10 <sup>20</sup>	28.9	3.21x10 <sup>20</sup>	16.2
HZB-2	3.24x10 <sup>20</sup>	28.5	3.64x10 <sup>20</sup>	30.9	3.18x10 <sup>20</sup>	18.8
AIST-1	3.25x10 <sup>20</sup>	33.9	3.55x10 <sup>20</sup>	37.3	3.26x10 <sup>20</sup>	26.6
AIST-2	3.04x10 <sup>20</sup>	35.0	3.67x10 <sup>20</sup>	40.8	3.28x10 <sup>20</sup>	27.9

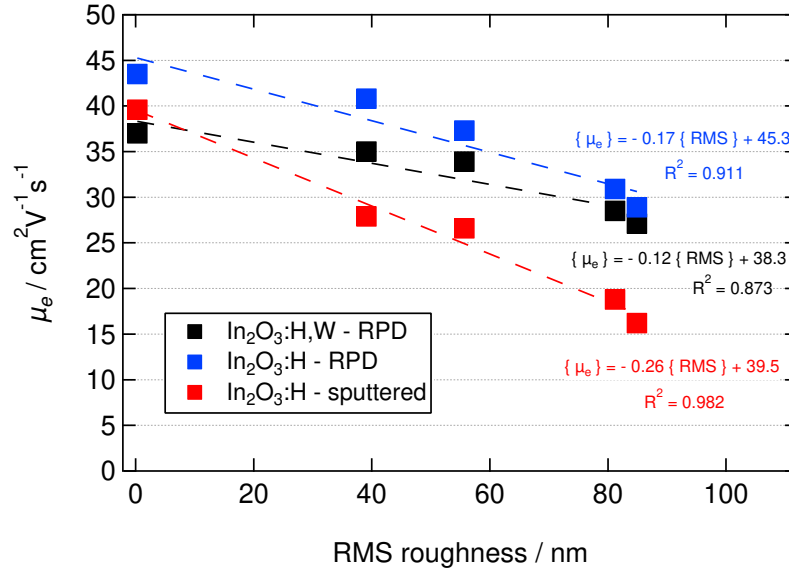


Figure 5.23: Dependence of the electron mobility of In<sub>2</sub>O<sub>3</sub>:H, In<sub>2</sub>O<sub>3</sub>:H,W, deposited by RPD and sputtered In<sub>2</sub>O<sub>3</sub>:H on the substrate's RMS roughness value; The films were grown on samples described in Table 5.2

the electron mobility of all three TCO layers with increased RMS roughness. The drop of the electron mobility can be described by a linear fit as well. The strongest decline was observed for the sputtered IOH films. Note that the slope is approximately the same as for the films grown on CIGS samples with different thicknesses, as shown in Figure 5.19. The lowest decline was found for the hydrogen and tungsten co-doped indium oxide layer grown by RPD. Compared to the sputtered hydrogen doped indium oxide films, it becomes apparent that the layers deposited by RPD show higher electron mobilities and a 34 % lower drop of  $\mu_e$  with increased RMS.

The drop in electron mobility can be correlated with the appearance of voids in the TCO layer. The structure of the as grown sputtered In<sub>2</sub>O<sub>3</sub>:H film, which was deposited on a CIGS sample with RMS  $\approx$  85 nm, was investigated by STEM measurements. Images of two significant regions of the sample In<sub>2</sub>O<sub>3</sub>:H/i-ZnO/CdS/CIGS are shown in Figure 5.24(a) and (b). Red arrows point towards the voids in the In<sub>2</sub>O<sub>3</sub>:H. In Figure 5.24(a) two voids in the In<sub>2</sub>O<sub>3</sub>:H layer with a width of  $\approx$  15 nm can be clearly observed. Figure 5.24(b) presents another void with a width of  $\approx$  5 nm. In Figures A.12 and A.13 in the appendix further examples are shown. The voids start in the In<sub>2</sub>O<sub>3</sub>:H layer, close to the ZnO interface. From Figure 5.24(b) it is apparent, that the void forms after  $\approx$  16 nm of In<sub>2</sub>O<sub>3</sub>:H were deposited. This value is lower than the estimated deposited amount during one path of the in-line sputtering process, which is  $\approx$  25 nm. This results indicate, that the cracks are formed due to geometry effects. The TEM measurements revealed that the CdS lattice follows the lattice of CIGS with many twins and defects. Furthermore some coherent lattice relationship between ZnO and CdS was observed. In contrast, no such relationship was found for In<sub>2</sub>O<sub>3</sub>:H and i-ZnO, thus the formation of crystalline nuclei on the surface of ZnO

must have been successfully suppressed by the increased water vapor supply and consequently hydrogen supply during deposition<sup>3</sup>. The results indicate that the voids form not due to change of the atomic structure across CIGS grain boundaries, but rather due to a geometry effect. Furthermore it can be seen that the voids form at triangle shaped regressions, which can be considered as a sharp transition. Figure A.11 presents images of the elemental compositions of the region showed in Figure 5.24(a), measured by EELS. The measurements confirm, that in the area of the voids no indium or other material was detected. In general it was found, that the majority of the voids could be aligned with CIGS grain boundaries.

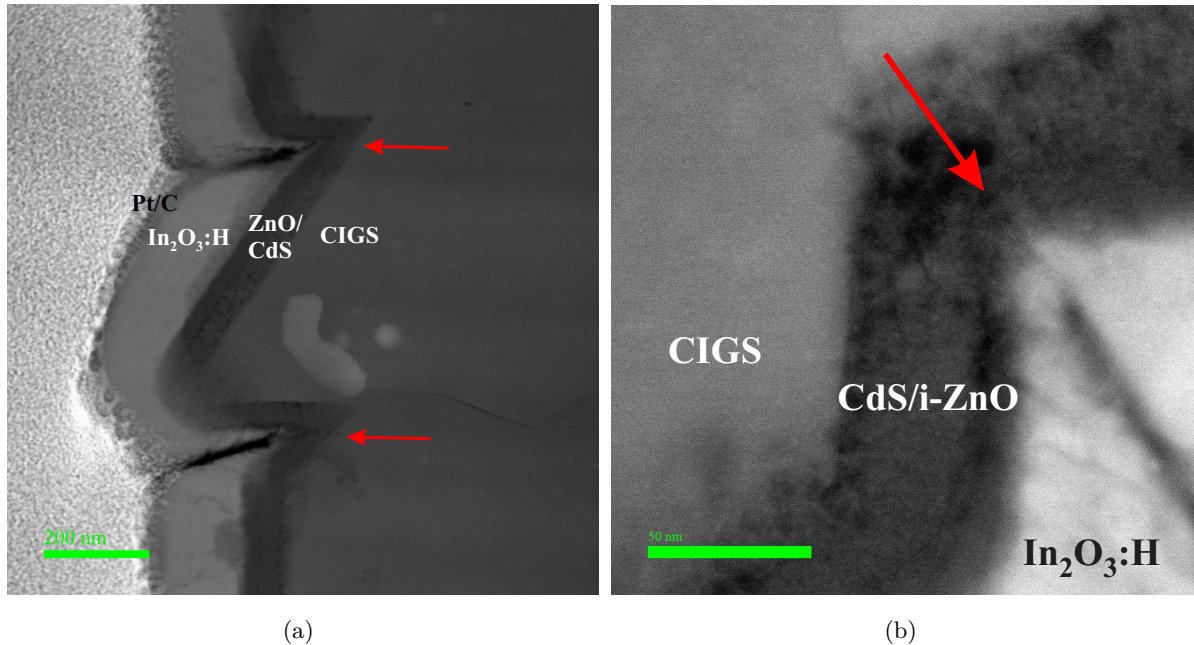


Figure 5.24: STEM measurements of as grown sputtered  $\text{In}_2\text{O}_3:\text{H}$  grown on  $\text{i-ZnO}/\text{CdS}/\text{CIGS}$ ; Voids are clearly visible in the  $\text{In}_2\text{O}_3:\text{H}$  layer (dark areas) and are indicated by red arrows

In the following the obtained findings are discussed. The results show how the electron mobility of indium oxide based TCOs is influenced when the films are grown on rough samples. The topography of the CIGS samples can be described in a first approximation by the root mean square (RMS) roughness, if it can be assumed, that the CIGS topography type is similar. We found by two independently taken studies that the electron mobility of indium oxide based TCOs such as  $\text{IWO}:\text{H}$  and  $\text{IOH}$  decreases with increased RMS of the sub-layer. This applies for films deposited by sputtering as well as RPD. The good electron mobility on textured glass, which showed smooth transitions on the surface, and STEM measurements confirmed that high local slopes and sharp transitions are detrimental. Such structures mainly appear along the grains, at

<sup>3</sup>here  $P_{\text{H}_2\text{O}} = 5.5 \times 10^{-3}$  Pa; for the experiment shown in section 5.1 and corresponding films grown on CIGS samples as shown in Figure 5.17 on page 78:  $P_{\text{H}_2\text{O}} \approx 2 \times 10^{-4}$  Pa

grain boundaries. The topographic structure of CIGS has therefore a high impact on the electrical properties of indium oxide based TCOs, as it was shown for  $\text{In}_2\text{O}_3\text{:H}$  and  $\text{In}_2\text{O}_3\text{:H,W}$ . Thus we conclude, that a specific amount of sharp transitions results in a defined amount of voids in the TCO layer. This also explains the limited mobility of  $\approx 30 \text{ cm}^2/\text{Vs}$  for  $\text{In}_2\text{O}_3\text{:H,W}$  films on CIGS samples, regardless of the improving electron mobility of the films deposited on glass substrates with increased oxygen supply during deposition, as observed in Figure 5.12. We conclude that the film quality in general improves also in the film deposited on CIGS. However, the amount of voids is assumed to be approximately the same in all of the films grown on CIGS. Therefore the fixed amount limits the electron mobility to  $\approx 30 \text{ cm}^2/\text{Vs}$  in general for all films, although the quality of the material itself may differ. Also after a thermal treatment the amount of voids most likely does not change significantly, resulting in a similar effect also for the crystallized films. Moreover the voids might promote effusion of hydrogen due to the increased surface area. This could explain the more pronounced decrease of mobility with increased RMS values after annealing, as mentioned on page 80 (compare Figure 5.19 and Figure A.7). The dependency of electron mobility of the as grown films on the RMS of the sub-layer was described by a linear progression with coefficients of determination higher than 0.87. However, the observed linear dependency can not be valid for very high RMS values, as the electron mobility can not drop below zero. It was found that the decline of  $\mu_e$  of  $\text{In}_2\text{O}_3\text{:H,W}$  and  $\text{In}_2\text{O}_3\text{:H}$  films deposited by RPD is not as strong as for sputtered  $\text{In}_2\text{O}_3\text{:H}$  films. As a significant difference between the two deposition techniques the energy of the deposition particles is suggested. In RPD it is less than 40 eV during ITO deposition. In contrast in sputtering methods particles such as backscattered argon and negative oxygen ions are considered to have high energies above 100 eV. The lower energies and higher ionization rates of the depositing particles are considered to be the origins of higher quality ITO films grown by RPD [151]. In this study the  $\text{In}_2\text{O}_3\text{:H}$  films grown by RPD also are of higher quality than the sputtered films. The lowest drop in electron mobility was found for tungsten and hydrogen co-doped indium oxide. Therefore we assume that tungsten reduces the formation of voids/cracks or promote their coalesce by changing the surface energy of the films.

In contrast to the indium oxide based TCOs the sheet resistance of aluminum doped zinc oxide films did not increase, as shown in Figure 5.18. Sputtered AZO thin films are known to grow crystalline [152–155]. In contrast the deposited indium oxide films are mainly amorphous, or can contain both, crystalline and amorphous fractions when ZnO is used as sub-layer. We assume that the crystalline AZO films, even though some voids might form, coalesce at very low thicknesses. We assume the origin in the preferred (002) columnar structure and the (partly) tilted growth on rough samples. In contrast the amorphous fractions of the indium oxide based films might lower the merging effect of separated film parts. Moreover we observed that the substrate roughness has no significant impact on the crystalline growth of the indium oxide based films, here IOH, as it is highly dependent on its sub-layer and in general the deposition conditions. The crystalline

structure of the as deposited IOH films was quite similar for films deposited on flat and rough substrates onto the sub-layers ZnO (pronounced crystallinity of IOH) and on Zn(O,S) (mainly amorphous IOH).

The surface of the sub-layers was also described by the median local slope and median local slope per grain size, which correlate the MLS and the structure or grain size estimated by the watershed method. A linear dependence of the decreased electron mobility on these values was detected as well. Comparing the MLS/GS values from Figure 5.19 and Table 5.2 it becomes apparent that the values show large differences, however, the indium oxide layers had similar electron mobilities. The origin of the differences lies in the estimated grain and structure size. For the samples described in Figure 5.19 AFM topography images of  $40\ \mu\text{m} \times 40\ \mu\text{m}$  were obtained, in contrast for the samples described in Table 5.2  $10\ \mu\text{m} \times 10\ \mu\text{m}$  AFM topography images were taken. Consequently more details are taken into account by the calculation routine of the grain size using the watershed method for the latter samples. Thus, the determined grain/structure size is lower than the one calculated for the CIGS samples with varying thicknesses from  $40\ \mu\text{m} \times 40\ \mu\text{m}$  images. The calculated MLS/GS value is consequently larger. Thus, this routine and the followed evaluation by MLS/GS can only be applied for topographic images of the same size.

In the following strategies for improved electron mobility of indium oxide based TCOs in the as deposited state grown on CIGS samples are presented. This is considered a key requirement to achieve high mobility after crystallization on CIGS.

*The main findings can be summarized as follows:*

- Formation of voids/cracks in the indium oxide layer when the films were deposited on rough CIGS samples.
- Voids/cracks mainly are located at sharp structures (e.g. cliffs at CIGS grain boundaries, sharp regressions).
- Voids and cracks in the indium oxide layers are the main cause for limited electron mobility; deficit is more pronounced for annealed films.
- In films grown on CIGS samples the electron mobility seems to decrease linearly with increase of the RMS roughness value.
- No difference for mainly amorphous grown and pronounced crystalline grown films was observed.
- No limitation of electrical properties in poly-crystalline AZO films grown on rough CIGS samples observed.

## 5.4 Strategies to improve the electron mobility of hydrogen doped indium oxide based TCOs on CIGS

As described in section 5.3 rough CIGS samples with sharp edges are the main cause of the increase of electron mobility of indium oxide based TCOs when the films contain amorphous regions. This section presents strategies which can be implemented in an already existing CIGS solar cell process line to improve the electron mobility of  $\text{In}_2\text{O}_3:\text{H,W}$  and hydrogen doped indium oxide ( $\text{In}_2\text{O}_3:\text{H}$ ) thin films. One possibility is to smooth the CIGS surface by the deposition of a spin-coated sol-gel layer or by etching. Furthermore the impact of the TCO thickness is discussed.

### 5.4.1 Spin Coated Sol-Gel Layers

As presented in section 5.2 spin coated gallium oxide sol-gel layers can serve as sub-layers for IOH thin films without deterioration of the electrical properties before and after annealing. Based on these results  $\text{Ga}_x\text{O}_y$  sol-gel layers were spin coated on CdS-coated CIGS samples prior to the IOH sputter deposition. The deposition process is described in section 3.1.2 on page 27. For this study the deposition routine was processed 1, 3 and 6 times, respectively. Figure 5.25 shows AFM topography images of the CIGS/CdS samples after 1, 3 and 6  $\text{Ga}_x\text{O}_y$  sol-gel depositions. The RMS value of the samples can be reduced significantly from 76 nm to 50 nm after 6 depositions. Here, the structure of the CIGS grains is still present, but the grains have a rounder shape. Table 5.4 summarizes the RMS value of the samples prior to IOH deposition and the resulting electrical properties of the IOH layers. Additionally a flat SLG sample was processed as reference. While the charge carrier density of the film remains unchanged, the electron mobility increases with increased deposition amount, as the surface becomes smoother. Note that after 6  $\text{Ga}_x\text{O}_y$  depositions the electron mobility is equal, even slightly higher than the electron mobility on SLG, even though the CIGS sample has a RMS value of 50 nm.

Table 5.4: Influence of spin coated sol-gel layers on the CIGS sample RMS roughness and the electrical properties of sputtered  $\text{In}_2\text{O}_3:\text{H}$  thin films

Sample	RMS (nm)	$n_e$ ( $\text{cm}^{-3}$ )	$\mu_e$ ( $\text{cm}^2/\text{Vs}$ )	$\rho$ ( $\mu\Omega\text{cm}$ )
Glass	0.3	$2.23 \times 10^{20}$	42.3	662
$1x\text{Ga}_x\text{O}_y$	76	$2.23 \times 10^{20}$	24.8	1130
$3x\text{Ga}_x\text{O}_y$	59	$2.44 \times 10^{20}$	35.9	712
$6x\text{Ga}_x\text{O}_y$	50	$2.37 \times 10^{20}$	43.7	602

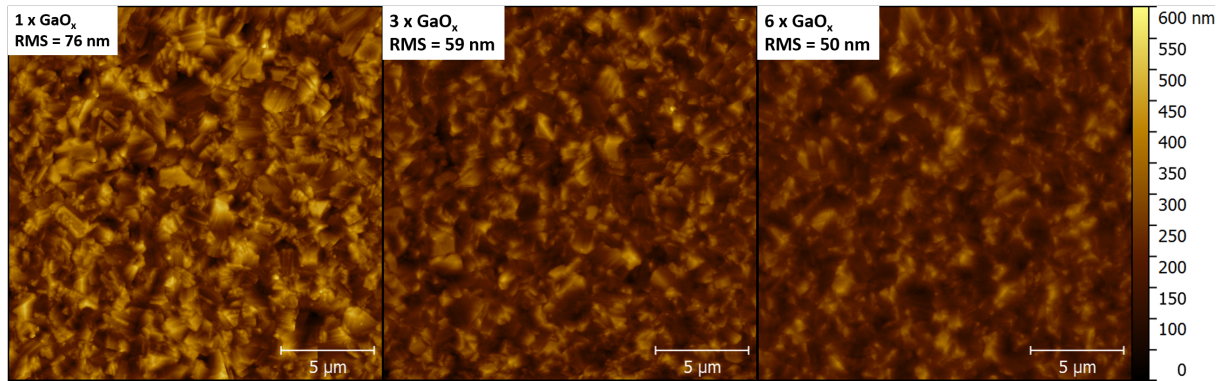


Figure 5.25: AFM topography images of CdS/CIGS samples which were coated with sol-gel  $\text{Ga}_x\text{O}_y$  layers; the amount of deposition repetitions and the determined RMS value are added

Figure 5.26 illustrates the change in  $\mu_e$  over RMS. For comparison data of the sputtered IOH film on different CIGS absorber types, as shown in Figure 5.23, is added to the graph. The graph shows a linear dependency of the electron mobility on the RMS value also for the films deposited on  $\text{Ga}_x\text{O}_y/\text{CdS}/\text{CIGS}$ . The CIGS samples with RMS values of around 80 nm were deposited following the same recipe as the CIGS absorber for the  $\text{Ga}_x\text{O}_y$  depositions. Prolonging the linear fit also leads to good agreement for these CIGS samples, which were fabricated with an i-ZnO layer instead of the  $\text{Ga}_x\text{O}_y$  layer. Thus, already one spin coating deposition led to a lower RMS value compared to the samples with i-ZnO. Further, it becomes apparent that the modification of the surface with spin-coated sol-gel layers is much more beneficial on the IOH electron mobility than the change of the CIGS absorber type.

The data shows that the spin coated  $\text{Ga}_x\text{O}_y$  layers smoothed the CIGS samples with increased deposition amount. We assume that the spin coating process rounds sharp grain structures and thus leads to smoother transitions between the CIGS grains on the CIGS surface. Note that the measured RMS value after 6  $\text{Ga}_x\text{O}_y$  depositions was 50 nm. High local slopes, as they appear at sharp grain edges, were found to be detrimental, as discussed in section 5.3. Thus, the impact of the surface becomes similar to the one of the textured glass as described in section 5.3. On the textured glass sample high IOH electron mobilities were achieved although the textured glass substrate had a RMS roughness of approx. 170 nm. When the surface showed smooth transitions, void formation in the IOH layer can be avoided and mobilities as high as on flat SLG are reached. These results serve as the basis for further annealing treatments to crystallize the amorphous IOH films. Despite of the improved electron mobility the implementation of such a deposition process might be challenging for an industry-like CIGS solar cell fabrication, as spin coating is not well scalable.

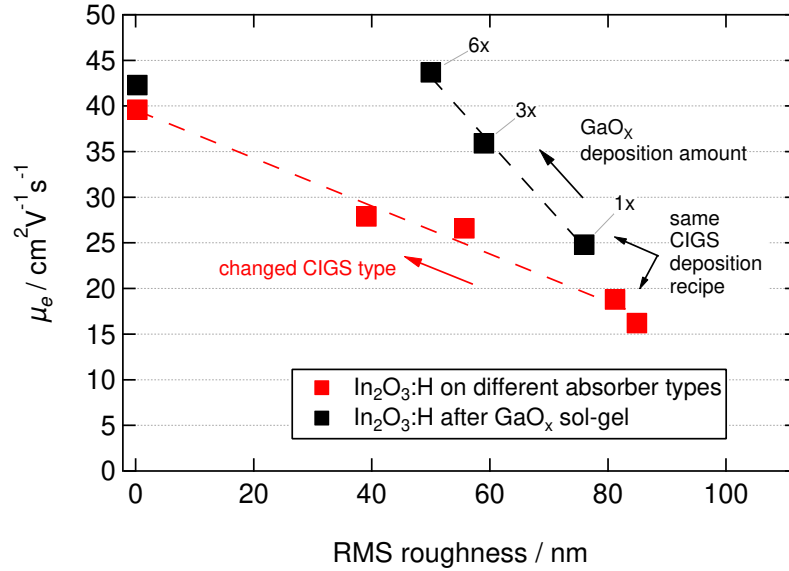


Figure 5.26: Electron mobility of sputtered In<sub>2</sub>O<sub>3</sub>:H in dependence of the substrate RMS roughness of CIGS samples of different process types and after Ga<sub>x</sub>O<sub>y</sub> spin coat deposition; values at RMS  $\approx$  0 nm are referred as flat SLG references

The main findings can be summarized as follows:

- Smoothing of CIGS samples by deposition of spin coated Ga<sub>x</sub>O<sub>y</sub> layers possible; reduction of sharp structures at the surface.
- Restored electron mobility in IOH films deposited on smoothed CIGS samples with thick spin coated Ga<sub>x</sub>O<sub>y</sub> layer (RMS = 50 nm).

#### 5.4.2 Etching of the CIGS Surface

Another possibility to smooth the CIGS surface is etching in an acid bromine solution [146, 147]. By etching with HBr solution CIGS is removed leading to thinner and smoother samples. In this study a set of four CIGS samples was prepared. The samples were etched for 0 s, 15 s, 30 s and 60 s in an acid bromine solution, the etching rate was estimated to 10 nm/min. The sample which is referred with an etch duration of 0 s was not etched with HBr and serves as a reference sample. During etching the solution was homogenized by a magnetic stirrer. Prior to the etching a previously deposited CdS layer was removed from all four samples in a 5 mol% HCl solution. After etching the CIGS samples in the HBr solution, a KCN treatment was done followed by the CdS and i-ZnO deposition.

Figure 5.27 illustrates the topographic images taken by AFM of the non-etched reference sample and samples after 15 s and 60 s of etching, respectively. The images were taken after CdS deposition. After 15 s of etching it can be observed, that the grain size does not change significantly, furthermore the RMS value is equal to the one of the non-etched reference sample, but that the surface of the grains was smoothed, less small particles are visible. The 60 s etched sample has an approx. 20 nm lower RMS value of 46 nm. The grains become rounder shaped. Figure 5.28 shows SEM cross section images of the surface near region of the CIGS samples. The results confirm the smoothing and rounding effect of the etching. After 60 s of etching the surface shows less structures with sharp slopes compared to the non-etched sample.

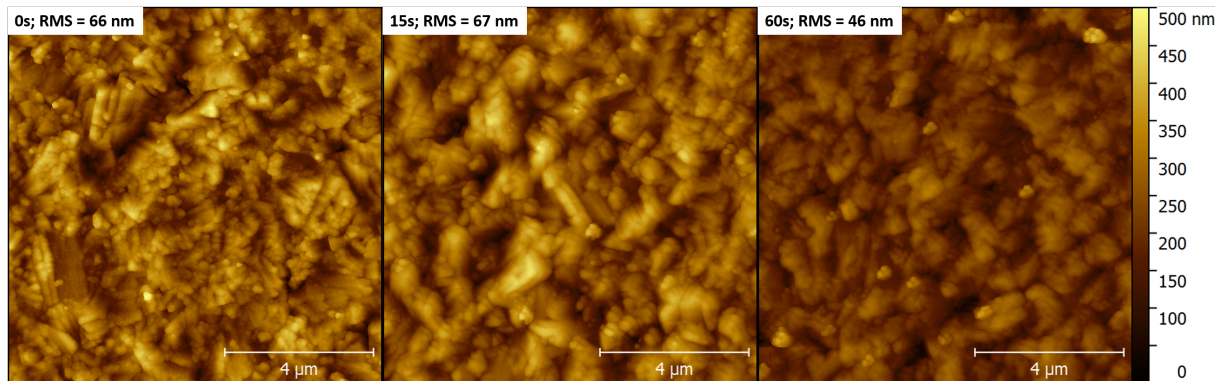


Figure 5.27: AFM topography images of etched CIGS sample after CdS deposition; the etch duration and the determined RMS value are insert; etch duration of 0 s represents the non-etched reference sample

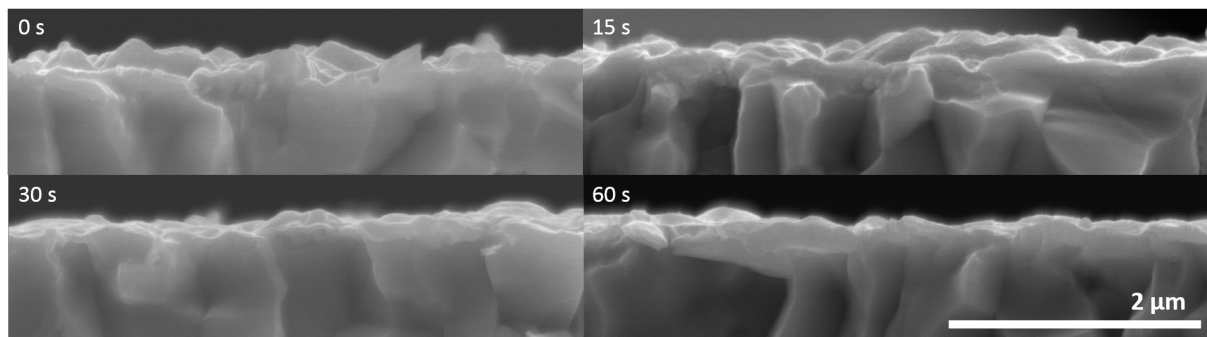


Figure 5.28: AFM topography images of etched CIGS sample after CdS deposition; the etch duration and the determined RMS value are insert; etch duration of 0 s represents the non-etched reference sample

Table 5.5 summarizes the RMS roughness of the CIGS samples in dependence of the etching duration and the electrical properties of RPD -  $\text{In}_2\text{O}_3\text{:H}$  thin films. Additionally a flat SLG sample was processed as reference. The data shows that the RMS value decreases with increased etching duration. Moreover, it becomes apparent that the charge carrier density of the films on CIGS samples is slightly lower than on the SLG reference and slightly increases with increased etch duration. As the calculation of the charge carrier density is dependent on the estimated

film thickness, it can not be excluded that this effect is due to uncertainties of the film thickness. With increased etching duration the electron mobility of the  $\text{In}_2\text{O}_3:\text{H}$  films increases. This effect is first determined after 15s of etching, although the RMS value remains unchanged. After 30s of etching the electron mobility does not further increase significantly.

Table 5.5: Influence of the CIGS etching on the roughness and electrical properties of RPD -  $\text{In}_2\text{O}_3:\text{H}$  thin films

Sample	RMS (nm)	$n_e$ ( $\text{cm}^{-3}$ )	$\mu_e$ ( $\text{cm}^2/\text{Vs}$ )	$\rho$ ( $\mu\Omega\text{cm}$ )
Glass	0.3	$3.37 \times 10^{20}$	50.0	370
0 s	66	$3.13 \times 10^{20}$	36.2	551
15 s	67	$3.15 \times 10^{20}$	41.2	480
30 s	55	$3.20 \times 10^{20}$	44.1	443
60 s	46	$3.24 \times 10^{20}$	44.4	433

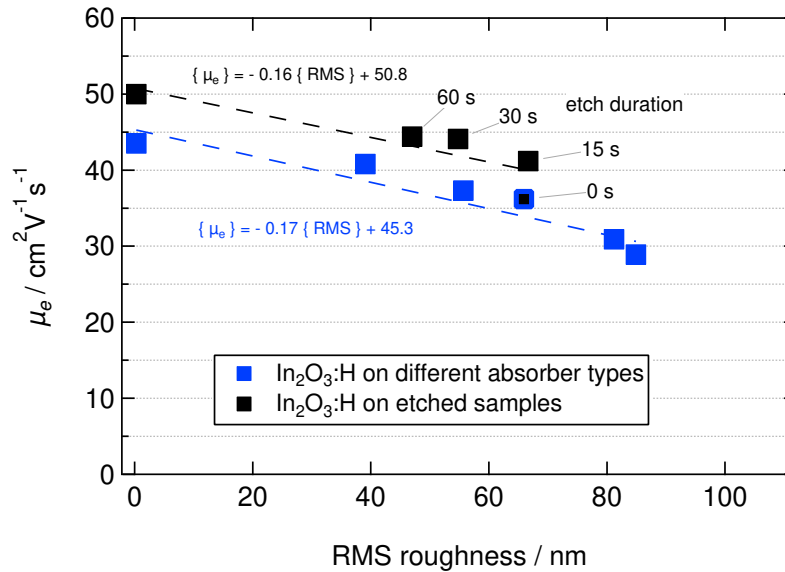


Figure 5.29: Electron mobility of RPD -  $\text{In}_2\text{O}_3:\text{H}$  in dependence of the substrate RMS roughness of CIGS samples of different process types and of etched CIGS samples; values at  $\text{RMS} \approx 0$  nm are referred as flat SLG references

Figure 5.29 shows the dependency of the electron mobility on the substrate RMS roughness of etched CIGS samples and of CIGS samples of different process types, taken from Figure 5.23 as comparison. Additionally the values of the SLG reference samples are added. It becomes apparent that the electron mobility increases with decreased RMS value. The slope was found to be equal to the slope of the films deposited on different types of CIGS. The electron mobility of the non-etched reference can be described by the  $\mu_e$  - RMS dependency as found for the films

deposited on different CIGS types, although the electron mobility of the SLG "etch" - reference film is higher. After 15s of etching the electron mobility increases while the RMS value remains unchanged. Further etching smooths the CIGS surface and leads to a decrease of the RMS value. The electron mobility increases according to the observed  $\mu_e$  - RMS dependency. However, the electron mobility does not reach the SLG reference value.

Etching in an acid bromine solution was carried out to smooth the CIGS surface and to reduce the amount of sharp structures by rounding the CIGS grains. These modifications led to an improved electron mobility. We assume that due to the smoother structure with more round grains less voids form in the  $\text{In}_2\text{O}_3:\text{H}$  layers. This reduced amount is beneficial for the electron mobility. As the used etching rate of 10 nm/min is quite low, the CIGS absorber were not reduced in thickness significantly, as the expected typical absorber thickness is in the range of 1.5  $\mu\text{m}$  to 2  $\mu\text{m}$ . Nevertheless, implementing this etching procedure into the CIGS solar cell fabrication might be unfavorable, as an additional wet chemical process is required.

*The main findings can be summarized as follows:*

- Etching of CIGS with acid bromine solution results in a smoothed surface with less sharp structures.
- Improved electron mobility of IOH films on etched, smoothed CIGS samples.

### 5.4.3 Influence of TCO thickness

It is known for AZO thin films, that an increased film thickness can have a beneficial effect on the electrical properties such as the electron mobility [36, 156]. This effect is caused by the increased crystallite size for increased thicknesses. Although an amorphous growth of the indium oxide based TCOs described in this study is required, the film thickness was found to also have an influence on the electron mobility of the films deposited on CIGS samples.

Figure 5.30 illustrates the charge carrier density and electron mobility of RPD -  $\text{In}_2\text{O}_3:\text{H},\text{W}$ ,  $\text{In}_2\text{O}_3:\text{H}$  and sputtered  $\text{In}_2\text{O}_3:\text{H}$  films on soda lime glass and CIGS samples with different RMS roughness values, respectively, in dependence on the film thickness. While the charge carrier density of RPD -  $\text{In}_2\text{O}_3:\text{H},\text{W}$  films is overall stable in the range of  $\approx 3 \times 10^{20} \text{ cm}^{-3}$  to  $4 \times 10^{20} \text{ cm}^{-3}$  on SLG and CIGS samples, a decrease for increased film thickness was observed for RPD -  $\text{In}_2\text{O}_3:\text{H}$  and sputtered  $\text{In}_2\text{O}_3:\text{H}$  thin films on both SLG and CIGS samples. In case of  $\text{In}_2\text{O}_3:\text{H}$  film deposited by RPD the overall lowest charge carrier density of  $\approx 1.1 \times 10^{20} \text{ cm}^{-3}$  to  $1.4 \times 10^{20} \text{ cm}^{-3}$  was observed for a film thickness of around 525 nm. The electron mobility of the indium oxide films deposited by RPD increased for increased film thickness when grown on CIGS samples. While the electron mobility of  $\text{In}_2\text{O}_3:\text{H},\text{W}$  grown on CIGS with RMS = 85 nm

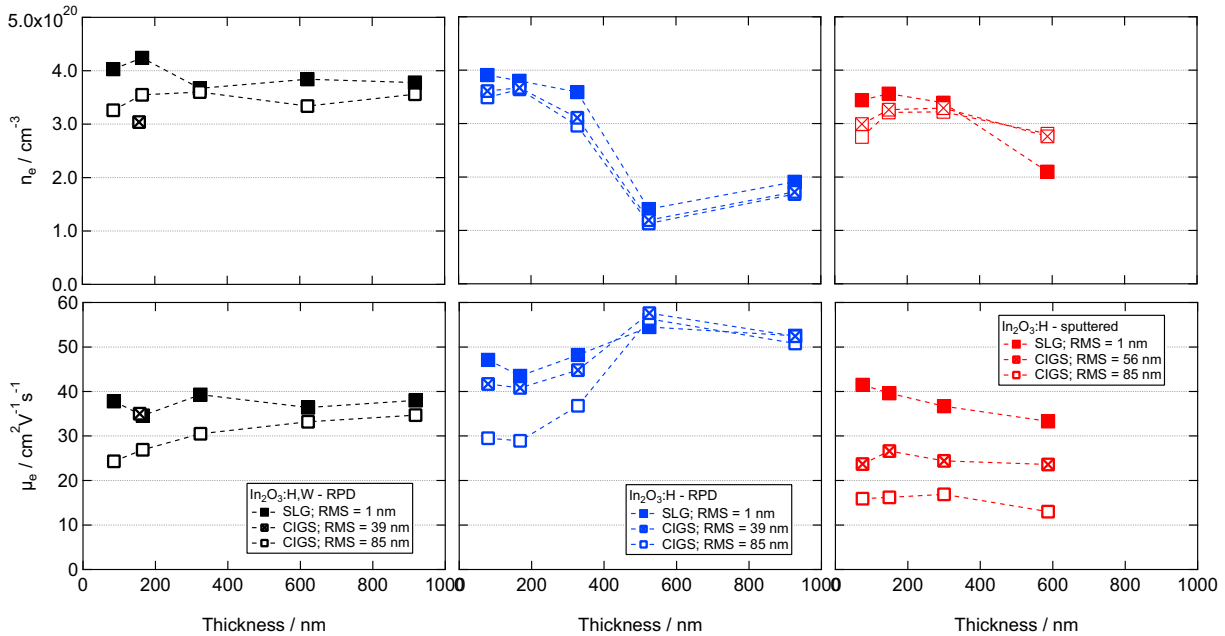


Figure 5.30: Charge carrier density and electron mobility of as-grown  $\text{In}_2\text{O}_3:\text{H,W}$ ,  $\text{In}_2\text{O}_3:\text{H}$  deposited by RPD and as-grown sputtered  $\text{In}_2\text{O}_3:\text{H}$  with different thicknesses grown on soda lime glass and CIGS samples with different RMS roughness values

rise up to 91 % of the  $\mu_e$  value of the SLG reference at a TCO film thickness of around 621 nm, the electron mobility of the  $\text{In}_2\text{O}_3:\text{H}$  film even exceeds the value on SLG at around 525 nm.

The results show that the electron mobility of films deposited on CIGS samples with  $\text{RMS} = 85 \text{ nm}$  by RPD increases with increased film thickness and that consequently the difference between the values on SLG and CIGS samples is reduced. This indicates that the isolated film parts merge at increased film thickness, similar to crystalline AZO films. In contrast to the films deposited by RPD the electron mobility of the sputtered  $\text{In}_2\text{O}_3:\text{H}$  drops with increased film thickness. This applies for films grown on SLG and CIGS samples with two different RMS roughness values. If coalescence of isolated film parts at increased film thicknesses is the origin of improvement of the electron mobility on CIGS samples, it can be assumed that this does not occur during the deposition by pulsed DC sputtering. It is possible that the unfavorable conditions during sputtering, as described on page 86, obstruct the coalescence of the films grown on CIGS samples. This effect seems to be less pronounced in the RPD layers.

For the RPD -  $\text{In}_2\text{O}_3:\text{H}$  layer a strong decrease of the carrier density at increased thicknesses was observed. This might be caused by irregularities during the film deposition or an increased film crystallinity in the as grown state, as also for the sputtered  $\text{In}_2\text{O}_3:\text{H}$  film a decreased carrier density at higher thicknesses was observed. As only the tungsten doped sample does not show

such a decrease, we assume that the tungsten prevents the formation of crystalline nuclei at increased thicknesses.

A disadvantage of thick indium oxide layers might be the consequently increased optical absorption and increased costs. Thus the beneficial effect of high mobility indium oxide based TCOs can be reduced or even eliminated compared to cheap zinc oxide based TCOs such as AZO.

*The main findings can be summarized as follows:*

- Improved electron mobility with higher film thicknesses possible (here, for films deposited by RPD).
- Material might merge at increased thicknesses, leading to a less voids/cracks.

## 5.5 Stability of IOH thin films

As already mentioned in section 4.4, the substrate morphology also influences the stability of IOH thin films. For evaluation IOH thin films with thicknesses of 270 nm were deposited on glass substrates with different morphologies and roughnesses, determined by AFM measurements with a measurement area of  $40\ \mu\text{m} \times 40\ \mu\text{m}$ . The corresponding topography images can be found in Figure 5.31. The textures of the glasses were produced by etching. The RMS roughness values of the glasses A, B and C were 1 nm, 76 nm and 122 nm, respectively. Thus, glass<sub>A</sub> can be considered to be smooth. Glass<sub>B</sub> showed a fine-meshed structure while glass<sub>C</sub> showed larger structures, but with similar heights as glass<sub>B</sub>. These two glasses are considered as rough.

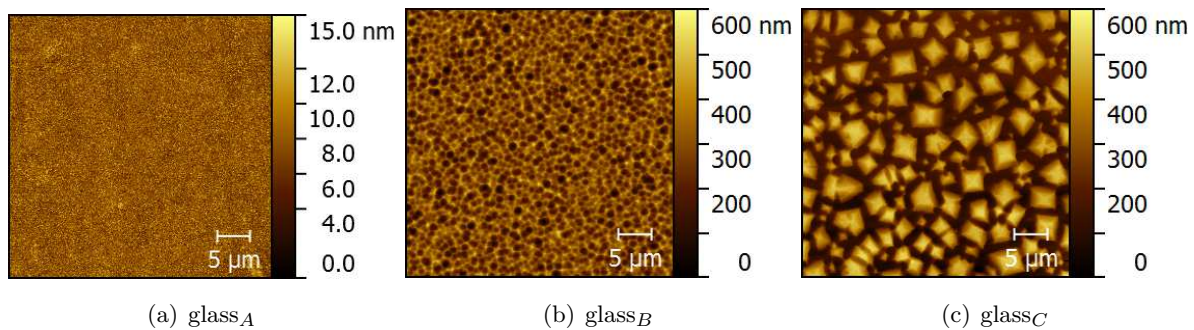


Figure 5.31: AFM topography images of glass substrates with different morphologies used for stability tests; left: glass<sub>A</sub>, RMS = 1 nm; middle: glass<sub>B</sub>, RMS = 76 nm; right: glass<sub>C</sub>, RMS = 122 nm; note that the scale of glass<sub>A</sub> differs from glass<sub>B</sub> and glass<sub>C</sub>

The results of the IOH stability tests carried out on these substrates are presented in Figure 5.32. Here, the change of the charge carrier density, electron mobility and resistivity of vacuum

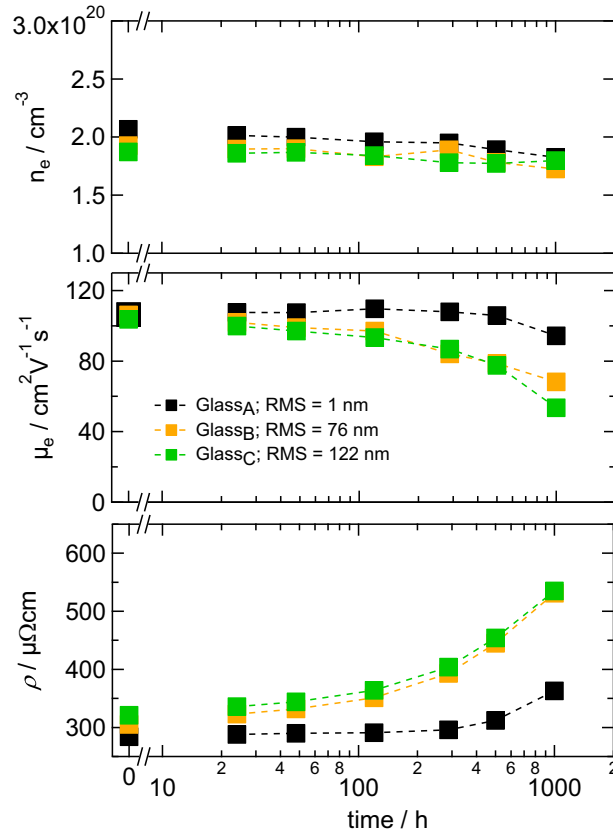


Figure 5.32: Change of the electrical properties of annealed IOH films during damp heat in dependence of the glass substrate RMS roughness

annealed IOH films during damp heat is shown. In the initial state the electrical properties of all samples were quite similar. It becomes apparent that IOH films degrade faster when deposited on rough glass. Here, after 1000 h of damp heat the resistivity of IOH deposited on glass<sub>B</sub> and glass<sub>C</sub> was found to increase by 74 % and 66 %, respectively. In contrast for the IOH film on glass<sub>A</sub> only an increase of 28 % was observed. Thus the degradation is more than two times faster on rough than on smooth glass substrates. Interestingly no large difference was found between the two rough glass substrates. According to the measured RMS roughness value a more pronounced degradation process was expected for the film deposited on glass<sub>C</sub>. The main cause for the accelerated degradation is the larger decrease in electron mobility. No differences in the change of charge carrier density were observed between the samples.

Additionally the stability of an approx. 340 nm thin IOH film on a CIGS sample was evaluated by changes of the sheet resistance, measured by 4 point probe. The architecture of the CIGS sample was glass/Mo/CIGS/InS/i-ZnO/IOH, after IOH deposition the sample was annealed in vacuum. The RMS roughness was calculated to be 123 nm. Note, that in this case the AFM measurement was conducted after IOH deposition with a reduced measurement area of 20  $\mu\text{m}$  x 20  $\mu\text{m}$ . The

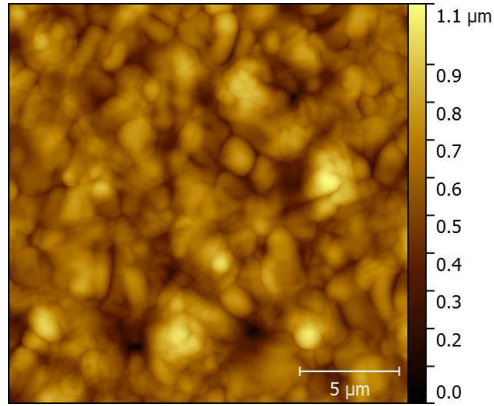


Figure 5.33: AFM topography image of the sample glass/Mo/CIGS/InS/i-ZnO/IOH before damp heat

corresponding AFM topography image is shown in Figure 5.33. As a reference an annealed IOH film of the same deposition run grown on a smooth glass substrate was evaluated. The results are shown in Figure 5.34. For comparison the change of  $R_{Sq}$  of the 270 nm thin IOH films deposited on glass<sub>A</sub> and glass<sub>B</sub> are added to the graph. The sheet resistance of IOH films deposited on glass substrates was calculated from the Hall data. The results show that the sheet resistance of IOH which was deposited on the CIGS sample increases more pronounced (+ 111 %) than that of the reference IOH thin film deposited on a smooth glass substrate (+ 29 %). Although the RMS value of the CIGS sample is comparable to the one of glass<sub>C</sub>, a significantly lower  $R_{Sq}$  increase of the IOH film on the rough glass substrate (+ 66 %) was found. No significant difference in the degradation of  $R_{Sq}$  was observed between the two IOH films which were deposited on smooth glass substrates.

The findings suggest that the morphology of the substrate has a large influence on the IOH stability. Similar results can be found in literature for AZO. While studies from Greiner et al. [115] suggested that grain boundaries are as such not strongly affected by damp heat for AZO thin films grown on smooth substrates, the accelerated degradation of conductivity of AZO grown on rough glass substrates was explained by the presence of local perturbations (extended grain boundaries (eGB)). These do not merely increase the penetration of water vapor into the film, but themselves block the current transport in the degraded state after damp heat. It is conceivable that this model can also be applied to IOH layers grown on rough substrates. The results suggest that the amount of eGB varies due to the substrate morphology and does not necessarily rely on the substrate roughness but on the specific morphology and structures. Thus, the resistivity of IOH thin films deposited on glass<sub>C</sub>, which had a high RMS, but showed rather large structures, decreased approximately as fast as that of IOH films deposited on glass<sub>B</sub>, which had a lower RMS, but a fine-meshed structure. We assume that eGB may be induced at rather sharp edges. As discussed before, IOH thin films which were deposited on CIGS samples showed presumably a high density of voids and cracks. This could additionally accelerate diffusion of

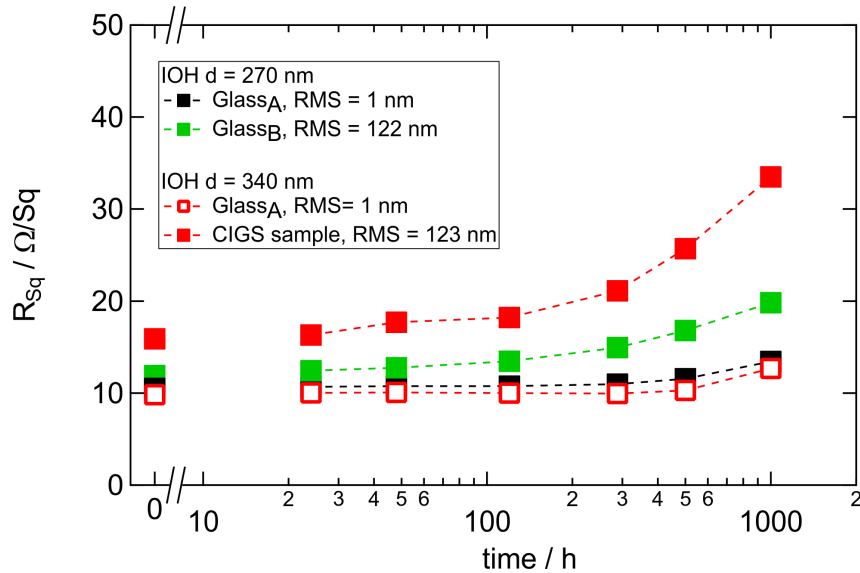


Figure 5.34: Comparison of the change of the sheet resistance of annealed IOH thin films during damp heat when deposited on smooth and rough glass substrates and a CIGS sample

water vapor into the films and enhance the degradation of IOH films. Therefore the pronounced  $R_{Sq}$  increase during damp heat of the IOH film grown on CIGS samples is probably caused by both effects.

*The main findings can be summarized as follows:*

- Accelerated degradation of electrical properties of IOH grown on rough substrates during damp heat tests.
- Morphology of the substrate and thus the resulting void density in the IOH film is crucial.

## 5.6 Conclusion

The findings obtained in this chapter are summarized in the chart diagram (Figure 5.35). In this study the influences of the substrate and sub-layers on the growth and properties of indium oxide based TCOs, i.e.,  $\text{In}_2\text{O}_3:\text{H}$  and  $\text{In}_2\text{O}_3:\text{H,W}$  were investigated and grouped in two aspects: (i) the structure and (ii) the roughness of the substrate/sub-layer. Two structural aspects of the sub-layers were studied. In the first case the sub-layer contained residual water, due to the deposition process. This led to degradation of the IOH films during annealing, as water from the sub-layer might interfere the crystallization process and diffuse into the IOH layer. Consequently the films exhibit poor electrical properties after annealing. In the second case the sub-layers

were poly-crystalline (ZnO). This promoted a crystalline growth of the deposited IOH layers and result to poor electrical properties before and after annealing. In additional experiments the hydrogen supply during the deposition of the first IOH layers at the ZnO interface were increased, resulting in a decreased crystalline fraction of the IOH films and improved electrical properties. The second main aspect was the roughness, i.e., the topography of the sub-layers or of the substrate. In a first approximation the topography can be categorized in two structures: (i) rounder shapes and grains on the surface with smooth transitions and (ii) sharp edged grains, sharp transitions and sinks. When the surface showed rather smooth transitions the deposition of a closed IOH films was possible. No adverse effect could be observed on the electrical properties, as these were similar to films deposited on planar glass substrates. In contrast in films that were deposited on sub-layers with sharp structures at the surface (in particular CIGS films) formation of voids and cracks was observed. The voids were located mainly at CIGS boundaries, as here the highest local slopes were observed. As the type of the topography was similar within the CIGS samples, the surface could be well described by the RMS roughness value. However, no significant influence of the deposition conditions or the crystalline fraction of the IOH films on the void formation was found. The disrupted film structure resulted in accelerated degradation of the electrical properties during damp heat and overall poor electron mobilities after deposition. This applied for  $\text{In}_2\text{O}_3\text{:H}$  deposited by sputtering or RPD and for  $\text{In}_2\text{O}_3\text{:H,W}$  films deposited by RPD. No sufficient improvement could be observed after annealing and solid phase crystallization of the indium oxide films. To improve the electron mobility of the indium oxide based TCOs on rough CIGS samples three different strategies were presented: (i) Sharp structures on the CIGS surface were etched in an acid bromine solution. This resulted in rounder shaped grains. Thus the deposited IOH films shows less voids and consequently higher electron mobilities. (ii) By spin coating  $\text{Ga}_x\text{O}_y$  sol-gel layers sharp edged grains and sinks on the surface of the CIGS sample were smoothed. The rounder shaped structures again led to formation of less voids and improved electron mobilities. (iii) Furthermore it was observed, that films with increased thicknesses also exhibit higher electron mobilities on rough CIGS samples. Therefore we assume, that the material might coalesce at increased thicknesses and thus led to the sealing of voids.

The findings show, that the substrate/sub-layers of the indium oxide based TCOs have a major effect on the growth and properties of the TCO films. Thus the application of such films in photovoltaic applications in not straightforward. The different effects need to be considered to achieve high-mobility indium oxide films.

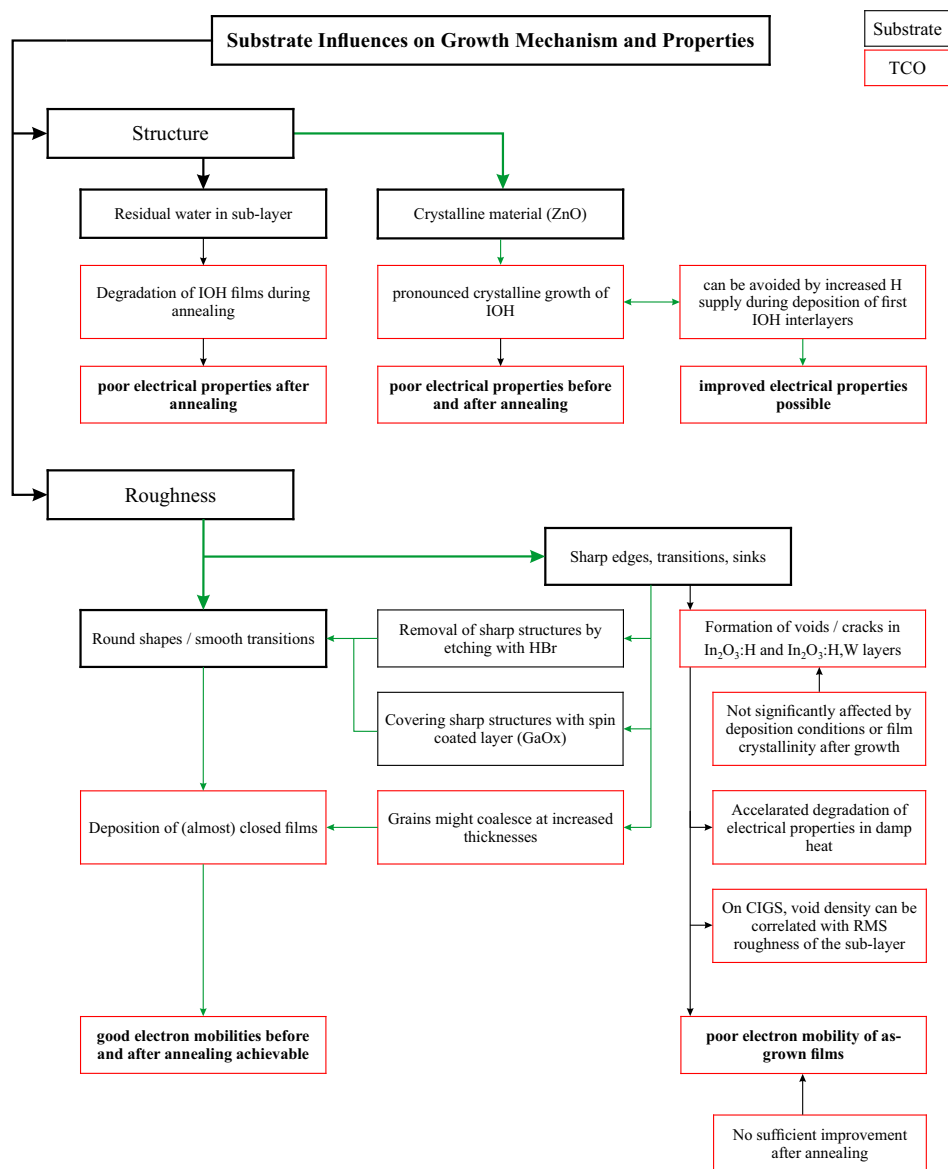


Figure 5.35: Main findings concerning the influence of the substrate and sub-layers on the growth and properties of indium oxide based TCO (i.e.,  $\text{In}_2\text{O}_3:\text{H}$ ,  $\text{In}_2\text{O}_3:\text{H,W}$ )

## CHAPTER 6

---

### Application of Indium Oxide based TCOs in CIGS solar cells

---

Due to their low optical absorption and high conductivity, as described in chapter 4, indium oxides doped with hydrogen or metals (such as W) are promising candidates as front contacts in solar cells. In chapter 5 influences of the sub-layers on the growth and properties of indium oxide based TCOs were identified. When applying the films as front contact in CIGS cells or modules, these influences have to be taken into account. In this we investigate indium oxide based TCO as front contact. Some basic requirements need to be fulfilled for a successful implementation. These are addressed in section 6.1. One requirement is a suitable band line up between the TCO and the rest of the device, such as the highly resistive layer. A large 'cliff' (negative conduction band offset) or 'spike' (positive conduction band offset) at the interface highly resistive layer/TCO would result in deterioration of the solar cell parameters, here, the fill factor. Similar effects were shown for the absorber/buffer interface [157, 158]. The band line up of crystalline hydrogen doped indium oxide and intrinsic zinc oxide (as the typical highly resistive layer between the buffer and TCO, as explained in section 2.2) is therefore studied in section 6.1.1. Another basic requirement is the thermal stability of the CIGS solar cells during the thermal treatment to induce solid phase crystallization of the amorphous phase of the indium oxide based films. Here, temperatures above 150 °C are applied. In section 6.1.2 the effect of thermal treatments of up to  $\approx 210$  °C on the solar cell performance of CdS buffered CIGS solar cells is studied. Additionally, alternative configurations are suggested to avoid or reduce an adverse effect. Only when these requirements are fulfilled, successful implementation of indium oxide based TCOs as front contact in CIGS solar modules might be achieved. However, additionally, loss-free current transport through the TCO on larger lateral distances than in a solar cell is required. Increased sheet resistance of TCO layers on CIGS samples will therefore limit the module characteristics. Thus, the implementation of hydrogen doped indium oxide as front contact in CIGS modules is discussed in section 6.2. In section 5.4 strategies for improved TCO sheet resistances on CIGS samples were suggested. The applicability of these approaches is tested in section 6.3. Note that the CIGS films presented

in this chapter were deposited at different points in time, by different techniques and recipes, resulting in CIGS absorbers with different properties and solar cell efficiency, as described in section 3.1.2. Therefore, only the experiments within one series can be compared directly.

## 6.1 Basic Requirements for the Application as Front Contact

The successful application of indium oxide based TCOs, as described in this thesis, depends on several requirements. One of two key aspects is a suitable band alignment of the front contact and the highly resistive layer, e.g. intrinsic zinc oxide. In the following section we therefore investigate the band line up of annealed hydrogen-doped indium oxide and intrinsic zinc oxide, the most common highly resistive layer. The second key aspect is the thermal stability of the solar cells, as temperatures above 150 °C are required for the initiation of the solid phase crystallization, depending on the TCO deposition conditions. The influence of the annealing treatment on the solar cell performance is therefore studied in section 6.1.2.

### 6.1.1 Band alignment IOH/ZnO

The band line up of the IOH/ZnO heterostructure can affect the solar cell properties, e.g. the fill factor. Kaspar et al. [159] investigated the band line-up of ZnO and ITO ( $\text{In}_2\text{O}_3:\text{Sn}$ ), determining a conduction band offset (CBO)  $\Delta E_{CBM} = 0.6$  eV (ZnO conduction band minimum (CBM) above ITO VBM). For the calculations an indium oxide band gap of 2.9 eV was assumed, the valence band offset (VBO) was determined to 0.05 eV to 0.25 eV (ZnO VBM above the ITO VBM). Such a large CBO of ZnO/IOH would lead to a significant deterioration of the FF in CIGS solar cells. We numerically calculated the FF for standard CIGS/CdS/i-ZnO/IOH solar cells for different CBOs. The results are shown in Figure 6.1 (a). For a fixed charge carrier density of i-ZnO (here  $n_e(i-ZnO) = 1 \times 10^{16} \text{ cm}^{-3}$ ) the FF drops with increased conduction band offset. For a conduction band offset  $\geq 0.4$  eV a more pronounced FF loss was calculated for decreased ZnO charge carrier density. The calculated band diagram of CIGS/CdS/i-ZnO/IOH with  $\Delta E_{CBM} = 0.5$  eV and  $n_e(i-ZnO) = 1 \times 10^{16} \text{ cm}^{-3}$  is shown in Figure 6.1 (b). To investigate the conduction band offset of ZnO/IOH we determined the band line-up of ZnO/annealed IOH by UPS and XPS measurements. For practical reasons the layer sequence was inverse to the one in solar cells and it is assumed here that this does not change the band line-up. We evaluated a bare annealed IOH film, IOH/ZnO heterostructures (ZnO was sputtered on annealed IOH in total for about 1 s, 2 s, 3 s) and a thick ZnO films (sputtered for 79 s).

Figure 6.2 shown the core levels Zn 2p (left), In 3d (middle), In 4d and Zn 3d (right) for different ZnO sputter duration. With increase of the sputter time the intensity of the In core peaks

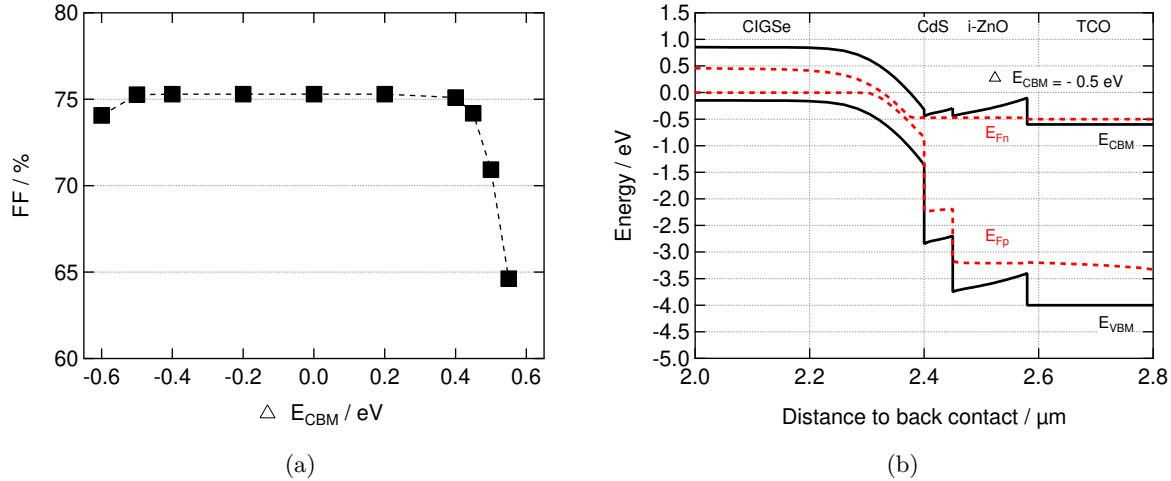


Figure 6.1: (a) Calculated FF (by SCAPS [160]) in dependence on the conduction band offset i-ZnO/TCO; (b) band diagram of CIGS/CdS/i-ZnO/TCO;  $E_{CBM}$  and  $E_{VBM}$  (black solid lines) are the conduction band minimum and valence band maximum, respectively,  $E_{Fn}$  and  $E_{Fp}$  (red dashed line) represent the quasi Fermi levels of electrons and holes [76], the negative conduction band offset at the i-ZnO/TCO interface indicate a 'cliff'

decreases while the Zn core peaks becomes more intense, indicating an increase of the ZnO film thickness. After 79 s of sputtering only the Zn core peaks are measurable, indicating that a sufficiently thick ZnO film was deposited. Measurements at the IOH/ZnO interface (1 s, 2 s, 3 s of ZnO sputtering) revealed that In core levels In 4d as well as In 3d 5/2 shifted towards lower binding energies compared to the uncoated film. The core level shifts are assumed to be due to band bending (rather than chemical shift) and are therefore used in the calculation of the band edges (see below). In contrast the Zn core levels Zn 2p and Zn 3d of the thin ZnO films (1 s, 2 s, 3 s) showed higher binding energies compared to the thick ZnO film. The measured valence band of the samples is shown in Figure 6.3. The determined average VBM  $E_{VBM}$  and binding energies of the core levels In 4d, In 3d 5/2, Zn 2p and Zn 3d are presented in Table 6.1, the error was calculated with the standard deviation of the linear regression.

The valence band maximum of the bare annealed  $\text{In}_2\text{O}_3\text{:H}$  film was observed at  $\approx 2.89 \text{ eV}$  below  $E_F$ , consistent with values found in literature for  $\text{In}_2\text{O}_3$  [161, 162]. For bulk ZnO a valence band maximum of  $E_{VBM}^{\text{ZnO}} \approx 3.35 \text{ eV}$  below  $E_F$  was obtained, which is also consistent with literature [163–165]. The valence band offset  $\Delta E_{VBM}$  was determined according to the method developed by Kraut et al. [166], which is well established [121, 167–170]:

$$\Delta E_{VBM} = (E_{CL}^{\text{ZnO}} - E_{VBM}^{\text{ZnO}}) - (E_{CL}^{\text{IOH}} - E_{VBM}^{\text{IOH}}) - \Delta E_{CL} \quad (6.1)$$

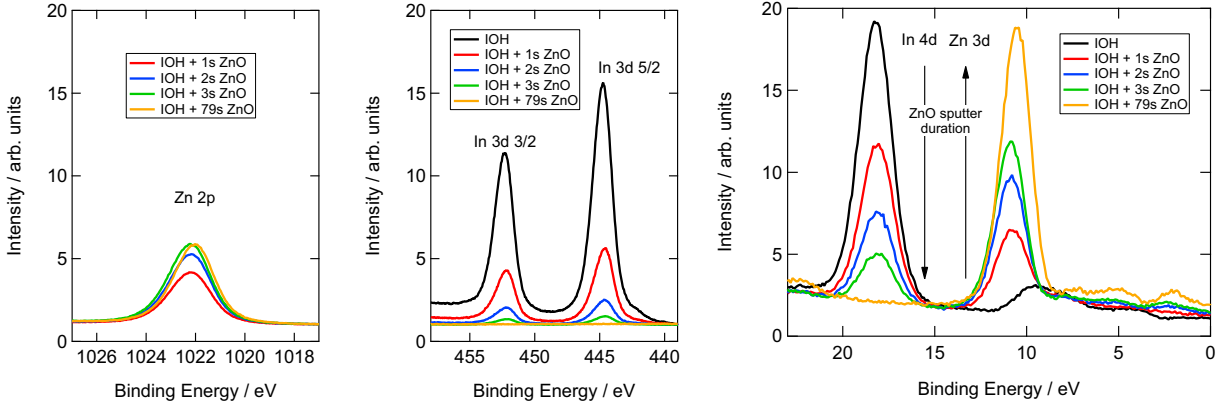


Figure 6.2: Core levels Zn2p (left), In3d (middle) and In4d & Zn3d (right) in dependence of the layer configuration with increasing ZnO thickness

Table 6.1: Valence band maximum  $E_{VBM}$  and binding energies of the core levels In 4d, In 3d 5/2, Zn 2p and Zn 3d measured by UPS and XPS, respectively, for different IOH/i-ZnO film configurations and ZnO sputter durations

Sample	$E_{VBM}$ (eV)	Error (eV)	$E_{CL}(In4d)$ (eV)	$E_{CL}(In3d_{5/2})$ (eV)	$E_{CL}(Zn2p)$	$E_{CL}(Zn3d)$
IOH	2.887	0.006	18.22	444.79	-	-
IOH + 1s ZnO	3.204	0.010	18.11	444.68	1022.2	10.803
IOH + 2s ZnO	3.333	0.008	18.13	444.69	1022.2	10.879
IOH + 3s ZnO	3.341	0.003	18.12	444.66	1022.3	10.902
IOH + 79s ZnO	3.351	0.006	-	-	1022.1	10.570

$$\Delta E_{CL} = E_{CL}^{ZnO}(i) - E_{CL}^{IOH}(i) \quad (6.2)$$

where  $E_{CL}^{ZnO}$  and  $E_{CL}^{IOH}$  are the binding energies of the core level of thick ZnO and bare IOH, respectively, (i) indicates values at the interface.  $E_{VBM}^{ZnO}$  and  $E_{VBM}^{IOH}$  represent the corresponding valence band maximum of thick ZnO and bare IOH, respectively. Calculations were conducted with the average  $E_{VBM}$  of the materials, as shown in Table 6.1. For better statistics, the average values of the core levels at the interface (1 s, 2 s, 3 s) were determined for  $E_{CL}^{ZnO}(i)$  and  $E_{CL}^{IOH}(i)$ , respectively. The  $\Delta E_{VBM}$  was calculated for all 4 combinations of both In and Zn core levels. The resulting valence band offset was determined to  $\Delta E_{VBM} = (-0.784 \pm 0.057)$  eV. The conduction band offset  $\Delta E_{CBM}$  can be estimated with the following equation:

$$\Delta E_{CBM} = \Delta E_{VBM} + E_g^{ZnO} - E_g^{IOH} \quad (6.3)$$

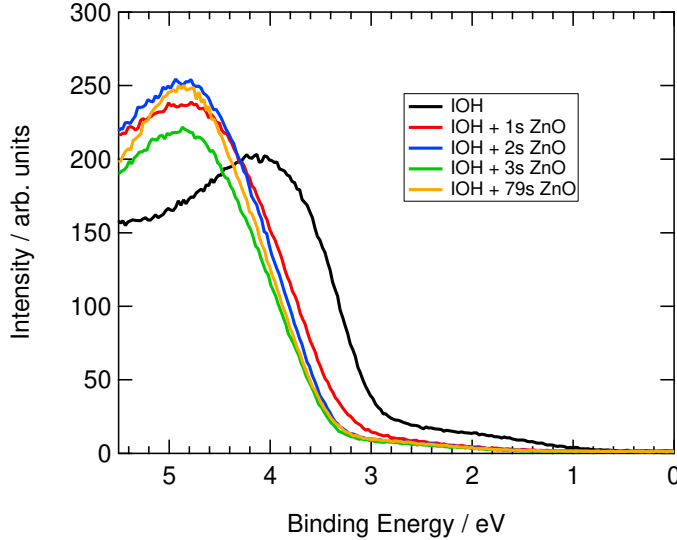


Figure 6.3: Valence band of bare and ZnO coated IOH after different ZnO sputter duration

with  $E_g^{ZnO}$  and  $E_g^{IOH}$  as the band gaps of ZnO and  $In_2O_3:H$ . The band gap of ZnO is well known as  $E_g^{ZnO} = 3.3$  eV [171]. Previous studies have reported that  $In_2O_3$  has a fundamental band gap of 2.6 eV - 2.9 eV [54–58], Walsh et al. [59] determined the upper limit of the fundamental band gap to 2.9 eV. Therefore we assumed  $E_g^{IOH} = 2.75 \pm 0.15$  eV. We calculated the CBO for IOH/ZnO to  $\Delta E_{CBM} = (-0.234 \pm 0.207)$  eV (CBM of  $In_2O_3:H$  below the CBM of ZnO). The large error is due to the large inaccuracy of the assumed indium oxide band gap. However, within this range we expect no adverse effect on the FF, as shown in Figure 6.1 (a).

These results contradict those of Kaspar et al. [159] who considered a cliff between the ZnO CBM and  $In_2O_3:Sn$  CBM. This can be attributed to the different (opposed) determined valence band offsets, as the authors concluded that the ZnO VBM is above the  $In_2O_3:Sn$  VBM. Similar findings were obtained by Kamiya et al. [172] by ultraviolet and inverse photoemission spectra. In contrast we observed the ZnO VBM below the  $In_2O_3:H$  VBM and the ZnO CBM below the  $In_2O_3:H$  CBM. These results are supported by the findings of Song et al. [173], who also reported a ZnO VBM below the  $In_2O_3:H$  VBM ( $\Delta E_{VBM} = 0.49 \pm 0.11$ ) eV). Assuming  $E_g^{ZnO} = 3.37$  eV and  $E_g^{In_2O_3} = 2.93$  eV a conduction band offset of  $(-0.05 \pm 0.26)$  eV was calculated.

We investigated the band line up by depositing ZnO on annealed IOH films. However, conventional CIGS solar cells are fabricated in the substrate configuration. In this case, IOH is deposited onto ZnO. Furthermore, the as grown IOH film is considered to be amorphous after growth and crystalline after the annealing. Therefore the band line up of ZnO/IOH might slightly differ when the materials are applied in CIGS solar cells. However, we found no evidence for an adverse effect on the fill factor by the band line up of ZnO/IOH.

*The main findings can be summarized as follows:*

- The conduction band offset of crystallized  $\text{In}_2\text{O}_3\text{:H}$  ( $E_g^{IOH} = 2.75 \pm 0.15$  eV) and intrinsic ZnO ( $E_g^{ZnO} = 3.3$  eV) was measured to be  $E_{CBM} = (-0.234 \pm 0.207)$  eV. For this offset, no adverse effect on the fill factor is expected. We therefore conclude that  $\text{In}_2\text{O}_3\text{:H}$  and i-ZnO have a suitable band line up.

### 6.1.2 Effect of Post Deposition Thermal Treatment on CIGS Solar Cells

As determined in the previous section the band alignment of crystalline  $\text{In}_2\text{O}_3\text{:H}$  and intrinsic ZnO is considered suitable for the application of  $\text{In}_2\text{O}_3\text{:H}$  as front contact in CIGS solar cells. Therefore one of the key requirements, as listed on page 102 is satisfied. A further key aspect is the thermal stability of the solar cells which will be investigated in this section.

Several groups studied the usability of hydrogen doped indium oxide films as front contact in CIGS solar cells [68, 71, 90, 91, 150, 174, 175]. Koida et al. [90] studied the impact of IOH front contacts in combination with different highly resistive layers on the performance of CIGS solar cells in relaxed and metastable states. Witte et al. [175] compared the cell performance for different window layer configurations. Similar or higher efficiencies were demonstrated with an as grown IOH front contact compared to an AZO front contact when a Zn(O,S) buffer was used. The CdS buffer cells showed in contrast lower efficiency due to reduced  $j_{sc}$  and  $FF$ . However, Keller et al. [68] showed that the short circuit current density of CdS buffered CIGS cells improved due to implementation of an annealed RF sputtered IOH front contact by  $\approx 3$  mA/cm<sup>2</sup>. The AZO reference cell had a  $j_{sc} \approx 31$  mA/cm<sup>2</sup>, the cell with annealed IOH an improved  $j_{sc}$  of  $\approx 34$  mA/cm<sup>2</sup>. Additionally an improved open circuit voltage but decreased fill factor were observed. In total, the cell with the annealed sputtered IOH front contact showed a higher average efficiency of  $\approx 15.4$  % than the reference with AZO with  $\eta \approx 14.7$  %.

However, we observed that the implementation of an annealed IOH layer into a standard CIGS sample with CdS/i-ZnO window is not straightforward. Solid phase crystallization of amorphous grown hydrogen doped indium oxide films requires temperatures of 150 °C to 220 °C, depending on the deposition conditions [5]. When applied as a front contact, the annealing procedure will also affect the CIGS cell. We therefore investigated the properties of CIGS solar cells with IOH front contact before and after annealing. A set of CIGS samples, fabricated by a sequential process, were coated with CdS buffer, i-ZnO as highly resistive layer and sputtered IOH front contact. The samples were annealed for 10 min, 20 min, 30 min and 60 min in vacuum with infrared heaters. The obtained average temperatures and electrical properties of the reference IOH films grown on glass substrates are shown in Table 6.2. The results indicate the initiation of solid phase crystallization already after 10 min of annealing at 157 °C, as a slight decrease in

$n_e$  and increase in  $\mu_e$  was measurable. However, only after 60 min and temperatures of 211 °C an electron mobility over 100 cm<sup>2</sup>/Vs was achieved.

Table 6.2: Electrical properties of reference IOH films deposited on glass substrates after annealing under varied conditions; for annealing different specimens of one glass substrate were used

t (min)	T (°C)	$n_e$ (cm <sup>-3</sup> )	$\mu_e$ (cm <sup>2</sup> /Vs)	$\rho$ ( $\mu\Omega\text{cm}$ )
0	23 ± 0	3.9x10 <sup>20</sup>	43.2	374
10	157 ± 4	3.7x10 <sup>20</sup>	47.1	362
20	179 ± 2	3.3x10 <sup>20</sup>	53.3	358
30	190 ± 2	2.8x10 <sup>20</sup>	60.6	368
60	211 ± 1	2.1x10 <sup>20</sup>	106.1	283

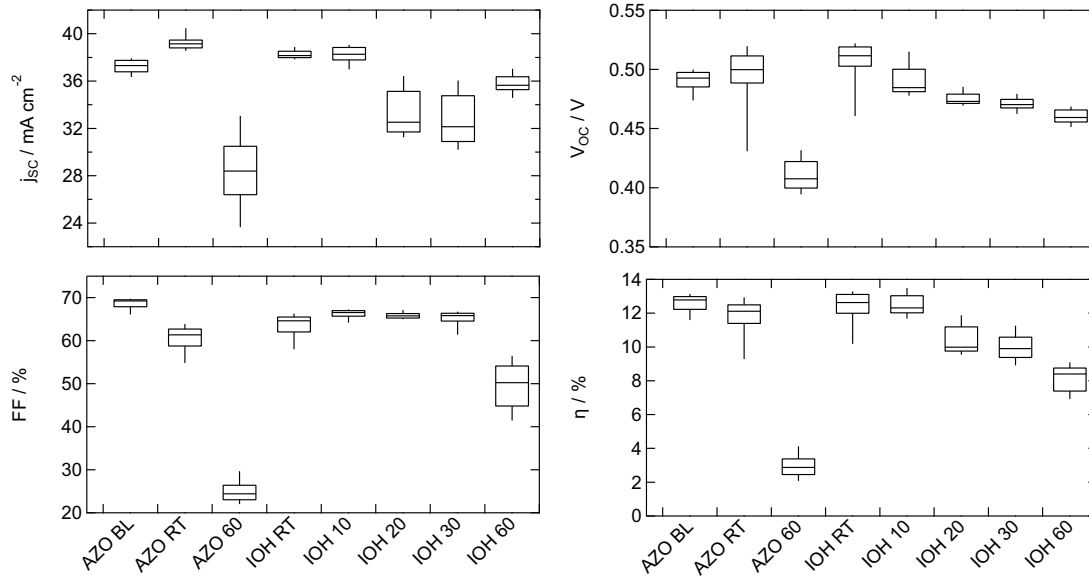


Figure 6.4: Box plots of  $j_{sc}$ ,  $V_{oc}$ ,  $FF$  and  $\eta$  of CIGS solar cells (60 cells each) with AZO or IOH front contact; the AZO baseline (BL) film was sputtered at  $\approx 165$  °C, RT: deposited at room temperature without intentional heating; numbers indicate the duration of annealing in minutes

The j-V characteristics of the corresponding CIGS solar cells (60 cells per sample) are shown in Figure 6.4. Further CIGS cells with AZO front contact were prepared in three configuration: 1) sputtered at a substrate temperature of  $\approx 165$  °C, 1.5 wt.% Al<sub>2</sub>O<sub>3</sub>; 2) sputtered without intentional heating, 1.0 wt.% Al<sub>2</sub>O<sub>3</sub>; 3) sputtered without intentional heating with subsequent annealing for 60 min, 1.0 wt.% Al<sub>2</sub>O<sub>3</sub>. The j-V characteristics were added to Figure 6.4 for comparison. In the following the average values of the cells serve for evaluation. For all cells the shunt resistance was found to be in the range of 1 k  $\Omega\text{cm}^2$  or higher, thus can be excluded to adversely affect the fill factor. Compared to the reference AZO BL sample, the non-annealed cells

with AZO and IOH front contact, sputtered without intentional heating, showed higher  $j_{sc}$  and  $V_{oc}$ , but a decreased fill factor by  $\approx 5\%$  to  $8\%$  absolute. After 10 min of annealing the IOH-cell showed a slightly improved fill factor, while the  $V_{oc}$  dropped in average by 25 mV. No significant change was observed for  $j_{sc}$ . However, further annealing up to 30 min results in an  $j_{sc}$  loss of almost  $6 \text{ mA/cm}^2$ , steadily decreased  $V_{oc}$  and fill factor by  $\approx 20 \text{ mV}$  and  $1.6\%$ , respectively. Note, that despite of the observed losses, no significant change of series resistance, ideality factor or saturation current density was determined. Nevertheless, after 60 min of annealing all three values increased significantly, indicating changes of the charge carrier recombination mechanism. Additionally the  $V_{oc}$  and  $FF$  decreased further. In contrast an improvement in  $j_{sc}$  by  $3 \text{ mA/cm}^2$  could be observed, still the determined value was in average  $2.6 \text{ mA/cm}^2$  lower than for the non annealed IOH sample. A similar effect was assessed for the cells with AZO front contact before and after annealing. Also here degradation of the  $j_{sc}$ ,  $V_{oc}$  and  $FF$  occurred after annealing, even more pronounced than for the cells with IOH. The samples which were annealed for 60 min both showed similar series resistances, ideality factors and saturation current densities. The j-V curves showed no kink effect.

Table 6.3: Average j-V characteristics of CIGS solar cells with different front contacts (AZO and IOH); the AZO baseline (BL) film was sputtered at  $\approx 165 \text{ }^\circ\text{C}$ , RT: deposited at room temperature without intentional heating; numbers indicate the duration of annealing in minutes; series resistance, shunt resistance, ideality factor and saturation current density were determined by fits of the dark curves (2 diode model) of cells with j-V characteristics close to the average values

sample	$j_{sc}$ ( $\text{mA/cm}^2$ )	$V_{oc}$ (V)	$FF$ (%)	$\eta$ (%)	$R_S$ ( $\Omega\text{cm}^2$ )	$R_{Sh}$ ( $\text{k}\Omega\text{cm}^2$ )	A	$J_0$ ( $\text{mA/cm}^2$ )
AZO BL	37.5	0.492	69.2	12.8	0.45	3.01	1.4	$4.9 \times 10^{-8}$
AZO RT	39.1	0.503	61.6	12.1	0.92	1.94	2.1	$1.5 \times 10^{-6}$
AZO 60	28.6	0.405	24.9	2.9	1.02	2.67	2.4	$2.9 \times 10^{-6}$
IOH RT	38.1	0.511	64.6	12.6	0.91	1.82	1.9	$8.0 \times 10^{-7}$
IOH 10	38.3	0.486	66.7	12.4	0.47	3.24	1.5	$7.6 \times 10^{-8}$
IOH 20	32.6	0.473	65.9	10.2	0.40	0.97	1.4	$5.6 \times 10^{-8}$
IOH 30	32.5	0.466	65.1	9.9	0.44	1.37	1.4	$4.3 \times 10^{-8}$
IOH 60	35.5	0.457	51.5	8.4	1.06	1.21	2.2	$2.0 \times 10^{-6}$

Furthermore EQE of the AZO baseline and the IOH cells was evaluated. The results are shown in Figure 6.5 (a). It is apparent, that the EQE of cells with AZO and as-grown IOH are very similar, for these cells no benefit due to the IOH layer can be observed. The sample annealed for 10 min shows an increased EQE in the near infrared region, indicating an increased transmittance due to decreased charge carrier density or improved electron mobility. However, in the short wavelength region the EQE decreased, resulting in a similar  $j_{sc,EQE}$  as the non-annealed IOH cell. For prolonged annealing duration the EQE drops over the whole, but more pronounced in

the short wavelength region. Similar to the results obtained by j-V measurements the EQE of the sample annealed for 60 min revealed a higher EQE and thus a higher  $j_{sc,EQE}$  compared to the samples annealed for 20 min or 30 min. However, for the short wavelength region still a loss was observed. Figure 6.5 (b) illustrates the doping profile of the CIGS samples with IOH front contact before and after several annealing durations, as determined by C-V measurements. The data revealed a decrease charge carrier density and a shift towards higher depletion widths with increased annealing time. After 60 min of annealing  $N_C$  decreased from  $\approx 2.5 \times 10^{15} \text{ cm}^{-3}$  to values as low as  $\approx 7.0 \times 10^{14} \text{ cm}^{-3}$  at the minimum.

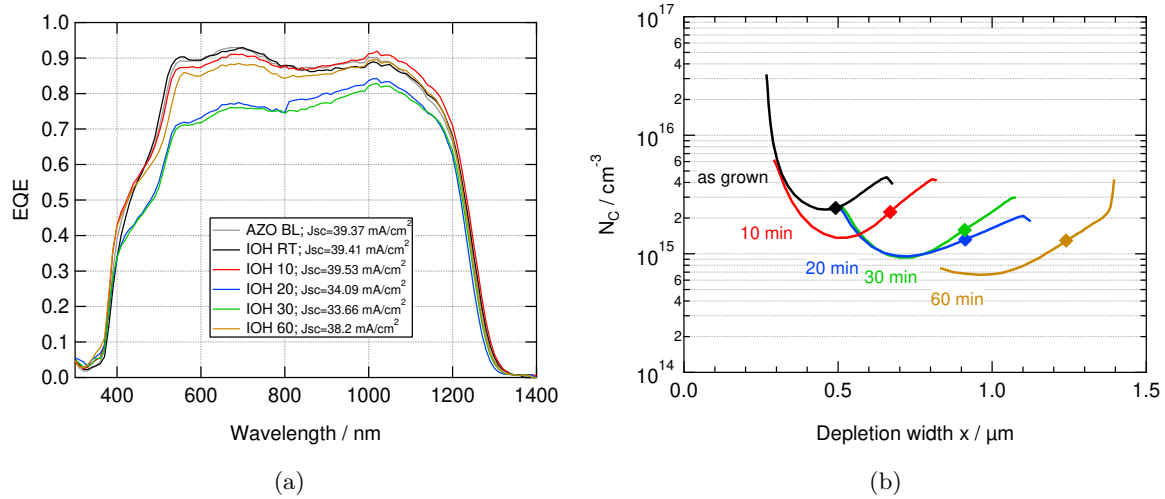


Figure 6.5: (a) External quantum efficiency of CIGS samples with baseline-AZO front contact (AZO BL), sputtered at  $\approx 165 \text{ }^\circ\text{C}$  or IOH front contact, deposited without intentional heating (IOH RT) and after several annealing durations, indicated by numbers; (b) Charge carrier densities in dependence of the depletion width of CIGS solar cells with IOH front contact in the as-grown state and after several annealing durations, determined by C-V measurements; values at  $V = 0 \text{ V}$  are marked with diamonds; corresponding temperatures can be found in Table 6.2

The results demonstrate degradation of the CIGS solar cells at increased temperatures, induced for the solid phase crystallization of the amorphous phase in IOH layers, applied as the front contact. With increased annealing temperature a steady drop of the  $V_{oc}$  from 0.511 V to 0.457 V was observed, which most likely results by the steady decrease of the charge carrier density, as determined by C-V measurements. The observed drop correlates well with calculated  $V_{oc}$  losses<sup>1</sup>.

<sup>1</sup>

$$\Delta V_{OC} = \frac{AkT}{q} \ln\left(\frac{N_1}{N_2}\right) \quad (6.4)$$

with A as diode quality factor, k as the Boltzmann constant, T as the temperature, q as elemental charge and  $N_1$ ,  $N_2$  as the charge carrier concentration of the absorber before and after annealing

The annealed cells showed an inclined EQE at small wavelengths, already after 10 min. Such an incline in combination with the observed decreased charge carrier density indicate Shockley-Read-Hall (SRH) bulk recombination, at least for the samples annealed up to 30 min. With decreased charge carrier density and increased space charge region (SCR) the SCR recombination area shift towards the CIGS bulk, resulting in a higher amount of recombined electrons and holes close to the window layer. As in this region mainly photons with higher energies are absorbed, the loss in photo-current is more pronounced at small wavelengths. The overall low EQE of the films annealed for 20 and 30 min, respectively, indicates bulk recombination over the whole absorber region. After 60 min of annealing (211 °C) the recombination mechanism seems to change significantly. Surprisingly the  $j_{sc}$  increased by 3 mA/cm<sup>2</sup>. Furthermore the FF dropped drastically while the ideality factor increased to values > 2, thus exceeding the limiting value for SRH recombination of 2.0. This also applies for cells with AZO front contact, which showed a similar drop of the  $V_{oc}$  and  $FF$ . As the j-V characteristics after 60 min of annealing were similar to the ones obtained for samples with IOH front contact, similar recombination mechanism are suggested. However, in order to confirm this surprising recovery of the  $j_{sc}$  in cells with IOH front contact the experiments must be reproduced.

These results are supported by the findings of Wi et al. [176] who reported degradation of CdS buffered CIS solar cells after annealing at temperatures above 200 °C. The authors attributed the degradation to Cd diffusion from the CdS buffer into the CIS absorber. Additionally it was demonstrated that CIS cells with Zn(O,S) buffer showed a better thermal stability (up to 300 °C). It was shown, that after annealing Zn atoms diffused not as far as Cd atoms into the CIGS absorber. The findings are consistent with the work of Park et al. [177] who reported Cd diffusion from the CdS buffer layer towards the CIGS absorber after annealing at 200 °C. Here the CIGS/CdS/ZnO interface was monitored in situ during annealing using TEM apparatus equipped with an in situ heating stage. Similar results were obtained by Kijima et al [178], but for temperatures above 360 °C. However, also in this study the ZnS(O,OH) showed a better thermal stability for temperatures up to 400 °C. Based on these findings we suggest that Cd diffusion might initiate the observed degradation of the solar cells annealed at higher temperatures, i.e., above 180 °C (20 min annealing). Furthermore the degradation might be due to additional processes, such as sodium diffusion. However, to study the degradation and recombination mechanism in more detail, further investigation, such as temperature dependent j-V measurements are necessary.

The findings show that the thermal treatment required for the solid phase crystallization of amorphous grown hydrogen doped indium oxide lead to degradation of the CdS buffered CIGS solar cells. The results are contrary to the findings reported by Keller et al. [68], where no degradation of the CdS buffered CIGS solar cell occurred after annealing in vacuum at 200 °C for 1 h. We therefore assume that the degradation mechanism highly depends on the condition

of the CdS/CIGS interface. To prevent cell degradation the interface must therefore be improved. Other approaches, such as the change of the TCO deposition conditions and change of the buffer layer are discussed in the following.

### Strategies for Improved Cell Performance After Annealing

As shown in the previous section degradation of the solar cell performance might occur after annealing of CIGS solar cells with CdS buffer and i-ZnO/IOH window. Notwithstanding possible improvement of the CdS/CIGS interface, which is not subject of this thesis, we suggest two approaches to prevent CIGS solar cell degradation caused by the post-deposition thermal treatment required to initialize solid phase crystallization of hydrogen doped indium oxide:

1. Change of the deposition conditions of IOH thin films to increase the nucleation density in the amorphous matrix of as grown films. This will lead to reduction of the required crystallization temperature [5] and the related heating of the CIGS solar cell. This will consequently minimize degradation.
2. Change of the applied buffer layer for improved thermal stability, e.g. Zn(O,S), as reported in literature [176, 178]. Steigert et al. [71] reported that solar cells with sputtered Zn(O,S) buffer layer and IOH front contact showed a slightly improved efficiency after annealing (180 °C, 10 min in ambient air) due to an improved  $j_{sc}$  by 0.3 cm<sup>2</sup>/Vs. However, still a slight decrease of the  $V_{oc}$  by 8 mV was observed. Overall the efficiencies of the cells with IOH were similar to the one with AZO as front contact.

Both approaches are briefly presented in the following.

#### Change of the TCO deposition conditions

Reduction of the water partial pressure during deposition of amorphous indium oxide based TCOs will result in an increased nucleation density in the amorphous matrix and thus reduce the crystallization temperature, as shown by Koida et al. [5]. However, a too low water partial pressure can cause crystalline grown, strained films and therefore lead to poor electrical properties (see section 4.2). This has to be considered for the application in CIGS. Following the work of Koida et al. [5] we deposited indium oxide films co-doped with hydrogen and tungsten by reactive plasma deposition on (multi-source) CIGS/CdS/IGZO (indium gallium zinc oxide)<sup>2</sup> at low ( $p_{H_2O} \approx 1 \times 10^{-5}$  Pa) and high ( $p_{H_2O} \approx 1 \times 10^{-4}$  Pa) water vapor pressures, the oxygen flow

---

<sup>2</sup>The IGZO in this case serves as an amorphous highly resistive layer replacing the standard i-ZnO

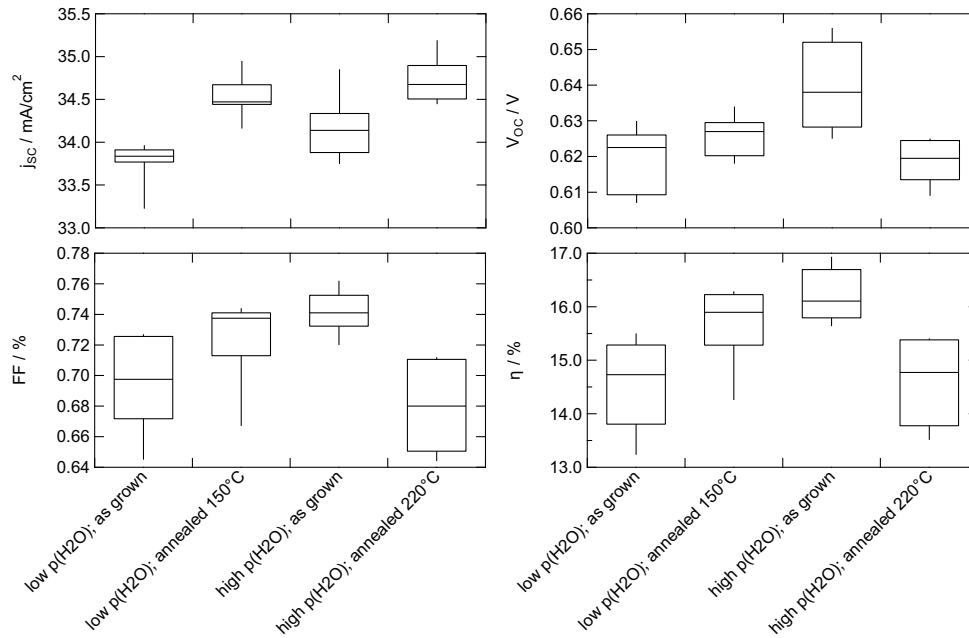


Figure 6.6: Box plots of  $j_{sc}$ ,  $V_{oc}$ ,  $FF$  and  $\eta$  of CIGS solar cells (8 cells each) with different window layers

was set to 60 ml/min. The experiments were carried out at AIST, where among other things IGZO is used as the highly resistive layer. The annealing conditions were optimized (as shown in section 5.3, i.e. in Figure 5.14) and set for low  $p_{H_2O}$  to 150 °C for 60 min and for high  $p_{H_2O}$  to 220 °C for 30 min in  $N_2$  atmosphere at a pressure of  $7 \times 10^4$  Pa. The main results obtained by j-V measurements are shown in Figure 6.6 and reported in the following. Cells annealed at low temperatures (150 °C) showed improved  $j_{sc}$ ,  $V_{oc}$  and  $FF$  after annealing. Consequently the efficiency improved in average from 14.7 % to 15.9 %. In contrast, cells that were annealed at higher temperatures (220 °C) degraded after annealing, although the  $j_{sc}$  improved in average by  $0.5 \text{ mA/cm}^2$ . The  $V_{oc}$  and  $FF$  decreased causing an efficiency drop from 16.1 % to 14.8 %. The high  $V_{oc}$  of the sample before annealing might result from inhomogeneities of the absorber.

### Change of the buffer layer

As discussed above Zn(O,S) might be a suitable substitutional buffer layer in CIGS solar cell, as it is suggested to be thermally more stable and therefore the more suitable buffer layer in CIGS solar cells with annealed indium oxide based TCOs. We therefore investigated the performance of (sequentially processed) CIGS solar cells with IOH front contact in combination with a Zn(O,S) buffer layer before and after an annealing in vacuum at 180 °C for 1 h. Note that at such temperatures a degradation of the CdS buffered solar cells was observed. We studied the impact of 280 nm thick AZO, as-grown and annealed IOH (120 nm) as well as the impact of the Zn(O,S) buffer layer, deposited by ALD. Although the IOH films are approx. half as thick as the AZO film, a sheet resistance of less than  $30 \text{ } \Omega/\text{Sq}$  on glass was achieved in the as grown state. The

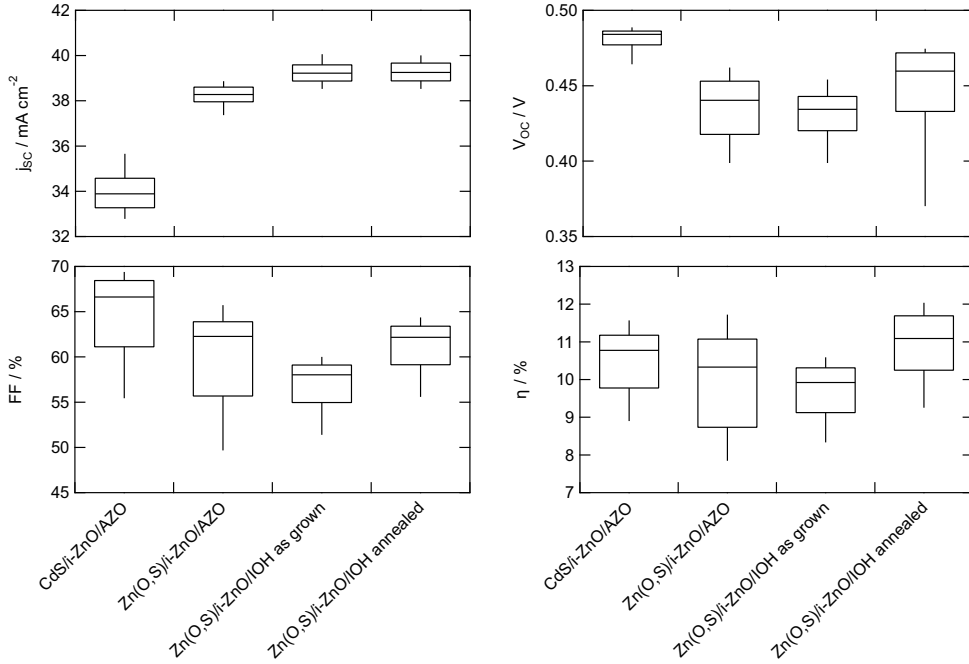


Figure 6.7: Box plots of  $j_{sc}$ ,  $V_{oc}$ ,  $FF$  and  $\eta$  of CIGS solar cells (60 cells each) with different window layers

AZO film was deposited in the sputtering tool VISS300 following the baseline recipe. These layers typically show sheet resistances of  $\approx 38 \Omega/\text{Sq}$  on glass. Figure 6.7 presents the results of  $j_{sc}$ ,  $V_{oc}$ ,  $FF$  and  $\eta$  of CIGS solar cells with different window layer configurations in box plots, obtained from j-V measurements. For each configuration 60 solar cells were processed. Table 6.4 summarizes the median solar cell parameters. By substituting the CdS layer with Zn(O,S) an increase in the short circuit current density of  $4.4 \text{ mA}/\text{cm}^2$  is observed. Merdes et al. [141] predicted that the exchange of the CdS buffer with Zn(O,S) can result in an improved  $j_{sc}$  of  $1.2 \text{ mA}/\text{cm}^2$ , due to the wider band gap of Zn(O,S) compared to CdS. Consequently the optical absorption loss in the short wavelength region decrease [71, 179]. The large increase in  $j_{sc}$  observed here can therefore not be attributed exclusively to the exchanged buffer layer, but might result also from more favorable interference fringes in the external quantum efficiency. The open circuit voltage and fill factor were found to decrease, which led to a lower median efficiency of the cells with Zn(O,S)/AZO. Replacing AZO with as grown IOH led to further improvement of the  $j_{sc}$  by  $0.9 \text{ mA}/\text{cm}^2$ , but also to additional losses in  $V_{oc}$ ,  $FF$  and efficiency. Note, that the AZO layer was deposited at  $\approx 165 \text{ }^\circ\text{C}$ , while the IOH layer was deposited without intentional heating. The heat during AZO deposition might have improved the CIGS/Zn(O,S) interface quality. The annealed IOH sample showed improved  $V_{oc}$ ,  $FF$  as well as  $j_{sc}$ . Consequently the efficiency of the annealed IOH sample was in median higher compared to the cells with as grown IOH. Also compared to the cells with AZO front contact the median efficiency improved by 0.8 % for Zn(O,S) and by 0.3 % for CdS buffered samples. The results show that no adverse effect can

be observed for the thermal treatment carried out at 150 °C, as even the solar cell parameters  $V_{oc}$  and  $FF$  improved. However, already in the as grown state the cells with IOH front contact had in average an improved  $j_{sc}$  compared to the cells with AZO front contact. The findings demonstrate, that the thin ( $\approx 120$  nm) IOH layer was sufficient for current collection and that in average a similar fill factors as for the cells with AZO front contact can be achieved.

In Figure 6.8 the internal quantum efficiencies of the best cells with Zn(O,S) buffer and AZO or annealed IOH front contact, respectively, are shown. The IQE spectra illustrates the beneficial effect of the IOH front contact over the whole wavelength region of the solar cell, especially in the near infrared region (800 nm to 1200 nm) compared to the standard AZO front contact. This results from the lower free carrier absorption of the IOH layer. It is further apparent, that the IQE is close to 1 in the range of approx. 500 nm to 900 nm. This result suggest that the current gain would be even higher than the obtained  $j_{sc}$ , when combining the sample stack with an anti reflective coating, such as MgF. However, already without an anti reflective coating the efficiency was improved in average by 0.8 % by replacing AZO with annealed IOH.

Table 6.4: Median parameters of CIGS solar cells with different window layers (60 cells per sample)

buffer	HR-layer	TCO	$j_{sc}$ (mA/cm <sup>2</sup> )	$V_{oc}$ (V)	$FF$ (%)	$\eta$ (%)
CdS	i-ZnO	AZO	33.9	0.484	66.6	10.8
Zn(O,S)	i-ZnO	AZO	38.3	0.440	62.3	10.3
Zn(O,S)	i-ZnO	IOH as grown	39.2	0.434	58.0	9.9
Zn(O,S)	i-ZnO	IOH annealed	39.3	0.460	62.2	11.1

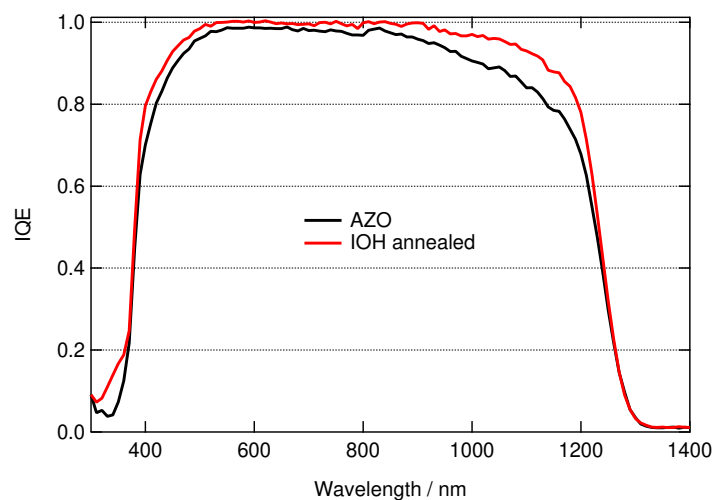


Figure 6.8: Internal quantum efficiency (IQE) of CIGS solar cells with Zn(O,S)/i-ZnO/AZO and Zn(O,S)/i-ZnO/IOH (annealed) window layers, respectively

Additional studies (not shown here) confirmed the thermal stability of CIGS cells with Zn(O,S) buffer (deposited by sputtering or ALD) and IOH front contact compared to CdS buffered Cells. For the same annealing conditions a degradation of the  $j_{sc}$ ,  $V_{oc}$  and  $FF$  was determined for the CdS buffered cells. In contrast, cells with the Zn(O,S) buffer layer improved in average in all j-V parameter after annealing. Consequently the efficiency could be improved by 1 % with stack ALD-Zn(O,S)/i-ZnO/IOH annealed compared to a reference CdS/i-ZnO/AZO stacked sample. Furthermore the results confirmed the beneficial effect of IOH as front contact in CIGS solar cells.

*The main findings can be summarized as follows:*

- The post deposition thermal treatment (T above  $\approx 160$  °C) can degrade CdS buffered solar cells when the absorber/buffer interface is of poor quality.
- Change of the  $\text{In}_2\text{O}_3\text{:X}$  deposition conditions for increased nuclei density in the amorphous matrix results in reduction of the crystallization temperature and thermal impact on the solar cell. Degradation can be avoided. However, this might lead to increased TCO sheet resistances.
- By substitution of the CdS buffer by a thermally more stable buffer layer (e.g. Zn(O,S)) degradation of the solar cells can be avoided.

## 6.2 Challenges in the Application as Front Contact in CIGS Modules

As shown in the previous section the basic requirements for the application of a high mobility indium based TCO, a suitable band line up and thermal stability can be satisfied. Therefore in this chapter we investigate the applicability of  $\text{In}_2\text{O}_3\text{:H}$  as front contact in CIGS modules (CIGS deposition by a sequential process). We study the structure and electrical properties of  $\text{In}_2\text{O}_3\text{:H}$  films before and after annealing, when deposited on the coated CIGS samples. Additionally we determine the module characteristics by j-V measurements and correlate them with the properties of the TCO layers.

Implementing  $\text{In}_2\text{O}_3\text{:H}$  or related high-mobility indium based TCOs as front contact in CIGS modules is not straightforward. As discussed in section 5.3 an increase of the sheet resistance was observed when the films were grown on rough CIGS samples. This holds for mainly amorphous as well as for pronounced crystalline growth. TCO film resistance is, however, a decisive parameter. In CIGS modules a sheet resistance of approx.  $10 \text{ } \Omega/\text{Sq}$  or less is required to avoid fill factor losses caused by an increased series resistance. To evaluate the impact of an ( $\approx 300 \text{ nm}$ ) IOH

front contact compared to AZO ( $\approx 865$  nm), CIGS modules with several buffer layers were fabricated. The overview of the samples is shown in Table 6.5.

Table 6.5: Sample assignment of CIGS modules with different buffer and TCO layers;  $A_{b,a}$ : annealing before/after TCO deposition, respectively, conducted in vacuum at  $\approx 180$  °C for 1 h

ID	buffer	HR-layer	$A_b$	TCO	$A_a$
M1	CBD CdS	sputter i-ZnO	-	AZO	-
M2	CBD CdS	sputter i-ZnO	-	IOH	-
M3	sputter Zn(O,S)	sputter i-ZnO	-	IOH	-
M4	sputter Zn(O,S)	sputter i-ZnO	-	IOH	+
M5	ALD Zn(O,S)	ALD i-ZnO	-	IOH	-
M6	ALD Zn(O,S)	ALD i-ZnO	-	IOH	+
M7	ALD Zn(O,S)	ALD i-ZnO	+	IOH	-
M8	ALD Zn(O,S)	ALD i-ZnO	+	IOH	+
M9	soda lime glass		-	IOH	-
M10	soda lime glass		-	IOH	+

The crystalline structure of the samples was evaluated by GI-XRD measurements. The different deposition techniques of the Zn(O,S)/i-ZnO layers result in ZnO films with different orientation. The ALD deposited ZnO films showed preferential orientation of crystallites in (100) and (101) direction of the surface normal while the sputtered ZnO films only show (002) peaks. The measurements also revealed a higher crystalline fraction of the as grown IOH film deposited on sputtered i-ZnO than the film on glass, in accordance to the findings described in sections 5.1 and 5.3. The corresponding X-ray diffraction patterns are shown in Figure 6.9 (a). The crystalline fraction of IOH was lower when the films were grown on i-ZnO layers deposited by ALD and decreased further when the ALD layers were annealed prior the IOH deposition. Annealing the samples in vacuum at 180 °C to 200 °C for 70 min led to solid phase crystallization of the IOH film, as revealed by X-ray diffraction measurements, shown in Figure 6.9 (b).

The sheet resistance of the TCO layers, as shown in Table 6.6, was determined by transmission line (TLM) and 4-point measurements. The determined values showed the same trend, though the values measured by TLM were slightly higher in average than the values determined by 4-point measurement, as illustrated in Figure 6.10. This systematic error might result from the different measurement set up, as for the 4 point measurements it is assumed, that the sample size is significantly larger than the distance of the probes.

Table 6.6 presents the module parameters  $j_{sc}$ ,  $V_{oc}$ ,  $FF$  and  $\eta$ , determined by j-V measurements as cell equivalent and the series and shunt resistance of the module, estimated by fits of the dark curves. Modules M1 and M2 were produced with a AZO and IOH (as grown) front contact,

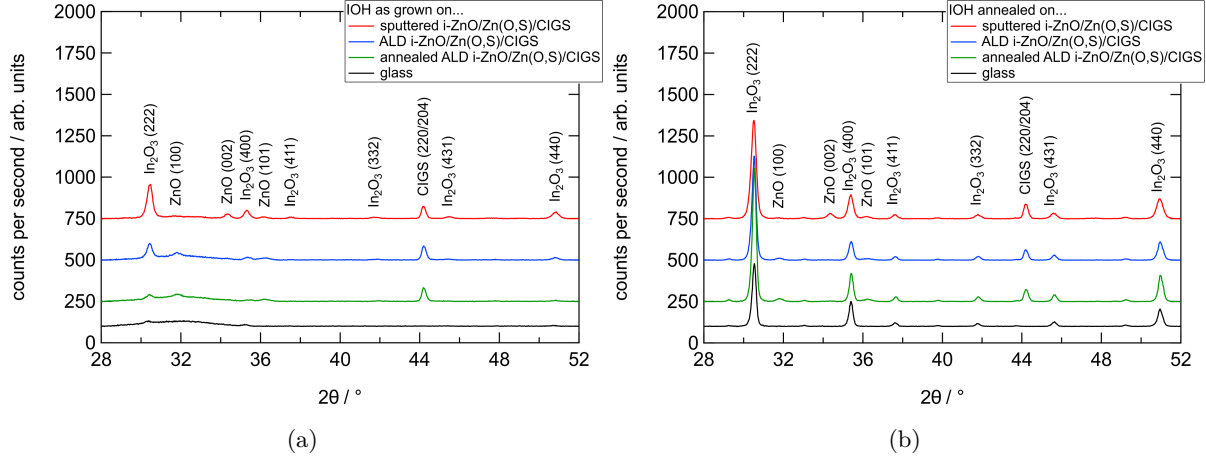


Figure 6.9: X-ray diffraction patterns of CIGS module samples with different window layer before (a) and after (b) annealing of the IOH films; IOH/glass is used as reference; reference patterns of  $\text{In}_2\text{O}_3$  were taken from PDF 00-006-0416, of ZnO from PDF 01-070-8070; patterns were shifted vertically for improved differentiation

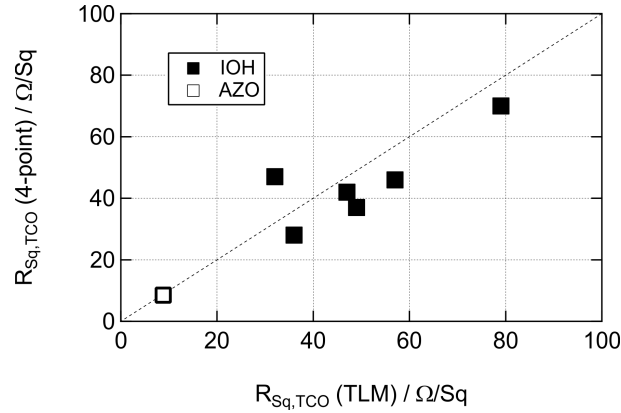


Figure 6.10: Correlation of the TCO sheet resistance on CIGS samples determined by transmission line (TLM) and by 4-point measurements

respectively, in otherwise the same layer configuration. By applying the as grown IOH, a gain of almost  $3 \text{ mA/cm}^2$  in  $j_{sc}$  was achieved while the open circuit voltage was not influenced. A major disadvantage of the modules with IOH was the significantly lower FF and high series resistance which was affecting the efficiency. As described in section 2.2, the series resistance depends on the TCO sheet resistance. Following the work of Hoppe et al. [180] we defined an effective TCO sheet resistance  $R_{eff,TCO}$ , which determines the contribution of the TCO sheet resistance  $R_{Sheet,TCO}$  to the total series resistance:

$$R_{eff,TCO} = \frac{R_{Sheet,TCO} \cdot l}{3w} \quad (6.5)$$

Table 6.6: Overview over the module properties determined by j-V measurements; series resistance of the module was determined by fits of the dark curves (2 diode model) and the sheet resistance of the samples, determined by TLM and 4 point measurements

Sample	$j_{sc}$ (mA/cm <sup>2</sup> )	$V_{oc}$ (V/cell)	$FF$ (%)	$\eta$ (%)	$R_{S,Module}$ ( $\Omega$ )	$R_{Sq,TLM}$ ( $\Omega/Sq$ )	$R_{Sq,4-point}$ ( $\Omega/Sq$ )
M1	32.7	0.492	59.5	9.6	8.6	8.8	8.5
M2	35.5	0.490	35.2	6.1	29.4	-	-
M3	24.4	0.299	27.9	2.0	50.2	57	46
M4	34.4	0.466	33.2	5.3	30.1	79	70
M5	37.1	0.435	42.3	6.8	12.4	53	37
M6	36.1	0.405	33.3	4.9	17.9	47	42
M7	38.4	0.495	44.7	8.5	12.3	36	28
M8	31.9	0.459	42.2	6.2	17.0	32	47
M9	-	-	-	-	-	-	12
M10	-	-	-	-	-	-	10

where  $l$  is the cell length and  $w$  the cell width. To calculate the total contribution of the TCO  $R_{S,TCO}$  to the series resistance in a module  $R_{S,Module}$  the effective sheet resistance  $R_{eff}$  is multiplied by the amount of cells connected in series  $N_s$ :

$$R_{S,TCO} = N_s \cdot R_{eff,TCO} \quad (6.6)$$

Figure 6.11 (a) presents the change of the modules series resistance  $R_{S,Module}$  over the determined contribution of the TCO  $R_{S,TCO}$  for modules with IOH and AZO front contact. For this calculation the sheet resistance determined by TLM was used. The dashed line represents equal values of  $R_{S,Module}$  and  $R_{S,TCO}$  for improved visualization. The lowest  $R_{S,TCO}$  and  $R_{S,Module}$  were determined for the AZO reference module. The results indicate, that the increased  $R_{S,Module}$  results almost exclusively from the increased  $R_{S,TCO}$ . An exception occurs for module *M3* (non-annealed IOH with sputtered Zn(O,S) buffer), here a significantly higher  $R_{S,Module}$  is observed. Therefore an additional major contribution to  $R_{S,Module}$  is assumed for this module. Additionally a significantly low open circuit voltage and short circuit current density were measured for this module. Note that other contributions to the module series resistance, e.g. contact resistance, Mo-resistivity, have to be taken into account. Therefore, the real module series resistance is  $> 0$  even for negligible TCO sheet resistance ( $R_{S,TCO} = 0$ ). The fill factor  $FF$  is known to depend on the series resistance, as described in equation (2.34) in section 2.2. Thus, with increased  $R_{S,TCO}$  also a drop of the fill factor occurs, as presented in Figure 6.11 (b). The dashed line estimates the calculated FF loss caused by the TCO resistance, according to equations (2.34) and (2.35).

The AZO module was taken as reference. It is apparent, that the experimental FF values are lower than the calculated values. Thus additional losses can be assumed, i.e., in the modules with the ID *M3*, *M6* and *M8* (see Table 6.5 and 6.6). The contact resistance, determined by TLM measurements, of modules with IOH and AZO were quite similar. The shunt resistance of the modules with IOH were approx. in the same range as the shunt resistance of the AZO module. Thus the IOH front contact had no influence on the shunt resistance.

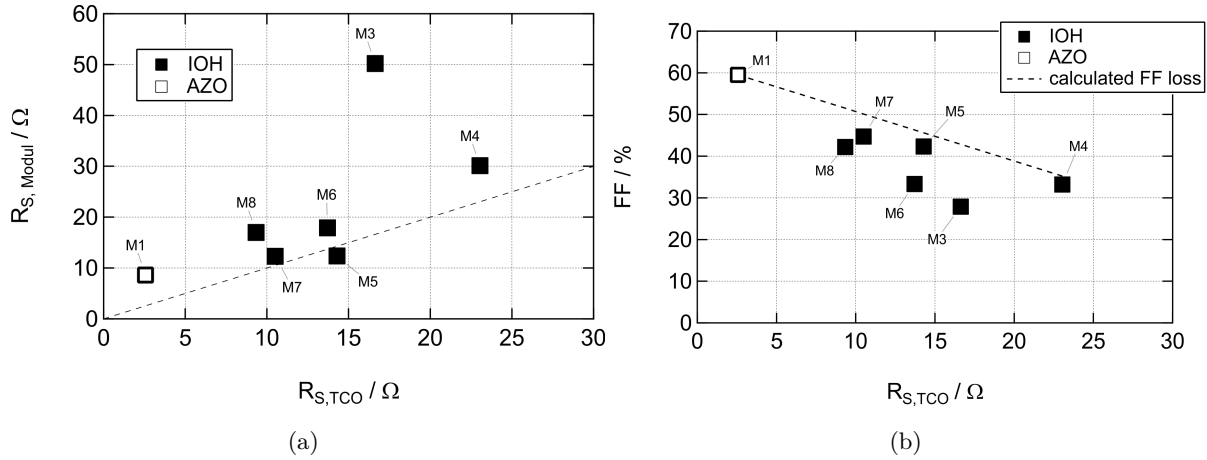


Figure 6.11: Correlation of the measured module series resistance (a) and fill factor (b) with the contribution of the TCO sheet resistance to the total module series resistance; the dashed line in (b) indicates the calculated FF loss caused by increased  $R_{S, TCO}$

The results support the findings discussed in sections 5.1 and 5.3, as again a dependency of the crystalline fraction of as grown IOH on the sublayer, here ZnO, was found. The IOH film grown on sputtered ZnO showed a higher crystalline fraction than the film on bare glass. The crystalline fraction of IOH films decreased when the films were deposited on ALD - ZnO. We assume that this is due to the different structure of the ZnO films, as the deposition technique of the ZnO layer influences its growth, structure and preferred orientation. Surprisingly, the crystalline fraction of IOH further decreased, when deposited on a pre annealed ALD - ZnO sample. We assume that the annealing may improve the grain quality of the ZnO films and lead to an increase of the grain size on the film surface. For the deposition by ALD  $H_2O$  is used as the precursor for the oxygen component. Therefore it is likely, that hydrogen or water molecules are incorporated in the films. The annealing may mobilize hydrogen and lead to its diffusion on the film surface, where it supports amorphous growth of the IOH film. Also in other experiments a lower crystalline fraction of as grown IOH and a consequently lower resistivity was found for IOH films which were grown on annealed ALD ZnO films compared to films grown on non-annealed ALD ZnO films. However, to fully understand this effect, further investigations are needed. The increased crystallinity of the as grown IOH films resulted in an increased sheet resistance, confirmed by both TLM and 4-point measurements. By the 4-point probe method

the resistance of the whole multilayer compound is measured, therefore an influence of the IOH sub-layers can not be excluded. However, as the conductivity of the IOH thin film is significantly higher than that of intrinsic ZnO or other sub-layers, we assume that the current mainly flows through the TCO layer rather than the sub-layers. Therefore we assume that the effect of the sub-layers during 4 point probe measurements is negligible. This is supported by the fact, that the determined values are similar to those measured by TLM. The increased sheet resistance resulted in an increased module series resistance and decreased fill factor. Although a mainly amorphous structure of the as grown IOH was found for module M7, the IOH sheet resistance was still higher than that on glass, which showed a comparable mainly amorphous structure. This raise in sheet resistance can be likely explained by the formation of voids/cracks, as described in section 5.3. Annealing of the samples after IOH deposition led to solid phase crystallization and to changes of the electronic properties of the IOH thin films. According to the 4-point probe measurements the IOH sheet resistance was higher after annealing when the films were deposited on CIGS samples. In contrast, a lower sheet resistance was determined when the films were deposited on glass substrates. Measurements by TLM revealed contrary results. Here a decrease of the sheet resistance after annealing was found for the IOH films which were deposited on ALD ZnO layers. However, the improvement was not sufficient, the poor efficiency was still determined by the low fill factor caused by the increased series resistance due to the high IOH sheet resistance.

Furthermore, the correspondingly low performance of module M3 can not only be attributed to a high TCO sheet resistance. For this module additionally to the low  $FF$  a major drop in  $j_{sc}$  and  $V_{oc}$  occurs. We relate this to a high acceptor defect density at the CIGS/Zn(O,S) interface, which might be caused by sputter damage [181]. Annealing of the sample after TCO deposition seems to reduce the acceptor defect density at the interface, resulting in a improved module performance.

The module efficiency was limited mainly by the high IOH sheet resistance, caused by an pronounced crystalline growth and/or presumably crack formation in the IOH layer. As discussed in section 5.3 voids or cracks in the IOH layer result in a poor electron mobility and thus a high sheet resistance. Therefore, to increase the IOH module efficiency, the electrical properties of the IOH layer, especially the electron mobility need to be improved. In section 5.4 strategies for improved IOH electron mobility on CIGS samples are presented. In the following these strategies are applied in CIGS solar cells and modules to evaluate their usability.

*The main findings can be summarized as follows:*

- A high  $\text{In}_2\text{O}_3\text{:H}$  sheet resistance limits the fill factor and therefore the efficiency of CIGS solar modules. The increased sheet resistance was caused by pronounced crystalline growth

on poly-crystalline ZnO sub-layers as well as by a high void/crack density when grown on CIGS with sharp structures.

## 6.3 Application of strategies for improved TCO electron mobility in CIGS solar cells

The last section pointed out, that unfavorable growing conditions of  $\text{In}_2\text{O}_3\text{:H}$  directly on the CIGS samples can result in high sheet resistances, high series resistances and therefore in limitation of the fill factor and module efficiency. The main goal is consequently to improve the sheet resistance of the TCO when grown on the CIGS samples. In section 5.4 three possibilities were presented, i.e., deposition of a spin coated sub-layer, etching of the CIGS absorber and significant increase of the film thickness. In this section we now investigate the applicability of these strategies into working devices.

### 6.3.1 Spin Coated Sol-Gel Layer

A spin coated sol-gel layer deposited on CdS buffered CIGS samples results in a smoother surface and an improved IOH electron mobility, as described in section 5.4.1. However, this procedure is only reasonable, if it does not adversely affect the solar cell properties. Figure 6.12 shows box plots of the characteristic  $j$ - $V$  values of 8 CIGS solar cells (CIGS by multi-source process), each with different highly resistive layers:  $i$ -ZnO as reference or spin coated  $\text{Ga}_x\text{O}_y$  layers, deposited multiple times, as described in section 3.1.2. The  $j$ - $V$  curves of the best cells are presented in Figure 6.13, the corresponding solar cell parameters are summarized in Table 6.7. The  $\text{Ga}_x\text{O}_y/\text{CdS}/\text{CIGS}$  samples are identical to the ones described in section 6.3.1. For all samples as-grown IOH (approx. 500 nm thick) was used as front contact. The observed trend of the cell properties is the same for the best cell and the average value, thus the properties of the best cells are discussed. The highest efficiency was achieved with the  $i$ -ZnO reference sample. Note that the CIGS deposition process is slightly inhomogeneous, the sample taken from the central position was found to show the highest  $V_{oc}$  and efficiency. The  $i$ -ZnO reference CIGS sample was fabricated on such a position. Replacing the  $i$ -ZnO layer with  $\text{Ga}_x\text{O}_y$  leads to deterioration of the solar cells with increasing amount of  $\text{Ga}_x\text{O}_y$  depositions and  $\text{Ga}_x\text{O}_y$  thickness, respectively, as a decrease in  $j_{sc}$ ,  $V_{oc}$  and  $FF$  was observed. With increased  $\text{Ga}_x\text{O}_y$  amount the series resistance increases significantly, while the parallel resistance drops. The  $j$ - $V$  curve of the sample "6x $\text{Ga}_x\text{O}_y$ " revealed a roll over effect, indicating a barrier for the diode current [76], caused by acceptor states or a positive conduction band offset at buffer/window interface, respectively. However, the sample processed with 1x $\text{Ga}_x\text{O}_y$  showed properties similar

to the reference cell. It can not be excluded, that the improved performance of the i-ZnO cell is due to the most favorable position during CIGS deposition.

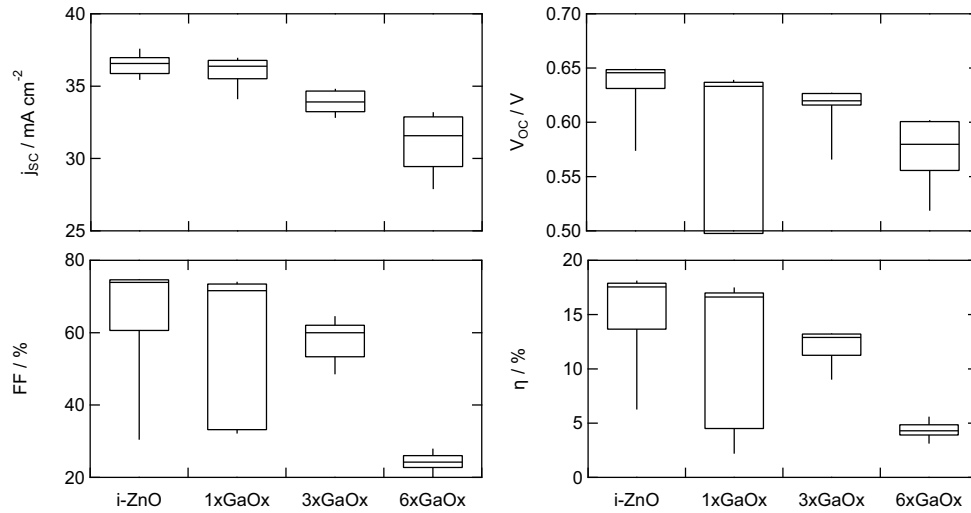


Figure 6.12: Box plots of characteristic properties of solar cells with different highly resistive layers: spin coated  $Ga_xO_y$ , deposited several times and i-ZnO in combination with as grown IOH as front contact on CdS buffered CIGS samples; 8 solar cells each

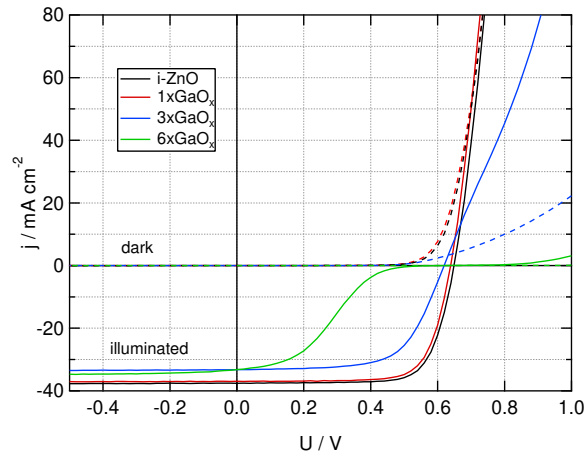


Figure 6.13:  $j$ - $V$  curves of solar cells with spin coated  $Ga_xO_y$ , deposited several times and i-ZnO as highly resistive (HR) layers

Based on these results CIGS modules with CdS/ $1xGa_xO_y$ /IOH were produced and compared with a CdS/i-ZnO/AZO reference module, before and after 2 h of light soaking. The  $\approx 580$  nm thick IOH film was deposited without intentional heating, after deposition the module was annealed in vacuum at  $\approx 180$  °C for 1 h. The  $\approx 865$  nm AZO film was deposited at  $\approx 165$  °C substrate temperature. The  $j$ - $V$  curves of the modules are shown in Figure 6.14, the characteristic values of the modules as cell equivalent are summarized in Table 6.8.

Table 6.7: Parameters of the best CIGS solar cell with spin coated  $\text{Ga}_x\text{O}_y$ , deposited several times and i-ZnO as highly resistive (HR) layers and IOH as front contact; fits were conducted for dark curves with a two diode model (see section 2.2.2)

HR-layer	TCO	$j_{sc}$ ( $\text{mA}/\text{cm}^2$ )	$V_{oc}$ (V)	$FF$ (%)	$\eta$ (%)	$R_s$ ( $\Omega\text{cm}^2$ )	$R_p$ ( $\text{k}\Omega\text{cm}^2$ )
i-ZnO	IOH	37.6	0.649	74.3	18.1	0.46	11.0
1x $\text{Ga}_x\text{O}_y$	IOH	37.0	0.639	74.1	17.5	0.53	32.1
3x $\text{Ga}_x\text{O}_y$	IOH	33.2	0.620	64.5	13.3	15.9	73.4
6x $\text{Ga}_x\text{O}_y$	IOH	33.2	0.602	28.0	5.6	6998	133.0

By implementing  $\text{Ga}_x\text{O}_y/\text{IOH}$  instead of i-ZnO/AZO as window layer, a gain in  $j_{sc}$  of  $\approx 2 \text{ mA}/\text{cm}^2$  was realized. In addition, the sample exhibits a 23 mV higher open circuit voltage before light soak. After light soak<sup>3</sup> the voltage of the i-ZnO/AZO module dropped surprisingly by 43 mV while the  $V_{oc}$  of the  $\text{Ga}_x\text{O}_y/\text{IOH}$  module decreases only by 4 mV. Also the FF of the i-ZnO/AZO module decreased after light soaking, while it increased in the  $\text{Ga}_x\text{O}_y/\text{IOH}$  module. The short circuit current density, however, slightly dropped in both modules after light soak. Nevertheless, these effects result in a higher efficiency of the module with  $\text{Ga}_x\text{O}_y/\text{IOH}$  of  $\Delta\eta = 1.1 \%$  before light soak and  $\Delta\eta = 2.7 \%$  after light soak. Note that the series resistance of the i-ZnO/AZO is  $2.3 \Omega$  before and after LS while the series resistance of the  $\text{Ga}_x\text{O}_y/\text{IOH}$  module decreased from  $4.4 \Omega$  to  $2.7 \Omega$ . Thus after LS similar series resistances for both module configurations were achieved.

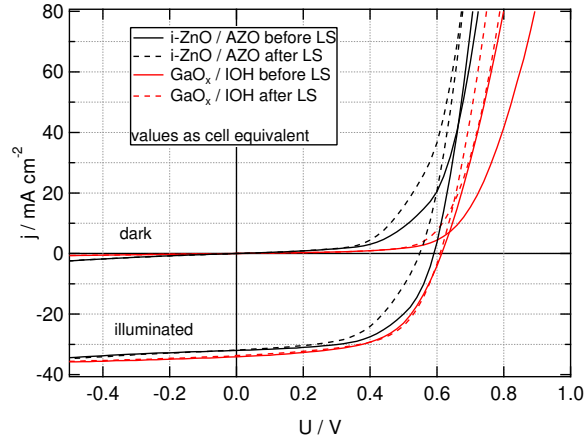


Figure 6.14:  $j$ - $V$  curves of modules with CdS/i-ZnO/AZO and CdS/ $\text{Ga}_x\text{O}_y/\text{IOH}$  window, respectively, before and after 2 h light soak (average values per cell)

<sup>3</sup>as mentioned in section 3.1.2 light soaking was a common procedure for CIGS devices and was performed for several modules within this thesis

Table 6.8: j-V parameter of modules with CdS/i-ZnO/AZO and CdS/Ga<sub>x</sub>O<sub>y</sub>/IOH window, respectively, before and after 2 h light soak;  $R_s$  was fitted with a 2 diode model for the dark curves

LS	HR-layer/TCO	$j_{sc}$ (mA/cm <sup>2</sup> )	$V_{oc}$ (V/cell)	$FF$ (%)	$\eta$ (%)	$R_s$ ( $\Omega$ )
before	i-ZnO/AZO	32.0	0.591	58.7	11.1	2.3
after	i-ZnO/AZO	31.9	0.548	55.7	9.7	2.3
before	Ga <sub>x</sub> O <sub>y</sub> /IOH	34.1	0.614	58.1	12.2	4.4
after	Ga <sub>x</sub> O <sub>y</sub> /IOH	33.7	0.610	60.2	12.4	2.7

The results show that application of a thin Ga<sub>x</sub>O<sub>y</sub> film (1 spin coat deposition) as the highly resistive layer leads to working solar cells and modules. Thicker Ga<sub>x</sub>O<sub>y</sub> layers smoothen the surface and gradually improve the electron mobility of IOH as reported in section 5.4.1, but lead to the formation of a barrier in the solar cells, which could be reduced after light soaking. We assume that the light soak did not affect the IOH layer or i-ZnO/AZO layers, as here no effect on the series resistance due to light soak was observed. Gallium oxide has a high optical band gap over 4 eV, depending on the O/Ga ratio [120, 182]. This is higher than the band gap of 3.3 eV for ZnO. Thus the Ga<sub>x</sub>O<sub>y</sub> layer has furthermore the potential to transmit more photons with higher energies to the absorber layer and consequently to reduce parasitic absorption in the blue optical region. Heinemann et al. [182] reported, that oxygen vacancy  $V_O$  donor states in Ga<sub>x</sub>O<sub>y</sub> cause defect bands below the conduction band maximum. Thus, a low (high) oxygen deficiency resulted in a high (low) optical band gap, correlated with a low (high) electron affinity. A low electron affinity can lead to a high barrier in the conduction band maximum at the Ga<sub>x</sub>O<sub>y</sub>/CdS interface. We assume that the deposited Ga<sub>x</sub>O<sub>y</sub> films have a low amount of  $V_O$ , as the films exhibit a very low conductivity, presumably resulting from a low charge carrier density. Moreover we assume that if a high density of  $V_O$  were present in the film, the charge carrier density and thus the conductivity would be higher. Additionally no optical band gap in the range below 5 eV was observed in spin coated Ga<sub>x</sub>O<sub>y</sub> films deposited on quartz glass (not shown). We assume that the 1xGa<sub>x</sub>O<sub>y</sub> layer is thin enough to allow tunneling or that the CIGS sample is not fully covered, yet. With increased deposition amount the layer thickness increases, resulting in a barrier for the passing current and the observed increase of the series resistance. By choosing a more conductive material with a suitable electron affinity or by induce  $V_O$  deep donor bands in Ga<sub>x</sub>O<sub>y</sub> the barrier might be reduced leading to working solar cells even with thicker spin coated sol-gel layers and without a the need of a light soak. However, the CIGS absorber might be damaged by the annealing process in air (200 *degree*C) of the sol-gel deposition procedure. Nevertheless, the combination of a thin (1 deposition) Ga<sub>x</sub>O<sub>y</sub> layer, which slightly smoothed the CIGS sample surface, and a thick (500 nm) annealed IOH layer resulted in a working module with an efficiency higher than that of the i-ZnO/AZO reference module. We assume that the increased IOH thickness was beneficial, since voids might coalesce at higher thicknesses, as discussed in

section 5.4.3. Therefore a respectively low series resistance and high fill factor was achieved with  $\text{Ga}_x\text{O}_y/\text{IOH}$ . A further approach might be the modification of the sol-gel layer, as described above, to realize working solar cells with thicker sol-gel layers, which additionally provide a smooth sample surface. This configuration allows the deposition of IOH with reasonable electron mobilities, without the formation of voids and cracks in the layer, as discussed in section 5.4.1. This further improvement of the IOH layer might enable a reduction of the film thickness to achieve reasonable sheet resistances  $< 10 \text{ } \Omega/\text{Sq}$  of IOH films on CIGS samples.

*The main findings can be summarized as follows:*

- Working devices can be realized with thin spin coated sol-gel  $\text{Ga}_x\text{O}_y$  layers. For the  $\text{In}_2\text{O}_3:\text{H}/\text{Ga}_x\text{O}_y$  configuration an improved CIGS module efficiency compared to the standard  $\text{i-ZnO}/\text{AZO}$  configuration was achieved.

### 6.3.2 Etched CIGS

As described in section 5.4.2 the CIGS surface can be smoothed by etching in a acid bromine solution which results in an improved electron mobility of hydrogen doped indium oxide grown on  $\text{i-ZnO}/\text{CdS}/\text{etched CIGS}$ . However, the etching in acid bromine solution followed by a KCN treatment changes the surface properties of the CIGS film. This might lead to poor solar cell performance. Therefore we investigate the potential of the etched CIGS samples described in section 5.4.2 as solar cells (CIGS deposited by multi-source process).

Figure 6.15 shows the  $j$ - $V$  curves (a) and the external quantum efficiency (b) of the samples. Table 6.9 summarizes the determined solar cell parameters. The improved electrical properties of the  $\text{In}_2\text{O}_3:\text{H}$  layer with increased etching duration (see section 5.4.2) result in a decreased series resistance, estimated by a two-diode fit of the dark  $j$ - $V$  curve. The current - voltage measurements revealed further that the short circuit current density slightly decreases from  $32.6 \text{ cm}^2/\text{Vs}$  to  $31.1 \text{ cm}^2/\text{Vs}$  with increased etch duration. This was confirmed by EQE measurements where the overall values were slightly lower. The loss occurs mainly in the range of around 700 nm to 1000 nm. The open circuit voltage was found to increase with increased etching duration. After 15 s of etching an increase of almost 30 mV could be observed. For a prolonged etch duration up to 60 s the  $V_{oc}$  increased only slightly by another 10 mV. Also the fill factor was found to improve from 73 % to 75 % after 60 s of etching. As a result the efficiency improved from 14.9 % for the non-etched reference up to 15.7 % for all etched samples. Due to the compensation of decreased  $j_{sc}$  but increased  $V_{oc}$  for increased etch duration the efficiency within the etched samples did not change.

We studied this unexpected effect of etching on cell performance, in particular on the  $V_{oc}$ , in more detail using CV to evaluate the doping profile of the etched samples. Figure 6.16 shows the doping profile of the etched samples after CdS deposition. The carrier concentration at  $V = 0$  V of the non etched reference is approx.  $8.0 \times 10^{14} \text{ cm}^{-3}$ . After 15 s of etching a decrease down to  $5.8 \times 10^{14} \text{ cm}^{-3}$  occurs. However, a longer etching time improves the carrier concentration up to  $1.7 \times 10^{15} \text{ cm}^{-3}$ .

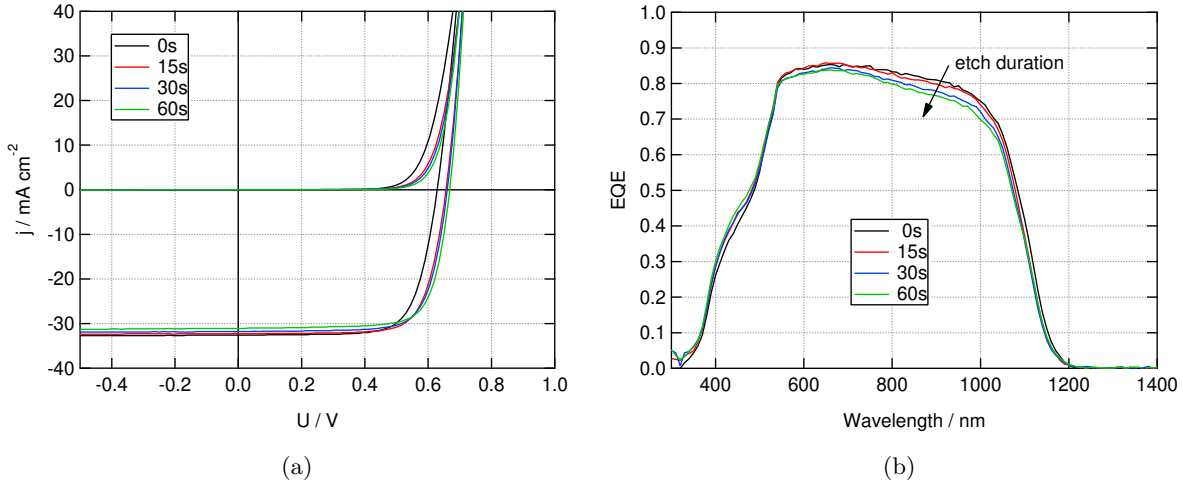


Figure 6.15: j-V (a) and EQE (b) curves of the etched CIGS samples with CdS/i-ZnO/IOH window layer in the as grown state

Table 6.9: Solar cell parameters of etched CIGS samples with as-grown IOH front contact;  $R_s$  and  $R_p$  were fitted with a 2 diode model for the dark curves

Etch (s)	$j_{sc}$ (mA/cm <sup>2</sup> )	$V_{oc}$ (V)	$FF$ (%)	$\eta$ (%)	$R_s$ ( $\Omega\text{cm}^2$ )	$R_p$ (k $\Omega\text{cm}^2$ )
0	32.6	0.628	73	14.9	1.03	25.660
15	32.3	0.656	74	15.7	0.62	18.99
30	31.8	0.660	75	15.7	0.42	12.31
60	31.1	0.668	75	15.7	0.36	9.06

The data shows that the solar cell performance was improved by the etching procedure, mainly by an increase of the  $V_{oc}$  up to 40 mV. It is known from literature that increased net acceptor density in polycrystalline  $\text{Cu}(\text{In,Ga})\text{Se}_2$  can improve the open circuit voltage [183]. However, the large increase of  $\approx 30$  mV after 15 s of etching can not be explained by this, as the carrier concentration was found to slightly decrease. According to the CIGS 3-stage deposition process the top layer, which forms in the 3rd stage, might be of poor quality compared the the film, which forms in the second stage. Here the film re-crystallizes, resulting in reduced stress and crystallographic disorder (see section 3.1.2). By etching the CIGS absorber in a bromine solution

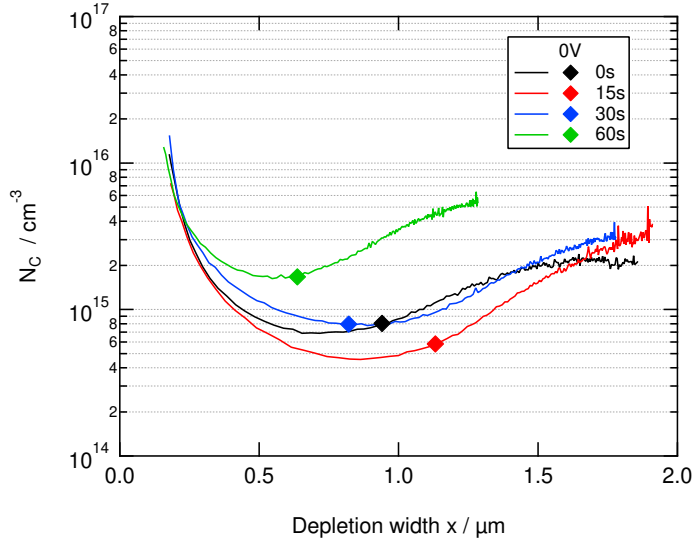


Figure 6.16: Doping profile (charge carrier concentration  $N_C$  versus depletion width  $x$ ) as calculated from CV-measurements from the etched CIGS samples

the low quality layer might be removed, resulting in an improved interface. This might be the cause of the improved open circuit voltage. The observed decreased short circuit current density of the bromine etched samples is likely due to reflection losses caused by smoothing of the surface, similar to the findings by Deprédurand et al. [149]. The actual reflection could not be measured, because the cell area was too small.

The results of this investigation show that by etching CIGS samples in an acid bromine solution in combination with a KCN treatment a capping layer with poor quality, according to the 3-stage deposition procedure, can be removed, which improved the solar cell performance of the samples. Additionally in section 5.4.2 it is shown that this process smoothed the surface and results in an improved electron mobility of the hydrogen doped indium oxide layer which were deposited on the ZnO-coated CdS/CIGS samples. However, no improvement of the  $j_{sc}$  was obtained due to the CIGS etching.

*The main findings can be summarized as follows:*

- Etching of CIGS absorber with an acid bromine solution improved the solar cell efficiency. This results most likely by the removal of absorber material of poor quality from the absorber surface.
- Improved electrical properties of  $\text{In}_2\text{O}_3\text{:H}$  on etched samples (see section 5.4.2) led to improved series resistances in the solar cells.

### 6.3.3 Increase of TCO thickness

An increased thickness of the IOH film can improve its electron mobility on CIGS samples as shown in section 5.4.3. However, an increased film thickness results in an increase of parasitic optical absorption and can decrease the short circuit current density in solar cells. We investigated therefore the usability of IOH front contacts with thicknesses in the range of approx. 450 nm to 750 nm in CIGS modules with Zn(O,S) as buffer layer and highly resistive layer and compared them to modules with AZO front contact. The CIGS absorber layer was deposited by a sequential process at AVANCIS. After IOH deposition the modules were annealed in vacuum at  $\approx 180$  °C for 1 h. As a reference one non-annealed module with 550 nm IOH was fabricated. Based on the results presented in section 5.4.3 we assumed an improvement of the series resistance with increased IOH thickness. However, CIGS samples with the present configuration and roughness were not studied before and can therefore result in unexpected results, as for this CIGS absorber a rather round-shaped grain structure with smooth surfaces is assumed. In fact, for this configuration an IOH thickness of 450 nm was sufficient to achieve series resistances as low as  $1.1 \Omega\text{cm}^2$ . Figure 6.17 presents the characteristic module parameters of the samples as cell equivalents, before and after light soaking. In the following the results are discussed in more detail.

After light soak the short circuit current density of the annealed IOH module is  $\approx 1.4 \text{ mA/cm}^2$  higher than the non-annealed reference module, indicating solid phase crystallization due to the annealing. Within the annealed IOH modules no trend in  $j_{sc}$  was observed. However, the  $j_{sc}$  after light soaking improved by  $\approx 0.5 \text{ mA/cm}^2$  when annealed IOH was applied as front contact instead of AZO. Modules with the annealed IOH showed average fill factors of  $\approx 67.7 \%$ , higher than the best FF of the AZO module with 64.8 %. The high FF results from the low series resistance of  $\approx 1 \Omega\text{cm}^2$  for the modules with annealed IOH, regardless of the IOH film thickness. No dependence was found between the shunt resistance and the variation of the front contact. However, a drop in  $V_{oc}$  was observed in the modules which were fabricated with IOH front contact, more pronounced in the annealed IOH modules after light soak. The efficiency of the best AZO reference module after light soak was 14.5 %. The best IOH modules after light soak (750 nm) had an efficiency of 14.3 % and before light soak (650 nm) 14.5 %.

The results show again that an IOH front contact can improve the short circuit current density in CIGS modules compared to an AZO reference. No adverse effect in  $j_{sc}$  was found with increased IOH thickness due to parasitic optical absorption. We assume that this effect results from a shift of the interference fringes to more favorable wavelengths, which counteracts absorption losses of the reflection spectra due to changes of the film thickness. This might result in a configuration most favorable for the module with 750 nm IOH, although the highest parasitic absorption and thus the lowest  $j_{sc}$  is expected. In the IOH modules the fill factor was not significantly limited

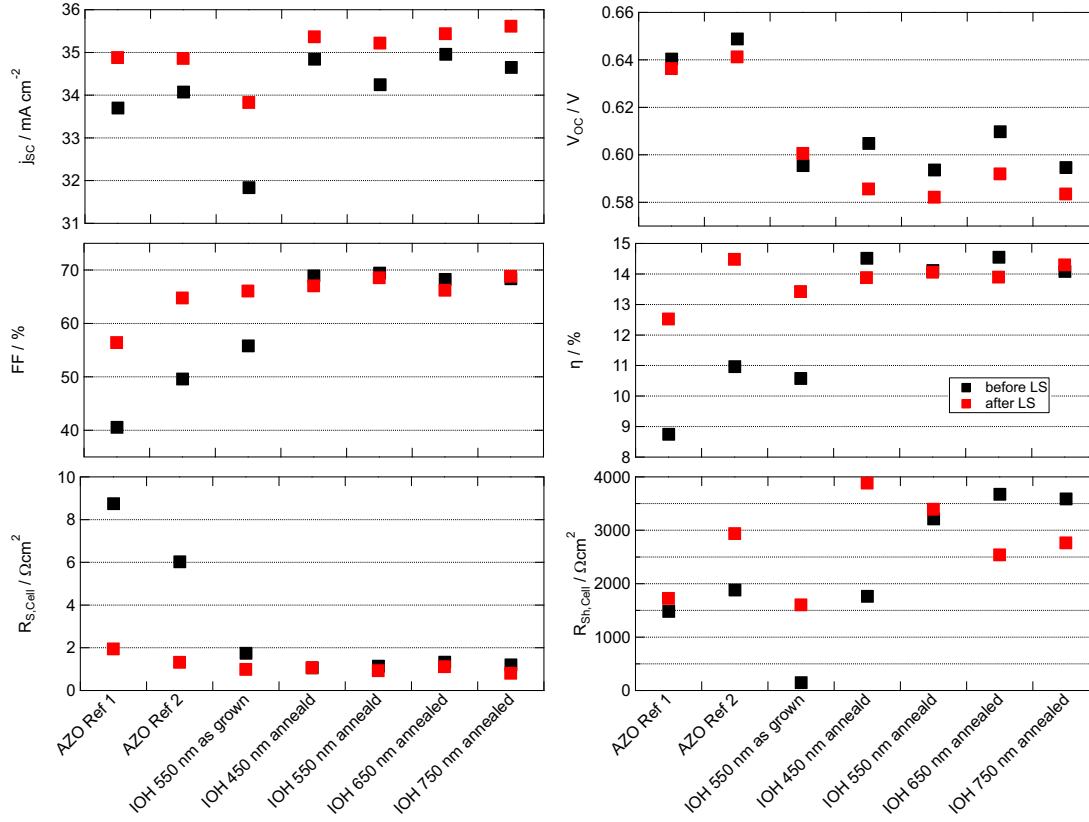


Figure 6.17: J-V parameter as cell equivalent of CIGS modules with different TCO configurations before (black) and after (red) light soaking

by the series resistance, as it is the case in the AZO reference modules. However, no dependence of the series resistance on the IOH film thickness was found, thus we assume that the TCO sheet resistance was similar for the annealed IOH films, although a low sheet resistance is expected for thicker films. This can be caused by the following: during deposition films are heated by plasma irradiation, which can induce crystalline nuclei in the films. With continued film deposition, these nuclei induce a crystalline phase in the newly deposited material, leading to an total increased crystalline fraction and to strain in the films. This deteriorates the electrical properties, limiting improvement of the sheet resistance at high film thicknesses [184].

The drop in  $V_{oc}$  was observed for the annealed as well as the non-annealed IOH modules, thus it can not be explained by deterioration of the absorber during annealing. We assume that the Zn(O,S) buffer layer might react with -OH or -H in the plasma during deposition of the first IOH layers. This could lead to changes in the Zn(O,S) composition and the formation of Zn(O,S,OH). Changes in composition can lead to unfavorable band alignments and recombination currents at the interface [185] lowering the open circuit voltage, similar to the observed results. However, no  $V_{oc}$  drop was observed by Steigert et al. [71] in CIGS cells with Zn(O,S)/IOH window.

*The main findings can be summarized as follows:*

- Thick  $\text{In}_2\text{O}_3\text{:H}$  did not reduce the short circuit current density in CIGS modules, probably due to shifts of reflection fringes.
- For this configuration a low series resistance and reasonable fill factor was achieved with annealed  $\text{In}_2\text{O}_3\text{:H}$ , also at film thicknesses of 450 nm.
- Similar module efficiencies could be achieved with  $\text{In}_2\text{O}_3\text{:H}$  and  $\text{ZnO:Al}$  front contact.

## 6.4 Conclusion

The findings obtained in this chapter are summarized in the following Chart diagram (Figure 6.18).

In this section the applicability of indium oxide based TCOs as front contact in CIGS cells and modules was studied. For the successful implementation as a front contact several requirements have to be fulfilled. Two basic requirements are (i) a suitable band line-up between the TCO (here annealed IOH) and the highly-resistive layer (here i-ZnO) and (ii) the thermal stability of the cell due to annealing of the TCO films. In this study the band line-up of annealed, crystallized IOH and i-ZnO was measured. The conduction band offset was calculated to be  $\Delta E_{CBM} = (-0.234 \pm 0.2)$  eV. The large error results from the large uncertainty of the assumed  $\text{In}_2\text{O}_3$  band gap. However, numerical simulations revealed no adverse effect on the solar cell parameter for such conduction band offset. Thus we conclude that the band alignment of these two materials is suitable for photovoltaic applications. Annealing of IOH layers, which were deposited on CdS buffered CIGS samples resulted in degradation of the solar cell parameter. We assumed that this was due to a poor CIGS/CdS interface quality. To improve the thermal stability of the cells, we suggested two different strategies beside the improvement of the interface: (i) The deposition parameter of the indium oxide based TCOs has to be modified in such a way, that low crystallization temperatures can be realized. Annealing of such TCO layers and corresponding CdS buffered CIGS solar cells at 150 °C revealed no adverse effect. In fact, the solar cell properties improved. (ii) Substitution of the CdS buffer to thermally more stable buffers (e.g.  $\text{Zn(O,S)}$ ) results in an increased temperature process window during annealing. In fact, no degradation of  $\text{Zn(O,S)}$  buffered solar cells could be observed after annealing at 180 °C.

As the mentioned requirements were satisfied, the IOH films were applied as front contacts in CIGS modules. Indeed a gain of the  $j_{sc}$  (up to 2.8 mA/cm<sup>2</sup>) was observed for modules with IOH front contact in comparison to a module with AZO front contact. However, the fill factor was limited due to a high series resistance. It was shown, that the increase of the series resistance

results from an increased TCO sheet resistance, caused by void formation in the layer and partly also by pronounced crystalline growth. To improve the series resistance in modules therefore the electrical properties, i.e., the electron mobility of the indium oxide based TCOs has to improve. Thus the strategies for an improved TCO electron mobility on CIGS samples presented in section 5.4 were evaluated for their applicability: (i) The deposition of spin coated  $\text{Ga}_2\text{O}_3$  sol gel layers as highly resistive layers resulted in a barrier with increased  $\text{Ga}_2\text{O}_3$  thickness. However, modules with a thin layer showed reduced series resistances and improved fill factors and even higher efficiencies than a reference module with standard i-ZnO/AZO window. This demonstrated the potential of the application of spin coated amorphous layers as template for IOH deposition. (ii) Etching of the CIGS absorber led beside of the improved electron mobility of the IOH films also to an improved  $V_{oc}$  by up to 40 mV compared to a non-etched reference. The etched solar cells showed an overall improved efficiency by  $\approx 0.8\%$ . Additionally the series resistance of the cell was found to decrease while the fill factor increased. Thus, also this strategy is suitable for the application in CIGS solar cells. (iii) No beneficial effect was observed in modules when thick IOH films were deposited as front contact (450 nm to 750 nm). For the used CIGS absorber type (rather smooth/rounder shaped surface) already a thickness of 450 nm was sufficient to achieve series resistances of  $\approx 1 \Omega\text{cm}^2$ . The fill factor was also reasonable high. However, for the applied layer configurations a reduced  $V_{oc}$  was observed. In total, similar high module efficiencies could be achieved with IOH front contacts.

We can conclude, that IOH films have a high potential as front contact in modules, as gain in the short circuit density with reasonable fill factors was demonstrated. However, specific CIGS layer configuration and surface topography is required to for full beneficial effects.

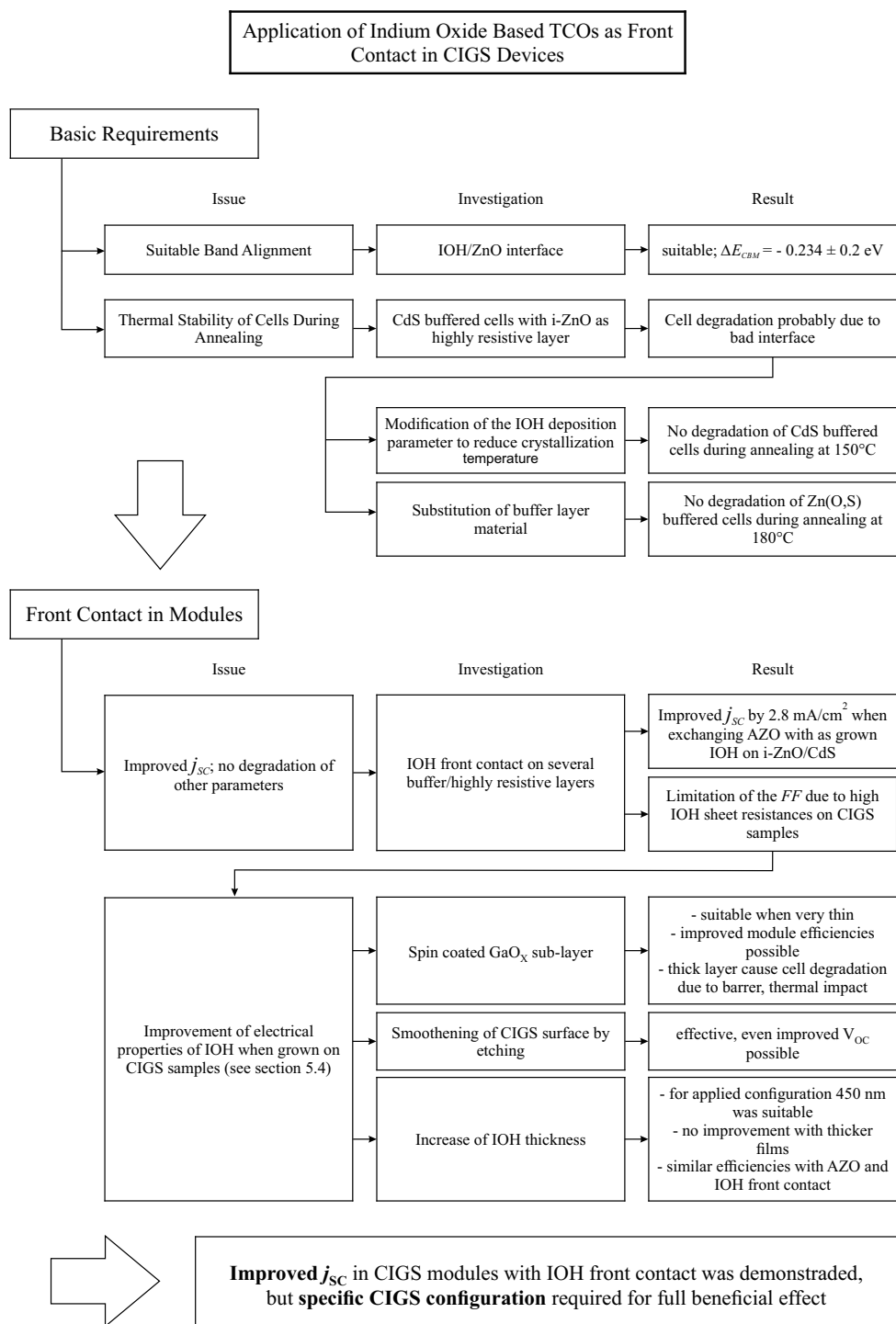


Figure 6.18: Main findings concerning the applicability of indium oxide based TCOs (i.e., In<sub>2</sub>O<sub>3</sub>:H, In<sub>2</sub>O<sub>3</sub>:H,W) as front contact in CIGS solar cells and modules

## CHAPTER 7

---

### Conclusions and Outlook

---

The topic of this thesis were new high-mobility transparent conductive oxides (TCOs) for the application as front contact in  $\text{Cu}(\text{In,Ga})(\text{S,Se})_2$  (CIGS) devices. For this hydrogen doped (and tungsten co-doped) indium oxide ( $\text{In}_2\text{O}_3:\text{H}$ ,  $\text{In}_2\text{O}_3:\text{H,W}$ ) thin films were investigated. The aim was to take advantage of the combined high transparency and low resistivity of these materials and to implement them as the front contact in CIGS solar cells and modules. The target was to improve the current collection and efficiency in CIGS modules and thus to reduce the relative losses with regard to CIGS solar cells. Moreover a successful implementation in modules requires a homogeneous large-scale process, which was developed in this thesis.

We successfully transferred the deposition process of  $\text{In}_2\text{O}_3:\text{H}$  to an in-line pulsed DC magnetron sputtering tool for thin film deposition on  $30 \times 30 \text{ cm}^2$  substrates. We achieved a homogeneous deposition with thickness variations of 2.1 %. The effect of the deposition parameter water vapor and oxygen partial pressure on the film properties was investigated. We observed, that compared to an RF sputtering process, the process window, depending on the pulse parameter during pulsed DC sputtering, might be more narrow for the water vapor supply when aiming for amorphous  $\text{In}_2\text{O}_3:\text{H}$  thin films. For a duty cycle of 96 % a pronounced crystalline growth was observed at  $p_{\text{H}_2\text{O}} = 0.2 \times 10^{-3} \text{ Pa}$ . Increased oxygen supply correlated well with reduction of the charge carrier density of the films, as oxygen vacancies are known to act as donors.

Furthermore the influences of the annealing atmospheres vacuum and air (220 °C 30 min) on the  $\text{In}_2\text{O}_3:\text{H}$  film properties were studied. We observed that both thermal treatments led to solid phase crystallization of the amorphous phase. Presumably due to diffusion of atmospheric species during annealing in air the charge carrier densities of those films was lower compared to films annealed in vacuum, resulting in an increased resistivity, a lower free carrier absorption in the near infrared region and a reduced Burstein-Moss shift of the optical band gap. A pronounced porous structure evolved after annealing of films deposited in high oxygen partial pressures, similar to

films deposited at high water vapor pressures. This resulted in an accelerated degradation of the electrical properties, i.e., the electron mobility, of the crystallized films in damp heat. To improve the charge carrier density and thus the conductivity of films after the annealing in air, we developed a bi-layered  $\text{In}_2\text{O}_3:\text{H}$  film with a thin (about 30 nm) partly crystalline cap layer, compared to the mainly amorphous bulk (about 160 nm). The cap-layer presumably counteracted diffusion of atmospheric species into the film during annealing in air and thus improved the charge carrier density of the films without significantly affecting the electron mobility or optical absorption of the films.

Implementation of the indium oxide based TCOs in CIGS devices requires their deposition on different sub-layers, which can affect the growth and properties of the TCOs. The poly-crystalline structure of i-ZnO was observed to promote crystalline growth of  $\text{In}_2\text{O}_3:\text{H}$  films, as revealed by X-ray diffraction measurements. This effect was observed on planar as well as on textured substrates, i.e., rough CIGS. The crystalline fraction of as-grown  $\text{In}_2\text{O}_3:\text{H}$  films increased with decreased ZnO grain size. Furthermore the preferred orientation of the films, as indicated by the texture coefficient, changed from (222) to (400) with increased crystallinity. The results indicate formation of crystalline nuclei especially at ZnO grain boundaries, presumably preferred in (400) orientation. In contrast,  $\text{In}_2\text{O}_3:\text{H}$ , deposited within the same deposition run on amorphous Zn(O,S) layers exhibit a mainly amorphous growth. The increased crystallinity after growth induced strain in the films and led to decreased charge carrier densities and mobilities, before, as well as after annealing. To suppress the crystalline growth of  $\text{In}_2\text{O}_3:\text{H}$  on poly-crystalline ZnO, the hydrogen supply during the growth of the first layers at the ZnO interface must be increased to facilitate the incorporation of hydrogen into the indium oxide film. However, this effect results in narrowing of the possible process window.

Residual water in sub-layers of  $\text{In}_2\text{O}_3:\text{H}$  affects the electrical properties of the TCO after annealing, presumably due to enhanced diffusion into the indium oxide layer and thus interference with the crystallization process. This effect was demonstrated with spin coated  $\text{In}_x\text{O}_y$  and  $\text{Ga}_x\text{O}_y$  sol-gel layers. Furthermore small crystallites within the spin-coated  $\text{In}_x\text{O}_y$  films promote crystalline growth of sputtered  $\text{In}_x\text{O}_x:\text{H}$  films, which were deposited on top, leading to poor electrical properties already after deposition. However, spin-coated  $\text{Ga}_x\text{O}_y$  films, which were pre-annealed at 200 °C provide a suitable template for the growth of amorphous  $\text{In}_x\text{O}_x:\text{H}$  films, which exhibit high electron mobility after annealing.

Furthermore the specific roughness of CIGS affects the growth and electrical properties of the indium oxide based TCOs  $\text{In}_2\text{O}_3:\text{H}$  and  $\text{In}_2\text{O}_3:\text{H,W}$ . Mainly amorphous  $\text{In}_2\text{O}_3:\text{H}$  films, grown on Zn(O,S)-coated CIGS samples, showed a reduced mobility with increased roughness.  $\text{In}_2\text{O}_3:\text{H}$  films that were grown on i-ZnO-coated Zn(O,S)/CIGS samples were partly crystalline and showed in addition to the decreased mobility also a reduced charge carrier density. The loss in electron

mobility was caused by the formation of voids inside the TCO film. As revealed by STEM and SEM measurements, the location of most of such voids could be correlated with CIGS grain boundaries. Spiky grain edges and sharp regressions induced void formation. The loss of the electron mobility could be correlated empirically with an increase of the RMS roughness by a linear regression. When compared to substrates with significantly changed topography, the loss of the electron mobility could be described more accurately by the ratio of the median local slope and the estimated grain size, as determined by the AFM measurement.

The slope of the linear regression was approximately equal for mainly amorphous grown and pronounced crystalline grown  $\text{In}_2\text{O}_3\text{:H}$  films, indicating that the increased crystalline fraction does not influence these observed losses or the formation of voids significantly. Solid phase crystallization did not lead to sufficient improvement of the electron mobility. In fact, the deficit in electron mobility was found to increase compared to reference films deposited on planar glass substrates. Thus we can conclude, that to achieve high-mobility indium oxide films on CIGS samples, the electron mobility has to be improved already in the as-grown state. No influence of the deposition parameters water vapor pressure and oxygen partial pressure as well as of the deposition rate on the limitation of the electron mobility by voids was observed. This was demonstrated for  $\text{In}_2\text{O}_3\text{:H,W}$  films, deposited by reactive plasma deposition and for  $\text{In}_2\text{O}_3\text{:H}$  films deposited by reactive plasma deposition and sputtering. However, the electron mobility of tungsten doped indium oxide films was found to be less affected when the films were grown on rough CIGS samples.

The degraded electrical properties of the TCOs on CIGS samples led to an increased sheet resistance and thus to an increased series resistance in CIGS modules, limiting the fill factor and efficiency.

Three strategies to minimize the observed losses in electron mobility in indium oxide films grown on CIGS samples were developed and applied to CIGS devices:

- Deposition of spin coated  $\text{Ga}_x\text{O}_y$  as the highly resistive layer smoothed the CIGS sample surface by covering spiky and sharp structures. This consequently improved the electron mobility to values equal to reference films deposited on planar glass substrates, although the CIGS samples showed still a RMS roughness of 50 nm. We demonstrated that by applying a thin  $\text{Ga}_x\text{O}_y$  layer as the highly resistive layer in CIGS modules in combination with  $\text{In}_2\text{O}_3\text{:H}$  front contact an improved  $j_{sc}$  by more than 2 mA/cm<sup>2</sup> and overall improved efficiency by more than 1 % can be achieved compared to a reference module with i-ZnO/ZnO:Al window. A potential barrier, induced by the  $\text{Ga}_x\text{O}_y$  layer was reduced significantly by light soaking.

- Etching of the CIGS surface with an acid bromine solution preferentially removes spiky structures. Consequently the electron mobility of  $\text{In}_2\text{O}_3\text{:H}$  deposited on the etched CIGS samples improved compared to films deposited on a non-etched reference. Corresponding solar cells with etched CIGS absorbers showed an improved  $V_{oc}$  and overall efficiency. Thus, etching of CIGS absorbers is an effective process for the improvement of the electron mobility of indium oxide TCOs on CIGS.
- At higher film thicknesses the grains may coalesce, thus leading to a less porous film. The electron mobility was observed to increase with higher thickness of the TCOs. The effect was more pronounced for films deposited by reactive plasma deposition than for the sputtered films. However, on rather smooth CIGS samples  $\text{In}_2\text{O}_3\text{:H}$  films with 450 nm thickness were sufficient to achieve a reasonable series resistance and fill factor in the respective CIGS module. Furthermore the  $j_{sc}$  of modules with  $\text{In}_2\text{O}_3\text{:H}$  front contact was higher than in the reference modules with  $\text{ZnO:Al}$  front contact.

Additionally the band alignment of crystallized  $\text{In}_2\text{O}_3\text{:H}$  and  $\text{ZnO}$  was evaluated by XPS/UPS measurements. We determined a valence band offset of  $\Delta E_{VBM} = (-0.78 \pm 0.06)$  eV and a conduction band offset of  $\Delta E_{CBM} = (-0.23 \pm 0.21)$  eV. Thus the conduction band of  $\text{In}_2\text{O}_3\text{:H}$  is energetically below the conduction band of  $\text{ZnO}$ . The large error resulted from the uncertainty of the assumed band gap of indium oxide. According to numerical calculations, such an offset has no negative influence on the solar cell properties, i.e. the fill factor.

The thermal treatment, which is required to initiate solid phase crystallization in the amorphous phase of indium oxide films can affect the properties of a corresponding solar cell. In particular CdS buffered solar cells were found to degrade due to annealing at temperatures above approx. 160 °C. With increased temperature the  $V_{oc}$  decreased due to reduction of the doping concentration of the CIGS absorber and the corresponding broadening of the depletion zone. However, we demonstrated that reduction of the required crystallization temperature to 150 °C did not lead to degradation of the CIGS solar cells with  $\text{In}_2\text{O}_3\text{:H}$  front contact. In fact, the solar cell parameters improved.

Substitution of the CdS buffer to a thermally more stable buffer, i.e.,  $\text{Zn(O,S)}$  led to more stable solar cells with  $\text{In}_2\text{O}_3\text{:H}$  front contact, no degradation of the solar cell parameter was observed after annealing at 180 °C. In fact, the efficiency improved. Moreover, an increased  $j_{sc}$  was demonstrated already prior to the annealing compared to a reference cell with  $\text{ZnO:Al}$  front contact.

The results show that by implementing high mobility indium oxide films as front contact in CIGS solar cells or modules, improved short circuit current densities and similar or even improved efficiencies compared to the corresponding reference samples can be achieved. To realize a

reasonable series resistance in CIGS modules, formation of voids in the amorphous grown TCOs needs to be avoided, e.g. by specific CIGS layer configurations.

### **Outlook**

Topics of future reasearch might be the development of additional stratagies for improved electron mobilities in indium oxide based TCOs grown on rough CIGS samples. Additionally sol-gel layers with improved conductivity might be beneficial for the application as highly resistive or buffer layers in CIGS solar cells in order to avoid the formation of a barrier while smoothing the CIGS sample surface.

Another topic might be detailed investigations of the stability of the pulsed DC magnetron sputtering process. Moreover the influence of the pulse parameters on the process stability and film properties needs to be analyzed.

# APPENDIX A

---

## Supplementary Information

---

### A.1 General description of standard characterization methods

In this section the standard methods, which were used to characterize the samples are described briefly.

#### Material characterization

##### *Spectral Ellipsometry (SE)*

With spectral ellipsometry the change of the optical polarization state of a electromagnetic wave can be described after linearly polarized light is reflected from a thin film sample. The change is determined by the ellipsometric angles  $\Psi$  and  $\Delta$ , which are related to the complex Fresnel reflection coefficients according to

$$\rho = \frac{r_P}{r_s} = \tan\Psi e^{i\Delta} \quad (\text{A.1})$$

where  $r_p$  and  $r_s$  are the Fresnel-reflection coefficients parallel and perpendicular to the plane of incidence.  $\tan\Psi$  represents the amplitude ratio between the parallel and vertical component,  $\Delta$  described the change in phase difference. By fitting the obtained data to a model, representing the sample, many film properties, such as the film thickness, optical constants and surface roughness can be determined.

*4 point probe*

The simplest way to measure the sheet resistance of a thin film is by 4 point measurements. 4 linearly aligned needles in equidistant distance are used. It is required that the distance between the needles is much smaller than the sample size, which is assumed to be infinite for simplicity. Current is applied through the two outer needles, the voltage is measured by the two inner needles. The sheet resistance is calculated by [19]

$$R_{Sq} = \frac{\pi}{\ln(2)} \frac{U}{I} \quad (\text{A.2})$$

*Hall effect measurements*

The film resistivity, charge carrier density and mobility can be extracted by measurements in the van der Pauw geometry. Four contact needles are set on the outer corner of the sample surface, the contacts must be small compared to the sample size. It is required that all sides of the sample are equal. For resistivity measurements current ( $I$ ) is applied at two contacts while voltage is measured via the two other contacts. This procedure is repeated in different sequences. From the followed Hall effect measurements the charge carrier density and mobility can be assessed. The basic principle is that a permanent magnetic field ( $B$ ) is applied perpendicular to the sample surface. Due to the Lorenz force moving charge carriers are forced transversely to the direction of movement, causing Hall voltage  $V_H$ . This procedure is repeated with altered polarity of the magnetic field. As a result the sheet carrier density ( $n_s$ ) can be calculated with

$$n_s = \frac{I_x B_y}{e V_H} \quad (\text{A.3})$$

where  $e$  is the carrier charge. With knowledge of the film thickness ( $d$ ) the charge carrier density can be assessed:

$$n = \frac{n_s}{d} \quad (\text{A.4})$$

The Hall mobility ( $\mu_H$ ) can be calculated with

$$\mu_H = \frac{1}{e n_s R_{Sq}} \quad (\text{A.5})$$

A detailed description of the measurement procedure can be found elsewhere [20, 186]. To obtain accurate results, the film must be homogeneous and without cracks. In multi-layered films all layers contribute to the measurements [187].

### *Glow Discharge Optical Emission Spectroscopy (GDOES)*

Glow Discharge Optical Emission Spectroscopy (GDOES) is a spectroscopic method for qualitative and quantitative analysis of the composition of materials. The cathode (sample) is set in an noble-gas environment and is bombarded by positive noble gas ions and atoms generated by an electrical discharge. Material of the sample is sputtered, partly ionized and excited to emit photons corresponding to characteristic spectral lines [95].

### *Transmission Electron Microscopy (TEM)*

Transmission Electron Microscopy (TEM) provides information on the structural properties on the nano and atomic scale. For such measurements uniformly thin samples are required to allow transmission of electrons. Lamellas of the specimen are typically prepared by conventional methods, such as mechanical dimpling and FIB. Thinning of the sample can induce damage or change the surface conditions.

### *Scanning Electron Microscopy (SEM)*

A scanning electron microscope (SEM) was used to image the sample with high magnifications. A focused electron beam scans the sample surface in high vacuum. To enable focusing of the beam, the sample surface must be conductive. The electrons are accelerated through an electric field towards the sample surface, where electrons are back-scattered or secondary electrons are released due to elastic and inelastic scattering. The electrons are imaged by detectors, therefore a high magnification of the sample surface can be realized. Images were taken in top view or cross section layout.

### *Electron Backscatter Diffraction (EBSD)*

Electron backscatter diffraction is a special form of electron microscopy. When an electron beam impinges a crystal located at the samples surface (which is tilted), backscattered electrons incident on lattice planes and are diffracted. The diffraction patterns (Kikuchi or EBSD pattern) provide information about the crystal orientation.

### *Photoelectron Spectroscopy*

XPS is a widely used surface analysis method based on the photoelectric effect and provides information of the surface composition. When X-rays with a defined energy  $h\nu$  ( $>1$  keV) impinge the sample surface, core electrons are excited and released from the atom. The kinetic energy

$E_{kin}$  of the electrons is measured by an electron detector. The electron binding energy  $E_B$  can be calculated as

$$E_B = E_{h\nu} - E_{kin} - \Phi_{spec} \quad (\text{A.6})$$

with  $\Phi_{spec}$  as the work function of the spectrometer. The electron binding energy depends on the specific element, electron orbital and chemical environment of the atom.

UPS is used to evaluate the valence band region. In contrast to XPS, ionizing radiation of a few eV is used to induce the photoelectric effect. Typically ultraviolet photons are produced by a gas discharge lamp filled with helium, resulting in energies of 21.2 eV (He I) (used in this study) and 40.8 eV (He II). More details concerning the methods can be found elsewhere [95, 121, 188].

#### *Atomic Force Microscopy*

Atomic force microscopy was used to evaluate the topography of the samples. In general either the height of the tip or the distance of tip/surface is held constant. The distance between the tip and the surface determines the predominate force and results by the measurement type. In contact mode the total van der Waals force becomes positive (repulsive), as the atoms are in contact. An advantage of this mode is the good resolution, but however, the surface of the sample easily gets damaged due to the contact with the tip. In true non contact mode the total van der Waals force is negative (attractive). The cantilever vibrates in free space in the vicinity of the resonant frequency. A change of the tip/sample distance results in a shift of the resonant frequency and change of the topographic information. The advantage of this method prevention of tip damage, but typically results in weak tip-surface interaction. A compromise between these two operation modes is the tapping or intermittent mode (Dynamic Force Microscope (DFM)). Similar to the non-contact mode the tip is vibrating in the free space, but repeatedly taps the surface, resulting in contact of the tip and surface, similar to the contact mode. This yields good resolution and low damage of the tip or surface [18, 189].

## A.2 Additional information concerning investigations of IOH layers on ZnO

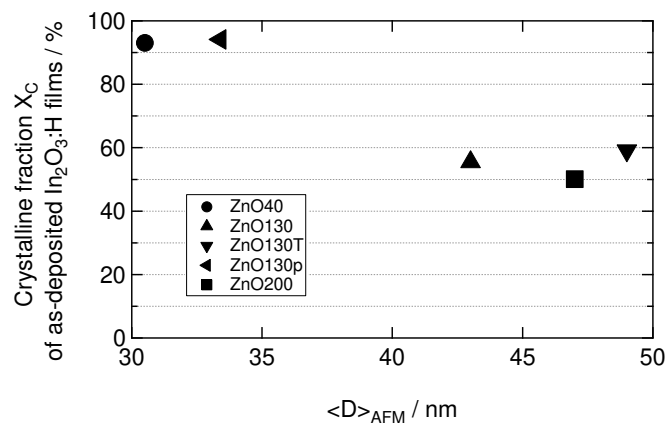


Figure A.1: Dependence of the crystalline fraction of as grown  $\text{In}_2\text{O}_3:\text{H}$  on the lateral grain size, adapted from Erfurt et al. (Supporting Information) [100]

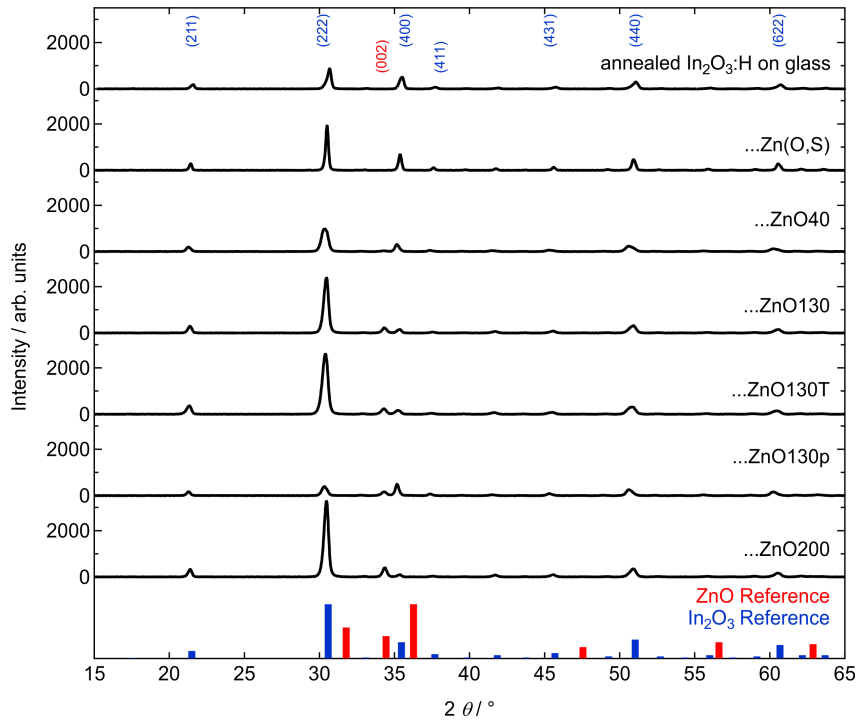


Figure A.2: X-ray diffraction patterns of annealed  $\text{In}_2\text{O}_3\text{:H}$  films grown on glass,  $\text{Zn(O,S)}$  and  $\text{ZnO}$  layers; Reference patterns of  $\text{In}_2\text{O}_3$  and  $\text{ZnO}$  were taken from PDF 00-006-0416 and PDF 01-070-8070, respectively; patterns were shifted for improved differentiation, adapted from Erfurt et al. (Supporting Information) [100]

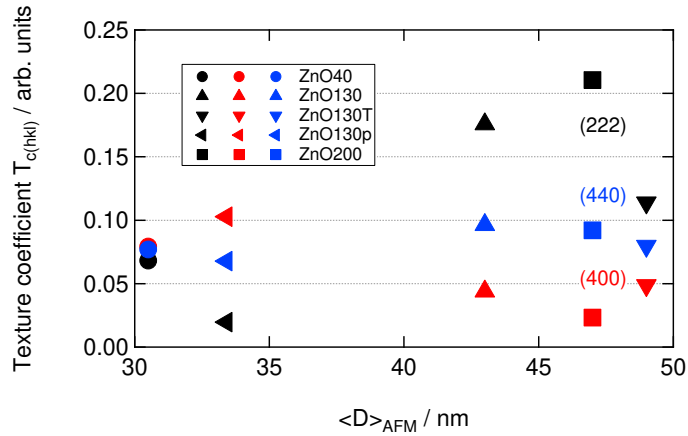


Figure A.3: Dependence of the texture coefficient of as grown  $\text{In}_2\text{O}_3\text{:H}$  on the lateral grain size, adapted from Erfurt et al. (Supporting Information) [100]

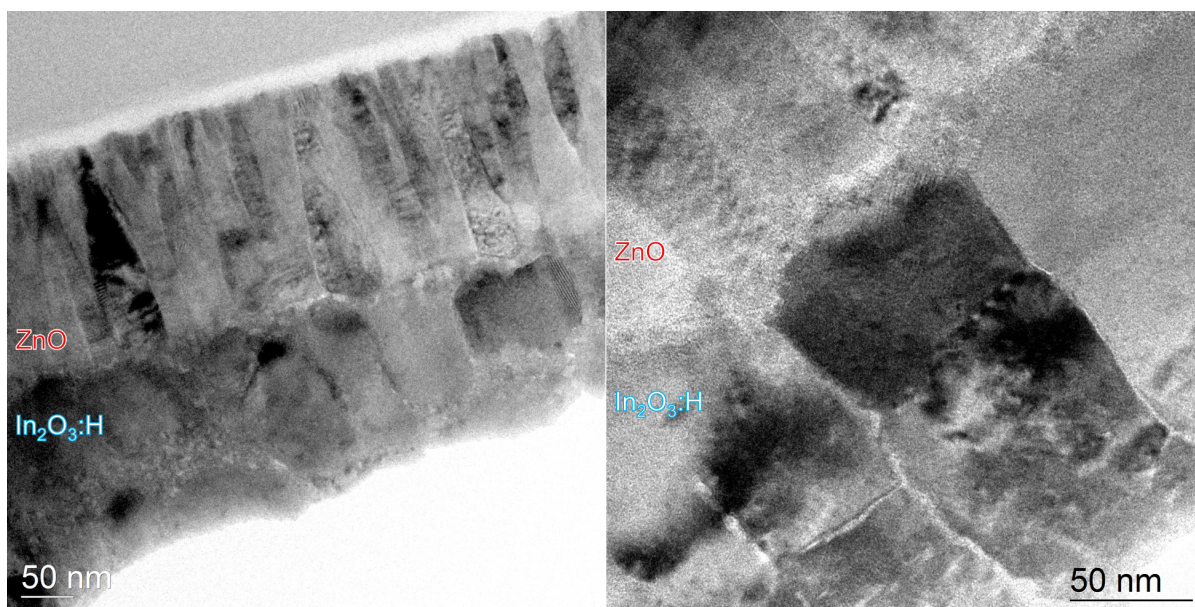


Figure A.4: TEM images of the interface of ZnO and  $In_2O_3 : H$ , adapted from Erfurt et al. (Supporting Information) [100]

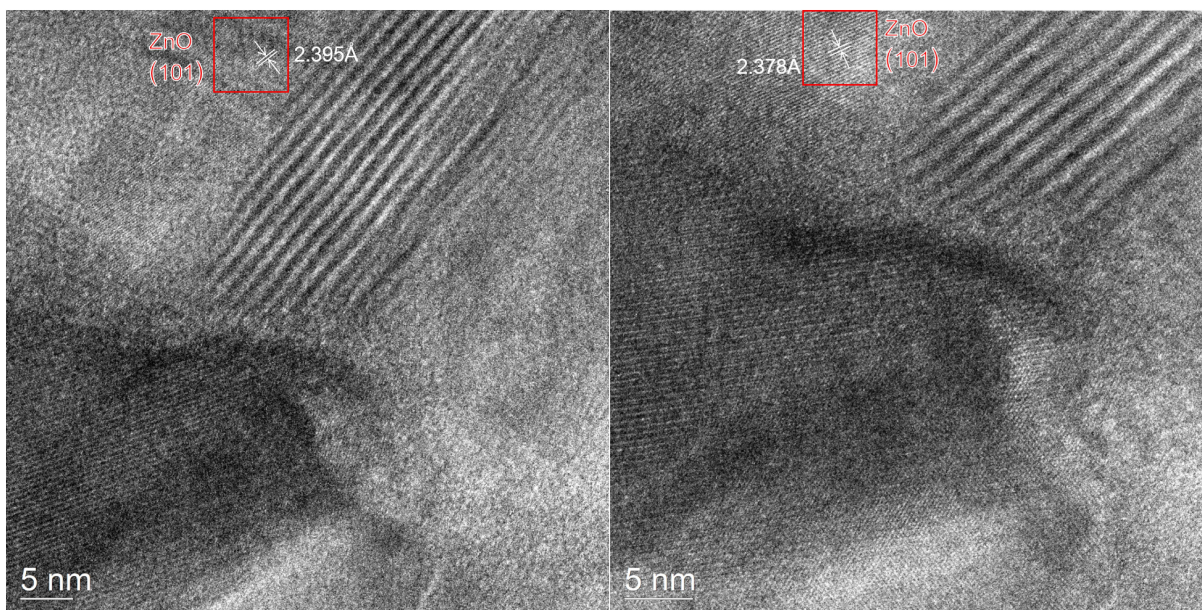


Figure A.5: TEM images of ZnO/ $In_2O_3:H$  with additional measurement spots in the ZnO film with measured inter-planar distances and the corresponding crystalline assignment, colored boxes represent the area taken for FFT analysis, adapted from Erfurt et al. (Supporting Information) [100]

### A.3 Additional information concerning investigations of the low TCO electron mobility on CIGS samples

Table A.1: Sample assignment; the thickness of the Zn(O,S), ZnO and IOH layers is 60 nm, 130 nm and 330 nm, respectively; note that samples 4-3998-15-0 and 4-4041-12-4 were prepared without a Zn(O,S) layer

Substrate	CIGS process time	ID .../Zn(O,S)/i-ZnO	ID .../Zn(O,S)	TCO	RMS
Mo/CIGS	107 min	4-3995-1-2	4-3995-1-4	IOH	118 nm
Mo/CIGS	71 min	4-3995-11-2	4-3995-11-4	IOH	89 nm
Mo/CIGS	46 min	4-3995-6-2	4-3995-6-4	IOH	27 nm
glass/CIGS	107 min	4-3998-2-2	4-3998-2-4	IOH	65 nm
glass/CIGS	71 min	4-3998-6-2	4-3998-6-4	IOH	55 nm
glass/CIGS	46 min	4-3998-4-2	4-3998-4-4	IOH	40 nm
glass	-	4-3998-15-0	4-3998-13-0	IOH	0.4 nm
glass	-	5-15-2-83	5-15-2-81	IOH	170 nm
Mo/CIGS	107 min	4-3996-18-4	-	AZO	113 nm
glass/CIGS	107 min	4-3998-11-4	-	AZO	59 nm
glass	-	4-4041-12-4	-	AZO	0.4 nm

As PDT the HZB-CIGS absorber were treated with NaF after deposition, the AIST-CIGS absorber with NaF/KF. In case of the PDT carried out at HZB two different deposition duration of 4 min and 8 min were done. GDOES measurements were carried out of AIST samples with and without a PDT and of HZB samples with 8 min and without PDT, each for a layer stack with and without an intrinsic ZnO layer. As no standard reference sample was measured, the intensities are only relative. The total relative intensities of the HZB samples without ZnO layers are overall higher, as these were measured with different Ar pressure than the other samples. No correlation between the relative sodium amount in the TCO layer and the electron mobility could be observed.

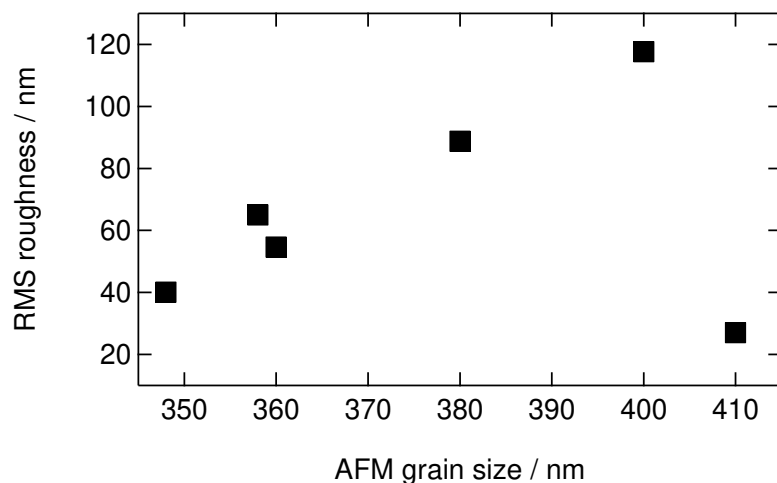


Figure A.6: Correlation of the CIGS sample RMS roughness and the determined AFM grain size using the Watershed method

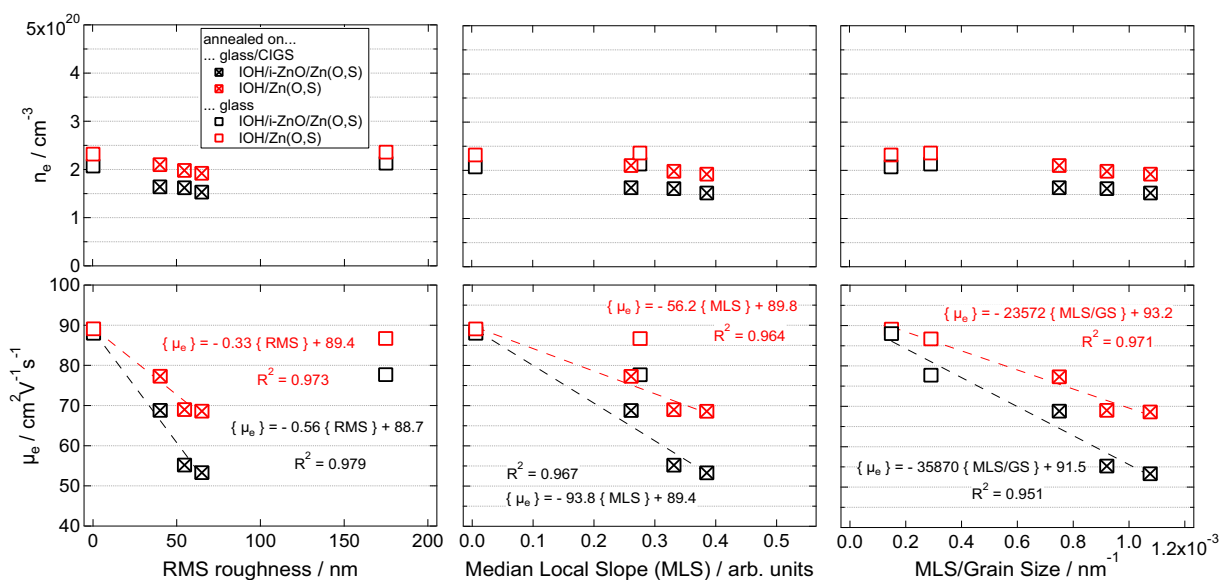


Figure A.7: Comparison of the impact of the RMS roughness, median local slope and median local slope per grain/structure size of the substrate/sub-layers on the charge carrier density and electron mobility of sputtered IOH films deposited on ZnO/Zn(O,S)- and Zn(O,S)-coated samples after annealing in vacuum at 180 °C for 1 h; for the linear fits the films on the textured glass sample were only taken into account for the fit on the dependence on the median local slope per grain size

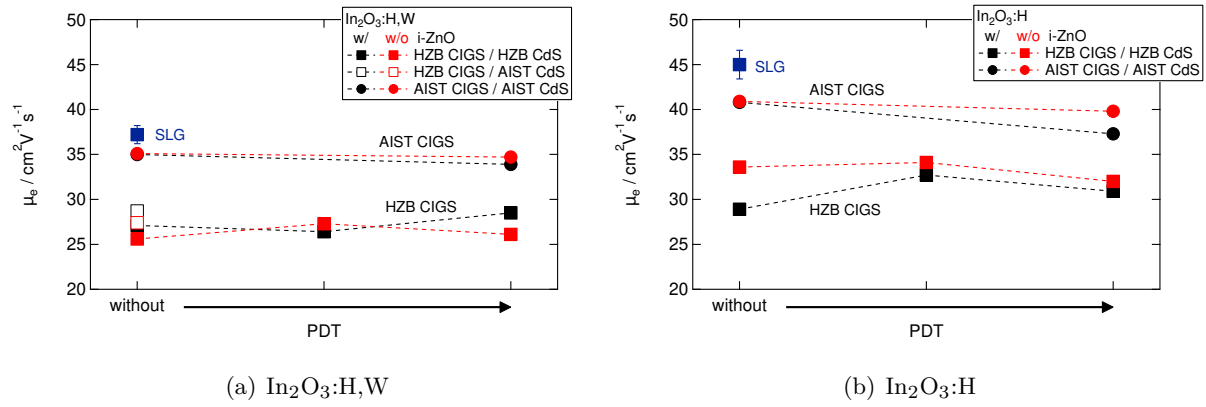


Figure A.8: Electron mobility of (a)  $\text{In}_2\text{O}_3:\text{H,W}$  and (b)  $\text{In}_2\text{O}_3:\text{H}$  thin films deposited on SLG and CIGS samples in dependence of the relatively PDT amount used for the CIGS absorber preparation

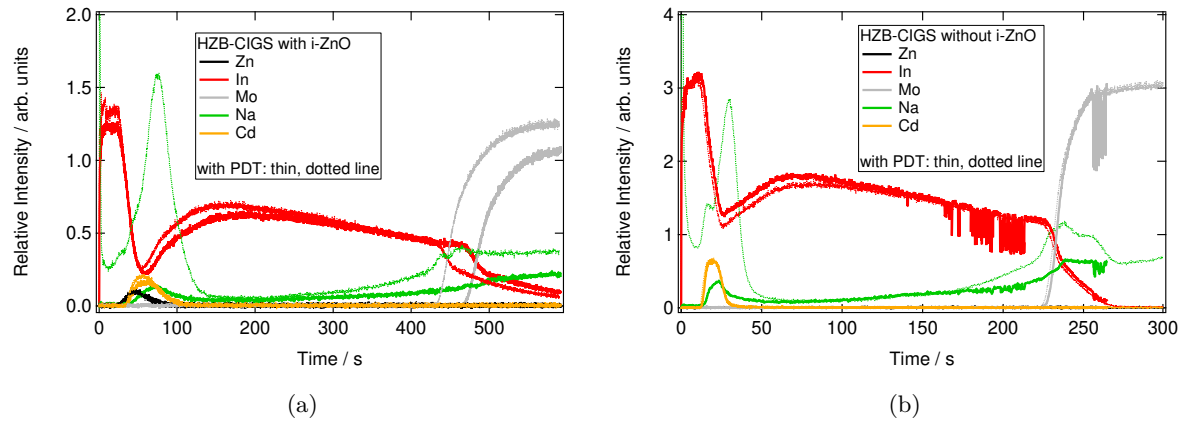


Figure A.9: GDOES measurements of (a) IOH/ZnO/CdS/CIGS/Mo and (b) IOH/CdS/CIGS/Mo, respectively with and without a NaF PDT; the CIGS absorber and PDT was deposited at HZB

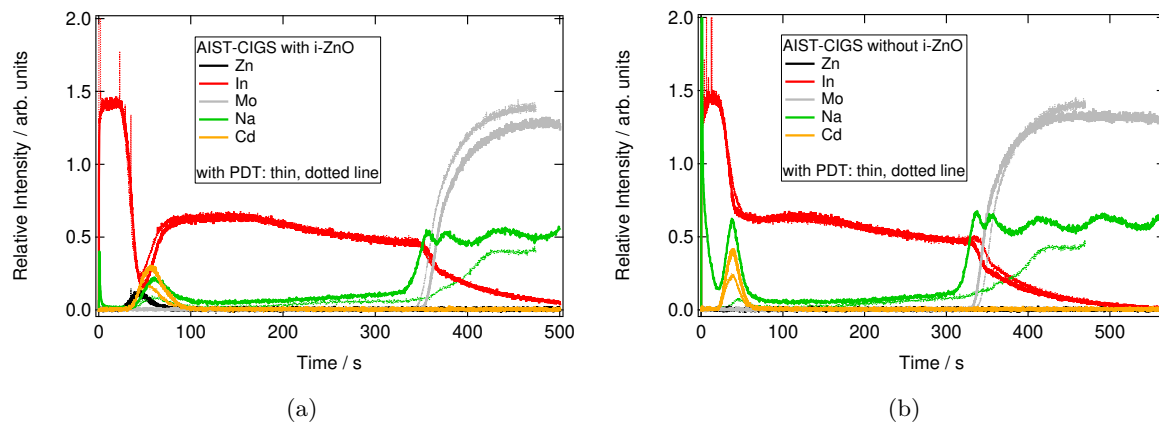


Figure A.10: GDOES measurements of (a) IOH/ZnO/CdS/CIGS/Mo and (b) IOH/CdS/CIGS/Mo, respectively with and without a NaF/KF PDT; the CIGS absorber and PDT was deposited at AIST

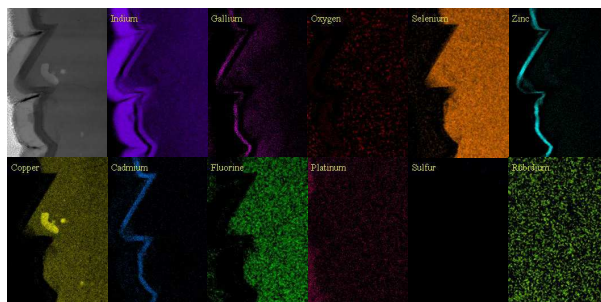


Figure A.11: Elemental composition the sample sputtered-In<sub>2</sub>O<sub>3</sub>:H/i-ZnO/CdS/CIGS; indium was not detected within the cracks

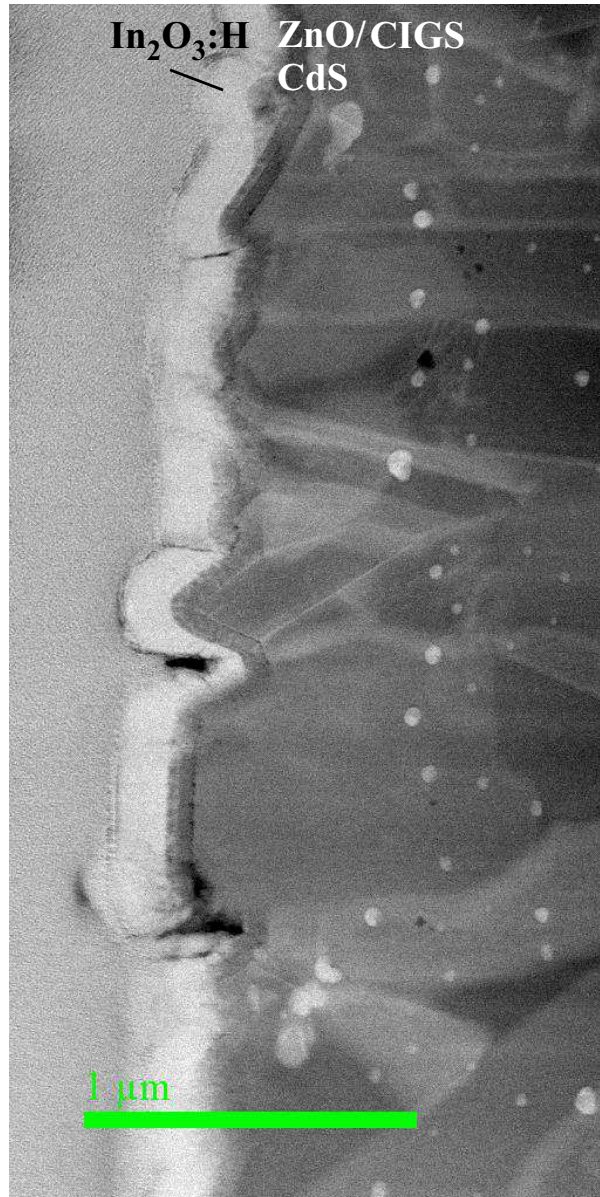


Figure A.12: Overview of as grown sputtered- $\text{In}_2\text{O}_3:\text{H}$  grown on  $\text{i-ZnO}/\text{CdS}/\text{CIGS}$ , measured by STEM; Voids are clearly visible in the  $\text{In}_2\text{O}_3:\text{H}$  layer

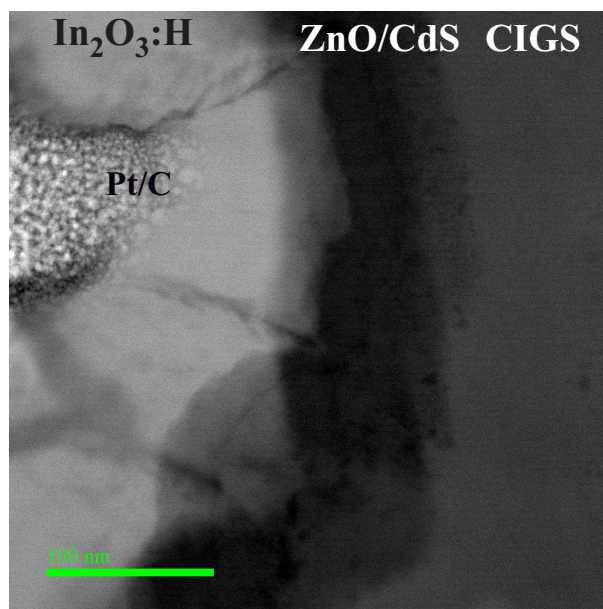


Figure A.13: Additional STEM measurements of as grown sputtered In<sub>2</sub>O<sub>3</sub>:H grown on i-ZnO/CdS/CIGS; Voids are clearly visible in the In<sub>2</sub>O<sub>3</sub>:H layer

---

## Symbols and Acronyms

---

$p_{O_2}$	Oxygen partial pressure
<b>IOH</b>	Hydrogen doped indium oxide
<b>NIR</b>	Near infrared
<b>TCO</b>	Transparent conductive oxide
<b>ALD</b>	Atomic Layer Deposition
<b>RPD</b>	Reactive Plasma Deposition
<b>DC</b>	direct current
<b>RF</b>	radio frequency
<b>i-ZnO</b>	intrinsic zinc oxide
<b>GI-XRD</b>	grazing incidence X-ray diffraction
<b>BB-XRD</b>	Bragg Brentano X-ray diffraction
<b>FFT</b>	Fast Fourier Transformation
<b>DFM</b>	Dynamic Force Microscope
<b>TEM</b>	Transmission Electron Microscopy
<b>STEM</b>	Scanning Transmission Electron Microscopy
<b>a-In<sub>2-2x</sub>Ga<sub>2x</sub>O<sub>3</sub></b>	amorphous indium gallium oxide
<b>FTIR</b>	Fourier-transform infrared spectroscopy
<b>eGB</b>	extended grain boundaries
<b>RMS</b>	root mean square

**MLS** median local slope

**RGA** residual gas analyzer

**HZB** Helmholtz-Zentrum Berlin für Materialien und Energie

**AIST** National Institute of Advanced Industrial Science and Technology

**PDT** post deposition treatment

**IGZO** Indium Gallium Zinc Oxide

**CIGS**  $\text{Cu}(\text{In,Ga})(\text{S,Se})_2$

**$\text{In}_2\text{O}_3\text{:H,W}$**  hydrogen and tungsten co-doped indium oxide

**$\text{In}_2\text{O}_3\text{:H}$**  hydrogen doped indium oxide

**CBO** conduction band offset

**VBO** valence band offset

**UPS** ultraviolet photoelectron spectroscopy

**XPS** X-ray photoelectron spectroscopy

**VBM** valence band maximum

**CBM** conduction band minimum

**EQE** external quantum efficiency

**IQE** internal quantum efficiency

**SRH** Shockley–Read–Hall

**CBD** chemical bath deposition

**HR** highly resistive

**AFM** atomic force microscopy

**FIB** focused ion beam

**TCO** transparent conductive oxide

---

## Bibliography

---

- [1] International Renewable Energy Agency (Irena). *Global energy transformation: A roadmap to 2050*. Policy report [2018]. Ww.irena.org/publications.
- [2] WWW.CIGS-PV.NET. *White Paper for CIGS Thin-Film Solar Cell Technology*. Tech. rep. [2015].
- [3] S. Frontier. *Solar Frontier Achieves World Record Thin-Film Solar Cell Efficiency of 22.9%* [2017].
- [4] V. Bermudez and A. Perez-Rodriguez. *Understanding the cell-to-module efficiency gap in Cu(In,Ga)(S,Se)<sub>2</sub> photovoltaics scale-up*. *Nature Energy*, 3(6):466–475 [2018]. ISSN 2058-7546. doi: 10.1038/s41560-018-0177-1.
- [5] T. Koida, Y. Ueno and H. Shibata. *In<sub>2</sub>O<sub>3</sub>-Based Transparent Conducting Oxide Films with High Electron Mobility Fabricated at Low Process Temperatures*. *physica status solidi (a)*, p. 1700506 [2018]. ISSN 18626300. doi: 10.1002/pssa.201700506.
- [6] A. E. Delahoy and S. Y. Guo. *Transparent and semitransparent conducting film deposition by reactive-environment, hollow cathode sputtering*. *Journal of Vacuum Science & Technology A: Vacuum, Surfaces, and Films*, 23(4):1215–1220 [2005]. ISSN 0734-2101, 1520-8559. doi: 10.1116/1.1894423.
- [7] F. Meng, J. Shi, Z. Liu *et al.* *High mobility transparent conductive W-doped In<sub>2</sub>O<sub>3</sub> thin films prepared at low substrate temperature and its application to solar cells*. *Solar Energy Materials and Solar Cells*, 122:70–74 [2014]. ISSN 09270248. doi: 10.1016/j.solmat.2013.11.030.
- [8] C. Warm Singh, Y. Yoshida, D. W. Readey *et al.* *High-mobility transparent conducting Mo-doped In<sub>2</sub>O<sub>3</sub> thin films by pulsed laser deposition*. *Journal of Applied Physics*, 95(7):3831–3833 [2004]. ISSN 0021-8979, 1089-7550. doi: 10.1063/1.1646468.
- [9] Y. Meng. *A new transparent conductive thin film In<sub>2</sub>O<sub>3</sub>:Mo*. *Thin Solid Films*, 394(1-2):218–222 [2001]. ISSN 00406090. doi: 10.1016/S0040-6090(01)01142-7.

- [10] M. F. A. M. van Hest, M. S. Dabney, J. D. Perkins *et al.* *Titanium-doped indium oxide: A high-mobility transparent conductor*. Applied Physics Letters, *87*(3):032111 [2005]. ISSN 0003-6951, 1077-3118. doi: 10.1063/1.1995957.
- [11] E. Fortunato, D. Ginley, H. Hosono *et al.* *Transparent Conducting Oxides for Photovoltaics*. MRS Bulletin, *32*(03):242–247 [2007]. ISSN 0883-7694, 1938-1425. doi: 10.1557/mrs2007.29.
- [12] S. C. Dixon, D. O. Scanlon, C. J. Carmalt *et al.* *n-Type doped transparent conducting binary oxides: an overview*. Journal of Materials Chemistry C, *4*(29):6946–6961 [2016]. ISSN 2050-7526, 2050-7534. doi: 10.1039/C6TC01881E.
- [13] J. K. Wassei and R. B. Kaner. *Graphene, a promising transparent conductor*. Materials Today, *13*(3):52–59 [2010]. ISSN 13697021. doi: 10.1016/S1369-7021(10)70034-1.
- [14] N. F. Mott and L. Friedman. *Metal-insulator transitions in  $VO_{2-x}$ ,  $Ti_2O_3$  and  $Ti_{2-x}V_xO_3$* . Philosophical Magazine, *30*(2):389–402 [1974]. ISSN 0031-8086. doi: 10.1080/14786439808206565.
- [15] P. P. Edwards and M. J. Sienko. *Universality aspects of the metal-nonmetal transition in condensed media*. Physical Review B, *17*(6):2575–2581 [1978]. ISSN 0163-1829. doi: 10.1103/PhysRevB.17.2575.
- [16] I. Hamberg and C. G. Granqvist. *Evaporated Sn-doped  $In_2O_3$  films: Basic optical properties and applications to energy-efficient windows*. Journal of Applied Physics, *60*(11):R123–R160 [1986]. ISSN 0021-8979, 1089-7550. doi: 10.1063/1.337534.
- [17] P. Drude. *Zur Elektronentheorie der Metalle*. Annalen der Physik, *306*(3):566–613 [1900]. ISSN 00033804, 15213889. doi: 10.1002/andp.19003060312.
- [18] S. Neubert. *Innovative front contact systems for a-Si:H/ $\mu$ c-Si:H solar cells based on thermally treated zinc oxide*. Dissertation, Technical University of Berlin, Berlin [2015].
- [19] D. S. Ginley, H. Hosono and D. C. Paine. *Handbook of transparent conductors*. Springer, New York [2010]. ISBN 978-1-4419-1637-2 978-1-4419-1638-9. OCLC: ocn495781319.
- [20] A. Luque and S. Hegedus. *Handbook of Photovoltaic Science and Engineering*. John Wiley & Sons, Ltd., second edn. [2011]. ISBN 978-0-470-72169-8.
- [21] Y. Zhang and M. H. White. *A quantum mechanical mobility model for scaled NMOS transistors with ultra-thin high-K dielectrics and metal gate electrodes*. Solid-State Electronics, *52*(11):1810–1814 [2008]. ISSN 00381101. doi: 10.1016/j.sse.2008.08.003.
- [22] D. B. Buchholz, Q. Ma, D. Alducin *et al.* *The Structure and Properties of Amorphous Indium Oxide*. Chemistry of Materials, *26*(18):5401–5411 [2014]. doi: 10.1021/cm502689x.

- 
- [23] H. Brooks. *Theory of the Electrical Properties of Germanium and Silicon*. In *Advances in Electronics and Electron Physics*, vol. 7, pp. 85–182. Elsevier [1955]. ISBN 978-0-12-014507-2. doi: 10.1016/S0065-2539(08)60957-9.
- [24] R. Dingle. *XCIV. Scattering of electrons and holes by charged donors and acceptors in semiconductors*. The London, Edinburgh, and Dublin Philosophical Magazine and Journal of Science, *46*(379):831–840 [1955]. ISSN 1941-5982, 1941-5990. doi: 10.1080/14786440808561235.
- [25] C. Erginsoy. *Neutral Impurity Scattering in Semiconductors*. Physical Review, *79*(6):1013–1014 [1950]. ISSN 0031-899X. doi: 10.1103/PhysRev.79.1013.
- [26] K. Seeger. *Semiconductor Physics: an introduction*. Advanced Texts in Physics. Springer Berlin, Berlin, 9. ed edn. [2010]. ISBN 978-3-662-09855-4 978-3-642-06023-6. OCLC: 846198919.
- [27] J. W. Orton. *The story of semiconductors*. Oxford University Press, Oxford [2004]. ISBN 978-0-19-853083-1. OCLC: ocm56694906.
- [28] R. L. Petritz. *Theory of Photoconductivity in Semiconductor Films*. Physical Review, *104*(6):1508–1516 [1956]. ISSN 0031-899X. doi: 10.1103/PhysRev.104.1508.
- [29] J. Y. W. Seto. *The electrical properties of polycrystalline silicon films*. Journal of Applied Physics, *46*(12):5247–5254 [1975]. ISSN 0021-8979, 1089-7550. doi: 10.1063/1.321593.
- [30] G. Baccarani, B. Riccò and G. Spadini. *Transport properties of polycrystalline silicon films*. Journal of Applied Physics, *49*(11):5565–5570 [1978]. ISSN 0021-8979, 1089-7550. doi: 10.1063/1.324477.
- [31] I. Hamberg, C. G. Granqvist, K. F. Berggren *et al.* *Band-gap widening in heavily Sn-doped In<sub>2</sub>O<sub>3</sub>*. Physical Review B, *30*(6):3240–3249 [1984]. ISSN 0163-1829. doi: 10.1103/PhysRevB.30.3240.
- [32] A. Pflug, V. Sittinger, F. Ruske *et al.* *Optical characterization of aluminum-doped zinc oxide films by advanced dispersion theories*. Thin Solid Films, *455-456*:201–206 [2004]. ISSN 00406090. doi: 10.1016/j.tsf.2004.01.006.
- [33] NREL. *Reference Solar Spectral Irradiance: Air Mass 1.5*. <https://rredc.nrel.gov/solar/spectra/am1.5/>; Accessed 12.08.2018.
- [34] R. Menner, D. Hariskos, V. Linss *et al.* *Low-cost ZnO:Al transparent contact by reactive rotatable magnetron sputtering for Cu(In,Ga)Se<sub>2</sub> solar modules*. Thin Solid Films, *519*(21):7541–7544 [2011]. ISSN 00406090. doi: 10.1016/j.tsf.2011.01.392.

- [35] S. Calnan and A. Tiwari. *High mobility transparent conducting oxides for thin film solar cells*. Thin Solid Films, 518(7):1839–1849 [2010]. ISSN 00406090. doi: 10.1016/j.tsf.2009.09.044.
- [36] C. Guillén and J. Herrero. *Optical, electrical and structural characteristics of Al:ZnO thin films with various thicknesses deposited by DC sputtering at room temperature and annealed in air or vacuum*. Vacuum, 84(7):924–929 [2010]. ISSN 0042207X. doi: 10.1016/j.vacuum.2009.12.015.
- [37] R. Cebulla, R. Wendt and K. Ellmer. *Al-doped zinc oxide films deposited by simultaneous rf and dc excitation of a magnetron plasma: Relationships between plasma parameters and structural and electrical film properties*. Journal of Applied Physics, 83(2):1087–1095 [1998]. ISSN 0021-8979, 1089-7550. doi: 10.1063/1.366798.
- [38] K. Tominaga, N. Umezū, I. Mori *et al.* *Transparent conductive ZnO film preparation by alternating sputtering of ZnO:Al and Zn or Al targets*. Thin Solid Films, 334(1-2):35–39 [1998]. ISSN 00406090. doi: 10.1016/S0040-6090(98)01112-2.
- [39] S. Körner, M. Hartig, R. Muydinov *et al.* *Serial cosputtering for aluminum doping manipulated zinc oxide as front contact for Cu(In,Ga)Se<sub>2</sub> solar cells*. Japanese Journal of Applied Physics, 57(8S3):08RC18 [2018]. ISSN 0021-4922, 1347-4065. doi: 10.7567/JJAP.57.08RC18.
- [40] Y. Igasaki and H. Saito. *The effects of deposition rate on the structural and electrical properties of ZnO:Al films deposited on (1120) oriented sapphire substrates*. Journal of Applied Physics, 70(7):3613–3619 [1991]. ISSN 0021-8979, 1089-7550. doi: 10.1063/1.349258.
- [41] K. Ellmer. *Resistivity of polycrystalline zinc oxide films: current status and physical limit*. Journal of Physics D: Applied Physics, 34(21):3097–3108 [2001]. ISSN 0022-3727, 1361-6463. doi: 10.1088/0022-3727/34/21/301.
- [42] O. Tuna, Y. Selamet, G. Aygun *et al.* *High quality ITO thin films grown by dc and RF sputtering without oxygen*. Journal of Physics D: Applied Physics, 43(5):055402 [2010]. ISSN 0022-3727, 1361-6463. doi: 10.1088/0022-3727/43/5/055402.
- [43] E. Terzini, P. Thilakan and C. Minarini. *Properties of ITO thin films deposited by RF magnetron sputtering at elevated substrate temperature*. Materials Science and Engineering: B, 77(1):110–114 [2000]. ISSN 09215107. doi: 10.1016/S0921-5107(00)00477-3.
- [44] K. Ellmer and R. Mientus. *Carrier transport in polycrystalline ITO and ZnO:Al II: The influence of grain barriers and boundaries*. Thin Solid Films, 516(17):5829–5835 [2008]. ISSN 00406090. doi: 10.1016/j.tsf.2007.10.082.

- [45] F. Kurdesau, G. Khripunov, A. da Cunha *et al.* *Comparative study of ITO layers deposited by DC and RF magnetron sputtering at room temperature.* Journal of Non-Crystalline Solids, *352*(9-20):1466–1470 [2006]. ISSN 00223093. doi: 10.1016/j.jnoncrysol.2005.11.088.
- [46] T. Koida, H. Fujiwara and M. Kondo. *Hydrogen-doped In<sub>2</sub>O<sub>3</sub> as High-mobility Transparent Conductive Oxide.* Japanese Journal of Applied Physics, *46*(No. 28):L685–L687 [2007]. ISSN 0021-4922. doi: 10.1143/JJAP.46.L685.
- [47] J. Keller, L. Stolt, M. Edoff *et al.* *Atomic layer deposition of In<sub>2</sub>O<sub>3</sub> transparent conductive oxide layers for application in Cu(In,Ga)Se<sub>2</sub> solar cells with different buffer layers: Atomic layer deposition of In<sub>2</sub>O<sub>3</sub> transparent conductive oxide layers.* physica status solidi (a), *213*(6):1541–1552 [2016]. ISSN 18626300. doi: 10.1002/pssa.201532883.
- [48] H. Scherg-Kurmes, S. Körner, S. Ring *et al.* *High mobility In<sub>2</sub>O<sub>3</sub>:H as contact layer for a-Si:H/c-Si heterojunction and  $\mu$ -Si:H thin film solar cells.* Thin Solid Films, *594*:316–322 [2015]. ISSN 00406090. doi: 10.1016/j.tsf.2015.03.022.
- [49] M. Morales-Masis, E. Rucavado, R. Monnard *et al.* *Highly Conductive and Broadband Transparent Zr-Doped In<sub>2</sub>O<sub>3</sub> as Front Electrode for Solar Cells.* IEEE Journal of Photovoltaics, *8*(5):1202–1207 [2018]. ISSN 2156-3381, 2156-3403. doi: 10.1109/JPHOTOV.2018.2851306.
- [50] E. Kobayashi, Y. Watabe and T. Yamamoto. *High-mobility transparent conductive thin films of cerium-doped hydrogenated indium oxide.* Applied Physics Express, *8*(1):015505 [2015]. ISSN 1882-0778, 1882-0786. doi: 10.7567/APEX.8.015505.
- [51] S. Z. Karazhanov, P. Ravindran, P. Vajeeston *et al.* *Phase stability, electronic structure, and optical properties of indium oxide polytypes.* Physical Review B, *76*(7) [2007]. ISSN 1098-0121, 1550-235X. doi: 10.1103/PhysRevB.76.075129.
- [52] R. S. Roth. *Classification of perovskite and other ABO<sub>3</sub>-type compounds.* J. Res. Nat. Bur. Stand., *58*(2):75–88 [1957].
- [53] M. Marezio. *Refinement of the crystal structure of In<sub>2</sub>O<sub>3</sub> at two wavelengths.* Acta Crystallographica, *20*(6):723–728 [1966]. ISSN 0365-110X. doi: 10.1107/S0365110X66001749.
- [54] R. L. Weiher and R. P. Ley. *Optical Properties of Indium Oxide.* Journal of Applied Physics, *37*(1):299–302 [1966]. ISSN 0021-8979, 1089-7550. doi: 10.1063/1.1707830.
- [55] K. Irscher, M. Naumann, M. Pietsch *et al.* *On the nature and temperature dependence of the fundamental band gap of In<sub>2</sub>O<sub>3</sub>: Nature and temperature dependence of the fundamental band gap of In<sub>2</sub>O<sub>3</sub>.* physica status solidi (a), *211*(1):54–58 [2014]. ISSN 18626300. doi: 10.1002/pssa.201330184.

- [56] V. Scherer, C. Janowitz, A. Krapf *et al.* *Transport and angular resolved photoemission measurements of the electronic properties of  $\text{In}_2\text{O}_3$  bulk single crystals.* Applied Physics Letters, *100*(21):212108 [2012]. ISSN 0003-6951, 1077-3118. doi: 10.1063/1.4719665.
- [57] C. Janowitz, V. Scherer, M. Mohamed *et al.* *Experimental electronic structure of  $\text{In}_2\text{O}_3$  and  $\text{Ga}_2\text{O}_3$ .* New Journal of Physics, *13*(8):085014 [2011]. ISSN 1367-2630. doi: 10.1088/1367-2630/13/8/085014.
- [58] P. D. C. King, T. D. Veal, F. Fuchs *et al.* *Band gap, electronic structure, and surface electron accumulation of cubic and rhombohedral  $\text{In}_2\text{O}_3$ .* Physical Review B, *79*(20) [2009]. ISSN 1098-0121, 1550-235X. doi: 10.1103/PhysRevB.79.205211.
- [59] A. Walsh, J. L. F. Da Silva, S.-H. Wei *et al.* *Nature of the Band Gap of  $\text{In}_2\text{O}_3$  Revealed by First-Principles Calculations and X-Ray Spectroscopy.* Physical Review Letters, *100*(16) [2008]. ISSN 0031-9007, 1079-7114. doi: 10.1103/PhysRevLett.100.167402.
- [60] Y. Shigesato, I. Yasui, Y. Hayashi *et al.* *Effects of water partial pressure on the activated electron beam evaporation process to deposit tin-doped indium-oxide films.* Journal of Vacuum Science & Technology A: Vacuum, Surfaces, and Films, *13*(2):268–275 [1995]. ISSN 0734-2101, 1520-8559. doi: 10.1116/1.579409.
- [61] T. Koida, M. Kondo, K. Tsutsumi *et al.* *Hydrogen-doped  $\text{In}_2\text{O}_3$  transparent conducting oxide films prepared by solid-phase crystallization method.* Journal of Applied Physics, *107*(3):033514 [2010]. doi: 10.1063/1.3284960.
- [62] S. Limpijumnong, P. Reunchan, A. Janotti *et al.* *Hydrogen doping in indium oxide: An *ab initio* study.* Physical Review B, *80*(19) [2009]. ISSN 1098-0121, 1550-235X. doi: 10.1103/PhysRevB.80.193202.
- [63] P. D. C. King, R. L. Lichti, Y. G. Celebi *et al.* *Shallow donor state of hydrogen in  $\text{In}_2\text{O}_3$  and  $\text{SnO}_2$ : Implications for conductivity in transparent conducting oxides.* Physical Review B, *80*(8) [2009]. ISSN 1098-0121, 1550-235X. doi: 10.1103/PhysRevB.80.081201.
- [64] B. Macco, H. C. M. Knoop and W. M. M. Kessels. *Electron Scattering and Doping Mechanisms in Solid-Phase-Crystallized  $\text{In}_2\text{O}_3\text{:H}$  Prepared by Atomic Layer Deposition.* ACS Applied Materials & Interfaces, *7*(30):16723–16729 [2015]. doi: 10.1021/acsami.5b04420.
- [65] T. Koida, H. Fujiwara and M. Kondo. *Structural and Electrical Properties of Hydrogen-Doped  $\text{In}_2\text{O}_3$  Films Fabricated by Solid-Phase Crystallization.* Journal of Non-Crystalline Solids, *354*(19-25):2805–2808 [2008]. ISSN 00223093. doi: 10.1016/j.jnoncrysol.2007.09.076.
- [66] H. Wardenga, M. Frischbier, M. Morales-Masis *et al.* *In Situ Hall Effect Monitoring of Vacuum Annealing of  $\text{In}_2\text{O}_3\text{:H}$  Thin Films.* Materials, *8*(2):561–574 [2015]. ISSN 1996-1944. doi: 10.3390/ma8020561.

- [67] B. Macco, Y. Wu, D. Vanhemel *et al.* *High mobility  $In_2O_3:H$  transparent conductive oxides prepared by atomic layer deposition and solid phase crystallization.* *physica status solidi (RRL) - Rapid Research Letters*, 8(12):987–990 [2014]. ISSN 18626254. doi: 10.1002/pssr.201409426.
- [68] J. Keller, A. Aijaz, F. Gustavsson *et al.* *Direct comparison of atomic layer deposition and sputtering of  $In_2O_3:H$  used as transparent conductive oxide layer in  $CuIn_{1-x}Ga_xSe_2$  thin film solar cells.* *Solar Energy Materials and Solar Cells*, 157:757–764 [2016]. ISSN 09270248. doi: 10.1016/j.solmat.2016.07.012.
- [69] L. Barraud, Z. Holman, N. Badel *et al.* *Hydrogen-doped indium oxide/indium tin oxide bilayers for high-efficiency silicon heterojunction solar cells.* *Solar Energy Materials and Solar Cells*, 115:151–156 [2013]. ISSN 09270248. doi: 10.1016/j.solmat.2013.03.024.
- [70] M. Boccard, N. Rodkey and Z. C. Holman. *Properties of hydrogenated indium oxide prepared by reactive sputtering with hydrogen gas.* In *2016 IEEE 43rd Photovoltaic Specialists Conference (PVSC)*, pp. 2868–2870 [2016]. doi: 10.1109/PVSC.2016.7750178.
- [71] A. Steigert, I. Lauermann, T. Niesen *et al.* *Sputtered  $Zn(O,S)/In_2O_3:H$  window layers for enhanced blue response of chalcopyrite solar cells.* *physica status solidi (RRL) - Rapid Research Letters*, 9(11):627–630 [2015]. ISSN 18626254. doi: 10.1002/pssr.201510318.
- [72] S. Li, Z. Shi, Z. Tang *et al.* *Study on the hydrogen doped indium oxide for silicon heterojunction solar cell application.* *Journal of Alloys and Compounds*, 705:198–204 [2017]. ISSN 09258388. doi: 10.1016/j.jallcom.2017.02.133.
- [73] J. Yu, J. Bian, W. Duan *et al.* *Tungsten doped indium oxide film: Ready for bifacial copper metallization of silicon heterojunction solar cell.* *Solar Energy Materials and Solar Cells*, 144:359–363 [2016]. ISSN 09270248. doi: 10.1016/j.solmat.2015.09.033.
- [74] F. Engelhardt, L. Bornemann, M. Köntges *et al.*  *$Cu(In,Ga)Se_2$  solar cells with a  $ZnSe$  buffer layer: interface characterization by quantum efficiency measurements.* *Progress in Photovoltaics: Research and Applications*, 7(6):423–436 [1999]. ISSN 1062-7995, 1099-159X. doi: 10.1002/(SICI)1099-159X(199911/12)7:6<423::AID-PIP281>3.0.CO;2-S.
- [75] U. Rau and H. Schock.  *$Cu(In,Ga)Se_2$  thin-film solar cells.* In *Solar Cells*, pp. 303–349. Elsevier [2005]. ISBN 978-1-85617-457-2. doi: 10.1016/B978-185617457-2/50013-5.
- [76] R. Scheer and H. W. Schock. *Chalcogenide photovoltaics: physics, technologies, and thin film devices.* Wiley-VCH, Weinheim, Germany [2011]. ISBN 978-3-527-31459-1. OCLC: ocn664325819.

- [77] D. Shvydka and V. Karpov. *Modeling of non-uniformity losses in integrated large-area solar cell modules*. In *Conference Record of the Thirty-first IEEE Photovoltaic Specialists Conference, 2005.*, pp. 359–362. IEEE, Lake buena Vista, FL, USA [2005]. ISBN 978-0-7803-8707-2. doi: 10.1109/PVSC.2005.1488143.
- [78] P. Grabitz, U. Rau and J. Werner. *A multi-diode model for spatially inhomogeneous solar cells*. *Thin Solid Films*, 487(1-2):14–18 [2005]. ISSN 00406090. doi: 10.1016/j.tsf.2005.01.027.
- [79] M. A. Green. *Accuracy of analytical expressions for solar cell fill factors*. *Solar Cells*, 7(3):337–340 [1982]. ISSN 03796787. doi: 10.1016/0379-6787(82)90057-6.
- [80] K. Iwata, T. Sakemi, A. Yamada *et al.* *Improvement of ZnO TCO film growth for photovoltaic devices by reactive plasma deposition (RPD)*. *Thin Solid Films*, 480-481:199–203 [2005]. ISSN 00406090. doi: 10.1016/j.tsf.2004.11.072.
- [81] M. D. Heinemann. *CIGSe Superstrate Solar Cells: Growth and Characterization of CIGSe Thin Films on Transparent Conductive Oxides*. Dissertation, Technical University of Berlin [2015].
- [82] P. Jackson, R. Wuerz, D. Hariskos *et al.* *Effects of heavy alkali elements in Cu(In,Ga)Se<sub>2</sub> solar cells with efficiencies up to 22.6%*. *physica status solidi (RRL) - Rapid Research Letters*, 10(8):583–586 [2016]. ISSN 18626254. doi: 10.1002/pssr.201600199.
- [83] N. Nicoara, T. Lepetit, L. Arzel *et al.* *Effect of the KF post-deposition treatment on grain boundary properties in Cu(In, Ga)Se<sub>2</sub> thin films*. *Scientific Reports*, 7(1) [2017]. ISSN 2045-2322. doi: 10.1038/srep41361.
- [84] A. Chirilă, P. Reinhard, F. Pianezzi *et al.* *Potassium-induced surface modification of Cu(In,Ga)Se<sub>2</sub> thin films for high-efficiency solar cells*. *Nature Materials*, 12(12):1107–1111 [2013]. ISSN 1476-1122, 1476-4660. doi: 10.1038/nmat3789.
- [85] J.-P. Bäcker. *In situ investigation of the rapid thermal reaction of Cu-In-Ga precursors to Cu(In,Ga)Se<sub>2</sub> thin-film solar cell absorbers*. Dissertation, Freie Universität Berlin [2018].
- [86] S. S. Schmidt, C. Wolf, H. Rodriguez-Alvarez *et al.* *Adjusting the Ga grading during fast atmospheric processing of Cu(In,Ga)Se<sub>2</sub> solar cell absorber layers using elemental selenium vapor: Adjusting the Ga grading in fast processing of CIGSe*. *Progress in Photovoltaics: Research and Applications*, 25(5):341–357 [2017]. ISSN 10627995. doi: 10.1002/pip.2865.
- [87] T. Dalibor, P. Eraerds, M. Grave *et al.* *Advanced PVD buffers on the road to GW-scale CIGSSe production*. pp. 1–5. IEEE [2017]. ISBN 978-1-5090-5605-7. doi: 10.1109/PVSC.2017.8366300.

- [88] C. A. Kaufmann. *Chemical Bath Deposition of Thin Semiconductor Films for Use as Buffer Layers in CuInS<sub>2</sub> Thin Film Solar Cells*. Dissertation, University of Oxford, Oxford [2002].
- [89] S. Merdes, F. Ziem, T. Lavrenko *et al.* *Above 16% efficient sequentially grown Cu(In,Ga)(Se,S)<sub>2</sub>-based solar cells with atomic layer deposited Zn(O,S) buffers: CIGSSe-based solar cells with atomic layer deposited Zn(O,S) buffers*. *Progress in Photovoltaics: Research and Applications*, 23(11):1493–1500 [2015]. ISSN 10627995. doi: 10.1002/pip.2579.
- [90] T. Koida, J. Nishinaga, Y. Ueno *et al.* *Impact of front contact layers on performance of Cu(In,Ga)Se<sub>2</sub> solar cells in relaxed and metastable states*. *Progress in Photovoltaics: Research and Applications* [2018]. ISSN 10627995. doi: 10.1002/pip.3017.
- [91] T. Koida, Y. Ueno, J. Nishinaga *et al.* *Cu(In,Ga)Se<sub>2</sub> Solar Cells with Amorphous In<sub>2</sub>O<sub>3</sub>-Based Front Contact Layers*. *ACS Applied Materials & Interfaces* [2017]. ISSN 1944-8244, 1944-8252. doi: 10.1021/acsami.7b07092.
- [92] N. Zhou, M.-G. Kim, S. Loser *et al.* *Amorphous oxide alloys as interfacial layers with broadly tunable electronic structures for organic photovoltaic cells*. *Proceedings of the National Academy of Sciences*, 112(26):7897–7902 [2015]. ISSN 0027-8424, 1091-6490. doi: 10.1073/pnas.1508578112.
- [93] M. Marinkovic. *Contact resistance effects in thin film solar cells and thin film transistors*. Dissertation, Jacobs University, Bremen [2013].
- [94] B. D. Viezbicke, S. Patel, B. E. Davis *et al.* *Evaluation of the Tauc method for optical absorption edge determination: ZnO thin films as a model system: Tauc method for optical absorption edge determination*. *physica status solidi (b)*, 252(8):1700–1710 [2015]. ISSN 03701972. doi: 10.1002/pssb.201552007.
- [95] U. Rau, D. Abou-Ras and T. Kirchartz. *Advanced characterization techniques for thin film solar cells*. Wiley-VCH, Weinheim, Germany [2011]. ISBN 978-3-527-41003-3. OCLC: ocn676728907.
- [96] *Electron Backscatter Diffraction (EBSD)*. [https://www.helmholtz-berlin.de/forschung/oe/ee/si-pv/analytik/rem/edx1\\_en.html](https://www.helmholtz-berlin.de/forschung/oe/ee/si-pv/analytik/rem/edx1_en.html); Accessed 09.08.2018.
- [97] M. Birkholz, P. F. Fewster and C. Genzel. *Thin film analysis by X-ray scattering*. Wiley-VCH, Weinheim [2006]. ISBN 978-3-527-31052-4.
- [98] K. Frost, D. Kaminski, G. Kirwan *et al.* *Crystallinity and structure of starch using wide angle X-ray scattering*. *Carbohydrate Polymers*, 78(3):543–548 [2009]. ISSN 01448617. doi: 10.1016/j.carbpol.2009.05.018.

- [99] R. A. Young, editor. *The Rietveld method*. No. 5 in International Union of Crystallography monographs on crystallography. International Union of Crystallography ; Oxford University Press, [Chester, England] : Oxford ; New York [1993]. ISBN 978-0-19-855577-3.
- [100] D. Erfurt, M. D. Heinemann, S. S. Schmidt *et al.* *Influence of zno-based sub-layers on the growth of hydrogen doped indium oxide*. ACS Appl. Energy Mater., 1:5490 – 5499 [2018]. doi: 10.1021/acsaem.8b01039.
- [101] R. Ajimsha, A. K. Das, V. K. Sahu *et al.* *Valance band offset of TiO<sub>2</sub>/CuGaO<sub>2</sub> hetero-structure measured by x-ray photoelectron spectroscopy*. Solar Energy Materials and Solar Cells, 140:446–449 [2015]. ISSN 09270248. doi: 10.1016/j.solmat.2015.04.035.
- [102] D. Nečas and P. Klapetek. *Gwyddion* [2016].
- [103] Bruker. *OPUS*. <https://www.bruker.com/de/products/infrared-near-infrared-and-raman-spectroscopy/opus-spectroscopy-software.html>; Accessed 10.08.2018.
- [104] WaveMetrics. *IGOR Pro* [2014].
- [105] D. Erfurt, M. D. Heinemann, S. Körner *et al.* *Improved electrical properties of pulsed dc magnetron sputtered hydrogen doped indium oxide after annealing in air*. Materials Science in Semiconductor Processing, 89:170 – 175 [2019]. ISSN 1369-8001. doi: <https://doi.org/10.1016/j.mssp.2018.09.012>.
- [106] T. Koida, H. Shibata, M. Kondo *et al.* *Correlation between oxygen stoichiometry, structure, and opto-electrical properties in amorphous In<sub>2</sub>O<sub>3</sub>:H films*. Journal of Applied Physics, 111(6):063721 [2012]. ISSN 0021-8979, 1089-7550. doi: 10.1063/1.3696978.
- [107] G. C. E. Jost, A. N. Hamri, F. Köhler *et al.* *Reliability aspects of hydrogen-doped indium oxide*. physica status solidi (a), 213(7):1751–1759 [2016]. ISSN 1862-6319. doi: 10.1002/pssa.201532806.
- [108] J. B. Varley, H. Peelaers, A. Janotti *et al.* *Hydrogenated cation vacancies in semiconducting oxides*. Journal of Physics: Condensed Matter, 23(33):334212 [2011]. ISSN 0953-8984, 1361-648X. doi: 10.1088/0953-8984/23/33/334212.
- [109] T. Koida. *Amorphous and crystalline In<sub>2</sub>O<sub>3</sub>-based transparent conducting films for photovoltaics*. physica status solidi (a), 214(2):1600464 [2017]. ISSN 1862-6319. doi: 10.1002/pssa.201600464.
- [110] H. Scherg-Kurmes, S. Seeger, S. Körner *et al.* *Optimization of the post-deposition annealing process of high-mobility In<sub>2</sub>O<sub>3</sub>:H for photovoltaic applications*. Thin Solid Films, 599:78–83 [2016]. ISSN 00406090. doi: 10.1016/j.tsf.2015.12.054.

- 
- [111] P. Prathap, G. G. Devi, Y. Subbaiah *et al.* *Growth and characterization of indium oxide films*. *Current Applied Physics*, 8(2):120–127 [2008]. ISSN 15671739. doi: 10.1016/j.cap.2007.06.001.
- [112] E. Burstein. *Anomalous Optical Absorption Limit in InSb*. *Physical Review*, 93(3):632–633 [1954]. ISSN 0031-899X. doi: 10.1103/PhysRev.93.632.
- [113] T. S. Moss. *The Interpretation of the Properties of Indium Antimonide*. *Proceedings of the Physical Society. Section B*, 67(10):775–782 [1954]. ISSN 0370-1301. doi: 10.1088/0370-1301/67/10/306.
- [114] T. Tohsophon, A. Dabirian, S. De Wolf *et al.* *Environmental stability of high-mobility indium-oxide based transparent electrodes*. *APL Materials*, 3(11):116105 [2015]. ISSN 2166-532X. doi: 10.1063/1.4935125.
- [115] D. Greiner, N. Papathanasiou, A. Pflug *et al.* *Influence of damp heat on the optical and electrical properties of Al-doped zinc oxide*. *Thin Solid Films*, 517(7):2291–2294 [2009]. ISSN 00406090. doi: 10.1016/j.tsf.2008.10.107.
- [116] D. Greiner, S. Gledhill, C. Köble *et al.* *Damp heat stability of Al-doped zinc oxide films on smooth and rough substrates*. *Thin Solid Films*, 520(4):1285–1290 [2011]. ISSN 00406090. doi: 10.1016/j.tsf.2011.04.190.
- [117] U. Rau and M. Schmidt. *Electronic properties of ZnO/CdS/Cu(In,Ga)Se<sub>2</sub> solar cells — aspects of heterojunction formation*. *Thin Solid Films*, 387(1-2):141–146 [2001]. ISSN 00406090. doi: 10.1016/S0040-6090(00)01737-5.
- [118] U. Rau, P. O. Grabitz and J. H. Werner. *Resistive limitations to spatially inhomogeneous electronic losses in solar cells*. *Applied Physics Letters*, 85(24):6010–6012 [2004]. ISSN 0003-6951, 1077-3118. doi: 10.1063/1.1835536.
- [119] R. Klenk, A. Steigert, T. Rissom *et al.* *Junction formation by Zn(O,S) sputtering yields CIGSe-based cells with efficiencies exceeding 18%: Junction formation by Zn(O,S) sputtering*. *Progress in Photovoltaics: Research and Applications*, 22(2):161–165 [2014]. ISSN 10627995. doi: 10.1002/pip.2445.
- [120] T. Koida, Y. Kamikawa-Shimizu, Akimasa Yamada *et al.* *Cu(In,Ga)Se<sub>2</sub> Solar Cells With Amorphous Oxide Semiconducting Buffer Layers*. *IEEE Journal of Photovoltaics*, 5(3):956–961 [2015]. ISSN 2156-3381, 2156-3403. doi: 10.1109/JPHOTOV.2015.2396356.
- [121] K. Ellmer, A. Klein and B. Rech, editors. *Transparent conductive zinc oxide: basics and applications in thin film solar cells*. No. 104 in Springer series in materials science. Springer, Berlin [2008]. ISBN 978-3-540-73611-0. OCLC: ocn181423059.

- [122] V. Gupta and A. Mansingh. *Influence of postdeposition annealing on the structural and optical properties of sputtered zinc oxide film*. Journal of Applied Physics, *80*(2):1063–1073 [1996]. ISSN 0021-8979, 1089-7550. doi: 10.1063/1.362842.
- [123] E. Bachari, G. Baud, S. Ben Amor *et al.* *Structural and optical properties of sputtered ZnO films*. Thin Solid Films, *348*(1-2):165–172 [1999]. ISSN 00406090. doi: 10.1016/S0040-6090(99)00060-7.
- [124] Y. E. Lee, J. B. Lee, Y. J. Kim *et al.* *Microstructural evolution and preferred orientation change of radio-frequency-magnetron sputtered ZnO thin films*. Journal of Vacuum Science & Technology A: Vacuum, Surfaces, and Films, *14*(3):1943–1948 [1996]. ISSN 0734-2101, 1520-8559. doi: 10.1116/1.580365.
- [125] W. Water and S.-Y. Chu. *Physical and structural properties of ZnO sputtered films*. Materials Letters, *55*(1-2):67–72 [2002]. ISSN 0167577X. doi: 10.1016/S0167-577X(01)00621-8.
- [126] S. Nasser, H. Afify, S. El-Hakim *et al.* *Structural and physical properties of sprayed copper–zinc oxide films*. Thin Solid Films, *315*(1-2):327–335 [1998]. ISSN 00406090. doi: 10.1016/S0040-6090(97)00757-8.
- [127] F. van de Pol, F. Blom and T. Popma. *R.f. planar magnetron sputtered ZnO films I: Structural properties*. Thin Solid Films, *204*(2):349–364 [1991]. ISSN 00406090. doi: 10.1016/0040-6090(91)90074-8.
- [128] O. Kluth, G. Schöpe, J. Hüpkes *et al.* *Modified Thornton model for magnetron sputtered zinc oxide: film structure and etching behaviour*. Thin Solid Films, *442*(1-2):80–85 [2003]. ISSN 00406090. doi: 10.1016/S0040-6090(03)00949-0.
- [129] S.-N. Bai and T.-Y. Tseng. *Electrical and optical properties of ZnO:Al thin films grown by magnetron sputtering*. Journal of Materials Science: Materials in Electronics, *20*(3):253–256 [2009]. ISSN 0957-4522, 1573-482X. doi: 10.1007/s10854-008-9712-3.
- [130] P. Cannard and R. Tilley. *New intergrowth phases in the ZnO-In<sub>2</sub>O<sub>3</sub> system*. Journal of Solid State Chemistry, *73*(2):418–426 [1988]. ISSN 00224596. doi: 10.1016/0022-4596(88)90127-2.
- [131] C. H. Yi, I. Yasui and Y. Shigesato. *Oriented Tin-Doped Indium Oxide Films on <001> Preferred Oriented Polycrystalline ZnO Films*. Japanese Journal of Applied Physics, *34*(Part 1, No. 3):1638–1642 [1995]. ISSN 00214922. doi: 10.1143/JJAP.34.1638.
- [132] Y.-C. Liang, C.-C. Liu, C.-C. Kuo *et al.* *Structural and opto-electronic properties of transparent conducting (222)-textured Zr-doped In<sub>2</sub>O<sub>3</sub>/ZnO bilayer films*. Journal of Crystal Growth, *310*(16):3741–3745 [2008]. ISSN 00220248. doi: 10.1016/j.jcrysgro.2008.05.053.

- 
- [133] D. Shin, J. H. Shin, H. Y. Lee *et al.* *Characteristics of IZO/AZO and AZO/IZO Bi-layer transparent conducting thin films prepared by using PLD.* Journal of the Korean Physical Society, *60*(10):1662–1665 [2012]. ISSN 0374-4884, 1976-8524. doi: 10.3938/jkps.60.1662.
- [134] X. Sun, L. Wang and H. Kwok. *Improved ITO thin films with a thin ZnO buffer layer by sputtering.* Thin Solid Films, *360*(1-2):75–81 [2000]. ISSN 00406090. doi: 10.1016/S0040-6090(99)01077-9.
- [135] P. Thilakan, C. Minarini, S. Loreti *et al.* *Investigations on the crystallisation properties of RF magnetron sputtered indium tin oxide thin films.* Thin Solid Films, *388*(1-2):34–40 [2001]. ISSN 00406090. doi: 10.1016/S0040-6090(01)00820-3.
- [136] H. Nakazawa, Y. Ito, E. Matsumoto *et al.* *The electronic properties of amorphous and crystallized In<sub>2</sub>O<sub>3</sub> films.* Journal of Applied Physics, *100*(9):093706 [2006]. ISSN 0021-8979, 1089-7550. doi: 10.1063/1.2358829.
- [137] Y. S. Jung and S. S. Lee. *Development of indium tin oxide film texture during DC magnetron sputtering deposition.* Journal of Crystal Growth, *259*(4):343–351 [2003]. ISSN 00220248. doi: 10.1016/j.jcrysgro.2003.07.006.
- [138] W. Yin, K. Smithe, P. Weiser *et al.* *Hydrogen centers and the conductivity of In<sub>2</sub>O<sub>3</sub> single crystals.* Physical Review B, *91*(7) [2015]. ISSN 1098-0121, 1550-235X. doi: 10.1103/PhysRevB.91.075208.
- [139] Y. Wu, B. Macco, D. Vanhemel *et al.* *Atomic Layer Deposition of In<sub>2</sub>O<sub>3</sub>:H from InCp and H<sub>2</sub>O/O<sub>2</sub>: Microstructure and Isotope Labeling Studies.* ACS Applied Materials & Interfaces, *9*(1):592–601 [2017]. ISSN 1944-8244, 1944-8252. doi: 10.1021/acsami.6b13560.
- [140] M. D. Heinemann, M. F. A. M. van Hest, M. Contreras *et al.* *Amorphous oxides as electron transport layers in Cu(In,Ga)Se<sub>2</sub> superstrate devices: Amorphous oxides in Cu(In,Ga)Se<sub>2</sub> superstrate devices.* physica status solidi (a), *214*(5):1600870 [2017]. ISSN 18626300. doi: 10.1002/pssa.201600870.
- [141] S. Merdes, R. Sáez-Araoz, A. Ennaoui *et al.* *Recombination mechanisms in highly efficient thin film Zn(S,O)/Cu(In,Ga)S<sub>2</sub> based solar cells.* Applied Physics Letters, *95*(21):213502 [2009]. ISSN 0003-6951, 1077-3118. doi: 10.1063/1.3266829.
- [142] P. Innocenzi. *Infrared spectroscopy of sol-gel derived silica-based films: a spectromicrostructure overview.* Journal of Non-Crystalline Solids, *316*(2-3):309–319 [2003]. ISSN 00223093. doi: 10.1016/S0022-3093(02)01637-X.
- [143] C. M. Ghimbeu, M. Lumberras, J. Schoonman *et al.* *Electrosprayed Metal Oxide Semiconductor Films for Sensitive and Selective Detection of Hydrogen Sulfide.* Sensors, *9*(11):9122–9132 [2009]. ISSN 1424-8220. doi: 10.3390/s91109122.

- [144] P. Singh and D. Kaur. *Room temperature growth of nanocrystalline anatase TiO<sub>2</sub> thin films by dc magnetron sputtering*. *Physica B: Condensed Matter*, 405(5):1258–1266 [2010]. ISSN 09214526. doi: 10.1016/j.physb.2009.11.061.
- [145] R. Henríquez, E. Muñoz, E. A. Dalchiele *et al.* *Electrodeposition of In<sub>2</sub>O<sub>3</sub> thin films from a dimethylsulfoxide based electrolytic solution*. *physica status solidi (a)*, 210(2):297–305 [2013]. ISSN 18626300. doi: 10.1002/pssa.201228534.
- [146] M. Bouttemy, P. Tran-Van, I. Gerard *et al.* *Thinning of CIGS solar cells: Part I: Chemical processing in acidic bromine solutions*. *Thin Solid Films*, 519(21):7207–7211 [2011]. ISSN 00406090. doi: 10.1016/j.tsf.2010.12.219.
- [147] Z. Jehl, F. Erfurth, N. Naghavi *et al.* *Thinning of CIGS solar cells: Part II: Cell characterizations*. *Thin Solid Films*, 519(21):7212–7215 [2011]. ISSN 00406090. doi: 10.1016/j.tsf.2010.12.224.
- [148] T. Mise and T. Nakada. *Microstructural properties of (In,Ga)<sub>2</sub>Se<sub>3</sub> precursor layers for efficient CIGS thin-film solar cells*. *Solar Energy Materials and Solar Cells*, 93(6-7):1000–1003 [2009]. ISSN 09270248. doi: 10.1016/j.solmat.2008.11.028.
- [149] V. Deprédurand, T. Bertram, M. Thévenin *et al.* *Alternative Etching for Improved Cu-rich CuInSe<sub>2</sub> Solar Cells*. *MRS Proceedings*, 1771:163–168 [2015]. ISSN 1946-4274. doi: 10.1557/opl.2015.447.
- [150] T. Jäger, Y. E. Romanyuk, S. Nishiwaki *et al.* *Hydrogenated indium oxide window layers for high-efficiency Cu(In,Ga)Se<sub>2</sub> solar cells*. *Journal of Applied Physics*, 117(20):205301 [2015]. ISSN 0021-8979, 1089-7550. doi: 10.1063/1.4921445.
- [151] H. Kitami, M. Miyashita, T. Sakemi *et al.* *Quantitative analysis of ionization rates of depositing particles in reactive plasma deposition using mass-energy analyzer and Langmuir probe*. *Japanese Journal of Applied Physics*, 54(1S):01AB05 [2015]. ISSN 0021-4922, 1347-4065. doi: 10.7567/JJAP.54.01AB05.
- [152] W. Yang, Z. Liu, D.-L. Peng *et al.* *Room-temperature deposition of transparent conducting Al-doped ZnO films by RF magnetron sputtering method*. *Applied Surface Science*, 255(11):5669–5673 [2009]. ISSN 01694332. doi: 10.1016/j.apsusc.2008.12.021.
- [153] W. Yang, Z. Wu, Z. Liu *et al.* *Room temperature deposition of Al-doped ZnO films on quartz substrates by radio-frequency magnetron sputtering and effects of thermal annealing*. *Thin Solid Films*, 519(1):31–36 [2010]. ISSN 00406090. doi: 10.1016/j.tsf.2010.07.048.
- [154] K. H. Kim, K. C. Park and D. Y. Ma. *Structural, electrical and optical properties of aluminum doped zinc oxide films prepared by radio frequency magnetron sputtering*.

- 
- Journal of Applied Physics, *81*(12):7764–7772 [1997]. ISSN 0021-8979, 1089-7550. doi: 10.1063/1.365556.
- [155] T. Koida, T. Kaneko and H. Shibata. *Carrier Compensation Induced by Thermal Annealing in Al-Doped ZnO Films*. *Materials*, *10*(2):141 [2017]. ISSN 1996-1944. doi: 10.3390/ma10020141.
- [156] W.-J. Jeong and G.-C. Park. *Electrical and optical properties of ZnO thin film as a function of deposition parameters*. *Solar Energy Materials and Solar Cells*, *65*(1-4):37–45 [2001]. ISSN 09270248. doi: 10.1016/S0927-0248(00)00075-1.
- [157] A. Grimm, D. Kieven, R. Klenk *et al.* *Junction formation in chalcopyrite solar cells by sputtered wide gap compound semiconductors*. *Thin Solid Films*, *520*(4):1330–1333 [2011]. ISSN 00406090. doi: 10.1016/j.tsf.2011.04.150.
- [158] J. Lindahl, J. Keller, O. Donzel-Gargand *et al.* *Deposition temperature induced conduction band changes in zinc tin oxide buffer layers for Cu(In,Ga)Se 2 solar cells*. *Solar Energy Materials and Solar Cells*, *144*:684–690 [2016]. ISSN 09270248. doi: 10.1016/j.solmat.2015.09.048.
- [159] T. C. Kaspar, T. Droubay and J. E. Jaffe. *ZnO/Sn:In<sub>2</sub>O<sub>3</sub> and ZnO/CdTe band offsets for extremely thin absorber photovoltaics*. *Applied Physics Letters*, *99*(26):263504 [2011]. ISSN 0003-6951, 1077-3118. doi: 10.1063/1.3672218.
- [160] M. Burgelman. *SCAPS* [2015].
- [161] P. D. C. King, T. D. Veal, D. J. Payne *et al.* *Surface Electron Accumulation and the Charge Neutrality Level in In<sub>2</sub>O<sub>3</sub>*. *Physical Review Letters*, *101*(11) [2008]. ISSN 0031-9007, 1079-7114. doi: 10.1103/PhysRevLett.101.116808.
- [162] F. Rüggeberg and A. Klein. *The In<sub>2</sub>O<sub>3</sub>/CdTe interface: A possible contact for thin film solar cells?* *Applied Physics A*, *82*(2):281–285 [2006]. ISSN 0947-8396, 1432-0630. doi: 10.1007/s00339-005-3329-7.
- [163] M. Ruckh, D. Schmid and H. W. Schock. *Photoemission studies of the ZnO/CdS interface*. *Journal of Applied Physics*, *76*(10):5945–5948 [1994]. ISSN 0021-8979, 1089-7550. doi: 10.1063/1.358417.
- [164] S.-K. Hong, T. Hanada, H. Makino *et al.* *Band alignment at a ZnO/GaN (0001) heterointerface*. *Applied Physics Letters*, *78*(21):3349–3351 [2001]. ISSN 0003-6951, 1077-3118. doi: 10.1063/1.1372339.

- [165] F. Säuberlich, J. Fritsche, R. Hunger *et al.* *Properties of sputtered ZnO films and its interfaces with CdS*. *Thin Solid Films*, 431-432:378–381 [2003]. ISSN 00406090. doi: 10.1016/S0040-6090(03)00251-7.
- [166] E. A. Kraut, R. W. Grant, J. R. Waldrop *et al.* *Precise Determination of the Valence-Band Edge in X-Ray Photoemission Spectra: Application to Measurement of Semiconductor Interface Potentials*. *Physical Review Letters*, 44(24):1620–1623 [1980]. ISSN 0031-9007. doi: 10.1103/PhysRevLett.44.1620.
- [167] M. Perego, G. Seguini and M. Fanciulli. *XPS and IPE analysis of HfO<sub>2</sub> band alignment with high-mobility semiconductors*. *Materials Science in Semiconductor Processing*, 11(5-6):221–225 [2008]. ISSN 13698001. doi: 10.1016/j.mssp.2008.10.008.
- [168] C. J. Dong, W. X. Yu, M. Xu *et al.* *Valence band offset of Cu<sub>2</sub>O/In<sub>2</sub>O<sub>3</sub> heterojunction determined by X-ray photoelectron spectroscopy*. *Journal of Applied Physics*, 110(7):073712 [2011]. ISSN 0021-8979, 1089-7550. doi: 10.1063/1.3641637.
- [169] X. K. Ning, Z. J. Wang, Y. N. Chen *et al.* *Valence-band offset and forward-backward charge transfer in manganite/NiO and manganite/LaNiO<sub>3</sub> heterostructures*. *Nanoscale*, 7(48):20635–20641 [2015]. ISSN 2040-3364, 2040-3372. doi: 10.1039/C5NR06026E.
- [170] J. Si, S. Jin, H. Zhang *et al.* *Experimental determination of valence band offset at PbTe/CdTe(111) heterojunction interface by x-ray photoelectron spectroscopy*. *Applied Physics Letters*, 93(20):202101 [2008]. ISSN 0003-6951, 1077-3118. doi: 10.1063/1.3028028.
- [171] V. Srikant and D. R. Clarke. *On the optical band gap of zinc oxide*. *Journal of Applied Physics*, 83(10):5447–5451 [1998]. ISSN 0021-8979, 1089-7550. doi: 10.1063/1.367375.
- [172] T. Kamiya and M. Kawasaki. *ZnO-Based Semiconductors as Building Blocks for Active Devices*. *MRS Bulletin*, 33(11):1061–1066 [2008]. ISSN 0883-7694, 1938-1425. doi: 10.1557/mrs2008.226.
- [173] H. Song, G. Zheng, A. Yang *et al.* *The growth of ZnO on buffer layers and the valence band offset determined by X-ray photoemission spectroscopy*. *Solid State Communications*, 150(41-42):1991–1994 [2010]. ISSN 00381098. doi: 10.1016/j.ssc.2010.08.022.
- [174] T. Jäger, Y. E. Romanyuk, B. Bissig *et al.* *Improved open-circuit voltage in Cu(In,Ga)Se<sub>2</sub> solar cells with high work function transparent electrodes*. *Journal of Applied Physics*, 117(22):225303 [2015]. ISSN 0021-8979, 1089-7550. doi: 10.1063/1.4922351.
- [175] W. Witte, R. Carron, D. Hariskos *et al.* *IZO or IOH Window Layers Combined with Zn(O,S) and CdS Buffers for Cu(In,Ga)Se<sub>2</sub> Solar Cells*. *physica status solidi (a)*, 214(12):1700688 [2017]. ISSN 18626300. doi: 10.1002/pssa.201700688.

- [176] J.-H. Wi, W.-J. Lee, D.-H. Cho *et al.* *Characteristics of temperature and wavelength dependence of CuInSe<sub>2</sub> thin-film solar cell with sputtered Zn(O,S) and CdS buffer layers: Temperature and wavelength dependence of CuInSe<sub>2</sub> thin-film solar cell.* *physica status solidi (a)*, *211*(9):2172–2176 [2014]. ISSN 18626300. doi: 10.1002/pssa.201431232.
- [177] S.-Y. Park, E.-W. Lee, S.-H. Lee *et al.* *Investigation of ZnO/CdS/CuIn<sub>x</sub>Ga<sub>1-x</sub>Se<sub>2</sub> interface reaction by using hot-stage TEM.* *Current Applied Physics*, *10*(3):S399–S401 [2010]. ISSN 15671739. doi: 10.1016/j.cap.2010.02.043.
- [178] S. Kijima and T. Nakada. *High-Temperature Degradation Mechanism of Cu(In,Ga)Se<sub>2</sub>-Based Thin Film Solar Cells.* *Applied Physics Express*, *1*:075002 [2008]. ISSN 1882-0778, 1882-0786. doi: 10.1143/APEX.1.075002.
- [179] S. Merdes, V. Malinen, F. Ziem *et al.* *Zn(O,S) buffer prepared by atomic layer deposition for sequentially grown Cu(In,Ga)(Se,S)<sub>2</sub> solar cells and modules.* *Solar Energy Materials and Solar Cells*, *126*:120–124 [2014]. ISSN 09270248. doi: 10.1016/j.solmat.2014.03.044.
- [180] H. Hoppe, M. Seeland and B. Muhsin. *Optimal geometric design of monolithic thin-film solar modules: Architecture of polymer solar cells.* *Solar Energy Materials and Solar Cells*, *97*:119–126 [2012]. ISSN 09270248. doi: 10.1016/j.solmat.2011.09.037.
- [181] N. F. Cooray, K. Kushiya, A. Fujimaki *et al.* *Large area ZnO films optimized for graded band-gap Cu(InGa)Se<sub>2</sub>-based thin-film mini-modules.* *Solar Energy Materials and Solar Cells*, *49*(1-4):291–297 [1997]. ISSN 09270248. doi: 10.1016/S0927-0248(97)00055-X.
- [182] M. D. Heinemann, J. Berry, G. Teeter *et al.* *Oxygen deficiency and Sn doping of amorphous Ga<sub>2</sub>O<sub>3</sub>.* *Applied Physics Letters*, *108*(2):022107 [2016]. ISSN 0003-6951, 1077-3118. doi: 10.1063/1.4938473.
- [183] M. Ruckh, D. Schmid, M. Kaiser *et al.* *Influence of substrates on the electrical properties of Cu(In,Ga)Se<sub>2</sub> thin films.* *Solar Energy Materials and Solar Cells*, *41-42*:335–343 [1996]. ISSN 09270248. doi: 10.1016/0927-0248(95)00105-0.
- [184] A. Steigert, I. Lauermann, R. Muydinov *et al.* *Crystallization of sputtered In<sub>2</sub>O<sub>3</sub> and In<sub>2</sub>O<sub>3</sub>:H* [2016].
- [185] D. Kieven, A. Grimm, I. Lauermann *et al.* *Band alignment at sputtered ZnS<sub>x</sub>O<sub>1-x</sub>/Cu(In,Ga)(Se,S)<sub>2</sub> heterojunctions.* *physica status solidi (RRL) - Rapid Research Letters*, *6*(7):294–296 [2012]. ISSN 18626254. doi: 10.1002/pssr.201206195.
- [186] National Institute of Standards and Technology (NIST). *Resistivity and Hall Measurements.* <https://www.nist.gov/pml/engineering-physics-division/popular-links/hall-effect/resistivity-and-hall-measurements>; Accessed 09.08.2018.

- [187] B. Arnaudov, T. Paskova, S. Evtimova *et al.* *Multilayer model for Hall effect data analysis of semiconductor structures with step-changed conductivity*. *Physical Review B*, 67(4) [2003]. ISSN 0163-1829, 1095-3795. doi: 10.1103/PhysRevB.67.045314.
- [188] R. W. Cahn, P. Haasen and E. J. Kramer. *Materials science and technology: a comprehensive treatment*. VCH, Weinheim ; New York [1991]. ISBN 978-3-527-26813-9.
- [189] Park Systems. *Basic Contact AFM & Dynamic Force Microscope (DFM)*. Tech. rep. [2018]. [https://www.parksystems.com/images/spmmodes/standard/2\\_Basic-Contact-AFM-and-Dynamic-Force-Microscopy-\(DFM\).pdf](https://www.parksystems.com/images/spmmodes/standard/2_Basic-Contact-AFM-and-Dynamic-Force-Microscopy-(DFM).pdf); Accessed 10.08.2018.

---

## List of Publications

---

### *First-authorship*

- Darja Erfurt, Marc D. Heinemann, Stefan Körner, Bernd Szyszka, Reiner Klenk, Rutger Schlatmann, "Improved electrical properties of pulsed DC magnetron sputtered hydrogen doped indium oxide after annealing in air", *Materials Science in Semiconductor Processing* 89 (2019) 170–175; doi: 10.1016/j.mssp.2018.09.012
- Darja Erfurt, Marc D. Heinemann, Sebastian S. Schmidt, Stefan Körner, Bernd Szyszka, Reiner Klenk, Rutger Schlatmann, "Substrate influence on the growth of hydrogen doped indium oxide", *ACS Appl. Energy Mater.* 2018, 1, 5490-5499; doi: 10.1021/acsaem.8b01039

### *Co-authorship*

- Houda Ennaceri, Darja Erfurt, Lan Wang, Tristan Köhler, Abdelhafed Taleb, Asmae Khaldoun, Abdallah El Kenz, Abdelilah Benyoussef, Ahmed Ennaoui, "Deposition of multifunctional TiO<sub>2</sub> and ZnO top-protective coatings for CSP application", *Surface & Coatings Technology* 298 (2016) 103–113; DOI: 10.1016/j.surfcoat.2016.04.048
- Houda Ennaceri, Lan Wang, Darja Erfurt, Wiebke Riedel, Gauri Mangalgiri, Asmae Khaldoun, Abdallah El Kenz, Abdelilah Benyoussef, Ahmed Ennaoui, "Water-resistant surfaces using zinc oxide structured nanorod arrays with switchable wetting property", *Surface & Coatings Technology* 299 (2016) 169–176; DOI: 10.1016/j.surfcoat.2016.04.056
- Sri Hari Bharath Vinoth Kumar, Ruslan Muydinov, Tat'yana Kol'tsova, Darja Erfurt, Alexander Steigert, Oleg Tolochko, and Bernd Szyszka, "Graphene assisted effective hole-extraction on In<sub>2</sub>O<sub>3</sub>:H/CH<sub>3</sub>NH<sub>3</sub>PbI<sub>3</sub> interface: Studied by modulated surface spectroscopy", *Appl. Phys. Lett.* 112, 011604 (2018); DOI: 10.1063/1.5017579
- Stefan Körner, Manuel Hartig, Ruslan Muydinov, Darja Erfurt, Reiner Klenk, Bernd Szyszka, and Rutger Schlatmann, "Serial cosputtering for aluminum doping manipulated

zinc oxide as front contact for Cu(In,Ga)Se<sub>2</sub> solar cells", *Japanese Journal of Applied Physics* 57, 08RC18 (2018); DOI: 10.7567/JJAP.57.08RC18

- Ruslan Muydinov, Alexander Steigert, Markus Wollgarten, Pawel Michalowski, Ulrike Bloeck, Andreas Pflug, Darja Erfurt, Reiner Klenk, Stefan Körner, Iver Lauermann, Bernd Szyszka, "Crystallisation phenomena of In<sub>2</sub>O<sub>3</sub>:H films", *Materials* 2019, 12(2), 266; DOI: 10.3390/ma12020266

#### Conference Contributions

- Darja Erfurt, Marc D. Heinemann, Stefan Körner, Bernd Szyszka, Reiner Klenk, Christian A. Kaufmann, Rutger Schlatmann, "Influence of the Zn(O,S) buffer onto the In<sub>2</sub>O<sub>3</sub>:H front contact in CIGS solar cells" *Poster presentation, IW-CIGSTech 7 Munic, Germany, 23.06.2016 - 23.06.2016*
- Marc D. Heinemann, Klaus Ellmer, Moritz Kölbach, Dieter Greiner, Darja Erfurt, Reiner Klenk, Rutger Schlatmann, Christian A. Kaufmann, "Amorphous InGaO<sub>x</sub>, a versatile electron transport layer for solar cells", *Oral presentation, 20th International Conference on Ternary and Multinary Compounds ("ICTMC-20") Halle (Saale), Germany, 05.09.2016 - 09.09.2016*
- Darja Erfurt, Marc D. Heinemann, Stefan Körner, Bernd Szyszka, Christian A. Kaufmann, Rutger Schlatmann, "Integration of IOH as a front contact layer for CIGS cells and modules", *Oral presentation, 6th International Symposium on Transparent Conductive Materials Platania-Chania Crete, Greece, 09.10.2016 - 13.10.2016*
- Darja Erfurt, "Wasserstoff-dotiertes In<sub>2</sub>O<sub>3</sub> als TCO mit hoher Mobilität", *Oral presentation, 6. EFDS-Workshop "Transparente leitfähige Materialien (TCO/TCM): Festkörperphysikalische Grundlagen und Technologien" Erfurt, Germany, 22.11.2016 - 23.11.2016*
- Darja Erfurt, Marc D. Heinemann, Stefan Körner, Bernd Szyszka, Reiner Klenk, Rutger Schlatmann, "In<sub>2</sub>O<sub>3</sub>:H with high mobility prepared by DC sputtering and annealing in air", *Oral presentation, EMRS Spring 2017 Strasbourg, France, 22.05.2017 - 26.05.2017*
- Darja Erfurt, Marc D. Heinemann, Stefan Körner, Bernd Szyszka, Reiner Klenk, Rutger Schlatmann, "Hydrogen doped Indium Oxide as a high mobility TCO prepared by DC sputtering and annealing in air", *Poster presentation, IW-CIGSTech8 Stuttgart, Germany, 30.05.2017 - 30.05.2017*
- Stefan Körner, Ruslan Muydinov, Darja Erfurt, Manuel Hartig, Bernd Szyszka, Reiner Klenk, "Doping manipulated AZO as front TCO by using serial co-sputtering for CIGS solar cells", *Oral presentation, PVSEC27 Otsu, Japan, 12.11.2017 - 17.11.2017*

- Darja Erfurt, Marc D. Heinemann, Stefan Körner, Bernd Szyszka, Reiner Klenk, Rutger Schlatmann, "Challenges of an Hydrogen Doped Indium Oxide Window Layer in CIGS Modules", *Oral presentation, PVSEC-27, 27th International Photovoltaic Science and Engineering Conference Otsu, Japan, 12.11.2017 - 17.11.2017*
- Darja Erfurt, Marc D. Heinemann, Reiner Klenk, Takashi Koida, Jiro Nishinaga, Yukiko Kamikawa, Hajime Shibata, Hasan A. Yetkin, Bernd Szyszka, Rutger Schlatmann, "Strategies to improve the electron mobility of IOH on CIGS samples", *Poster presentation, IW-CIGSTech 9 Stuttgart, Germany, 18.06.2018 - 18.06.2018*
- Stefan Körner, Darja Erfurt, Reiner Klenk, Michael Kirsch, Bernd Szyszka, Rutger Schlatmann, "Thickness variation of zinc magnesium oxide as buffer layer in CIGS solar cells", *Poster presentation, IW-CIGSTech 9 Stuttgart, Germany, 18.06.2018 - 18.06.2018*
- Bernd Szyszka, Ruslan Muydinov, Stefan Körner, Manuel Hartig, Marlene Härtel, Darja Erfurt, Reiner Klenk, Christian A. Kaufmann, Bernd Stannowski, Rutger Schlatmann, Alexander Steigert, Michael Siemers, Stephan Ulrich, Volker Sittinger, Andreas Pflug, "High mobility TCOs for photovoltaics", *Oral presentation to be published at 7th International Symposium on Transparent Conductive Materials Crete, Greece, 14.10.2018 - 19.10.2018*

---

## Acknowledgement

---

First I would like to thank Prof. Dr. Bernd Szyszka for supervising this thesis. In addition I want to thank Prof. Dr. Rutger Schlatmann for the opportunity to do my PhD at the PVcomB. I am also very grateful to Prof. Dr. Günter Bräuer for reviewing this thesis. Dr. Jürgen Bruns is acknowledged for being the chairperson of the defence.

My sincere thanks to Dr. Marc Heinemann and Dr. Reiner Klenk for the continuous support, your feedback and the great supervision. Also Christian Kaufmann is acknowledged for his supervision, in particular at the beginning of my PhD. Especially I want to thank Prof. Dr. Rutger Schlatmann and Dr. Takashi Koida for the change to join the AIST for four months. Dr. Takashi Koida is further acknowledged for supervising me at AIST and introducing me into the Japanese culture. I had a wonderful time and learned a lot! Furthermore I want to acknowledge Dr. Hajime Shibata, Dr. Jiro Nishinaga and Dr. Yukiko Kamikawa and all former colleagues at AIST for their support during my stay.

Katja Mayer-Stillrich and Manuel Hartig are acknowledged for the support on the LOS1, Michael Kirsch for the deposition of ZnO and Zn(O,S) films. Carola Klimm and Iris Dorbandt are acknowledged for support with EBSD and SEM measurements, respectively. I also want to thank Ulrike Bloek, Dr. Sebastian Schmidt and Dr. Chen Li for sample preparation and providing TEM measurements. Also I want to thank Alexander Steigert for the support and help with XPS/UPS measurements.

Many thanks to the whole PVcomB and especially the CIGS-team for maintain the systems and labs, for providing all kind of samples and the general support. Among other things I acknowledge Bianka Bunn for the preparation of glass substrates, Christian Wolf, Ralf Habrecht, Marc Heinemann, Jakob Lauche, Tim Münchenberg and Tobias Bertram for the preparation of CIGS absorber. Iris Dorbandt and Tim Münchenberg are acknowledged for CdS deposition. I acknowledge all students at PVcomB for the support to characterize the solar cells. Sonja Cinque and Guillermo Farias are acknowledged for the module structuring. Dr. Reiner Klenk, Alexandros Cruz and Matthias Müller are acknowledged for proof reading the manuscript of this thesis.

Furthermore I want to acknowledge all members of the PVcomB for the great working atmosphere and distinct cake culture. Special thanks to my PhD colleagues, i.e. Stefan Körner, Tim Kodalle, Alexandros Cruz, Jan-Peter Bäcker, Natalie Preissler, Hasan Yetkin and more for the great time in the "Doktorandenbüro". In addition I would like to thank Daniel Meza for being such a nice PhD spokesperson and for organizing the "Stammtisch".

I acknowledge the German Federal Ministry for Economic Affairs and Energy for the financial support and for founding the TCO4CIGS project (contract number 0325762). Also I would like to thank all the partners of the project for the continuous exchange of knowledge.

In particular I want to thank my friends and especially my parents for the unlimited support during the last years.